Regge models of hadronic elastic scattering at all angles

Kearney, P. J.

Regge Models of Hadronic Elastic Scattering

at All Angles

Thesis submitted to the University of Durham for the Degree of Doctor of Philosophy by

P. J. Kearney, B. Sc. (Liverpool)

September 1982

For Ann

Abstract

A Regge-based model for the elastic scattering of hadrons at all angles is developed, which combines the best features of a conventional Regge model with those of a quark interchange model. As t tends to $-\infty$ the meson Regge trajectories approach negative integers, while their residues vary like negative integer powers of t, the sum of the two integers being such that the Dimensional Counting Rule is satisfied.

Within this framework nucleon-nucleon differential cross sections, polarizations and spin correlation parameters, and $\pi^{\pm}p$ differential cross-sections are studied. It is found that the Regge pole terms dominate for $-t \lesssim 1$ $(GeV/c)^2$; Regge cuts become important at intermediate t values, but at large angles the meson-Reggeons (with trajectories now approaching integers) re-emerge as the most important contributions. Fits are presented which give a good account of the experimental data at all angles for the pp, pn and $\bar{p}p$ differential cross-sections, polarizations and spin correlation parameters (where available) and the $\pi^{\pm}p$ differential cross-sections.

Acknowledgements

I would like to thank, in particular, my wife Ann for helping me retain some vestige of sanity, my parents for their help when time seemed to be running out, my supervisor Dr. P. D. B. Collins and the rest of the Physics Dept. at Durham for their advice and assistance, the Departments of Physics and Applied Maths and Theoretical Physics of the University of Liverpool for allowing me use of their facilities, and my typist Elaine Bennett for transforming an illegible manuscript. Three years of the research for this thesis were funded by a Science Research Council grant.

Table of Contents

LIST OF FIGURES

Introduction

Hadronic interactions are usually viewed in one of two ways, depending on the degree of momentum transfer (p_T) involved. When $|p_T|$ is small a hadron behaves as a single particle of finite size, but as $|p_T|$ increases more detail can be resolved until the hadron looks like a collection of point-like constituents. In a similar way small momentum transfer reactions are most simply described in terms of exchange of Regge trajectories on which lie composite hadrons, while large momentum transfer phenomena are best explained by exchange of the constituents. In between there lies a grey area where both viewpoints become complicated.

The aim of this work is to develop a Regge-based picture of elastic hadronic scattering throughout the angular range from 0° to 90° centre of mass scattering angle. This model will embody the strengths of traditional Regge phenomenology at small angles and the properties predicted by constituent models at large angles.

Chapter 1 reviews the Regge and constituent models. These are developed into the basis for an all angle model in Chapter 2, which is then applied to studies of p-p, n-p and $\bar{p}p$ differential cross-sections (Chapter 3), pp, n-p and $\bar{p}p$ Polarization and spin correlation parameters (Chapter 4) and $\pi^{\pm}p$ differential cross sections (Chapter 5). The definitions and conventions used throughout the thesis are given in Appendix A. The figures are located at the end of each chapter.

CHAPTER 1

THEORETICAL BACKGROUND

1.1 Introduction

In High Energy Physics, interactions between particles are usually described as occurring via the exchange of field quanta. In most such theories (e.g. Quantum Electrodynamics) calculation of observable quantities can only be performed for diagrams and sums of diagrams containing a limited number of exchanges. Where the coupling of the quanta to the physical particles is small, a theory (if renormalisable) can make a precise prediction of an observable by the summation of relatively few contributing diagrams.

In the strong interaction, however, the couplings need not be small. Quantum Chromodynamics (Q.C.D.), the currently favoured hadronic theory, predicts a renormalised coupling of coloured quarks and gluons, which is dependent on kinematical variables; for $Q^2 >> Q_o^2$

$$\alpha_s(Q^2) = \frac{\alpha_s(Q_o^2)}{1 + \frac{(11.N_c - 2.N_F)}{12\pi}\alpha_S(Q_o^2)\ln\left[\frac{Q^2}{Q_o^2}\right]} \qquad (1.1.1)$$

where N_c = number of colours (=3) and N_F = number of flavours; Q^2 is a (4-momentum transfer)^2 variable and Q_o^2 is the renormalization point (see e.g. Politzer (1974)). For processes involving large Q^2, $\alpha_s(Q^2)$ is much less than one and quark scattering amplitudes are easy to calculate. Since quarks are confined, however, estimation of physical observables involves making assumptions about the effects which bind the hadrons together, so that the predictive power of Q.C.D. is limited even at large Q^2. When Q^2 is small, $\alpha_s(Q^2)$ is large, so diagrams involving many elementary exchanges are important and the situation becomes much too complicated to calculate in perturbative Q.C.D.

These multiple exchanges may however be regarded as being combined into particles. For large $\alpha_s(Q^2)$ they are bound into colour singlet states corresponding to mesons, baryons and perhaps "glueballs". In this view, the small Q^2 region is simplified, being governed by the exchange of Regge pole trajectories. But at larger Q^2 the picture is complicated by multiple particle exchanges i.e. Regge cuts.

Hadronic scattering at small angles and high incident energy is, thus, described simply in terms of Regge theory, and at large angles and high energy by the exchange of elementary quarks and gluons. This first chapter is concerned with a more detailed discussion of the theoretical situation, prior to the proposal of a model to account for the elastic scattering data over the whole angular range. Section 1.2 looks at the Dimensional Counting Rule, which successfully predicts the energy dependence of elastic differential cross-sections at fixed large-angles. The large-angle experimental results are outlined in Section 1.3, while Section 1.4 discusses the merits of various quark and gluon exchange scattering mechanisms. In Section 1.5 we turn to small angle scattering and describe the particular Regge model to be used later as a basis for fitting this kinematical region.

1.2 The Dimensional Counting Rule

At large centre of mass scattering angles (θ_{cm}), hadronic $2\rightarrow2$ scattering differential cross sections, when multiplied by an integer power of s, are found to scale (i.e. are independent of any dimensional variable). Thus it is found that

$$s^N \frac{d\sigma}{dt}(AB\rightarrow CD) = f\left(\frac{t}{s}\right) \qquad (1.2.1)$$

(s, t, u are Mandelstam variables – see App. A)

where $f\left(\frac{t}{s}\right)$ is independent of dimensional variables. The power of s for a given reaction is predicted by the Dimensional Counting Rule:

$$N \equiv n - 2 = n_A + n_B + n_C + n_D - 2 \qquad (1.2.2)$$

where $n_i \equiv$ number of elementary (quark) constituents of hadron i ($i = A, B, C, D$) (See e.g. Brodsky et al (1975a)).

A simple, naive derivation of the rule is as follows. Postulate that the incident and final state hadrons are each composed of n_i elementary constituents which have their momenta aligned with that of the hadron (a reasonable assumption in the infinite momentum frame). Assume that the interactions between constituents of the same hadron or between constituents of different hadrons are scale invariant, though not necessarily the same. Such an interaction might be gluon exchange between quarks (see fig. (1.2.1)). The amplitude for this diagram is

$$A \propto u(p_A)\gamma^\mu \bar{u}(p_C) \frac{g_{\mu\nu}}{(p_A-p_C)^2+i\varepsilon} u(p_B)\gamma^\nu \bar{u}(p_D) \qquad (1.2.3)$$

where the $u(p_i)$ are the wave functions of the free quarks in momentum space. At high energy each wave function contributes a factor proportional to $(\text{momentum})^{\frac{1}{2}}$ to this amplitude. The gluon propagator $(g_{\mu\nu}/(p_A-p_C)^2 + i\varepsilon)$ contributes a factor proportional to $(\text{momentum})^{-2}$, so that if all momentum variables are scaled by a factor, λ, say, then the amplitude is independent of λ and is said to be scale invariant.

Returning to the derivation, hard scattering now occurs between two elementary constituents of the incident hadrons (fig. (1.2.2)). Further exchanges (of number m, say) occur among the constituents to bind them into the final state hadrons. Since the interactions between contituents are scale invariant, the only dimensional variables entering the scattering amplitude will be a factor of q^{-2} ($q^2=(\text{momentum transfer})^2$) for each of the internal constituent propagators (marked with —•— in fig. (1.2.2) of which there are m, so that

$$\text{amplitude, } A \propto \left(\frac{1}{q^2}\right)^m F\left(\frac{t}{s}\right) \tag{1.2.4}$$

The leading contributions to the amplitude at large q^2 will be the diagrams with the lowest value of m,

$$m_{min} = n_c + n_d - 2 \tag{1.2.5}$$

so that for q^2 large

$$A \propto \left(\frac{1}{q^2}\right)^{n_c+n_d-2} F\left(\frac{t}{s}\right) \tag{1.2.6}$$

Note that for q - q scattering as in fig. (1.2.1), $n_c+n_d=2$ and the amplitude is scale invariant as expected. Since $q^2 \propto S$ and $n_A + n_B = n_C + n_D$

$$\frac{d\sigma}{dt} \propto \frac{1}{S^2} |A|^2 \propto \frac{1}{S^{n-2}} F^2\left(\frac{t}{S}\right) \tag{1.2.7}$$

with $n \equiv n_A + n_B + n_C + n_D$.

The Fock-space components of the initial and final state hadrons which give the leading behaviour as $s\to\infty$ can be seen to be those containing the smallest number of constituents, so from now on n_i is assumed to be the number of valence constituents of hadron i. The behaviour of $d\sigma/dt$ in N-N and π-N elastic scattering are thus predicted to be

$$\begin{aligned} \frac{d\sigma}{dt}\ (NN \to NN) &\propto \frac{1}{s^{10}}\ f_{NN}\left(\frac{t}{s}\right) \\ \frac{d\sigma}{dt}\ (\pi N \to \pi N) &\propto \frac{1}{s^{8}}\ f_{\pi N}\left(\frac{t}{s}\right) \end{aligned} \tag{1.2.8}$$

at large t and s.

(1.2.8) only gives the leading behaviour at high energy and large angle, of course. At smaller values of s corrections proportional to $s^{-(n+i)}$ (i=1,2,3) must be added, making $d\sigma/dt$ more strongly dependent upon s at fixed angle in this energy region.

The Dimensional Counting Rule, then, gives very definite predictions for the behaviour of elastic scattering data, provided high enough energies are studied. In the following section, these predictions are compared to the available experimental data.

1.3 Large Angle Scattering Data

A. Differential Cross Sections

Measurements of large angle differential cross sections are available up to $s \simeq 50$ $(GeV/c)^2$ for p-p scattering over a wide range of energies (see Fig. (1.3.1)). Other reactions are less well studied (see e.g. Figs. (1.3.2-4)), but nevertheless provide a good test of the predictions of Section (1.2). The form of (1.2.1) has been fitted to experimental data and some of the results are summarized in Table (1.3.1). Those results marked "own fit" are described in more detail in Section 2.2 and depicted in Figs. (2.2.2) and (2.2.3). The Dimensional Counting Rule predictions give generally excellent agreement with the data, especially considering their asymptotic nature and the limited energy ranges so far covered by experiments.

B. Spin Measurements

Recent experiments at the Z.G.S. at Argonne have produced large angle measurements of pp spin-spin asymmetry parameters which, together with polarization measurements, can give further insight into the underlying scattering process.

The polarization parameter is defined by

$$P \equiv \frac{d\sigma/dt\ (\uparrow) - d\sigma/dt\ (\downarrow)}{d\sigma/dt\ (\uparrow) + d\sigma/dt\ (\downarrow)} \qquad (1.3.1)$$

(either beam or target polarized)

and the spin-spin correlation parameters by

$$A_{ij} \equiv \frac{d\sigma/dt\ (\uparrow,\uparrow) + d\sigma/dt\ (\downarrow\downarrow) - d\sigma/dt\ (\uparrow\downarrow) - d\sigma/dt\ (\downarrow\uparrow)}{d\sigma/dt\ (\uparrow,\uparrow) + d\sigma/dt\ (\downarrow\downarrow) + d\sigma/dt\ (\uparrow\downarrow) + d\sigma/dt\ (\downarrow\uparrow)} \qquad (1.3.2)$$

where $\uparrow$, $\downarrow$ refer to the polarization state of the beam and target, and i, j refer to the directions relative to which the beam and target polarizations are measured.

$$i, j = n, l, s$$

where n = normal to the scattering plane

l = longitudinal (along beam direction)

s = "sideways" (perpendicular to n and l).

Polarization and A_{nn} measurements are available over the complete angular range in p-p at p_{lab} = 6 GeV/c and 12 GeV/c and other A_{ij} at p_{lab} = 6 GeV/c (Figs. 1.3.5-7). Additionally there are 90^{o}cm data for A_{nn} between these two energies (Fig. (1.3.8)).

Because of the symmetry of pp→pp scattering, P must vanish at 90^{o}cm independent of the model; and this, of course is confirmed by the data. In contrast in np→np at p_{lab} = 6 GeV/c, $P \simeq -.4$ at 90^{o} (Fig. (1.3.9)).

At p_{lab} = 11.75 GeV/c A_{nn} is seen to rise steeply to ~ 0.6 at 90^{o}cm, corresponding to

$$\frac{d\sigma(\uparrow\uparrow)}{dt} \Big/ \frac{d\sigma}{dt}\ (\uparrow\downarrow) = 3.9 \begin{matrix} +1.5 \\ -1.0 \end{matrix} \qquad (1.3.3)$$

This value is surprisingly large considering the smallness of A_{nn} at lower angles, and provides a test of theoretical models. It is impossible to tell from the available data whether A_{nn} is continuing to rise to 90^{o}cm or levels off before this point. The amazing similarities between Figs. (1.3.6) and (1.3.8) should be noted.

A_{ll} and A_{ss} show a much smoother rise in magnitude than A_{nn}, and A_{ss} seems to be effectively zero throughout the angular range.

The various asymmetry parameters thus exhibit a number of features, which should help in deciding upon the nature of the large angle scattering mechanism.

To summarise this section, any successful model for hadronic elastic scattering at large angles must:

a) predict a fixed angle energy dependence for the differential cross section in accordance with the Dimensional Counting rule.

b) reproduce the angular dependence of the differential cross section at fixed energy.

c) account for the relative signs and magnitudes of the asymmetries, A_{ij}, at large angle.

d) explain the relative magnitudes of amplitudes in related processes.

e) be compatible with theories of small angle scattering.

In Section 1.4 various possible mechanisms are discussed and the most likely one chosen.

1.4 The Nature of the large angle scattering mechanism

So far, nothing has been specified about the exchange between the composite hadrons except that it must be scale invariant. The two most obvious candidates to compose such an exchange are quarks and gluons. Consider first gluon exchange.

A. Exchange of a single gluon between the hadrons

In the spirit of the parton model the $q\bar{q}g$ coupling is taken to be small for large momentum transfer processes, due to asymptotic freedom. If colour confinement is neglected for the present, the dominant contribution from gluon exchanges will come from single gluon diagrams (see Fig. (1.4.1) for a typical leading contribution to N-N scattering). q-q scattering via a gluon is scale invariant so that hadron-hadron scattering by this mechanism obeys the Dimensional Counting Rule.

Redrawing Fig. (1.4.1) as Fig. (1.4.2) and comparing with Fig. (1.4.3), it becomes obvious that

$$\frac{d\sigma}{dt}\ (AB\to AB) \;=\; C\,\frac{d\sigma}{dt}\ (qq\text{-}qq)\ F_A^{\,2}(t)\ F_B^{\,2}(t) + u \text{ channel exchange} \qquad (1.4.1)$$

where F_A and F_B are the electromagnetic form factors for hadrons A and B, and $C \leqslant 81$ is a factor counting the number of coherent diagrams.

Now, at $p_{lab} = 11.75$ GeV/c and $\theta_{cm} = 90^\circ$

$$\frac{d\sigma^{expt.}}{dt}\ (pp\to pp) \simeq 10^{-5}\ \text{mb/(GeV)}^2 \qquad (1.4.2)$$

(from Crabb et al (1978))

which, when substituted into (1.4.1) together with a proton electromagnetic form factor $F_p(t) \sim t^{-2}$ gives

$$\frac{d\sigma^{expt}}{dt}\ (qq\to qq) \;\geqslant\; 100\ \text{mb/(GeV)}^2 \qquad (1.4.3)$$

compared with the naive Q.C.D. prediction

$$\frac{d\sigma^{QCD}}{dt}\ (qq\to qq) = \frac{2}{q}\ \alpha_s^{\,2}(t)\ \frac{4\pi}{t^2} \simeq 10^{-3}\ \text{mb/GeV}^2 \qquad (1.4.4)$$

with $\alpha_s(-10) \simeq 0.15$.

Not only is the naive QCD prediction much smaller than the experimental value, but single gluon exchange between colour singlet states, such as the physical hadron, is forbidden. At least two gluons must be exchanged between the quarks so that the hadrons remain colourless, thus at least two extra powers of $\alpha_s(t)$ are needed in (1.4.4) making the Q.C.D. estimate even smaller.

Furthermore, if the data are fitted with a single effective Regge pole, i.e.

$$\frac{d\sigma}{dt} \propto \frac{1}{s^2}\, s^{2\alpha^R_{eff}(t)}\, |\beta(t)|^2 \qquad (1.4.5)$$

the effective Regge trajectory $\alpha^R_{eff}(t)$ in Fig. (1.4.4) is obtained. It has been argued (Coon et al (1978)) that the form

$$\frac{d\sigma}{dt} \propto \frac{1}{s^2}\, u^{2\alpha^R_{eff}(t)}\, |\beta(t)|^2 \qquad (1.4.6)$$

is a better one to use to obtain $\alpha^R_{eff}(t)$ in which case Fig. (1.4.5) results. In either case, at large -t $\alpha^R_{eff}(t)$ is seen to fall below -1, whereas exchange of vector gluons would produce $\alpha^R_{eff} \simeq 1$. Thus, apart from the Dimensional Counting Rule there is little evidence in the differential cross section data for gluon exchange being the dominant mechanism, and plenty against it. It may, however, have a place in describing large p_T jet phenomena.

B. Landshoff triple-gluon exchange

The above arguments make it unlikely that qq→qq scattering via vector gluons is responsible for large angle elastic scattering of hadrons. Landshoff (Landshoff (1974)) put forward an alternative mechanism whereby, instead of one large momentum transfer occurring between one quark from each hadron, several transfers of lesser p_T occur between different pairs of nearly on shell quarks. In N-N scattering

(see Fig. (1.4.6)) each quark would scatter through an angle θ so that the three quarks from each nucleon would emerge in the same direction, eliminating any need for further gluon exchange in leading order diagrams to rebind the quarks into their parent particles.

The amplitude for this reaction is given by

$$A(pp\to pp) = \left[\frac{i}{(stu\mu^2)^{\frac{1}{2}}} \right]^2 A^3(qq\to qq) \qquad (1.4.7)$$

where μ^2 is a hadronic scale size (see e.g. Farrar and Wu (1975)). This corresponds to

$$\frac{d\sigma}{dt}(pp) \propto \frac{1}{s^8} f\left[\frac{t}{s}, \frac{u}{s}\right] \qquad (1.4.8)$$

The pinch singularity caused by multiple exchange of gluons between the protons gives rise to a slower energy dependence than given by the Dimensional Counting Rule, so that this amplitude would dominate at high energy. This s^{-8} energy dependence, however, is not seen at currently accessible large angles.

As in section A the effective Regge trajectory for this process must be $\alpha^R_{eff} = 1$. This, again, is in contradiction with the available large angle data which exhibit $\alpha_{eff} < -1$. Thus, although the triple scattering mechanism may be important to large angle scattering at very high energies, there is no sign of it being present at the moment. Furthermore, Brodsky et al (Brodsky et al (1979c)) have shown that when Sudakov form factors are included in the $q\bar{q}g$ vertices of Fig. (1.4.6), the Landshoff contribution is asymptotically damped, so it may never be significant.

The highest energy pp data currently available are the Cern I.S.R. measurements. These are at large $|t|$, but at energies such that $|t| \ll S$. In this regime the triple scattering formula (1.4.7) gives

$$\frac{d\sigma}{dt}\ (pp\to pp) \propto \frac{1}{t^8}\ , \qquad (1.4.9)$$

independent of s, assuming $\alpha^R_{eff} = 1$. This agrees very well with the data at large $|t|$ (see Fig. (1.4.7), but being a real contribution, cannot interfere with the almost totally imaginary Pomeron (dominant at small $|t|$) to give the observed sharp dip at $t \simeq -1.4$. The whole of this region can, however, be explained by models using a Pomeron plus a Pomeron $\otimes$ Pomeron cut (again see Fig. (1.4.7)) which accurately reproduce the dip structure.

Another point against the triple scattering mechanism in the I.S.R. region is that Landshoff and Pritchard (Landshoff and Pritchard (1980)) have calculated the effect of gluon exchange across the $q\bar{q}g$ vertices in Fig. (1.4.6). These modify 1.4.7 in the limit $s \to \infty$, $|t|$ large but $\ll s$ by a factor

$$\exp\left[-2\, b_1 \log s \log\log t + b_2 \log^2 t\right] \qquad (1.4.10)$$

with $b_1 = \frac{g^2}{8\pi^2} N_c\, n$; $b_2 = \frac{g^2}{8\pi^2} \frac{(N_c^2+1)n}{N_c}$;

N_c = no. of colours (=3) and n = no. of multiple scatterings (=3 for pp). The resulting behaviour of $d\sigma/dt$ is no longer able to describe the I.S.R. data. There is, thus, little phenomenological evidence that the Landshoff mechanism contributes to hadron-hadron scattering.

C. Quark interchange

(1) Energy dependence and form factors

Having discussed and rejected gluon exchange the other constituent-level candidate from which to compose the large $|t|$ inter-hadronic exchange is the quark. One of the principal objections to the gluon exchange mechanism discussed in part A of this section was that the predicted magnitude of the differential cross-section is much smaller than that

observed. This is because a gluon of the high momentum required couples only weakly to the valence quarks of the hadrons. Now, most of the momentum of a high energy hadron is possessed by its valence quarks. Transfer of a valence quark from one hadron to another would, then, also involve a large transfer of momentum. At least two quarks must be involved in the exchange so that all initial and final states may be colour singlets.

Fig. (1.4.8) shows a leading order (in α_s) quark interchange diagram contributing to nucleon-nucleon scattering. Notice that this contains the same number of $q\bar{q}g$ vertices as does the gluon exchange diagram of Fig. (1.4.1). However, as it is the two quarks in Fig. (1.4.8) that transfer the high momentum, the (running) strong coupling constant can be greater than in the earlier diagram, in which case this contribution to the scattering amplitude will also be greater. The possibility thus exists that such quark interchange diagrams account for the major part of the large angle scattering amplitudes.

The quark interchange mechanism is used by Brodsky et al in their Constituent Interchange Model (CIM) (e.g. Brodsky et al (1973a), (1973b), (1977) and also Brodsky et al (1979b) for a description in terms of Q.C.D.). In Brodsky et al (1977) the magnitude of the large transverse momentum differential cross section for a variety of processes, both elastic and inelastic, are fitted successfully within CIM, using only two parameters. These are constant couplings for the baryon-quark-diquark and meson-quark-antiquark vertices. There is thus no reason to suppose that the quark interchange mechanism cannot account for the size of the large-angle differential cross-sections.

The fixed angle energy dependence of a diagram such as Fig. (1.4.8) can be determined from (1.2.4), here rewritten with s replacing q^2

$$A \propto \frac{1}{s^m} \; F\left[\frac{t}{s}\right] \tag{1.4.11}$$

where m is the number of internal quark propagators (marked as —●—). Comparing Fig. (1.4.8) with Fig. (1.2.2) it can be seen that the value of m is the same in both cases, and a short investigation soon reveals that the lowest value of m possessed by an interchange diagram for a given process is determined as in (1.2.5). Thus the quark interchange mechanism obeys the Dimensional Counting Rule.

A lowest order quark interchange diagram contributing to a process AB→CD may be factorised in the following way (see also Fig. (1.4.9a))

$$A(AB \rightarrow CD) = A(Aq \rightarrow Cq) \cdot F_{BD}(t) \tag{1.4.12}$$

where $F_{BD}(t)$ is the lowest order contribution to the electromagnetic form factor. The validity of this is further illustrated by Fig. (1.4.9b) which compares the appropriate lowest order contribution to $F_{NN}(t)$ with the bottom vertex in Fig. (1.4.8). Calculation of the form factors, and of the appropriate vertices of interchange diagrams gives the following behaviour

$$F_{BD}(t) \propto \frac{1}{t^N} \tag{1.4.13}$$

where N = (number of valence quarks and antiquarks in hadrons B and D)-1

i.e. N = 1 for mesons

= 2 for baryons.

Good fits to the measured electromagnetic form factors are obtained with

$$F_{meson}(t) = \left[1 - \frac{t}{m_\rho^2}\right]^{-1}$$

and (1.4.14)

$$F_{nucleon}(t) = \left[1 - \frac{t}{m_\rho^2}\right]^{-1} \left[1 - \frac{t}{0.9}\right]^{-1}$$

where m_ρ is the mass of the ρ meson (see Collins et al (1978)). These agree with (1.4.13) in the limit at $t \to -\infty$ as expected.

The Drell-Yan-West relation (Drell and Yan (1970), West (1970)) can be used to predict the behaviour of the deep inelastic electron-proton scattering structure functions W_1 and νW_2 from (1.4.16). This states that if $F(t) \sim |t|^{-p}$ for large $|t|$, then $W_1(x)$, $\nu W_2(x) \sim (1-x)^{2p-1}$ for x close to 1 (x being the fraction of the momentum of the parent hadron formed by the longitudinal momentum of the struck constituent). So, from (1.4.13) and Drell-Yan-West

$$W_1(x), \quad \nu W_2(x) \sim (1-x)^3 \text{ as } x \to 1 \qquad (1.4.15)$$

for deep inelastic scattering of electrons off protons. The distribution of momentum among the valence quarks of a proton is found to agree well with this prediction.

(2) Angular dependence of the differential cross-section.

Gluon exchange fell down heavily in its prediction of the effective Regge trajectory, α^R_{eff}. Quark interchange is now examined for consistency with experiment in this regard.

Looking at (1.4.12) one sees that α^R_{eff} of a quark interchange diagram for a process AB→CD is determined by $A(A_q \to C_q)$ (or by $A(B_q \to D_q)$, whichever gives the highest α^R_{eff}). The form of this quark-hadron scattering amplitude is highly dependent on the precise model used. For instance, in most papers describing CIM*, Brodsky et al find

$$A_{CIM}(A_q \to C_q) \propto F_{AC}(u)$$

$$\propto \frac{1}{u^N} \qquad (1.4.16)$$

*Note: The three CIM results quoted here all relate to the version of the model which represents the proton as three q state rather than a q + core state) and hence obey the D.C.R.

where N = 1 for mesons

= 2 for baryons

Which yields in the Regge limit ($s \to \infty$, t fixed)

$$A_{CIM}\,(AB \to CD) \propto \frac{1}{s^N}\ \frac{1}{t^N} \tag{1.4.17}$$

and hence

$$\alpha^R_{CIM} = -N \tag{1.4.18}$$

In contrast, Brodsky et al (1977) contains the results

$$\frac{d\sigma}{dt}\,(\pi p \to \pi p) \propto \frac{1}{s^2}\left[\alpha \frac{s}{t^4 u^3} + \beta\, \frac{u}{t^4 s^3}\right] \tag{1.4.19}$$

(where the two terms in the brackets correspond to the two interchange topologies (see Fig. (1.4.11)) present in πp scattering and α and β are constants given by simple quark counting).

and

$$\frac{d\sigma}{dt}\,(pp \to pp) \propto \frac{1}{s^2}\left[\frac{s^2 + t^2}{t^6 u^4} + \frac{s^2 + u^2}{t^4 u^6}\right] \tag{1.4.20}$$

These yield

$$\alpha^R_{CIM}(pp) = \alpha^R_{CIM}\,(\pi p) = -1 \tag{1.4.21}$$

A third result for p-p scattering is quoted in Coon et al (1978):

$$\frac{d\sigma}{dt}\ (pp \to pp) \propto \frac{1}{s^2}\ \left[\frac{s^2}{t^3 u^3}\right]^2 \tag{1.4.22}$$

which again gives $\alpha^R_{CIM}(pp) = -1$.

The above results are all considerably closer to the α^R_{eff}'s extracted from the data (Figs. (1.4.4),(1.4.10)) than were the predictions of the gluon exchange models. Nevertheless, in the pp scattering case, where the data is most abundant and α^R_{eff} can best be pinned down, the theoretical values seem too high at large $|t|$. However, the quantities α^R_{CIM} obtained above are not the best quantities to compare with the large angle experimental results — α^R_{CIM} being appropriate for $s \to \infty$ at fixed t (and hence $s>>-t$), whereas at large angles, t is of the order $-\frac{s}{2}$. A more valid comparison may be made using the parameter

$$\tilde{\alpha}^R_{CIM} \equiv \frac{\frac{s}{2}\frac{\partial}{\partial s}\left[s^2 \frac{d\sigma}{dt}\,CIM\right]}{s^2 \frac{d\sigma_{CIM}}{dt}} \qquad (1.4.23)$$

The three versions of CIM quoted above each yield $\tilde{\alpha}^R_{CIM}(pp) \simeq -4$ at 90^ocm, which for $s = 38\ (GeV/c)^2$ corresponds to $t \simeq -19\ (GeV/c)^2$. A comparison of $\tilde{\alpha}^R_{CIM}(pp)$ at $s = 38\ (GeV/c)^2$ with results obtained from data in the range $(20 \leqslant s \leqslant 50\ (GeV/c)^2$ is shown in Fig. (1.4.12). Note that at large $|t|$ α^R_{eff} is extracted only from data at the higher end of this energy range. Although agreement is not perfect, the theoretical curves are sufficiently close to the experimental results at large -t for the discrepancy to be made up by minor changes to the assumptions used in the calculations or by higher order corrections.

(3) Helicity amplitudes and crossing relations

The spin-flavour part of the proton helicity wave function is given by

$$\sqrt{18}|p,+) = 2|u,+)|u,+)|d,-)+2|u,+)|d,-)|u,+)+2|d,-)|u,+)|u,+)$$
$$-|u,+)|u,-)|d,+) - |u,+)|d,+)|u,-) - |d,+)|u,+)|u,-)$$
$$-|u,-)|u,+)|d,+) - |u,-)|u,+)|u,+) - |d,+)|u,-)|u,+) \qquad (1.4.24)$$

$$-\sqrt{18}|p,-) = 2|u,-)|u,-)|d,+)+2|u,-)|d,+)|u,-)+2|d,+)|u,-)|u,-)$$
$$-|u,-)|u,+)|d,-) - |u,-)|d,-)|u,+) - |d,-)|u,-)|u,+)$$
$$-|u,+)|u,-)|d,-) - |u,+)|d,-)|u,-) - |d,-)|u,+)|u,-)$$

where $|q,\lambda)$ signifies the wave function of particle q of helicity $\lambda(=\pm\frac{1}{2})$. The importance of the order of the quark wave functions reflects the three possible values of the colour quantum number. Each quark must have a different colour so that the proton is a singlet under $SU(3)_{colour}$. The neutron wave function may be obtained by substituting $|u) \rightarrow -|d)$ and $|d) \rightarrow |u)$.

Using the φ_i notation outlined in Appendix B, and $\tilde{\varphi}_i$ to denote the "forward" scattering amplitude only (i.e. prior to incorporation of Fermi statistics), the experimentally measured N-N helicity amplitudes are derived below within the framework of a simple quark interchange model. Since the elementary exchanges between the consitutent quarks are via spin-1 gluons, it is assumed that the quarks do not flip helicity. It is further assumed that the amplitude of an individual diagram is independent of the flavour and helicity of the interchanged quarks, and of the nucleon flavour and helicity. Similar assumptions will be made for mesons when these are considered later. Note that only quarks of the same colour may be interchanged.

The wave functions, (1.4.25), and simple counting give, for pp scattering (see e.g. Brodsky et al (1979a))

$$\left.\begin{aligned}
\tilde{\varphi}_1 &= \left[\frac{25}{9} + \frac{1}{9} + \frac{1}{9} + \frac{4}{9}\right] f(s,t,u) = \frac{31}{9} f(s,t,u) \\
\tilde{\varphi}_3 &= \frac{14}{9} f(s,t,u) \\
\tilde{\varphi}_4 &= \frac{-17}{9} f(s,t,u) \\
\tilde{\varphi}_2 &= \tilde{\varphi}_5 = 0
\end{aligned}\right\} \quad (1.4.25)$$

where $f(s,t,u)$ is independent of the baryons involved.

Similarly for $np \to np$

$$\left.\begin{aligned}
\tilde{\varphi}_1 &= \frac{14}{9} f(s,t,u) \\
\tilde{\varphi}_3 &= \frac{22}{9} f(s,t,u) \\
\tilde{\varphi}_4 &= \frac{8}{9} f(s,t,u) \\
\tilde{\varphi}_2 &= \tilde{\varphi}_5 = 0
\end{aligned}\right\} \quad (1.4.26)$$

Fermi statistics may be incorporated into the full scattering amplitudes by combining the forward and backward scattering amplitudes according to the rules given in Appendix C. The full amplitudes are then, for pp

$$\left.\begin{aligned}
\varphi_1 &= \frac{1}{9} [31 f(s, t, u) + 31 f(s, u. t)] \\
\varphi_3 &= \frac{1}{9} [14 f(s, t, u) + 17 f(s, u, t)] \\
\varphi_4 &= \frac{-1}{9} [17 f(s, t, u) + 14 f(s, u, t)] \\
\varphi_2 &= \varphi_5 = 0
\end{aligned}\right\} \quad (1.4.27)$$

and for $np \to np$

$$\left.\begin{aligned}
\varphi_1 &= \frac{1}{9} [14 f(s, t, u) + 17 f(s, u, t)] \\
\varphi_3 &= \frac{1}{9} [22 f(s, t, u) + 25 f(s, u, t)] \\
\varphi_4 &= \frac{1}{9} [8 f(s, t, u) + 8 f(s, u, t)] \\
\varphi_2 &= \varphi_5 = 0
\end{aligned}\right\} \quad (1.4.28)$$

The $\bar{p}p$ amplitudes are obtained from (1.4.28) by crossing

$$\left.\begin{aligned} \varphi_1 &= \tfrac{1}{9}\,[17\ f(u,\ t,\ s) + 14\ f(u,\ s,\ t)] \\ \varphi_3 &= \tfrac{1}{9}\,[31\ f(u,\ t,\ s) + 31\ f(u,\ s,\ t)] \\ \varphi_4 &= \tfrac{1}{9}\,[14\ f(u,\ t,\ s) + 17\ f(u,\ s,\ t)] \\ \varphi_2 &= \varphi_5 = 0 \end{aligned}\right\} \qquad (1.4.29)$$

Table (1.4.1) compares predictions of the three types of model discussed in this section for the helicity amplitudes at 90°cm. Derivations of the Landshoff scattering amplitudes may be found in Farrar and Wu (1975). The predictions given by Farrar and Wu are more exact than those quoted in Table (1.4.1), which are approximations obtained using a simplified version of the model.

The spin averaged differential cross-section, in terms of the helicity amplitudes is

$$\frac{d\sigma}{dt} = \left[\,|\varphi_1|^2 + |\varphi_2|^2 + |\varphi_3|^2 + |\varphi_4|^2 + 4|\varphi_5|^2\,\right] K(S) \qquad (1.4.30)$$

where K(S) is a kinematical factor independent of nucleon flavour. The quark interchange prediction for the ratio of $d\sigma/dt$ ($np\to np$) to $d\sigma/dt$ ($pp\to pp$) at 90°cm is

$$\frac{\frac{d\sigma}{dt}\,(np\to np;90^{\circ}\text{cm})_{QI}}{\frac{d\sigma}{dt}\,(pp\to pp;90^{\circ}\text{cm})_{QI}} = \frac{(31)^2 + (47)^2 + (16)^2}{(62)^2 + (31)^2 + (31)^2} \simeq 0.59 \qquad (1.4.31)$$

In the triple gluon exchange model, this ratio is $\simeq 0.31$, while in the single gluon exchange model it is $\simeq 0.33$. These are compared with experiment in Fig. (1.4.13). All three predictions are in qualitative agreement with the data, the gluon scattering figures being rather better, but the data is at relatively low energies ($s<25(\text{GeV}/c)^2$), where pre-asymptotic corrections may be needed to all the theories.

The ratio $d\sigma/dt\ (\bar{p}p \to \bar{p}p)/d\sigma/dt(pp-pp)$ is not well determined experimentally at high energy and large angle. At p_{lab} = 5 GeV/c and 90^{o}cm its value is ~1/100 (Chabaud et al (1972)). The only 90^{o}cm measurement at higher energy is from preliminary data at 12 GeV/c (de Bellefon et al (1978)) which yields $\lesssim \frac{1}{30}$. Single gluon exchange predicts the ratio to be 0.068 at 90^{o}cm, while the Landshoff mechanism gives 0.39. The CIM prediction is

$$\frac{d\sigma}{dt}(\bar{p}p) \Big/ \frac{d\sigma}{dt}(pp) = \left[\frac{s}{u}\right]^{-4} \simeq 2^{-4} \simeq 0.063 \qquad (1.4.32)$$

although this ratio is very sensitive to the angular dependence of the pp scattering amplitudes, and other interpretations of quark interchange give different answers. No firm conclusions can be drawn from these results, but experiment seems to favour theories which predict $\frac{d\sigma}{dt}(pp)$ to be much larger than $\frac{d\sigma}{dt}(\bar{p}p)$.

The asymmetries, A_{ij}, and polarization are easily determined from the predictions summarized in Table (1.4.1) using their definitions in terms of helicity amplitudes from Appendix B. These are compared with the experimental values at 90^{o}cm in Table (1.4.2) (see Figs. (1.3.5-7) for data). In general, quark interchange, gluon exchange and Landshoff predictions are all in qualitative agreement with experiment or else plausible excuses can be found why this is not so. It is thus impossible to discriminate between the mechanisms using spin data alone. Measurements at higher energies would be welcomed as tests of these constituent models.

The relations between πp elastic scattering amplitudes are easier to derive because pions have spin zero and hence there is only one helicity wave function for each type of pion. The charged pion helicity wave functions are

$$|\pi^+) = \frac{1}{\sqrt{2}} \left[|\bar{d}^+)|u^-) - |\bar{d}^-)|u^+) \right]$$
$$|\pi^-) = \frac{1}{\sqrt{2}} \left[|d^+)|\bar{u}^-) - |d^-)|\bar{u}^+) \right] \qquad (1.4.33)$$

The quark interchange predictions for $\pi^{\pm}p$ elastic scattering helicity amplitudes may be obtained using (1.4.25) and (1.4.34) and simple counting. These are, for $\pi^+p \to \pi^+p$

$$\varphi^{\text{nonflip}} = \frac{12}{36} F(s,t,u) + \frac{6}{36} F(u,t,s) \qquad (1.4.34)$$
$$\varphi^{\text{flip}} = 0$$

and for $\pi^-p \to \pi^-p$

$$\varphi^{\text{nonflip}} = \frac{6}{36} F(s,t,u) + \frac{12}{36} F(u,t,s) \qquad (1.4.35)$$

where $F(s,t,u)$ is independent of the flavour of the external particles.

The ratio of the cross sections at 90°cm is again strongly affected by the angular dependence of the amplitudes. Brodsky et al [Brodsky et al (1973a)] find that

$$\frac{F(s,t,u)_{CIM}}{F(u,t,s)_{CIM}} = 4 \text{ at } 90^\circ\text{cm}$$

leading to a prediction of

$$\frac{d\sigma}{dt}(\pi^+p \to \pi^+p)_{CIM} \Big/ \frac{d\sigma}{dt}(\pi^-p \to \pi^-p) = \frac{81}{36} = 2.25 \qquad (1.4.36)$$

The large angle data at present contains no clearly discernible difference between π^+p and π^-p differential cross-sections, however, the error bars are such as to tolerate easily ratios of the order of (1.4.36).

In this section three alternative models for large angle elastic scattering of hadrons have been considered and assessed in the light of the criteria listed at the end of Section 1.3. Exchange of gluons between one quark from each hadron was excluded because it could not account for the magnitude of the large angle differential cross section nor its

angular dependence. Triple gluon exchange does not reproduce the DCR prediction and encounters the same problem with the angular dependence. The quark interchange mechanism, however, does not meet with these difficulties, and gives predictions for crossing relations between different processes, and between different helicity amplitudes of the same reaction, which are always at least in qualitative agreement with the data. For these reasons, the quark interchange mechanism will be assumed to be the correct model for elastic scattering in the limits of $\theta_{cm} \to 90^{\circ}$ and $s \to \infty$. A review of many of the topics discussed in this section can be found in Brodsky et al (1979a). Having now dealt with large angle scattering, Section 1.5 will be concerned with the small angle regime. Ways in which these two kinematical regions may be linked by a single theory will be examined in Chapter 2.

1.5 A Regge model for small angle scattering

The Regge theory approach to small angle scattering is well established and very successful. A Regge amplitude is composed of contributions from exchanges of trajectories on which lie the physical hadrons. A trajectory, $\alpha(t)$, is the path across the complex angular momentum plane traced by a singularity in the scattering amplitude. When a trajectory passes through either an even or an odd (dependent on it signature) positive integer for a positive value of t, there is a pole in the amplitude corresponding to a resonance of mass $\sqrt{t}$ and with the quantum numbers of the trajectory. Extrapolated to negative values of t, the trajectory governs the behaviour of its contributions to the scattering amplitude. A pole trajectory yields a contribution of the form

$$A_R = \begin{bmatrix} 1 \\ i \end{bmatrix} T_R(t)\, e^{-i\frac{\pi}{2}\alpha_R(t)}\, s^{\alpha_R(t)} \qquad (1.5.1)$$

where $T_R(t)$ is a real function and the factor of 1 or i depends on whether the signature of the trajectory is +1 or -1. (1.5.1) is valid in the limit as $s \to \infty$ with t fixed.

If sufficiently large energies are taken, only a few contributions like (1.5.1) should be necessary to approximate an amplitude. These are the ones whose trajectories are highest lying at the value of t being considered. In elastic scattering amplitudes it is the vacuum quantum number Pomeron (P) trajectory, with $\alpha_P(0) \simeq 1$ which dominates at highest energy and $-t \lesssim 1$. At lower energies the next highest lying trajectories become important. For small $|t|$, these are the natural parity meson poles, ρ, A_2, ω, f, with $\alpha_R(0) \simeq 0.5$. At larger $|t|$, cuts (multiple exchanges), whose trajectories have smaller gradients than those of the poles which compose them, should become significant. The Regge picture, thus becomes more complicated as one moves from small $|t|$ to large $|t|$, as more and more cuts become involved. A comprehensive review of Regge-physics is found in Collins (1977).

The model adopted here as a basis for small angle scattering is the Reggeon Photon Coupling Analogy (R.P.C.A.) of Collins et al (Collins et al (1978 a,b,c)). This predicts relationships among the couplings of the leading exchanges, P, ρ, A_2, ω, f. The pairs f, ω and A_2, ρ are considered as approximately exchange degenerate (EXD). Exchange degeneracy requires that the two exchanges, one of each signature, have the same couplings, residues and trajectories, so that their sum constitutes a purely real amplitude as required by duality in processes where the s-channel quantum numbers are exotic. The P and f couplings are related by the f-Dominated Pomeron hypothesis, and the isoscalar to isovector meson couplings by the Vector Dominance hypothesis.

Within the R.P.C.A. model, trajectories are assumed to be straight lines. The Pomeron trajectory is determined to be

$$\alpha_P(t) = 1.067 + 0.1\ t \qquad (1.5.2)$$

by fitting to $d\sigma/dt$ ($pp \to pp$) at very high energies. The meson trajectories are fitted as

$$\left.\begin{aligned} \alpha_f(t) &= 0.50 + t \\ \alpha_\omega(t) &= 0.40 + 0.96\,t \\ \alpha_\rho(t) &= 0.51 + 0.85\,t \\ \alpha_{A_2}(t) &= 0.42 + 0.85\,t \end{aligned}\right\} \qquad (1.5.3)$$

using data from a variety of processes.

The contribution of a pole trajectory, α_R is written in the form

$$A^{\lambda_A\lambda_C}_{\lambda_B\lambda_D}(AB\to CD;\,R) = -\left[\frac{2\sqrt{-t}}{m_A}\right]^{|\lambda_A-\lambda_C|}\cdot\left[\frac{2\sqrt{-t}}{m_B}\right]^{|\lambda_B-\lambda_D|}\cdot R(t)\cdot\frac{1}{\Gamma(\alpha_R(t))}$$

$$\beta^{\lambda_A\lambda_C}(AC;R)\cdot\beta_{\lambda_B\lambda_D}(BD;R)\cdot\frac{1}{\left(1-\frac{t}{0.9}\right)^N}\cdot$$

$$e^{-\frac{i\pi\alpha_R(t)}{2}}\; s^{\alpha_R(t)} \qquad (1.5.4)$$

where the λ's are the helicities of the initial and final state hadrons; N is the number of $B\bar{B}$ R or $B\bar{B}$ P vertices to allow for the difference between baryon and meson electromagnetic form factors, N = 0 for $\pi\pi\to\pi\pi$, N = 1 for $\pi p\to\pi p$, N = 2 for $pp\to pp$;

$$\left.\begin{aligned} R(t) &= \frac{1}{2\sin(\pi\alpha(t)/2)} \quad \text{for signature +1 exchanges} \\ \text{and} &= \frac{i}{2\cos(\pi\alpha(t)/2)} \quad \text{for signature -1 exchanges} \end{aligned}\right\} \qquad (1.5.5)$$

The β's are real and in general are functions of t.

A small EXD-breaking term is introduced between the couplings of the f and $\overset{\omega}{\Phi}$ to baryons, so that $\beta(\text{baryon baryon};f;t=0) = (1+0.14)\cdot\beta(\text{baryon baryon};\omega;t=0)$. The following changes are made to allow for absorption in the helicity non-flip amplitudes due to the presence of cuts:

a) A factor of $0.435.\left[1 - \frac{t}{0.9}\right]$ is included in the real and imaginary parts of the ρ and A_2 amplitudes.

b) The factor of $\alpha_\rho(t)$ in the imaginary part of the amplitude becomes

$$\alpha_\rho(0) \left[1 + \frac{t}{0.19}\right] e^{1.9t} \left[1 - \frac{t}{0.9}\right] \qquad (1.5.6)$$

c) The factor of $\alpha_\omega(t)$ in the real and imaginary parts of the ω amplitude becomes

$$\alpha_\omega(0) \left[1 + \frac{t}{0.19}\right] \left[1 - \frac{t}{0.9}\right]^2$$

This model provides a good simultaneous fit to many reactions for $s \gtrsim 10$ $(GeV/c)^2$ and $|t| \lesssim 1$ $(GeV/c)^2$ as illustrated by Figs. (1.5.1). Further details relevant to particular processes will be described where necessary.

Models have now been established for both large and small angle scattering. The problem of integrating these into a single model covering all angles will be dealt with in Chapter 2.

1.6 Conclusion

In this chapter, hadronic elastic scattering has been examined from two view points. In the Regge theory view, small $|t|$ scattering at high energy is simply described in terms of the exchange of a small number of pole trajectories. At large $|t|$, the picture is complicated by the presence of multi-particle-exchange cuts - more and more cuts becoming important as t becomes more negative. Conversely, if the interaction is seen as the exchange of elementary quarks and gluons, it is the large-momentum-transfer region, where the strong coupling, α_s is small, that presents the simple picture. The small angle regime, where α_s is large, is complicated by the importance of diagrams involving very large numbers of elementary exchanges.

The quark interchange mechanism has been selected as the most likely model for large angle scattering after comparison with other elementary exchange mechanisms. In Chapter 2 quark interchange and Regge models will be examined more closely with particular reference to the no-man's-land of intermediate angle. A model will then be formulated to describe hadronic elastic scattering across the whole angular range. This model will be refined and applied to various processes in the ensuing chapters.

Table (1.3.1)

Reaction	D.C.R. value of n	Fitted n	Data range and reference for fit
$np \to np$	10	10.40 ± 0.34	$10 < s < 22.4$ (GeV/c)^2 (Stone et al (1977))
		9.81 ± 0.05	
		9.7 ± 0.5	all pp data for $\|t\|$, $\|u\| > 2.3$ (GeV/c)^2 (Landshoff and Polkinghorne 1973))
$pp \to pp$	10		
		9.9 ± 0.3	all pp data f $\|t\| > 2.5$, $s < 50$ (GeV/c)^2 (Own result)
$\pi^- p \to \pi^- p$	8	8 ± 1	Brodsky et al (1973c))
$\pi^+ p \to \pi^+ p$	8	7 ± 1	
$K^+ p \to K^+ p$	8	8 ± 1	
$K_L p \to K_s p$	8	8.5 ± 1.4	
$K_o p \to \pi^+ \Lambda$	8	7.4 ± 1.4	
$K_o p \to \pi^+ \Sigma$	8	8.1 ± 1.4	
$\pi^\pm p \to \pi^\pm p$	8	8.0 ± 0.5	(Own result; angular form taken from Brodsky et al (1973a) fitted for $19 < s < 60$, large angle)

Table (1.4.1)

	C I M	Triple gluon	Single gluon
pp→pp			
φ_1	Q, say	L, say	S, say
φ_2	0	0	0
φ_3	Q/2	3L/8	$\frac{13}{28}$ S
φ_4	-Q/2	-3L/8	$-\frac{13}{28}$ S
φ_5	0	0	0
np→np			
φ_1	Q/2	L/2	S/2
φ_2	0	0	0
φ_3	49Q/62	3L/8	$\frac{13}{28}$ S
φ_4	16Q/62	0	0
φ_5	0	0	0

Table (1.4.2)

Process	Parameter	CIM	Triple gluon	Single gluon	Agreement with experiment
pp→pp	P	0	0	0	Good, but the value of 0 at 90^{o}cm is guaranteed by symmetry considerations
	A_{nn}	0.33	0.22	.30	Experiment gives 0.59±0.1 at p_{lab} = 11.75 GeV/c and 90^{o}cm. A_{nn} seems to be levelling out after a steep rise and may fall at larger values of s and $\|t\|$ to a predicted value. Qualitative agreement in that values higher than small $\|t\|$ measurements are predicted.
	A_{11}	-0.33	-0.36	-.40	Qualitative agreement. It is difficult to say whether the data exhibits dip/peak structure towards large angle due to large error bars.
	A_{ss}	-0.33	-0.22	-.30	Largest angle measurement ($\simeq 45^{o}$cm at p_{lab} =6 GeV/c) shows a fall towards the predicted values.
	A_{sl}	0	0	0	Data are consistent with zero.
np→np	P	0	0	0	Only available large angle data (90^{o}cm 6 GeV/c) give P ≃ -0.3. Discrepancy may be due to low energy effects.
	A_{nn}	-0.44	0	0	)) No large angle data available, but for 6 GeV/c,)) t = ≃-1, A_{nn} ≃-0.2 perhaps indicating a large negative)) A_{nn} at large angle, which would favour quark)) interchange.
	A_{11}	0.44	-0.36	-.07	
	A_{ss}	0.44	0	0	
	A_{sl}	0	0	0	

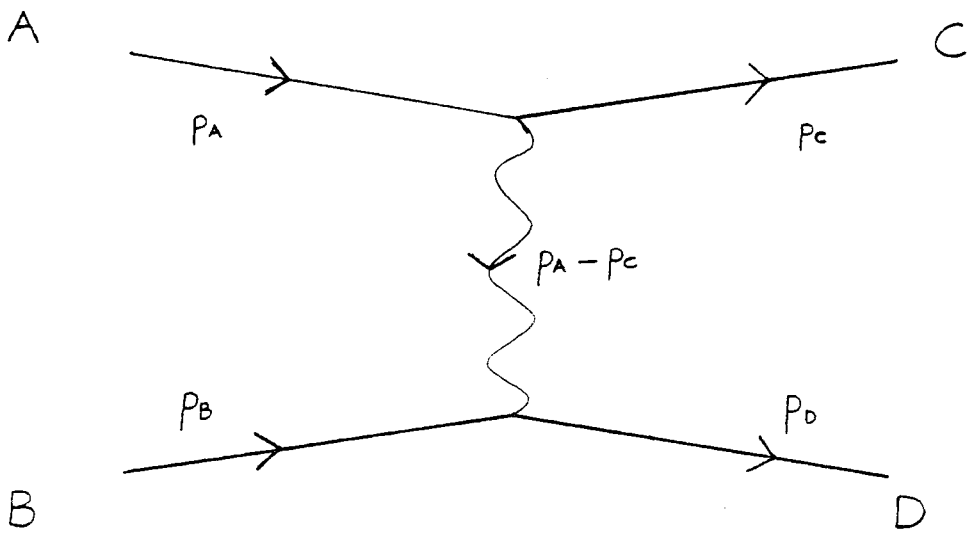

Fig. (1.2.1)

Quark-quark scattering via a single gluon exchange

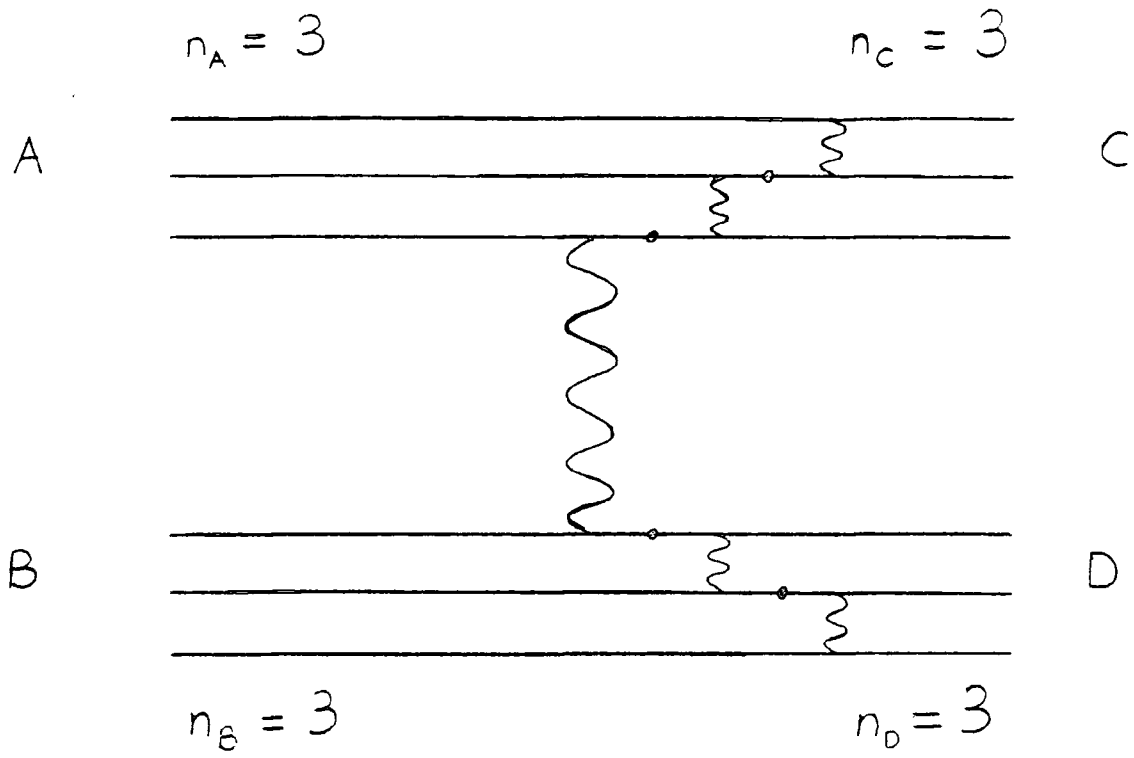

Fig. (1.2.2)

A typical diagram contributing in leading order to N-N scattering by a process obeying the Dimensional Counting Rule. The dots indicate the off mass shell fermion propagators which contribute to the scaling behaviour in (1.2.4).

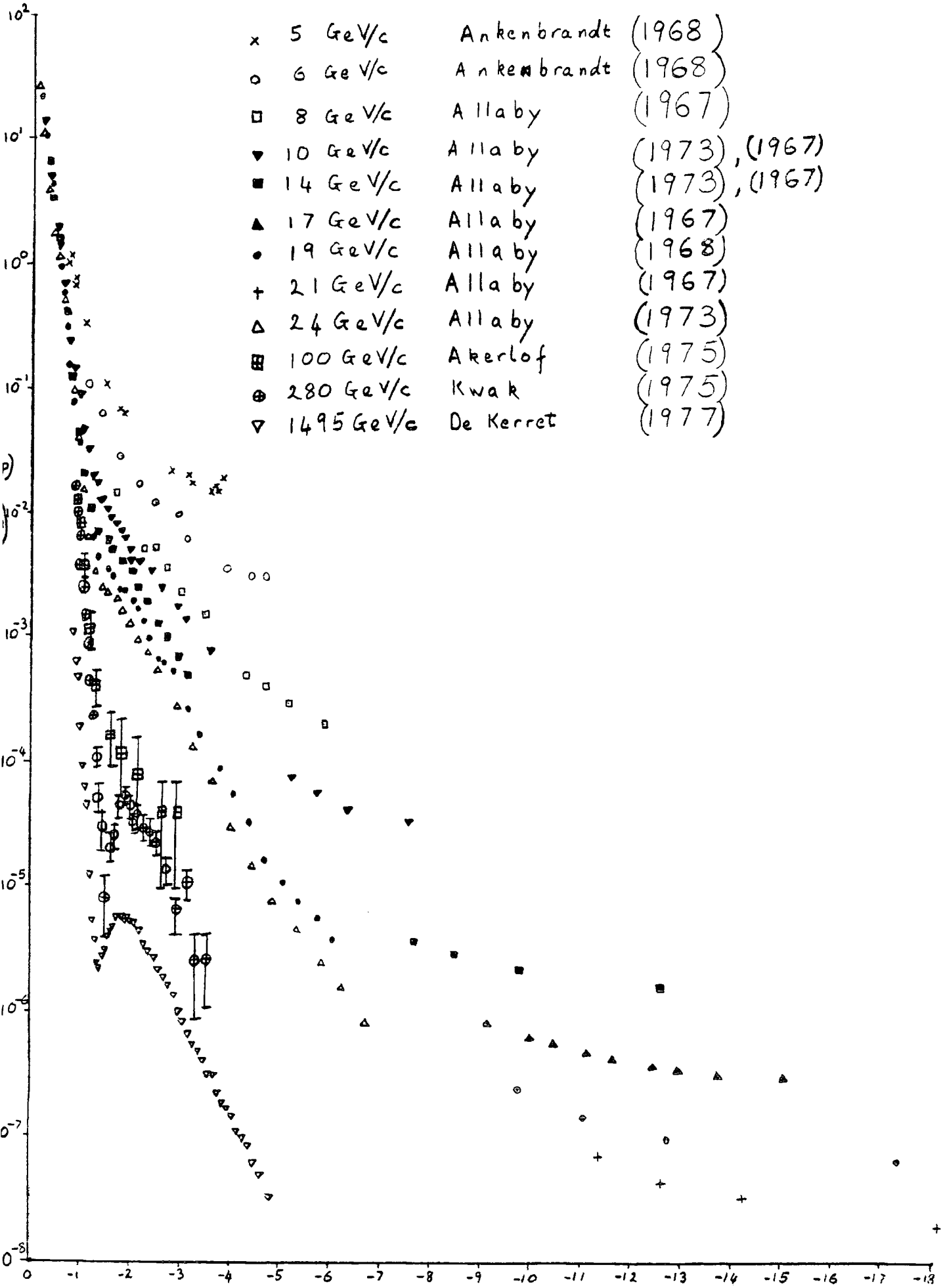

Fig. (1.3.1): Experimental measurements of $\frac{d\sigma}{dt}$ (pp)

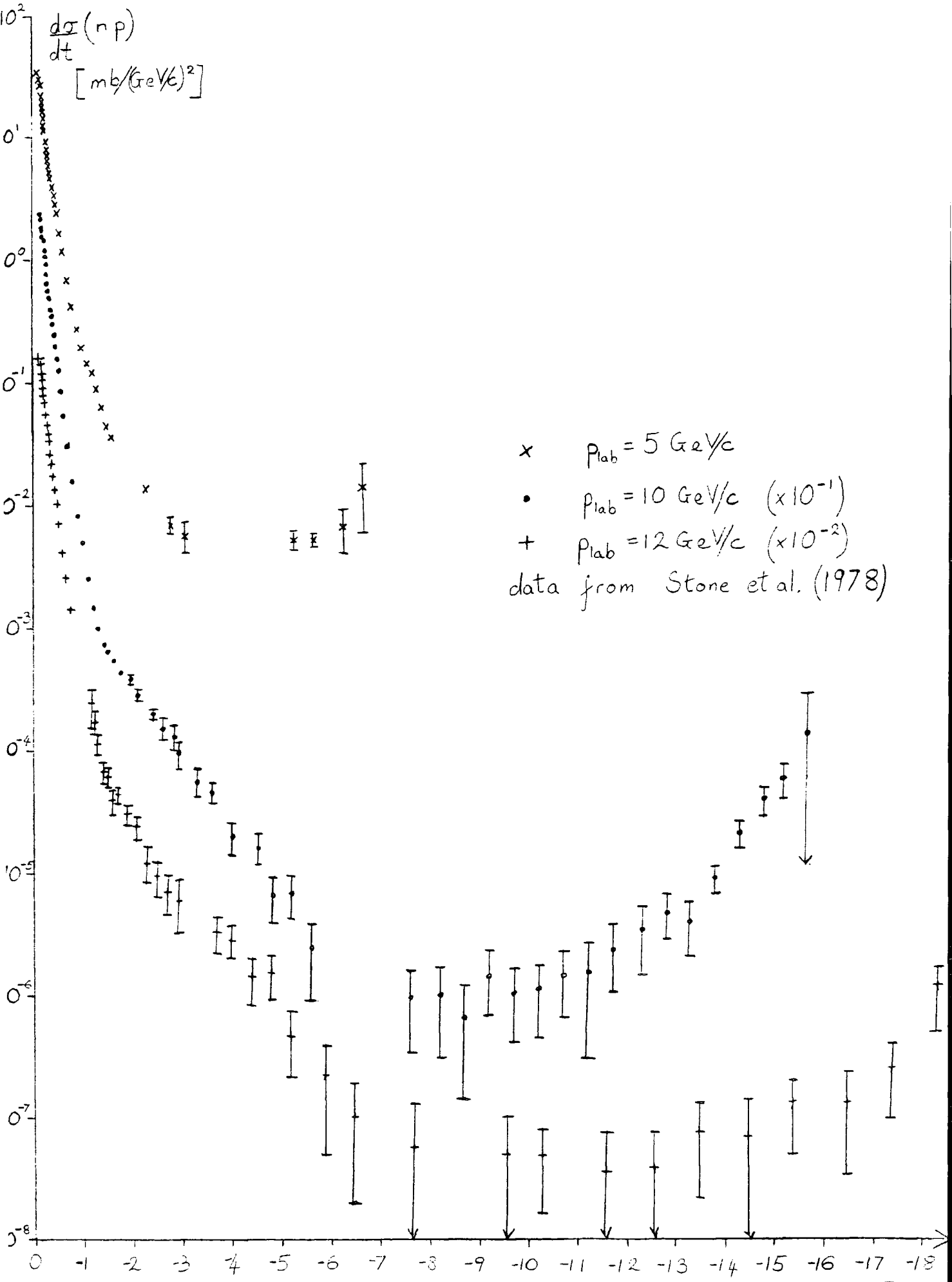

Fig. (1.3.2): Experimental measurements of $\frac{d\sigma}{dt}$ (pn)

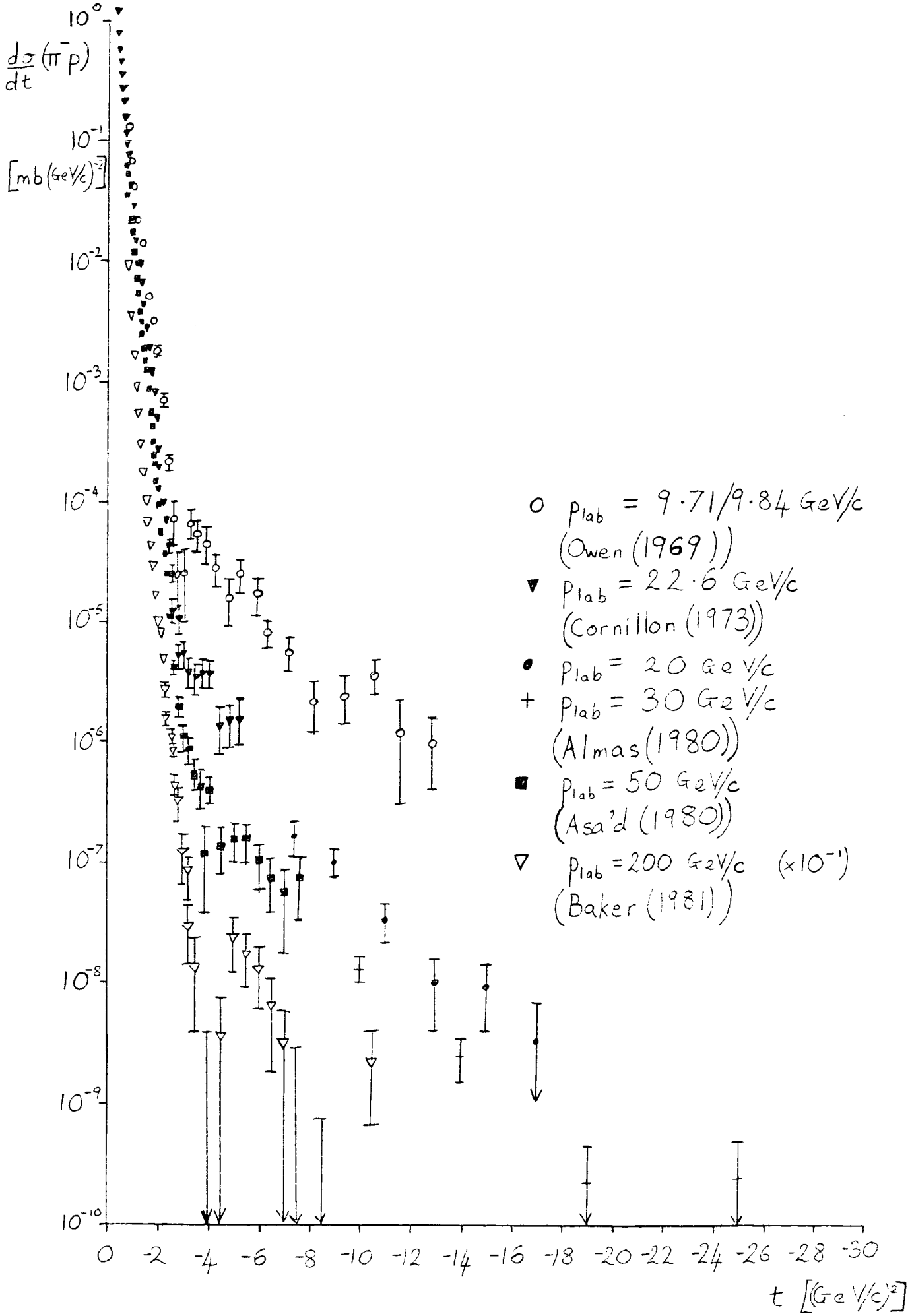

Fig. (1.3.3) : Experimental measurements of $\frac{d\sigma}{dt}$ $(\pi^- p)$

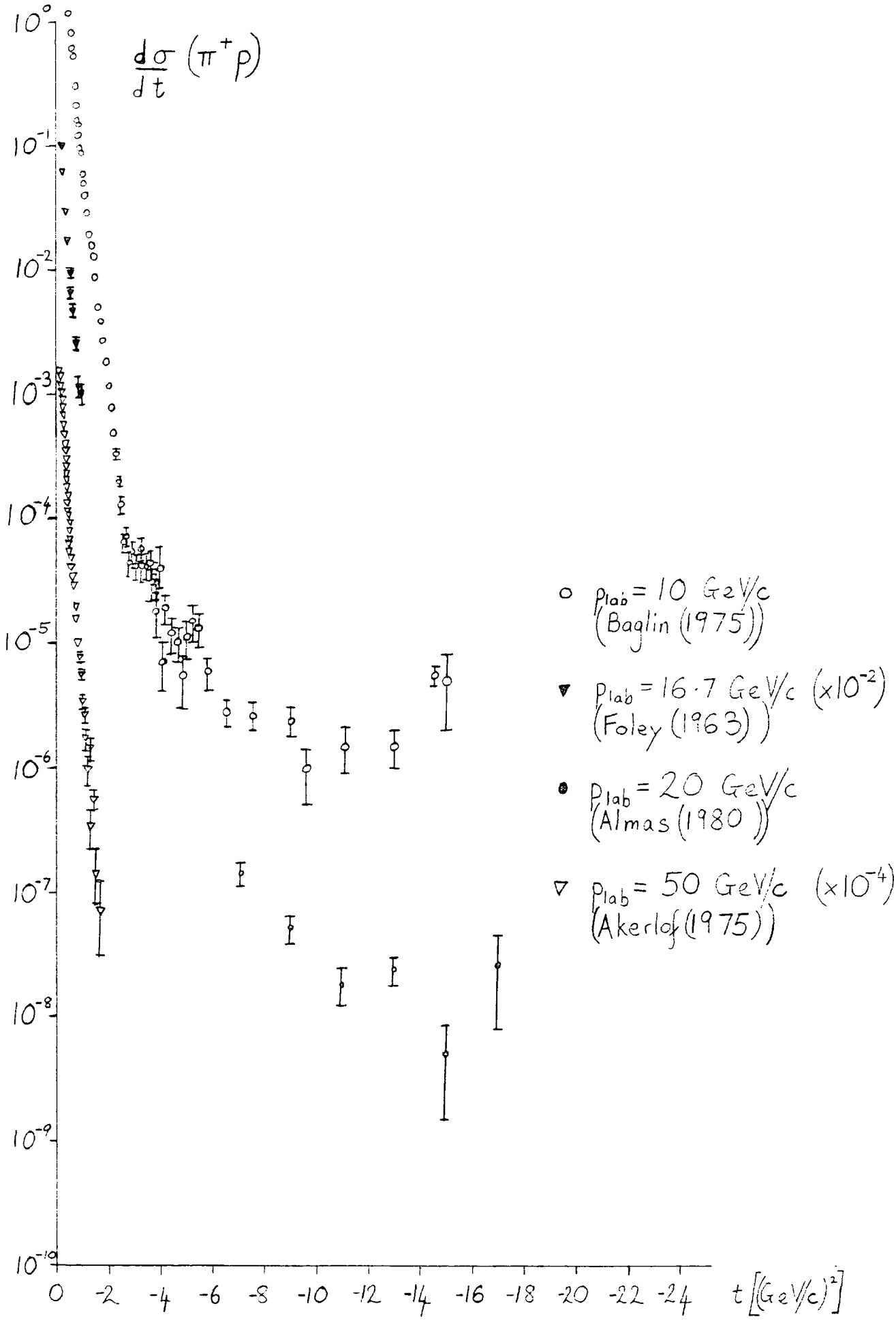

Fig. (1.3.4) : Experimental measurements of $\frac{d\sigma}{dt}(\pi^+ p)$

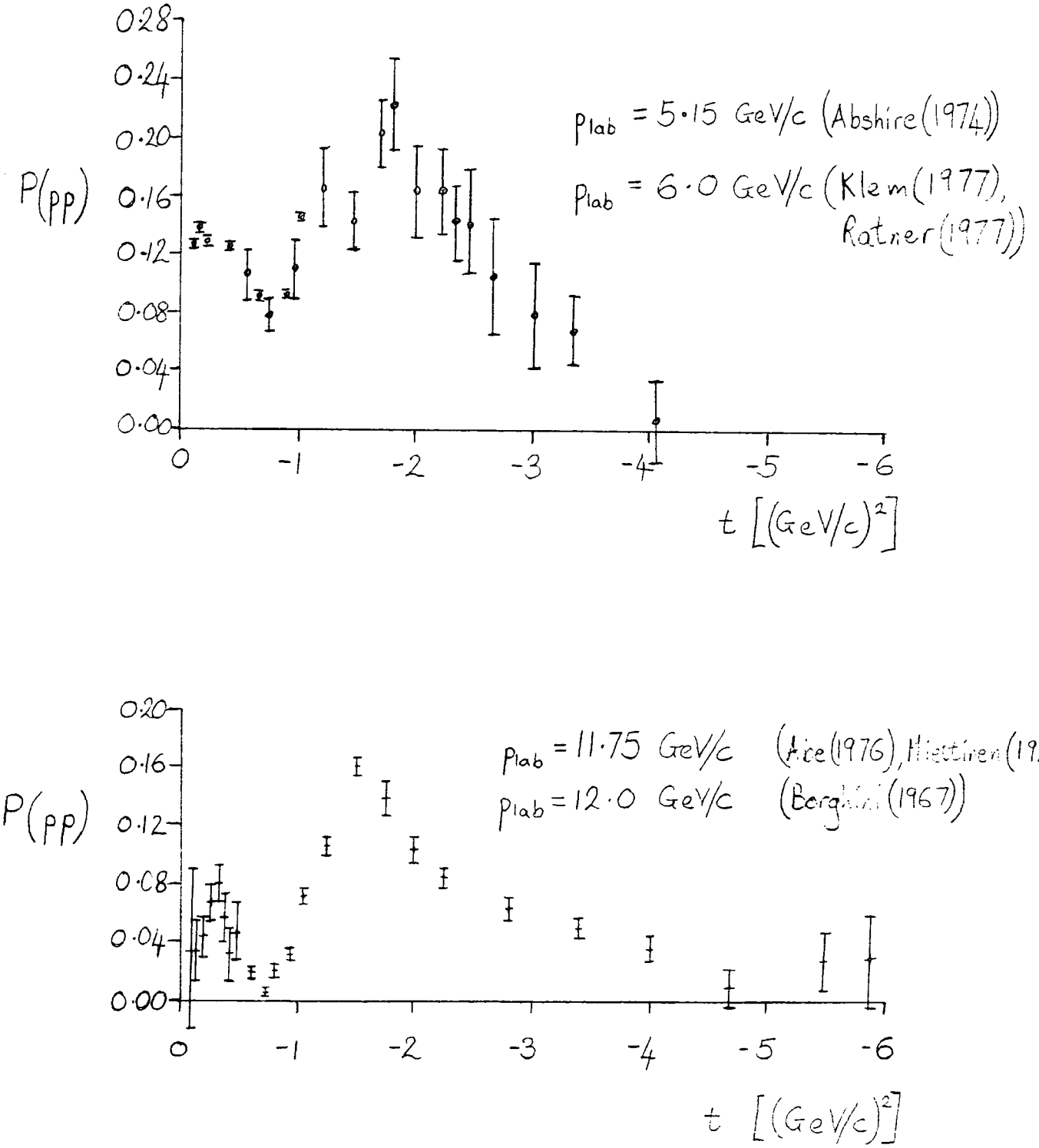

Fig. (1.3.5)

Experimental measurements of P(pp) at large angles

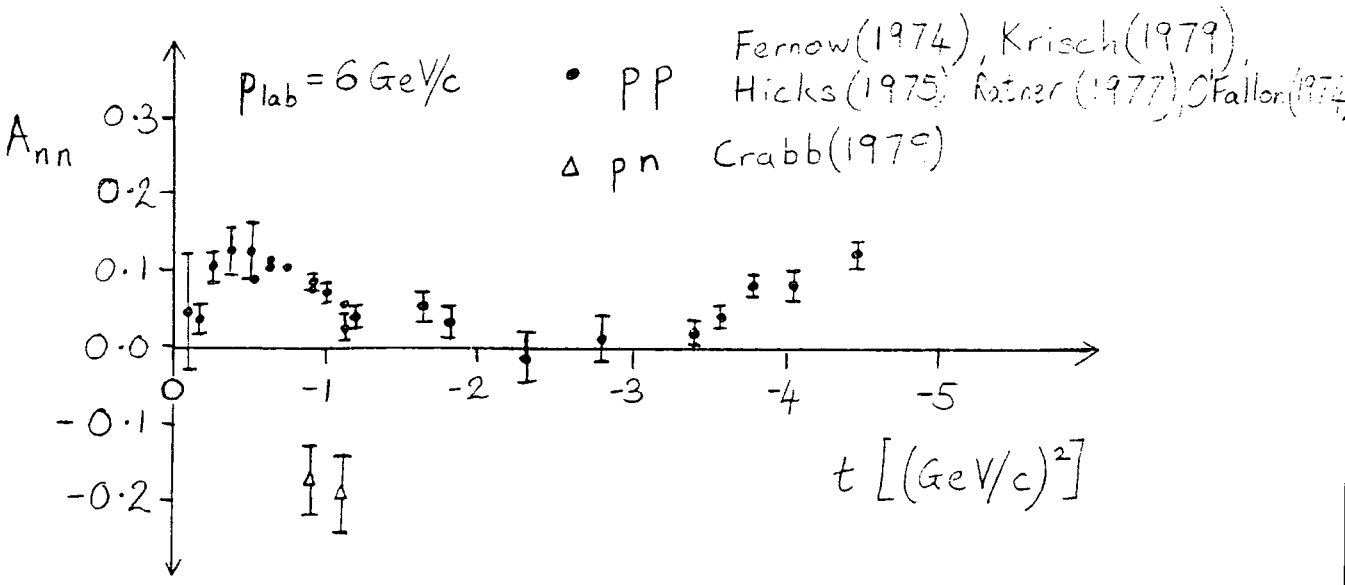

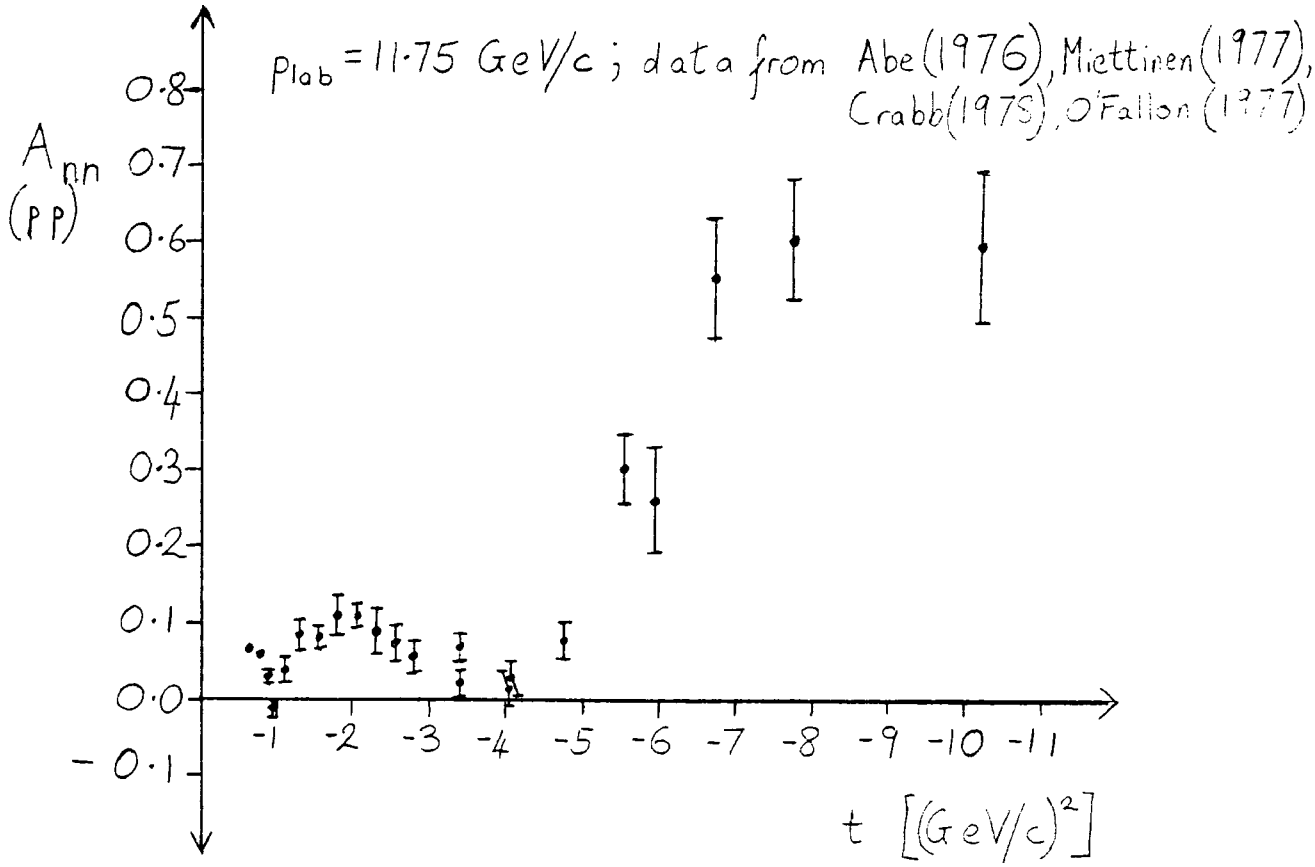

Fig. (1.3.6)

Experimental measurements of A_{nn}

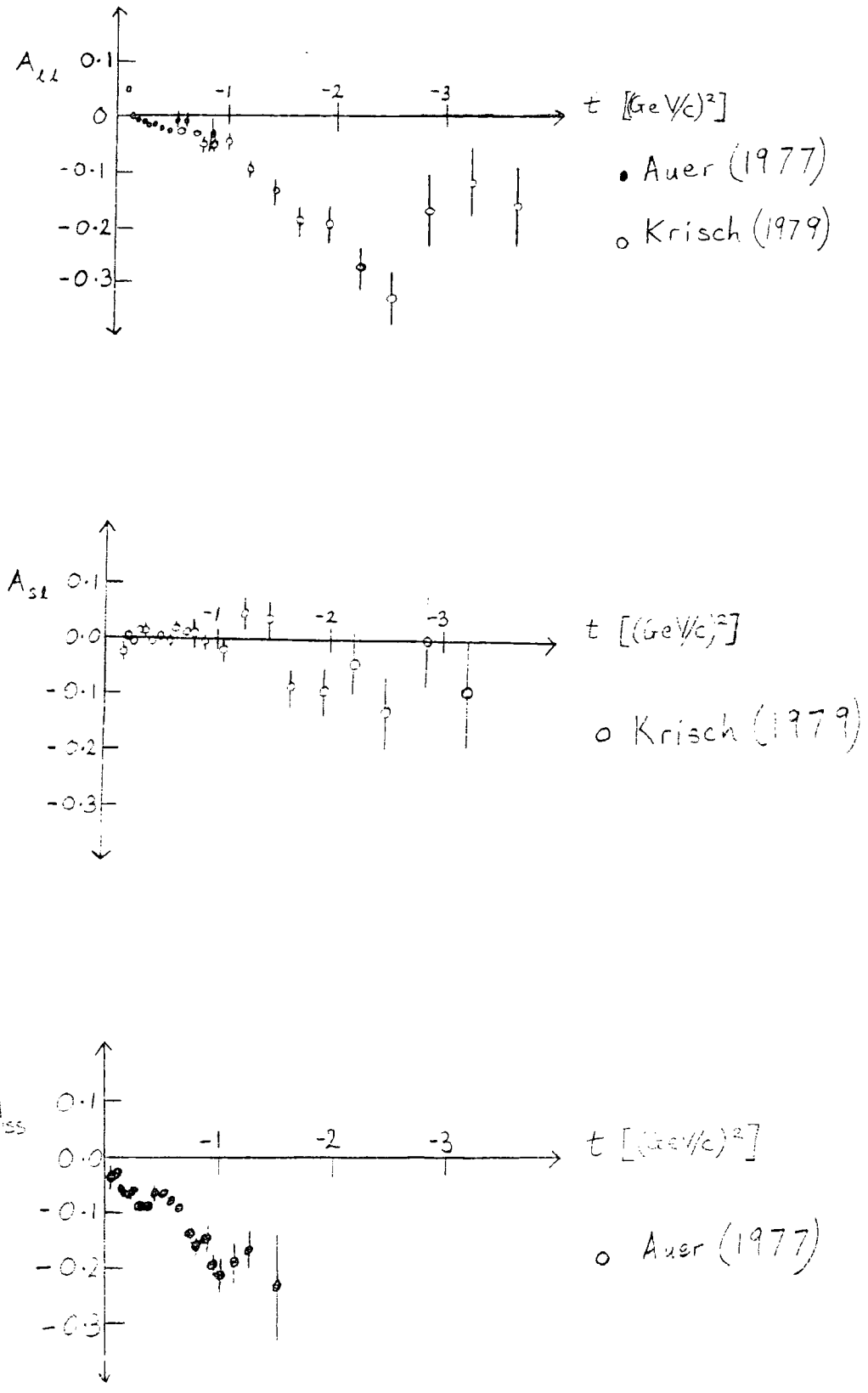

Fig. (1.3.7)

Experimental measurements of $A_{11}(pp)$ $A_{s1}(pp)$ $A_{ss}(pp)$ at p_{lab} = 6 GeV/c

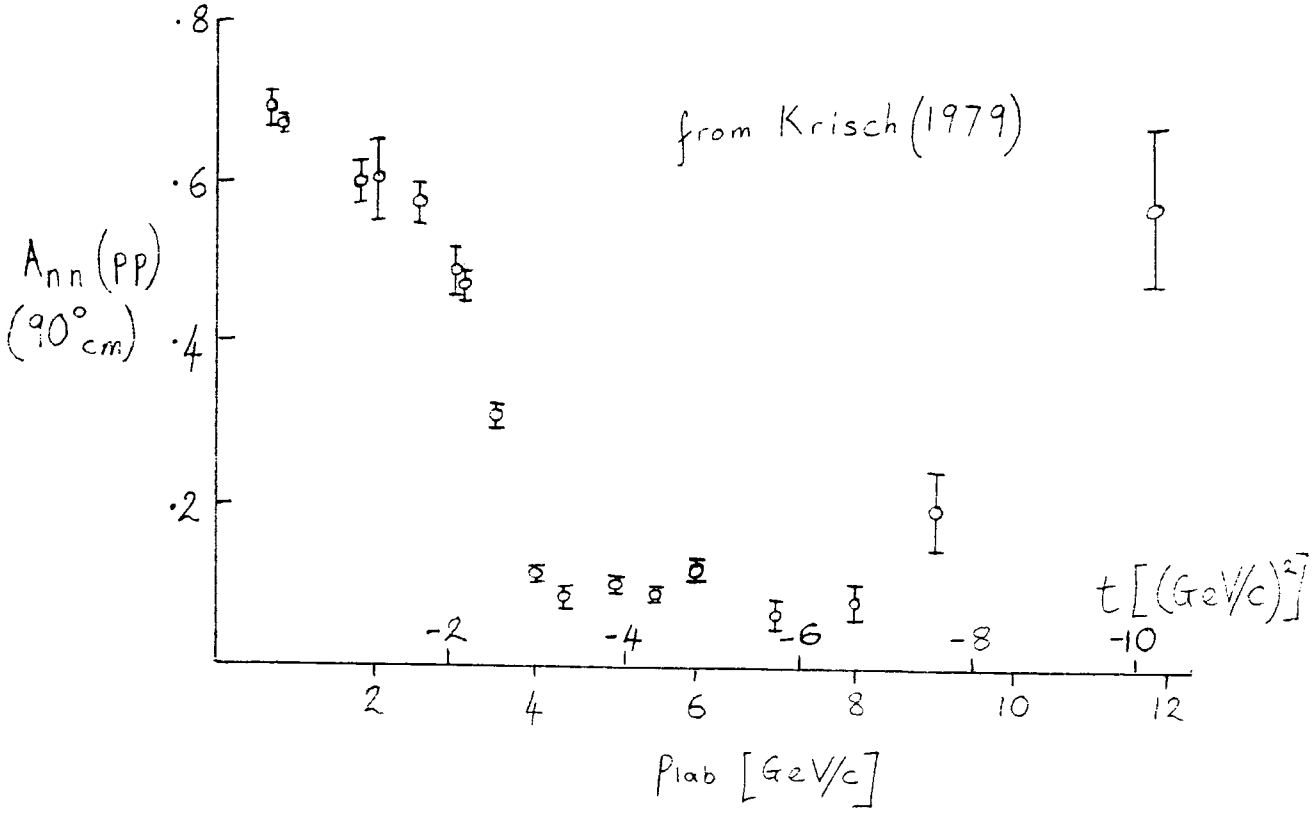

Fig. (1.3.8)

A_{nn} (pp) at $90°_{cm}$

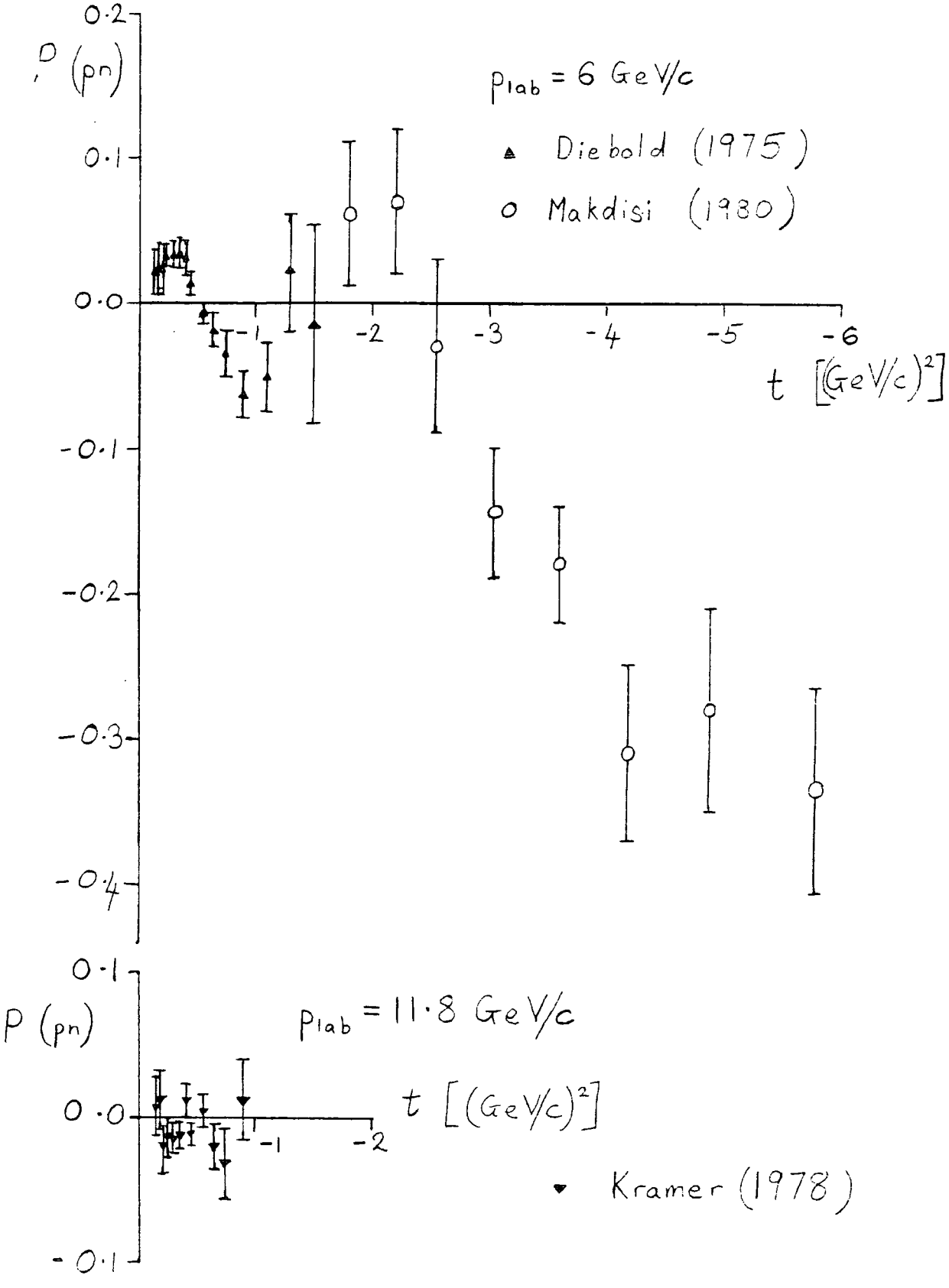

Fig. (1.3.9)

Experimental Measurements of P(pn)

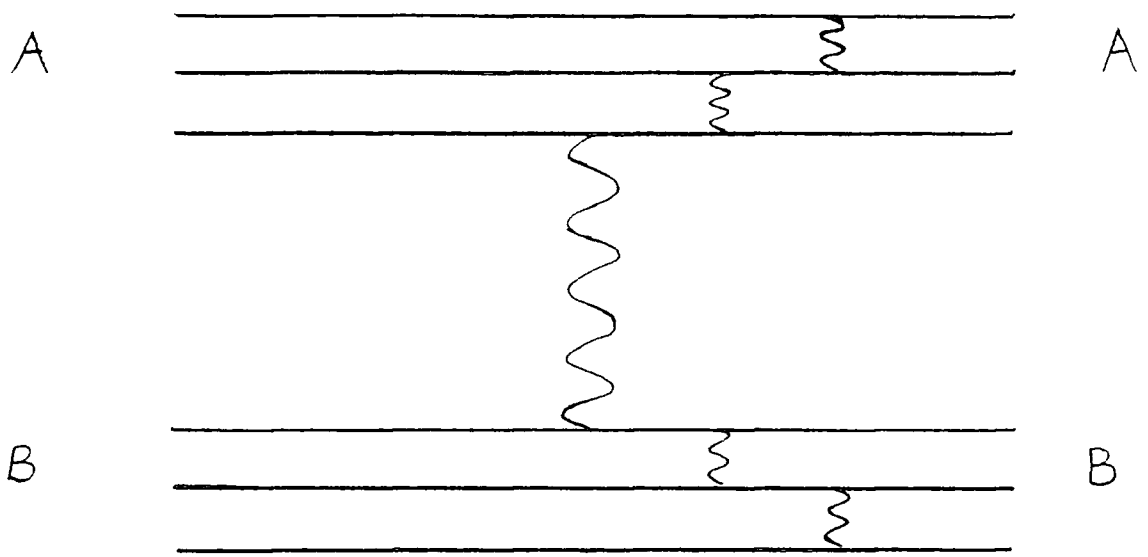

Fig. (1.4.1)

A diagram contributing to N-N scattering via single gluon exchange

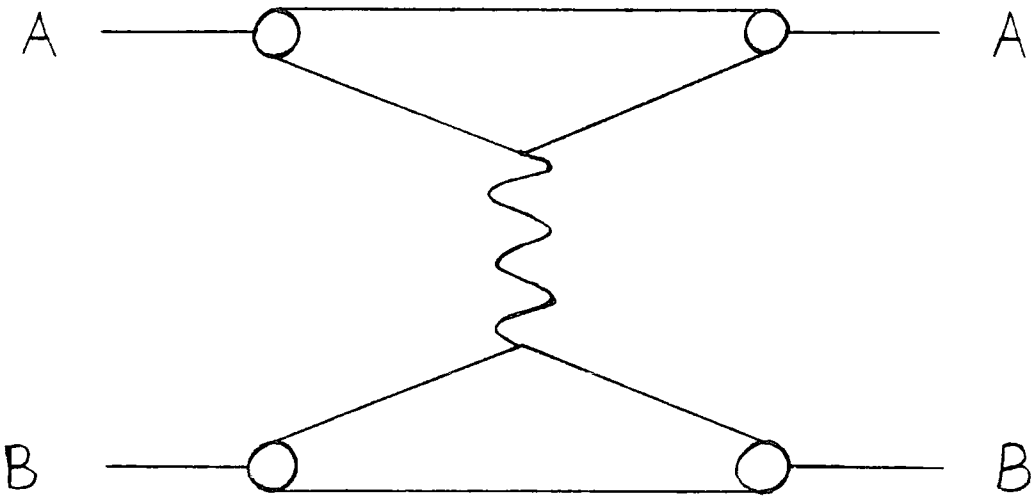

Fig. (1.4.2);

Fig. (1.4.1) redrawn in terms of electromagnetic form factors

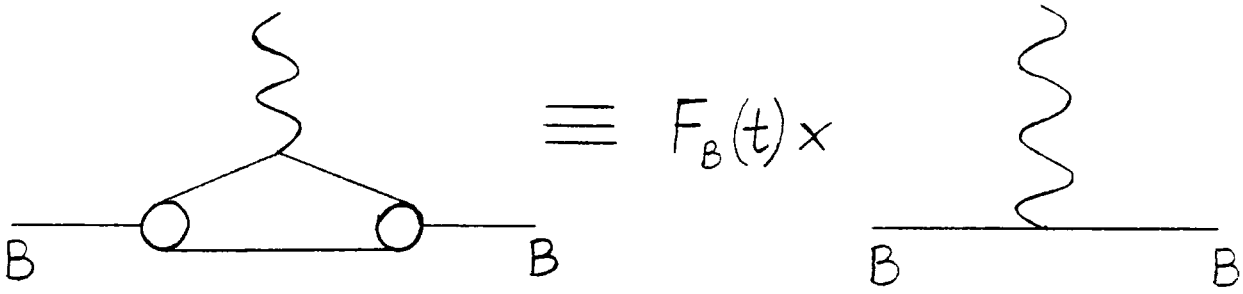

Fig. (1.4.3)

An electromagnetic form factor, $F_B(t)$

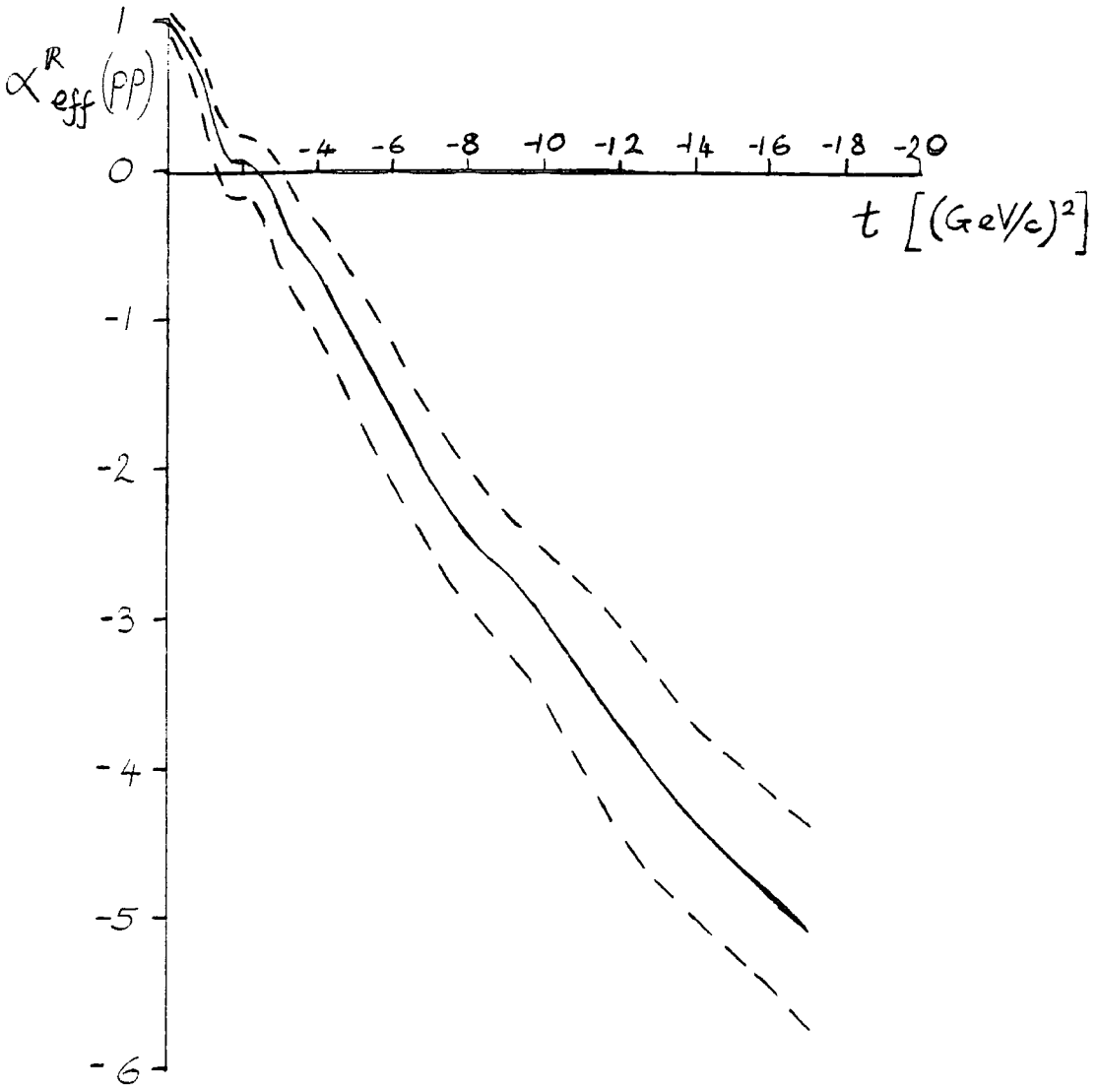

Fig. (1.4.4)

Effective Regge trajectory (with tolerance band) for pp scattering in the range $20 \leqslant s \leqslant 50\ (GeV/c)^2$; $\alpha^{R}_{eff}(t)$ defined by (1.4.5)

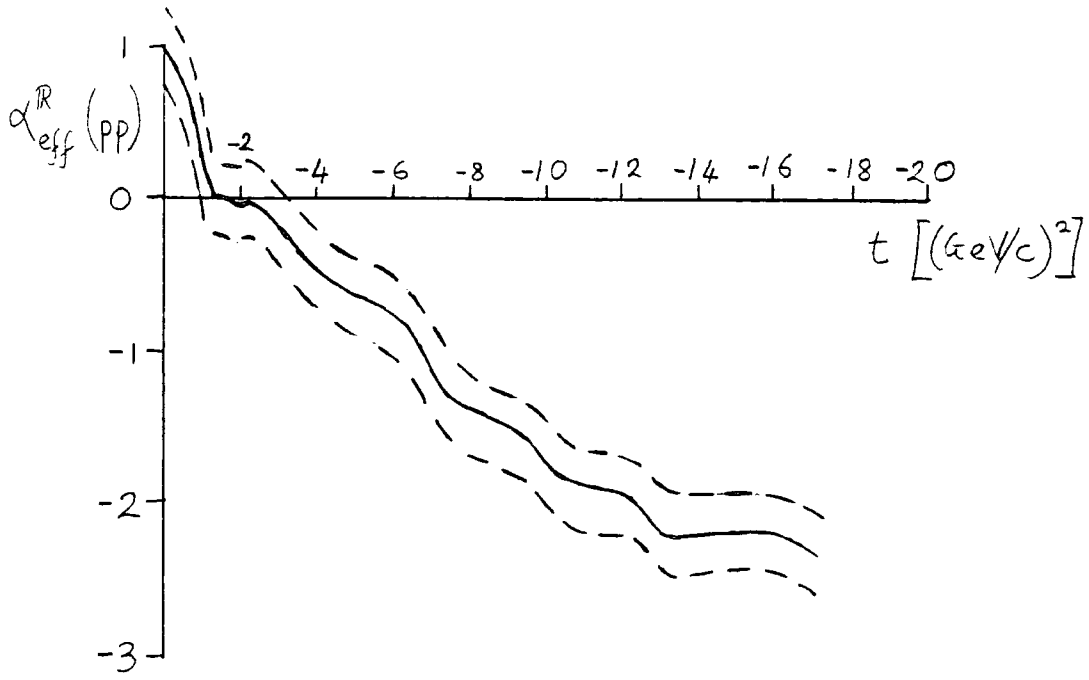

Fig. (1.4.5)

Effective trajectory (with average tolerance band) for pp scattering with $p_{lab} < 30$ GeV/c; $\alpha^{R}_{eff}(t)$ defined by (1.4.6)

(Taken from Coon et al (1978))

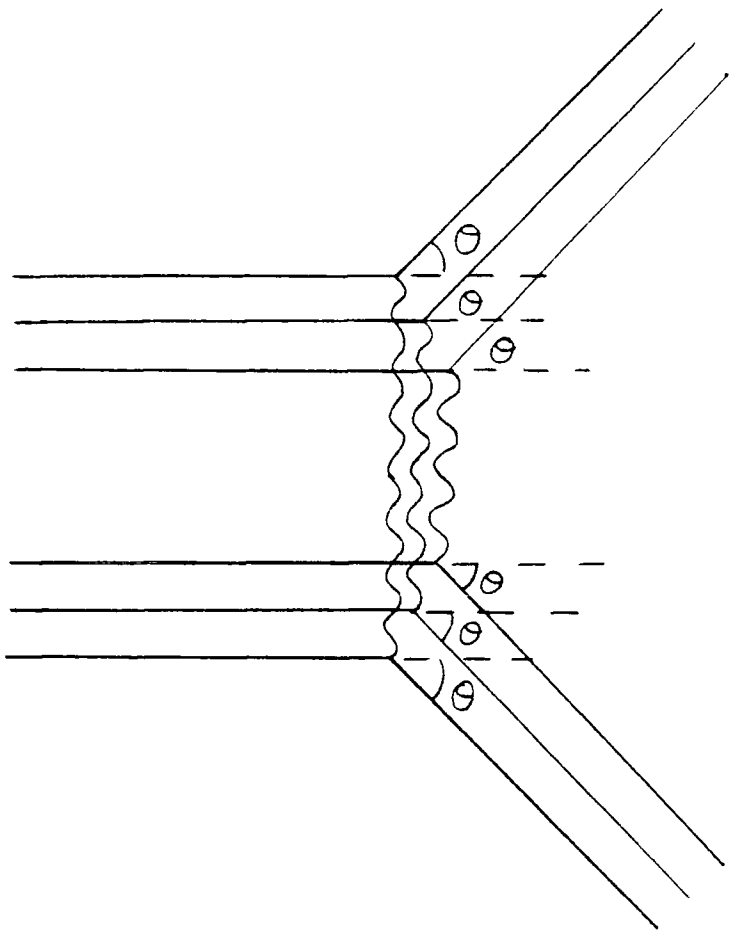

Fig. (1.4.6)

Landshoff triple gluon scattering

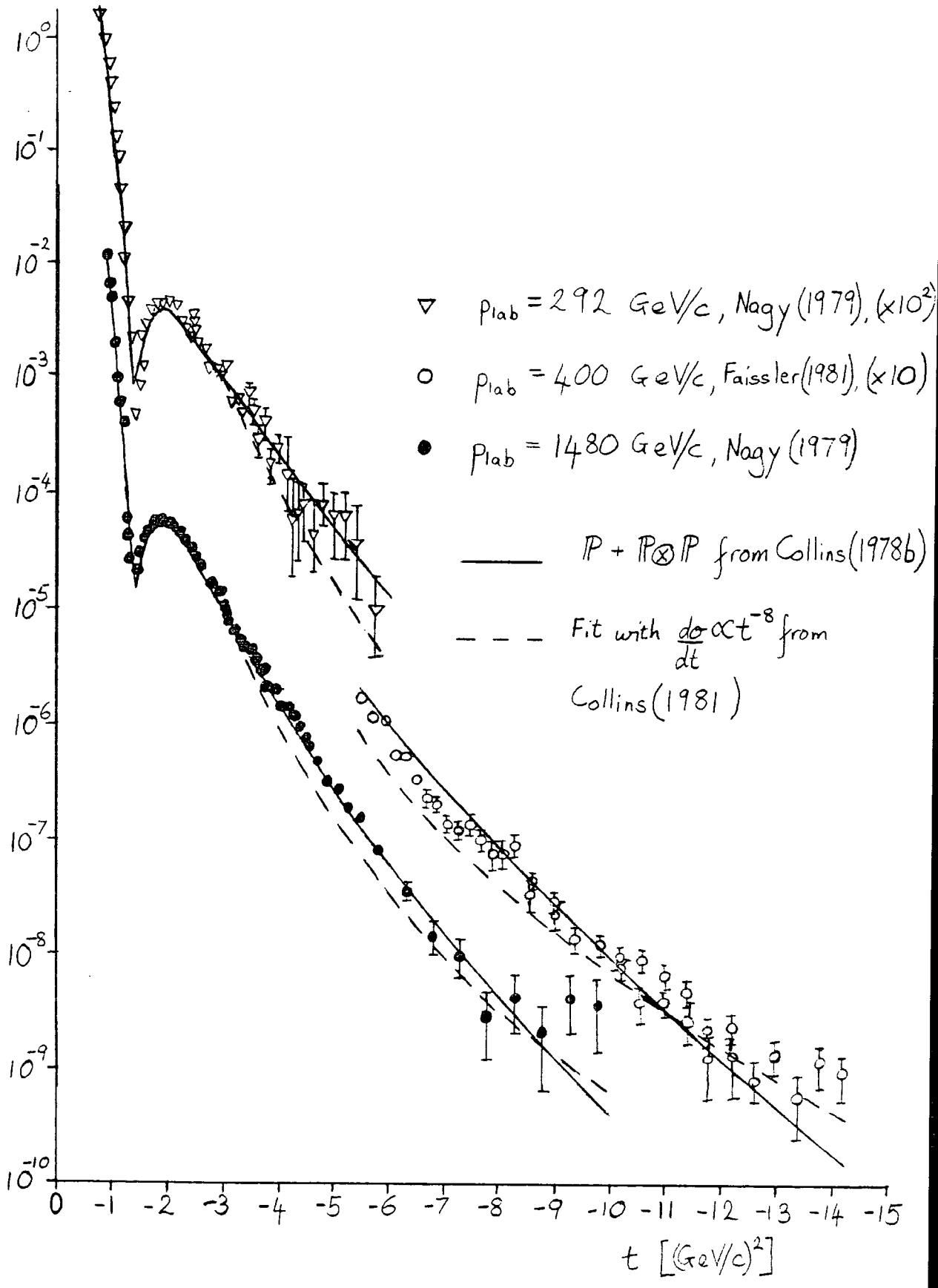

Fig. (1.4.7)

Data for $\frac{d\sigma}{dt}$ (pp) at high energies compared with $\mathbb{P}+\mathbb{P}\otimes\mathbb{P}$ and triple gluon scattering fits

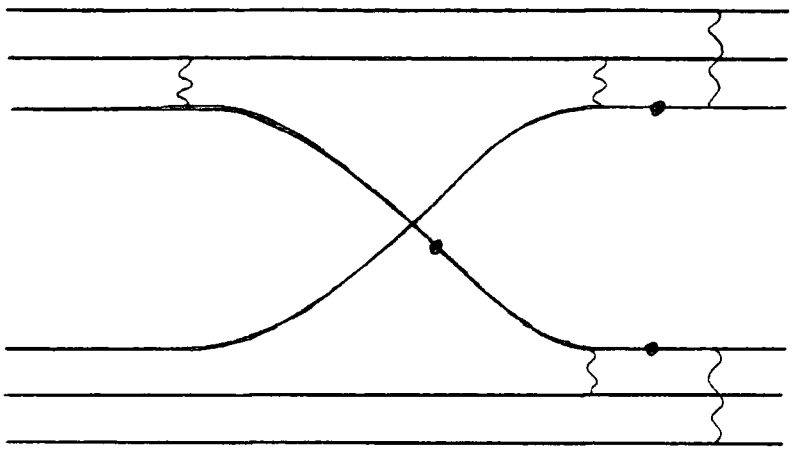

Fig. (1.4.8)

A leading order Quark Interchange Diagram (N-N scattering)

The dots indicate off mass shell fermion propagators

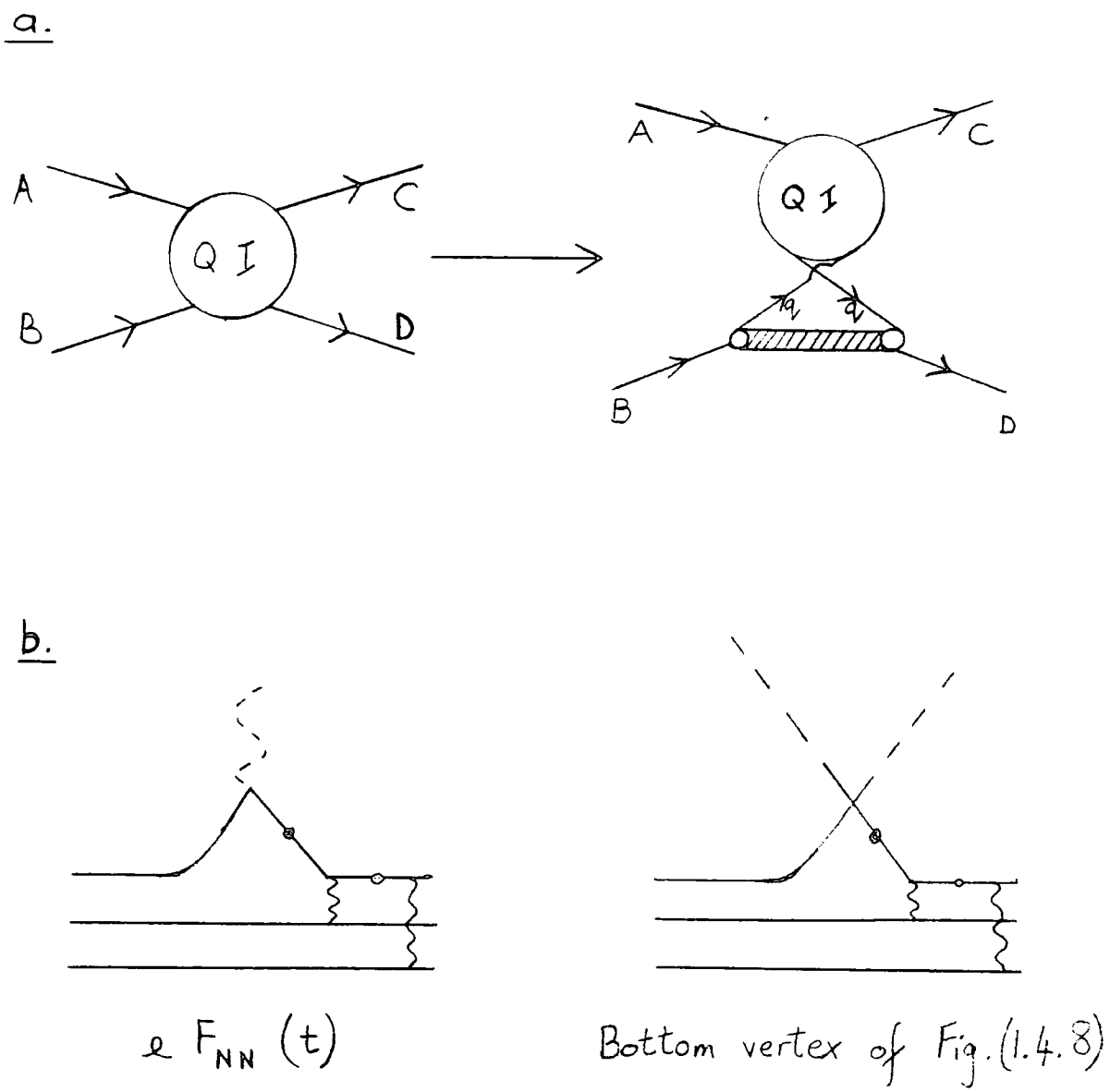

Fig. (1.4.9)

Contribution of the nucleon electromagnetic form factor to a Quark Interchange diagram

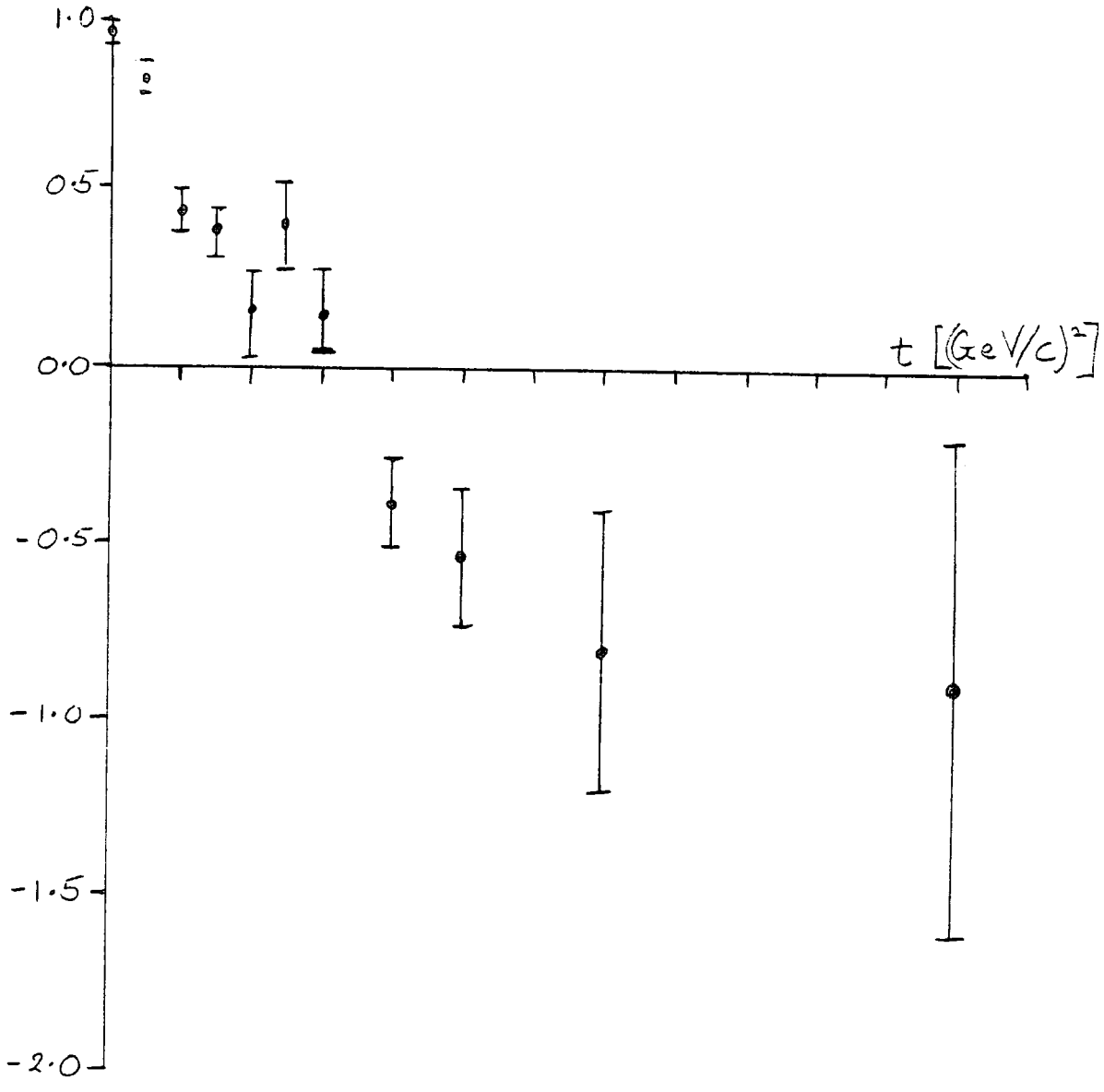

Fig. (1.4.10)

Effective Regge trajectory for $\pi^- p$ scattering in the range $10 \leqslant p_{lab} \leqslant 50$ GeV/c; $\alpha^R_{eff}(t)$ defined by (1.4.5)

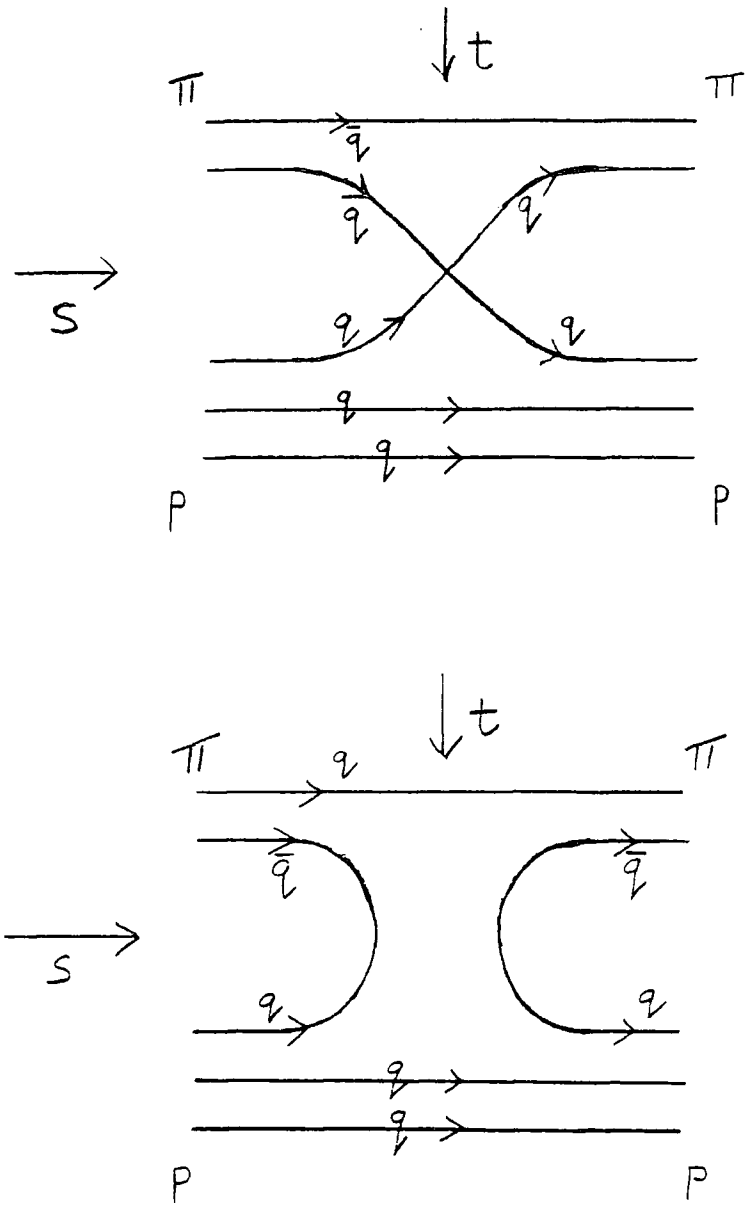

Fig. (1.4.11)

The two interchange topologies contributing to πp scattering

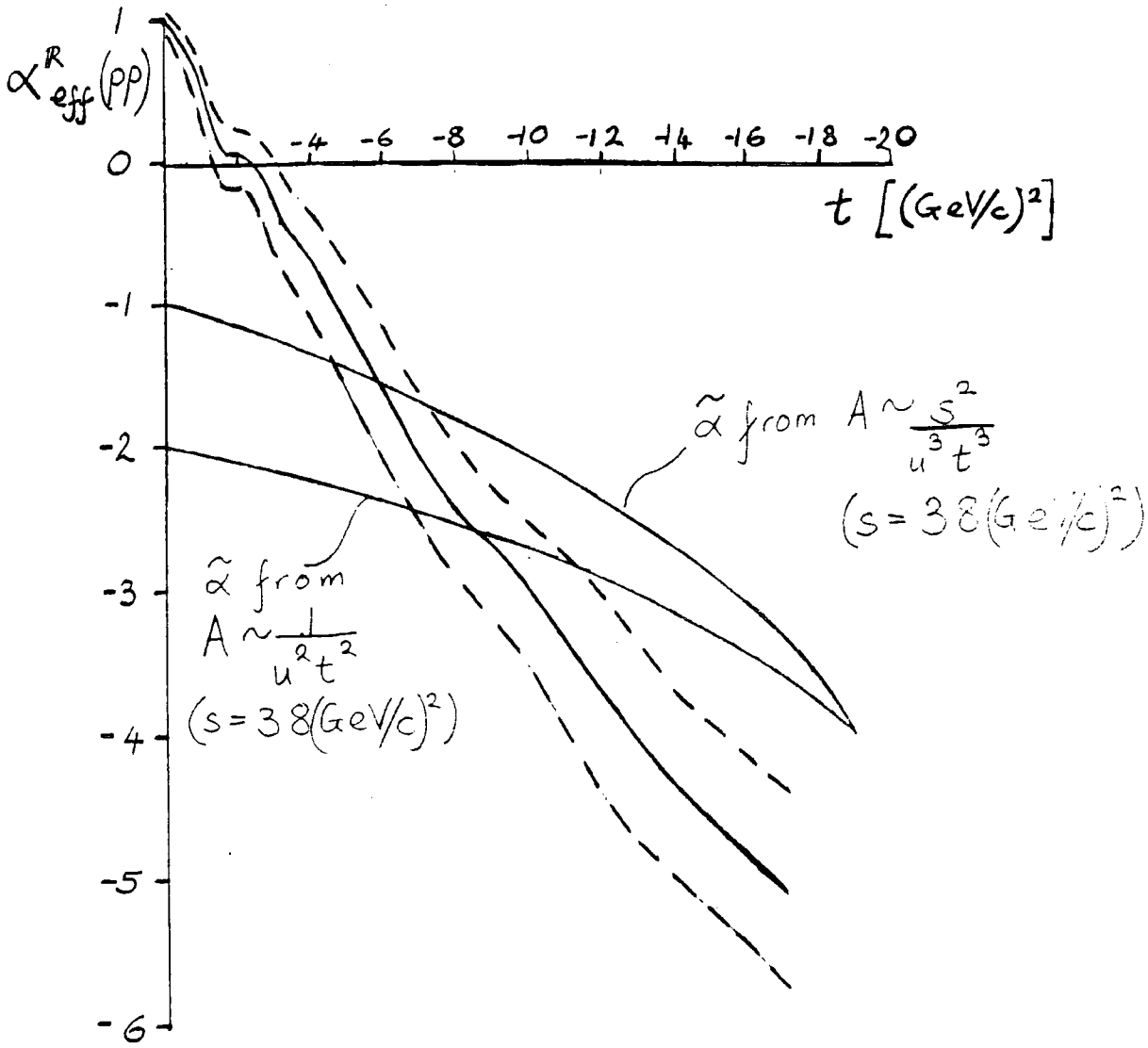

Fig. (1.4.12)

Comparison of $\tilde{\alpha}^R_{QIM}$ for pp at s = 38 $(GeV/c)^2$ with effective trajectory data

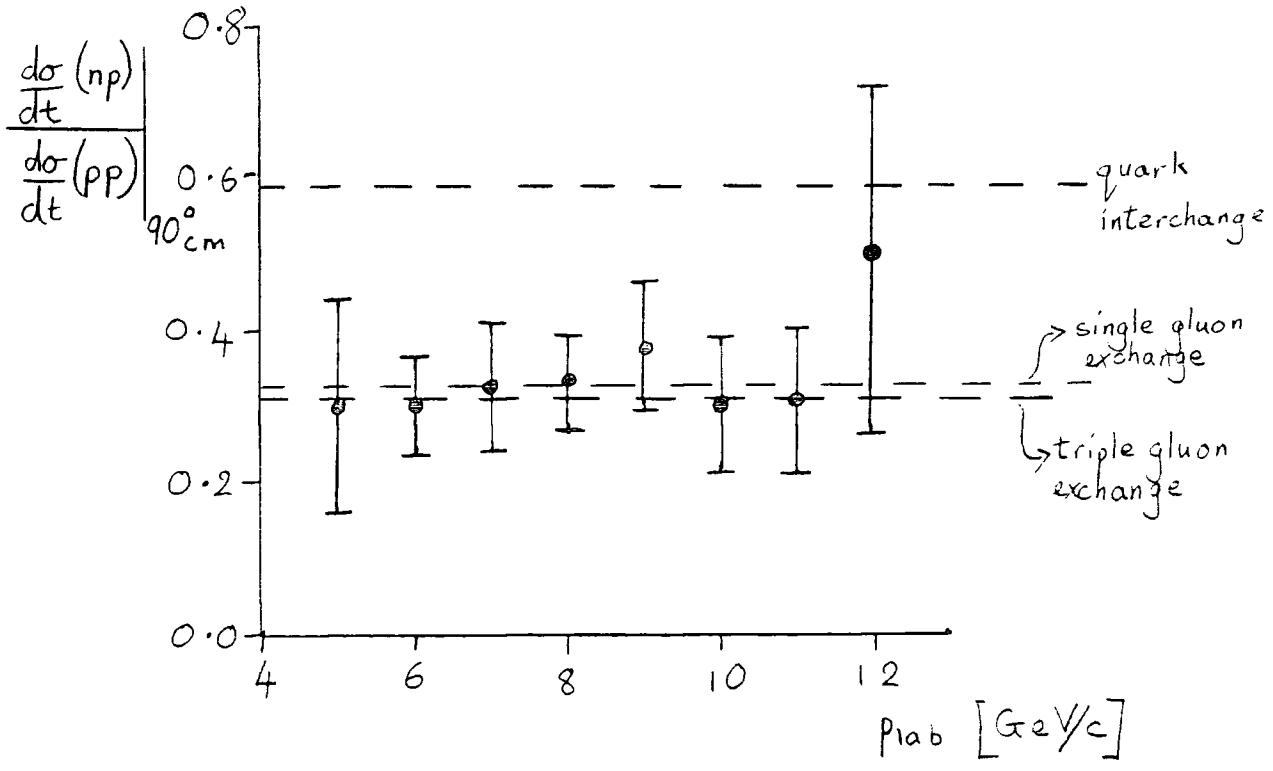

Fig. (1.4.13)

$\frac{d\sigma}{dt}(np) \Big/ \frac{d\sigma}{dt}(pp)$ at 90°_{cm} : Theory vs. experiment

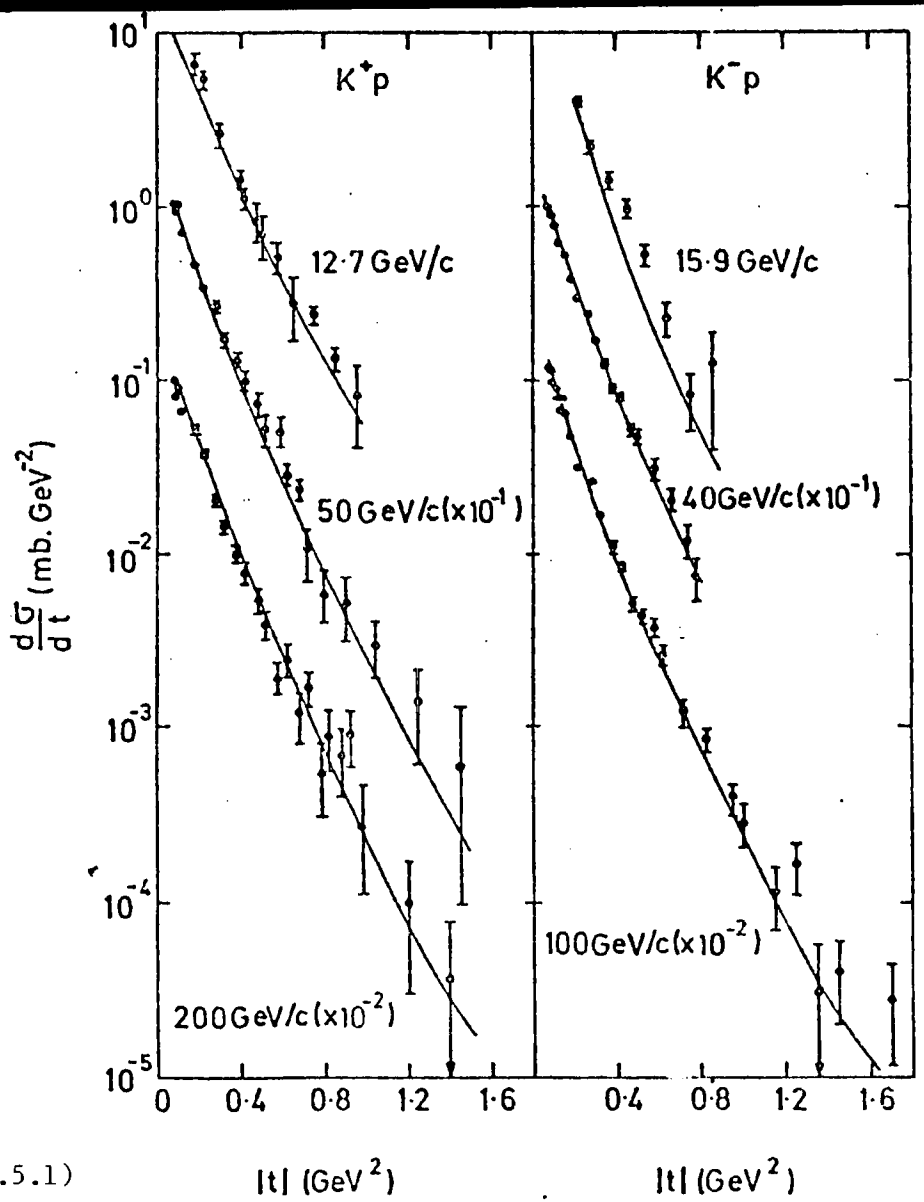

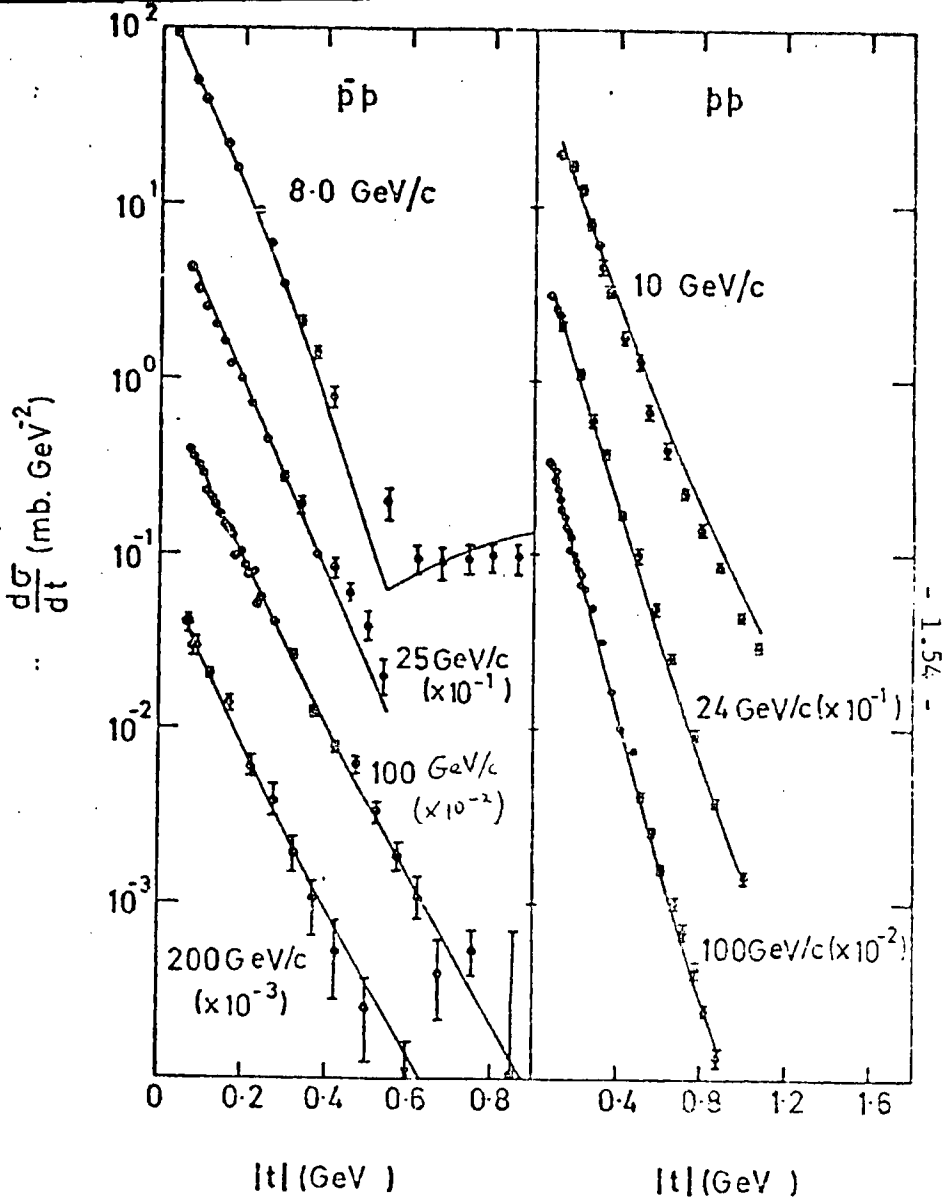

Fig. (1.5.1)

RPCA model fits to dσ/dt for a) $K^+p \to K^+p$ b) $K^-p \to K^-p$ c) $\bar{p}p \to \bar{p}p$ d) $pp \to pp$

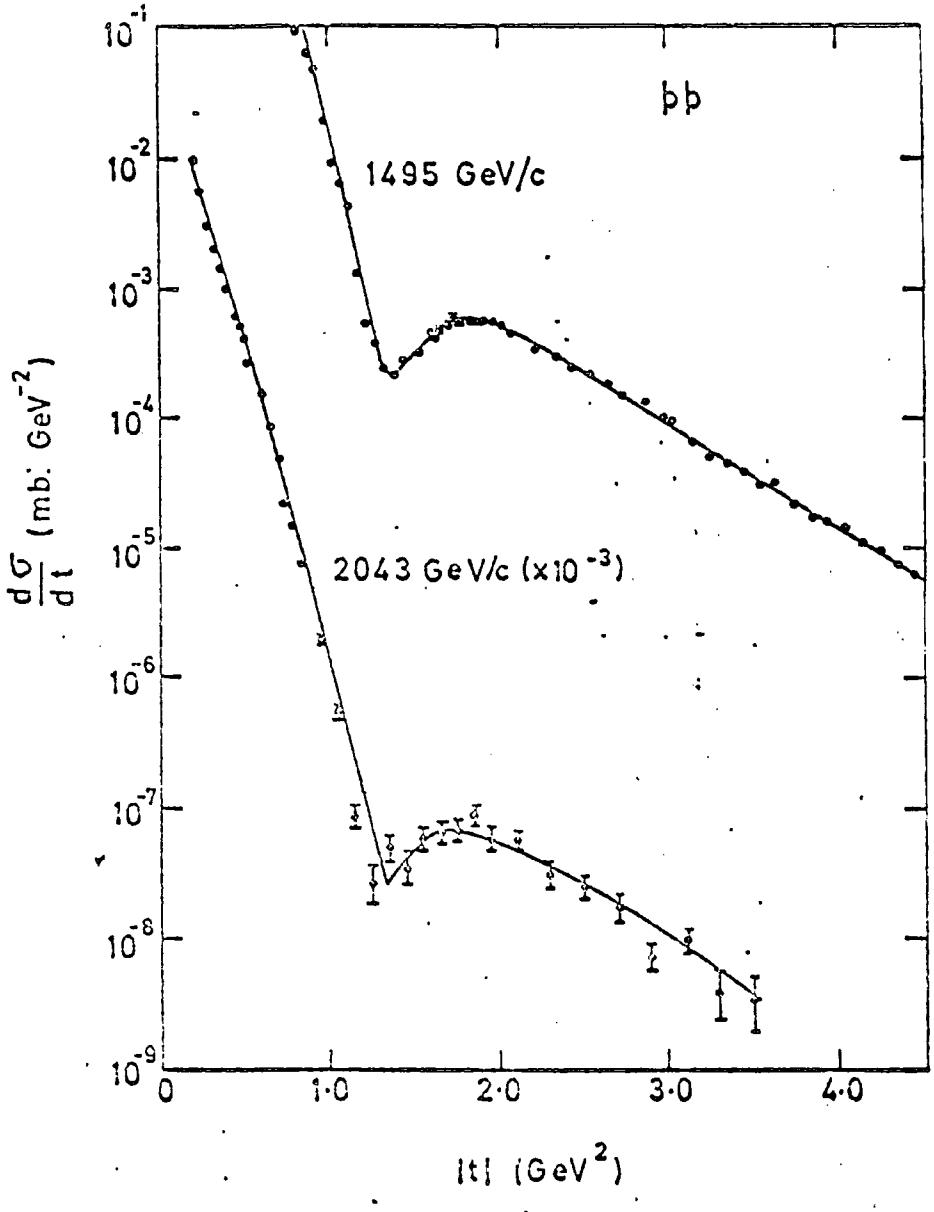

Fig. (1.5.1) continued

ℓ) pp → pp .

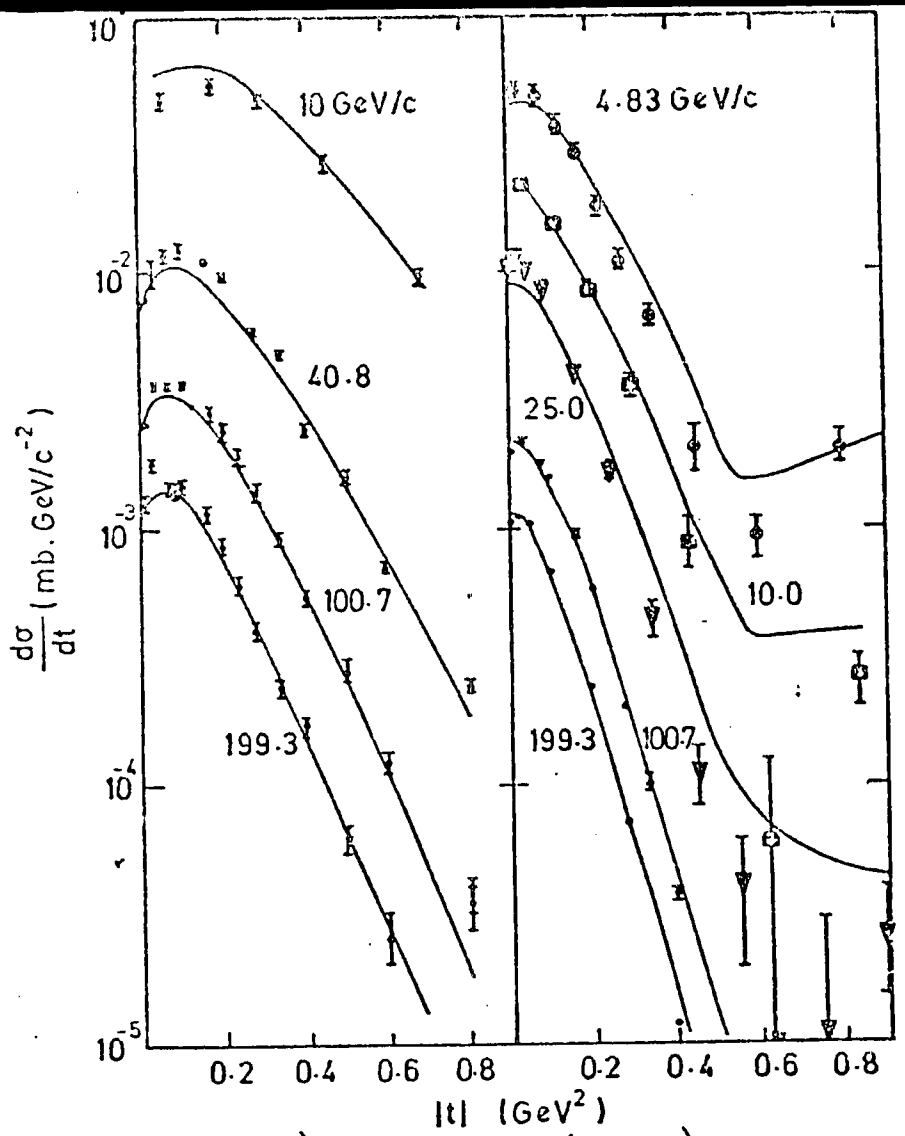

f) $\pi^- p \to \eta n$ g) $\pi^- p \to \pi^0 n$

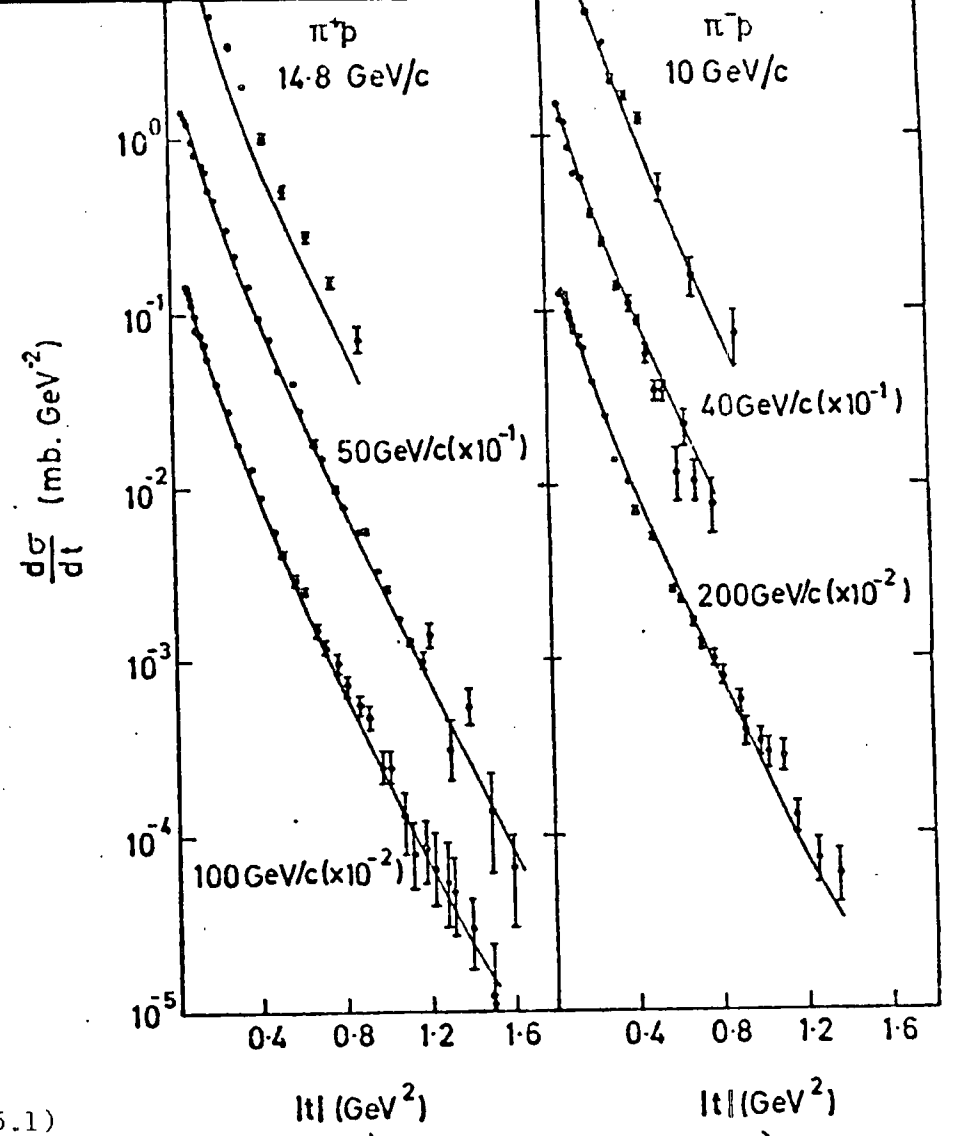

h) $\pi^+ p \to \pi^+ p$ i) $\pi^- p \to \pi^- p$

Fig. (1.5.1) continued

CHAPTER 2

THEORETICAL DEVELOPMENT

2.1 Introduction

The purpose of this chapter is to form an integrated picture of hadronic elastic scattering at all angles. Section 2.2 looks at fits to large angle data using parametrizations based on the QI mechanism and examines the possibility that simple additive combination of these with small angle Regge fits can adequately account for the intermediate angle transition region. Section 2.3 considers the possibility that Regge and constituent-exchange views are not distinct, but are each simplifications of the complete picture, valid in their own kinematic region. Plausible identifications are made between sums of certain quark- and gluon-exchange diagrams and sums of Regge exchanges and an outline for an all-angle Regge model is formulated. Section 2.4 then looks at the properties required of the Regge terms at large angles.

2.2 Fit to large and small angle data

Before formulating a model to account for elastic scattering at all angles, it is important to look more closely at the R.P.C.A. and quark interchange models, which so successfully describe the small and large angle regimes respectively. Valuable information may be gained from an examination of these models, of their strengths and weaknesses, of the extent of the regions of their appropriateness and for what reasons they fail outside these regions.

In Section 1.5 it was shown that R.P.C.A. accounts very well for the differential cross sections of numerous processes for $p_{lab} \simeq 10$ GeV/c and above, and $-t \lesssim 1$ $(\text{GeV/c})^2$ (see Figs. (1.5.1)). Additionally, $\frac{d\sigma}{dt}(pp \to pp)$ for $p_{lab} \gtrsim 100$ GeV/c is well fitted out to very large -t by the inclusion of a Pomeron ● Pomeron cut. When these Regge fits, extrapolated to large

angles, are compared with pp and πp elastic differential cross section data, in each case the fit below $p_{lab} \simeq 50$ GeV/c breaks down for $-t \gtrsim 1$ $(GeV/c)^2$. This is particularly apparent for $d\sigma/dt$ (pp→pp) (see Fig. (2.2.1)).

At high energy ($p_{lab} \gtrsim 100$ GeV/c), this large $|t|$ region of $d\sigma/dt$ (pp→pp) is dominated by the $P \otimes P$ cut. This contribution, however, is much too small to account for the lower energy data. Moreover, the effective trajectory for $10 \lesssim p_{lab} \lesssim 50$ GeV/c, $-t \gtrsim 1$ (as witnessed by Fig. (1.4.4) lies well below that expected for $P \otimes P$ which (having an intercept $\simeq +1$ and a very small slope) should be close to +1 out to relatively large $|t|$. Further trajectories, more cuts or grossly flattened Reggeon pole trajectories, must be introduced to fit the data successfully (see Collins and Gault (1976a)). Furthermore, in order to obtain the power law behaviour of the Dimensional Counting Rule results, and hence describe well large angle scattering (i.e. close to 90°cm), a conventional Regge model involving straight line trajectories would need to embody fixed poles at negative integers for which there is no other evidence. Such an explanation would lose the elegance and simplicity of the constituent view of large angle scattering and gain little in return.

Fig. (2.2.2) presents a fit to $\frac{d\sigma}{dt}$ (pp→pp) for $t > 2.5$ $(GeV/c)^2$ $5 \leqslant p_{lab} \leqslant 24$ GeV/c using a power law scaling parametrization similar to that suggested in Brodsky et al (1973a):

$$\frac{d\sigma}{dt}(pp \to pp) = A \frac{1}{(s+s_1)^n} \cdot \frac{1}{(z_1^2 - z^2)^m} \qquad (2.2.1)$$

where $z \equiv \cos\theta_{cm} = 1 + \frac{2t}{s-4m_p^2}$

$$z_1 = 1 + \frac{2t_1}{s-4m_p^2}$$

A, n, m, s, t, are free parameters of the fit whose values are given in Table (2.2.1). t_1 and s_1 allow for corrections to power law scaling at other than higher energies and large angles. The account of the data is a good one, especially considering the wide angular range covered. Similar fits to π^+p and π^-p are shown in Fig. (2.2.3) using the parametrization

$$\frac{d\sigma}{dt}\ (\pi^+p\to\pi^+p) = \frac{A}{s^n}\ \frac{1+z}{(1-z)^4}\ (8(1+z)^{-2}+1)^2$$

$$\frac{d\sigma}{dt}\ (\pi^-p\to\pi^-p) = \frac{A}{s^n}\ \frac{1+z}{(1-z)^4}\ (4(1+z)^{-2}+2)^2 \qquad (2.2.2)$$

The angular dependence is taken from Brodsky et al (1973a) and is predicted by CIM. The fitted values of the magnitude and the energy dependence are shown in Table (2.2.2).

The large angle regime is well described in terms of forms suggested by quark interchange models and the D.C.R. But it is not clear how to extend the predictive power of constituent models away from large $|t|$ and s. Purely real terms, such as (2.2.1) and (2.2.2) cannot by themselves account for interference phenomena such as are observed at $1 \lesssim -t \lesssim 2$ $(GeV/c)^2$ in $\frac{d\sigma}{dt}$ (pp) and at $t \simeq -3$ $(GeV/c)^2$ in $\frac{d\sigma}{dt}$ (πp). Such power law scaling predictions are, of course, completely at odds with the Regge behaviour observed at small angles.

Having two models, each successful in its own region of validity, but with grave shortcomings away from it, the next step must be to try to combine them in order to obtain a good account of the data at all angles. The most obvious way in which to try and do this is simply to add together the amplitudes i.e.

$$A_{total} = A_{Regge} + A_{QI} \qquad (2.2.3)$$

At first glance, this approach seems promising. For example in $\frac{d\sigma}{dt}$ ($pp \to pp$) for $10 \lesssim p_{lab} \lesssim 25$ GeV/c, the RPCA model is good for $|t| \lesssim 1 (GeV/c)^2$ and the QI form (2.2.1) works well for $|t| \gtrsim 2.5$ $(GeV/c)^2$, while both models are small (relatively) away from their regions of validity. Interference between the two would only be expected between $|t|$ of 1 and 2 $(GeV/c)^2$, which is just where it is observed. Unfortunately, the energy dependence of this interference does not match what is seen in nature as will now be shown.

The experimental $\frac{d\sigma}{dt}$ has a sharp dip at $t \simeq -1.4$ $(GeV/c)^2$ at energies $\gtrsim p_{lab}$ of 200 GeV/c. This region is well accounted for by the sum of the Pomeron and a Pomeron $\otimes$ Pomeron cut each with very flat trajectories near $\alpha = 1$ and hence the amplitude is virtually entirely imaginary, while at lower energies conventional Reggeons add an important real part. Between $10 \lesssim p_{lab} \lesssim 25$ GeV/c the dip is replaced by a shoulder and by $p_{lab} \simeq 5$ GeV/c there is a smooth transition between small and large angles. Thus the interference is greatest at high energy and steadily decreases (or is masked) with decreasing energy. Now the Q.I. term is purely real, and to reproduce the shoulder shape at intermediate energies it must have the opposite sign to the real part of the Regge term. At lower energy $Re(A_{Regge})$ grows compared to $Im(A_{Regge})$ and hence the interference between A_{Regge} and A_{QI} becomes more severe; the opposite behaviour to that seen experimentally.

It is not surprising that such a simplistic attempt as (2.2.3) has failed. The Regge and constituent models are pictures of hadronic elastic scattering from different view points. But there is no reason to suppose that they are pictures of entirely different mechanisms, and there may well be a large degree of overlap between A_{Regge} and A_{QI}. If so, simple addition of the two terms involves double counting. The following section will develop a picture in which the constituent view melds smoothly and naturally into the Regge one, rather than adding to it.

2.3 The link between small and large angle scattering

Regge models describe the small angle scattering of hadrons in terms of the exchange of particles, which, though once thought to be elementary, are now known to be bound states composed of quarks, antiquarks and gluons. Large angle scattering, on the other hand, is best seen as the exchange of these "more elementary" constituents. Could it be, then, that the Regge and constituent models are the same mechanism seen in different kinematical regions? The two interchanged quarks of a QI diagram such as Fig. (2.3.1) could be identified with the valence quark and antiquark of a meson-Reggeon, the difference between the two situations being the strength of the quark-gluon coupling and hence the amount of binding or "dressing" of the valence pair.

Consider, for example, a lowest order QI diagram for baryon-baryon scattering (Fig. (2.3.1)). For large momentum transfer, where the strong coupling, α_s, is small, such diagrams are a valid approximation to the complete amplitude, but they form only the first term in a perturbative expansion (Fig. (2.3.2)). α_s becomes stronger for smaller momentum transfer, and diagrams involving more and more gluon exchanges become important. At small $|t|$, α_s is large, and the most important diagrams are those with many gluons coupling to the exchanged quarks, binding and dressing them. The perturbative view is then no longer valid and all the diagrams must be summed. Such sums of diagrams have been shown to lie on Regge trajectories in certain field theories (see e.g. Collins (1977) pp 94-99).

In the above reference a Born amplitude

$$A_B \sim \frac{1}{s^I} \quad \text{as} \quad \begin{matrix} s \to \infty \\ t \text{ fixed} \end{matrix} ; \quad I \text{ is an integer} \qquad (2.3.1)$$

is iterated to form a series of ladder diagrams see Fig. (2.3.3). In ϕ^3 field theory an n-rung ladder is found to behave as

$$A_n \sim \frac{1}{(n-1)!} (K(t)\ln s)^{n-1} \frac{1}{s^I} \qquad (2.3.2)$$

where $K(t) \to 0$ as $t \to -\infty$

Summing the ladders gives

$$A_{tot} = \sum_{n=1}^{\infty} A_n \sim \frac{1}{s^I} \exp (K(t)\ln s) \qquad (2.3.3)$$

i.e. the total amplitude behaves like a Regge pole with trajectory

$$\alpha (t) = - I + K(t) \qquad (2.3.4)$$

Since $K(t) \to 0$ as $t \to -\infty$

the energy dependence of A_{tot} at large -t will be the same as that of the Born amplitude A_B. In Brodsky et al (1973b) an iterative series generated by applying the Bethe-Salpeter equation to a quark interchange kernel is summed with results again of the form (2.3.4). It will be necessary to understand the confinement problem properly before series such as Fig. (2.3.2) can be summed exactly, but it is reasonable to hope that the total amplitude will be a sum of Regge pole and cut terms with trajectories behaving as (2.3.4).

Assuming this to be so, the sum of all diagrams in Fig. (2.3.2) in which one valence quark from each hadron ends up in the other hadron, can be identified as the sum of all meson pole trajectories contributing to the process in question. Note that this sum contains the Q.I. kernel diagram, Fig. (2.3.1), so that it is the large momentum transfer limit of meson-type Reggeon (R) exchange which results in the observed behaviour of the elastic differential cross sections at large angle.

Those diagrams which contain two or three pairs of valence quarks being exchanged between the hadrons sum to produce $R \otimes R$ and $R \otimes R \otimes R$ cuts respectively. It may be seen that if each exchange of a valence quark pair is replaced by a single meson line coupling to a quark in each hadron, the result is non-planar - the hallmark of a Regge cut.

All the exchanges in Fig. (2.3.2) involve at least one pair of valence quarks being interchanged. Baryon-baryon scattering diagrams in which gluons transfer the momentum (and hence no flavour is exchanged) are illustrated in Fig. (2.3.4). The sum of diagrams in which all the inter-baryon momentum transfer is between one quark from each baryon may plausibly be identified with the flavourless Pomeron (P) exchange (see e.g. Nussinov (1976a)). Diagrams involving two or three such exchanges between different pairs of valence quarks sum to $P \otimes P$ and $P \otimes P \otimes P$ cuts respectively.

Additionally, diagrams such as those shown in Fig. (2.3.5) will contribute to the total scattering amplitude. Fig. (2.3.5)a) is part of a $P \otimes R$ cut, Fig. (2.3.5)b) of a $P \otimes P \otimes R$ cut and Fig. (2.3.5)c) of a $P \otimes R \otimes R$ cut. There are other diagrams which are more difficult to interpret in terms of conventional Regge amplitudes such as Fig. (2.3.6).

Although only baryon-baryon scattering has been discussed above, the same principles of interpretation may be applied to meson-baryon and meson-meson scattering. There would, in general, be two quark interchange topologies involved rather than the one in the baryon-baryon case (see Fig. (2.3.7)).

Now that these identifications have been made, certain properties of the Regge amplitudes at intermediate and large angles can be deduced. At small $|t|$ the conventional view of scattering via Regge pole exchange is valid. The trajectories of these poles are found to be approximately rectilinear in this region. At large $|t|$ but with $s \gg |t|$, cuts may become important because their trajectories are flatter and so will be higher than those of their component poles (see equation (3.3.1)). The residues of these cuts, however, should rapidly decrease as $|t|$ increases, since at large angles (i.e. $|t|$ of the order of s) it is the meson-type poles which should dominate, summing as they do to the Q.I. kernel.

Assuming the Reggeon trajectories behave as (2.3.4), at large -t they must tend to the integer corresponding to the energy dependence of the appropriate kernel diagram. Some evidence that Reggeon trajectories do indeed bend at large -t from the rectilinear shape seen for $t \gtrsim 1$ $(GeV/c)^2$ may be found in Barnes et al (1978). If a trajectory takes an integer value the Regge pole amplitude is either purely real or purely imaginary. Since the Q.I. kernel amplitude with vector gluon exchange is real, the residues of those meson-Reggeon poles which become imaginary as $t \to -\infty$, must vanish at large -t. The residues of the remaining poles must be such as to give the DCR-predicted power law energy dependence at fixed angle. Building the amplitude from Regge contributions does not restrict the angular dependence in this power law scaling region since many daughter trajectories (displaced by negative integers from the parent trajectories) may contribute to the leading fixed angle term (i.e. the term corresponding to the Q.I. kernel). The residue of such a daughter with trajectory, say $\alpha_{parent} - M$ $(M = 1,2...\infty)$ would have to differ from that of its parent by t^M to preserve the DCR behaviour.

At large angles the amplitude will then take the form

$$A \sim s^{\alpha_{parent}} \underbrace{\left[a + b\frac{t}{s} + \frac{ct^2}{s^2} + \cdots\cdots \right]}_{\text{parent} \quad \text{daughters} \quad \ldots} (-t)^L \qquad (2.3.5)$$

where L is an integer and a,b,c are real constants.

Rewriting this gives

$$A \sim s^{\alpha_{parent}+L} \; F\left(\frac{t}{s}\right) \qquad (2.3.6)$$

where $F\left(\frac{t}{s}\right)$ is a scale-independent function giving the angular dependence of the amplitude. Comparing (2.3.6) with (1.2.7) yields that

$$\alpha_{parent} + L = -(N-2)/2 \qquad (2.3.7)$$

with N defined by (1.2.2). Note that for $s \gg |t|$ only the parent term (with coefficient a) in (2.3.5) is significant.

A Regge model based on the R.P.C.A, including

1) a Pomeron, important at small $|t|$

2) various cuts, possibly important for $t \gtrsim 1\ (\mathrm{GeV}/c)^2$, but $\frac{t}{s} \ll 1$

3) meson-Reggeons including daughters with trajectories tending to integers as $t \to -\infty$, and residues chosen so as to give DCR-power law scaling at large angles

should be able to give a good account of hadronic elastic scattering processes throughout the angular range from 0°_{cm} - 90°_{cm}. Further large angle properties of such a model are investigated in the following section.

2.4 The Structure of the Regge Amplitudes at Large Angles

In order to establish the behaviour of the meson-Reggeon terms at large -t it is necessary to take a closer look at the angular dependence of the QI amplitude. In particular it is vital to determine its effective Regge trajectory, α^R_{QI}, since it is to this value that the leading meson trajectories will tend as -t becomes large. Now, an amplitude which obeys the D.C.R. is constructed of terms of the form

$$A_{DCR} \propto s^a u^b t^c \qquad (2.4.1)$$

where $a+b+c = -\frac{(N-2)}{2}$ with N defined by (1.2.2).

In the Regge limit ($s \to \infty$, t fixed) this becomes

$$A_{DCR} \sim s^{a+b} t^c \qquad (2.4.2)$$

and hence

$$\alpha^R_{DCR} = a + b = -\frac{(N-2)}{2} \qquad (2.4.3)$$

It was shown previously that the contribution to the hadron-hadron scattering amplitude of a QI diagram can be rewritten as the product of a quark-hadron amplitude and a hadron electromagnetic form factor (see (1.4.12)). The form factor depends only on t and at large $|t|$ varies as an inverse power (see 1.4.13). The simplest assumption is that no further t dependence is introduced by the quark-hadron amplitude in which case the power c is determined entirely by the form factor. So, from (1.4.13)

$C = -1$ for a meson vertex

$C = -2$ for a baryon vertex

α^R_{QI} can then be obtained from (2.4.3):

$$\alpha^R_{QI} = -1 \quad \text{for meson-meson scattering}$$
$$\alpha^R_{QI} = -2 \quad \text{for baryon-baryon scattering} \qquad (2.4.4a)$$

Meson-baryon scattering receives contributions with $\alpha = -1$ and -2, however the term with the higher lying trajectory will dominate for large s, hence

$$\alpha^R_{QI} = -1 \quad \text{for meson-baryon scattering.} \qquad (2.4.4b)$$

These values agree with the result (1.4.18) which was obtained within CIM using a similar line of reasoning to that given above (see e.g. Brodsky et al (1973c)).

As noted in Section 1.4(2), however, predictions for angular behaviour in CIM depend strongly on assumptions made during the calculations. Results quoted from Brodsky et al (1977) and Coon et al (1978) in equations (1.4.19-21) and (1.4.22) respectively were obtained using quark-hadron amplidues dependent on t. Each of these versions predicts

$$\alpha^R_{CIM}\,(\text{meson-meson}) = \alpha^R_{CIM}(\text{meson-baryon}) = \alpha^R_{CIM}(\text{baryon-baryon}) = -1 \qquad (2.4.5)$$

There are good reasons (expounded below) for supposing α^R_{QI} to be the same in all three cases and hence for preferring models yielding results such as (2.4.5) to those giving (2.4.4).

a) The close connection between the electromagnetic form factor and one of the vertices of a QI diagram has already been noted: the lower vertices of the two diagrams in Fig. (2.4.1), for instance behave as do the meson and baryon form factors respectively. Now the upper vertices in Fig. (2.4.1) differ from each other in the same way as do the lower vertices. It is reasonable, therefore, to suppose that the ratio of the upper vertices is simply the ratio of the form factors, at least to leading order in $\frac{1}{s}$ Hence, using (1.4.13)

$$A(BB\to BB) \sim \frac{1}{t} A(MB\to MB) \sim \frac{1}{t^2} A(MM\to MM) \qquad (2.4.6)$$

and so

$$\alpha^R_{QI}\,(BB) = \alpha^R_{QI}\,(MB) = \alpha^R_{QI}\,(MM) \qquad (2.4.7)$$

b) At small $|t|$ the most important meson-Reggeon contributions to $d\sigma/dt$ (πp) and $d\sigma/dt$ (pp) are made by the same group of trajectories, the leading natural parity trajectories, f, ω, ρ, A_2. (All four are exchanged in pp scattering, but ω and A_2 are forbidden in π p scattering by G parity conservation). It is reasonable also to suppose that if a set of trajectories is important at large $|t|$ in pp scattering, then it will also be important at large $|t|$ for πp. Then, since it is argued that the QI kernel diagrams correspond to the large $|t|$ limit of sums of meson-Reggeon exchange diagrams, the effective trajectory α^R_{QI} should be the same for pp as for πp. This argument can be extended to reach once again the conclusion (2.4.7).

c) There is a family of lowest order Q.I. diagrams for which the value of α^R_{QI} may be readily determined. This is the family in which momentum is transferred between the interchanged quarks. A typical baryon-baryon diagram of this type is shown in Fig. (2.4.1). In such cases the quark-hadron amplitude can be expressed as the product of the quark-quark amplitude and the electromagnetic form factor of the hadron (1.4.12) then becomes

$$A(AB\to CD) = A(qq\to qq) \cdot F_{AC}(t)\, F_{BD}(t)$$

$$\sim \frac{t}{s}\, F_{AC}(t)\, F_{BD}(t) \quad \text{as } s \to \infty,\ t \text{ fixed} \qquad (2.4.8)$$

α^R_{QI} is then -1 regardless of the nature of hadrons A, B, C, D.

The link between the QI mechanism and meson-Reggeon exchange is particularly well illustrated using this type of diagram. Iteration of the gluon exchange between the interchanged quarks of Fig. (2.4.1) produces a set of ladder diagrams which sum to give a Regge-behaved amplitude (see Fig. (2.4.2)).

$$\sum_{i=1}^{\infty} A_i(AB\to CD) = A^R_{tot}(AB\to CD) \underset{\substack{s\to\infty \\ t \text{ fixed}}}{\sim} \beta^{A\ C}_{B\ D}(t)\, s^{\alpha^R(t)} \qquad (2.4.9)$$

Each of the terms in the sum can be factorised, in the same way as the kernel term, into hadron form factors and a quark-quark scattering amplitude, and hence so can the sum (see Fig. (2.4.3)).

$$\sum_{i=1}^{\infty} A_i(AB\to CD) = F_{AC}(t)\, F_{BD}(t) \sum_{i}^{\infty} A_i(qq\to qq) \sim F_{AC}(t)\, F_{BD}(t)\, \beta^{qq}_{qq}\, s^{\alpha^R(t)} \qquad (2.4.10)$$

Clearly, then, the effective Regge trajectory of the sum is independent of the nature of A,B,C,D. By the arguments of Section 2.3 $\alpha^R(t)$ will tend to -1 (the value obtained for the kernel alone) as -t becomes large.

It should be noted that Brodsky et al specifically exclude diagrams such as (2.4.1) from CIM calculations. They argue that the couplings of the gluons exchanged between quarks of the same hadron are amplified by the hadron wave function, whereas those of the gluon exchanged between the interchanged quarks are not. Thus Fig. (2.3.1) (which is included in CIM) is claimed to make a larger contribution to the scattering amplitude at large angles than does Fig. (2.4.1). Since both diagrams obey the DCR, if this is true at one energy and scattering angle it is true at all energies for this same angle.

Conversely, however, it is argued in Shijong Ryang (1978) that CIM diagrams involve a greater number of large momentum transfer gluon exchanges than do diagrams such as Fig. (2.4.1). Since the strong interaction (running) coupling decreases with increasing momentum transfer this means that CIM diagrams would be expected to contribute less to the total scattering amplitude at large angles.

It is, for the purposes of determining α^R_{QI} immaterial which, if either, of the above lines of reasoning is correct. Diagrams of the type illustrated by Fig. (2.4.1) must contribute to hadronic elastic scattering and, as shown above, behave like $\frac{1}{s}$ as $s \to \infty$ with t fixed. The total QI contribution to MM, MB or BB scattering cannot therefore have an effective trajectory lower than -1.

The consensus of the above arguments is that

$$\alpha^R_{QI}(MM) = \alpha^R_{QI}(MB) = \alpha^R_{QI}(BB) = -1$$

and hence from now on it will be accepted that the leading meson-Reggeon trajectory tends to this value as -t becomes large. This is not to say that lower lying trajectories are not important at large angles. Any number of daughter poles can contribute to the same order in $\frac{1}{s}$ at fixed $\frac{t}{s}$ as shown in (2.3.5). It is to be hoped, however, that an adequate account of the data can be obtained using a relatively small number of Regge pole terms.

In Fig. (2.4.4) the differential cross-sections corresponding to several amplitudes of the form (2.4.1) are compared with the pp elastic scattering data at $p_{lab} = 19.3$ GeV/c. The expressions for the theoretical curves are symmetrical about 90°_{cm} as required by the identity if the scattered particles, and are all normalized to agree with the data at 90°_{cm}. None of the curves give a good account of the data over a large range of t. The curves with $\alpha^R = a + b = -1$ and hence $c = -3$ (using the notation of (2.4.1)) tend to fare better at smaller angles, while those with $\alpha^R = -2$ ($c = -2$) seem more appropriate at large angles, although these trends also depend on the value of b. This indicates that 1st daughter Reggeons may well make important contributions to $d\sigma/dt$ as the scattering angle becomes large.

The required properties of a meson-Reggeon term are then, as follows:

a) For $t \gtrsim -1$ $(GeV/c)^2$ the term must behave approximately like the corresponding term in the RPCA model. The trajectory must be almost a straight line, a typical expression for which would be

$$\alpha = 0.5 + 0.9\ t$$

in the case of a leading natural parity trajectory.

b) At large -t the trajectory must approach a constant value (-1 in the case of a leading order trajectory). The residue must, in this region, behave approximately like

$$\beta(-t \text{ large}) = t^c \qquad (2.4.11)$$

where $c = -\alpha(t = -\infty) - \frac{(N-2)}{2}$

with N defined as in (1.2.2).

2.5 Conclusion

A basis has been proposed for the interpretation of elastic hadronic scattering amplitudes at all angles, in terms of a Regge model. For $t > -1$ $(GeV/c)^2$ such a model must approximate to the traditional Regge picture - straight line trajectories, Pomeron dominant but with meson-Reggeons important at lower energies, etc. As $|t|$ becomes larger, but still with $|t| \ll s$, cuts may become important (e.g. the $P \otimes P$ cut is evident in pp scattering at ISR energies). At large angles, however, the principal contribution to the differential cross section comes from the meson-Reggeons. The meson trajectories approach integer values at large $-t$, the leading ones tending to -1. Their residues are such that $d\sigma/dt$ approximately obeys the DCR at large angle.

In the following chapters experimental data for N-N and πp scattering processes are examined using this model. Chapter 3 deals with $d\sigma/dt$ (NN), Chapter 4 with NN spin asymmetries and Chapter 5 with $d\sigma/dt$ $(\pi^{\pm} p)$.

Table (2.2.1)

$A = 4.56 \times 10^8$

$n = 10.02$

$m = 7.52$

$t_1 = 0.20 \quad (GeV/c)^2$

$s_1 = -0.56 \quad (GeV/c)^2$

Table (2.2.2)

$A = 448.0$

$n = 7.97$

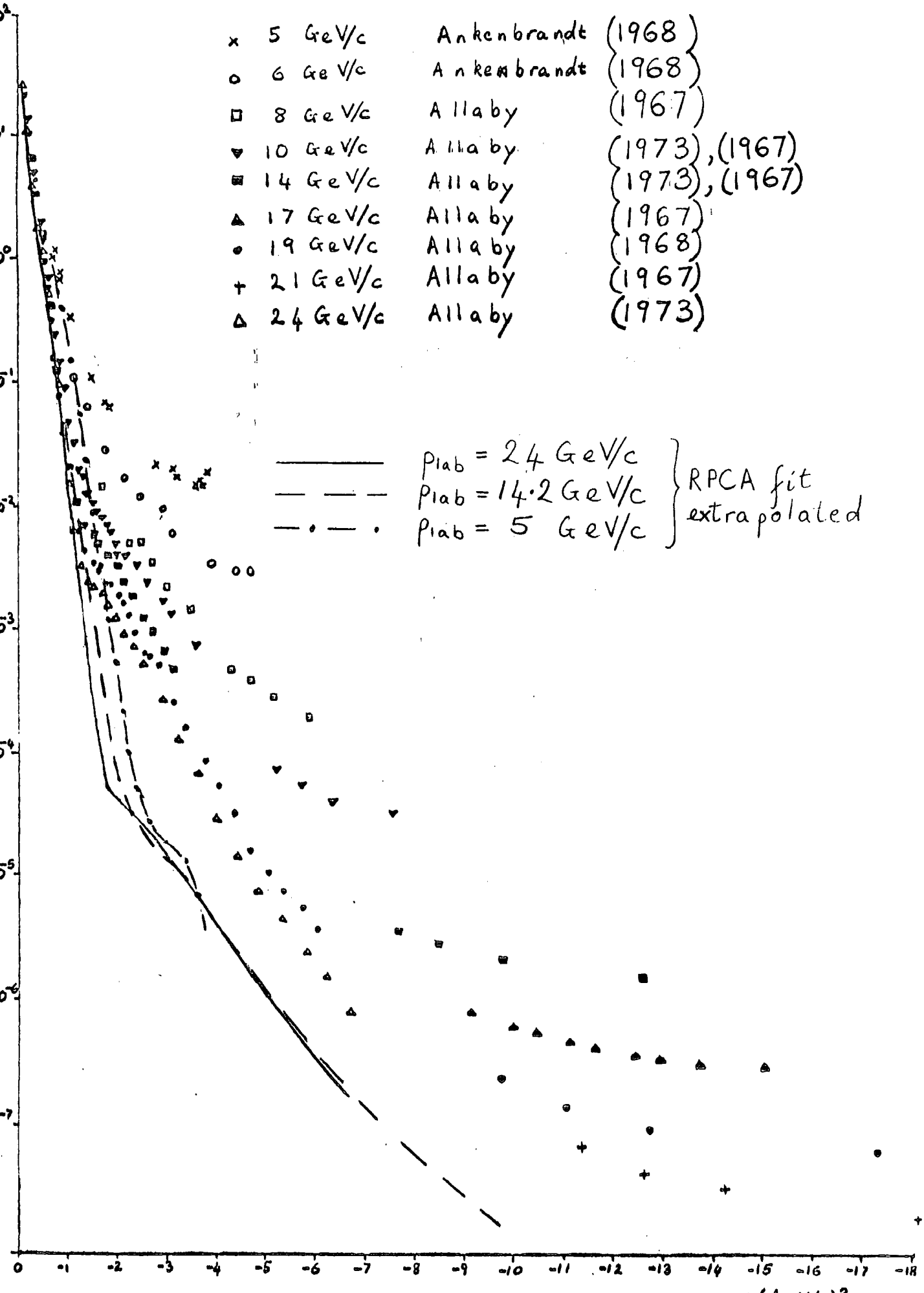

Fig. (2.2.1) : Extrapolation of RPCA fit to large angles

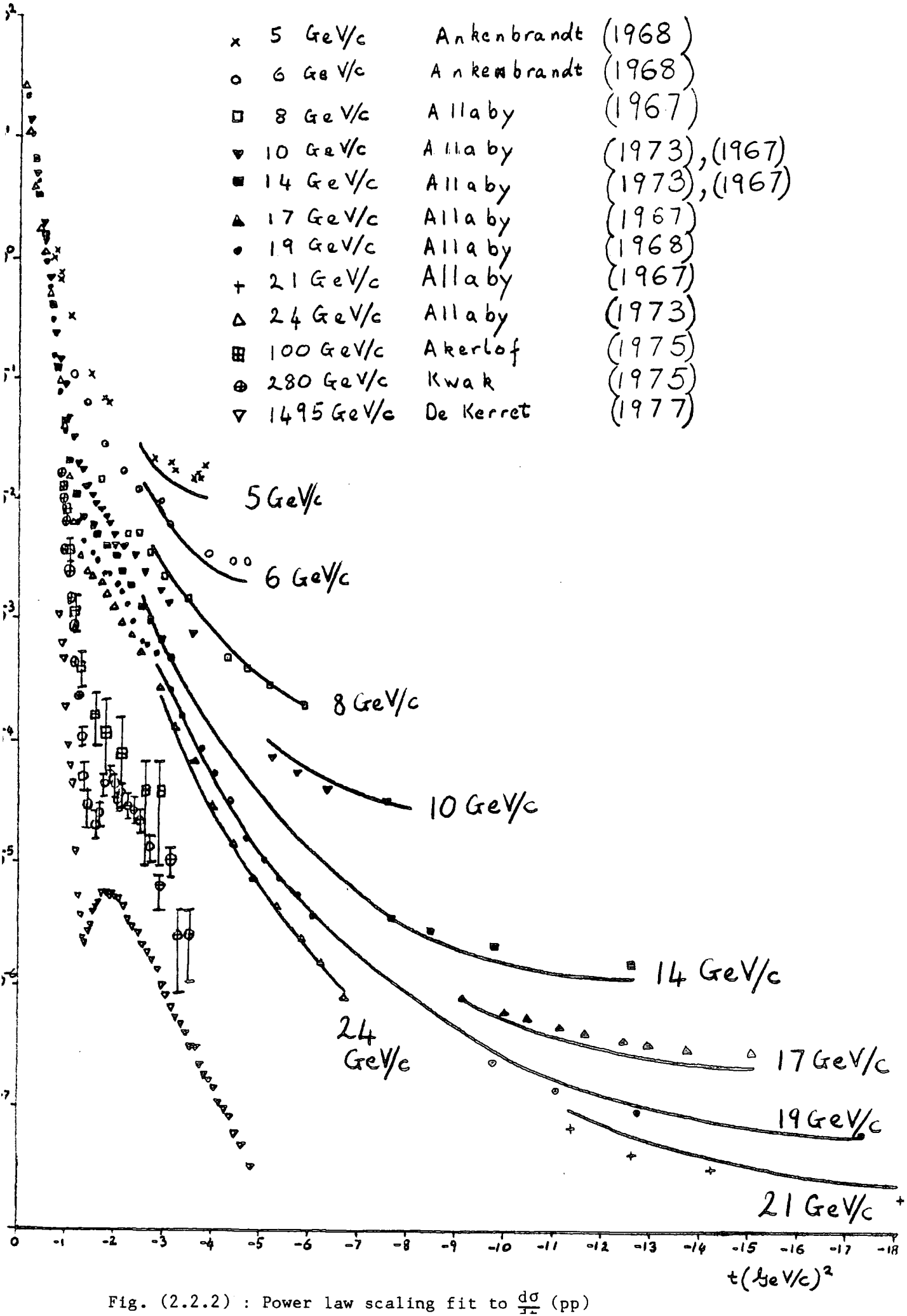

Fig. (2.2.2) : Power law scaling fit to $\frac{d\sigma}{dt}$ (pp)

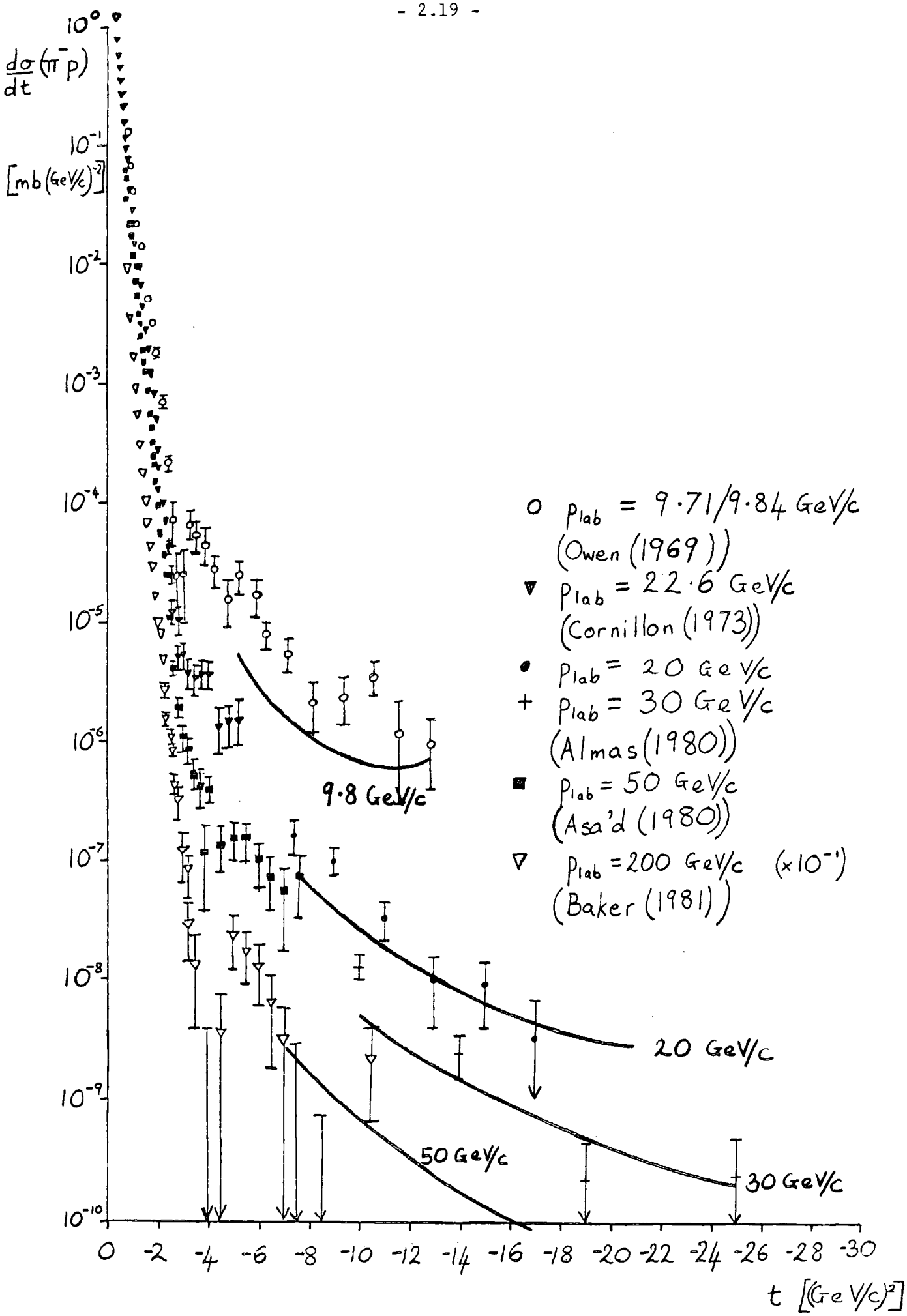

Fig. (2.2.3a) : Power law scaling fit to $\frac{d\sigma}{dt}$ (π^-p)

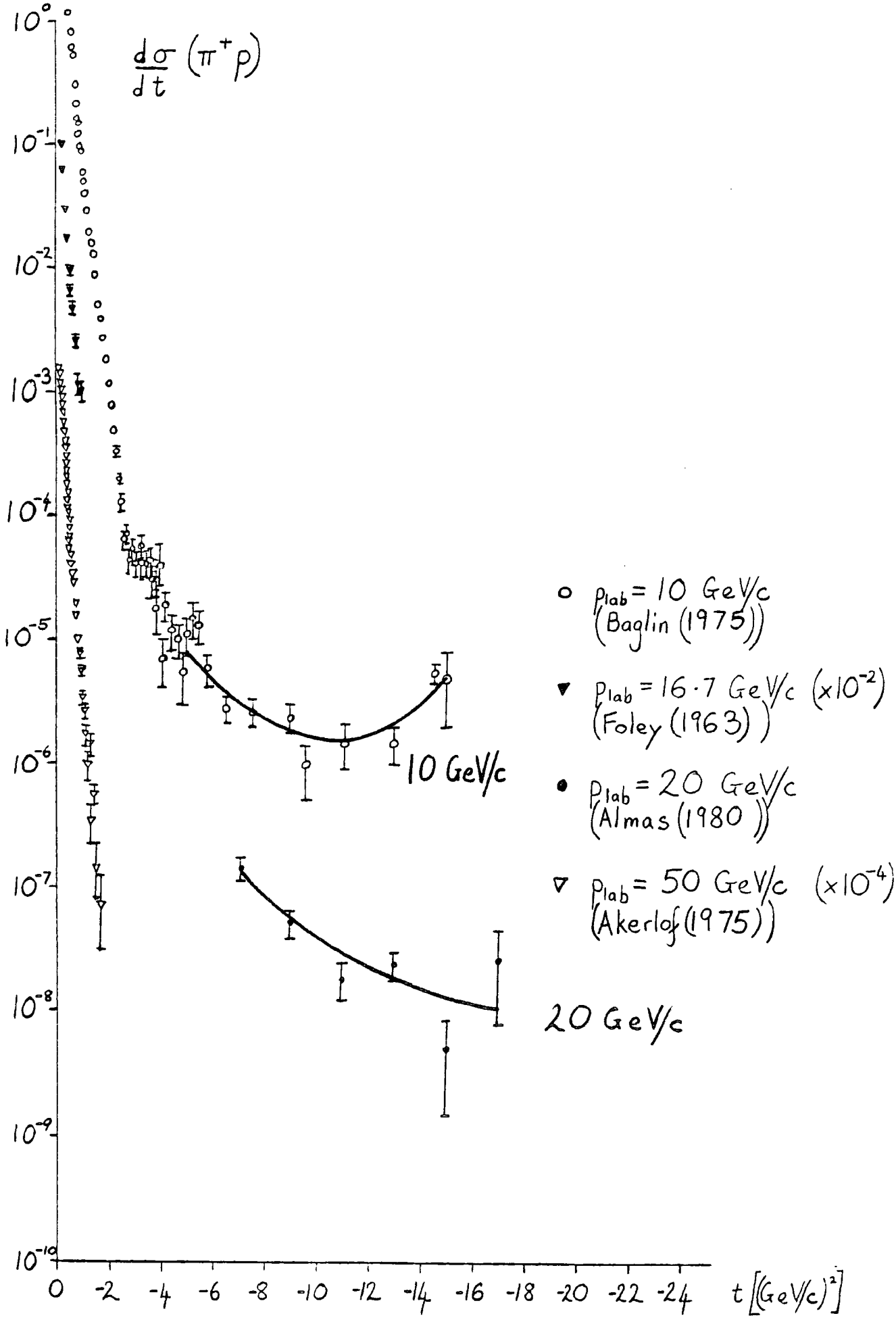

Fig. (2.2.3b) : Power law scaling fit to $\frac{d\sigma}{dt}(\pi^+ p)$

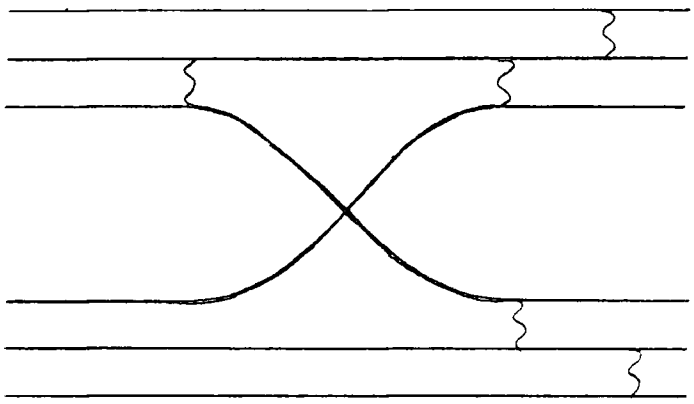

Fig. (2.3.1)

A lowest order baryon-baryon quark interchange diagram

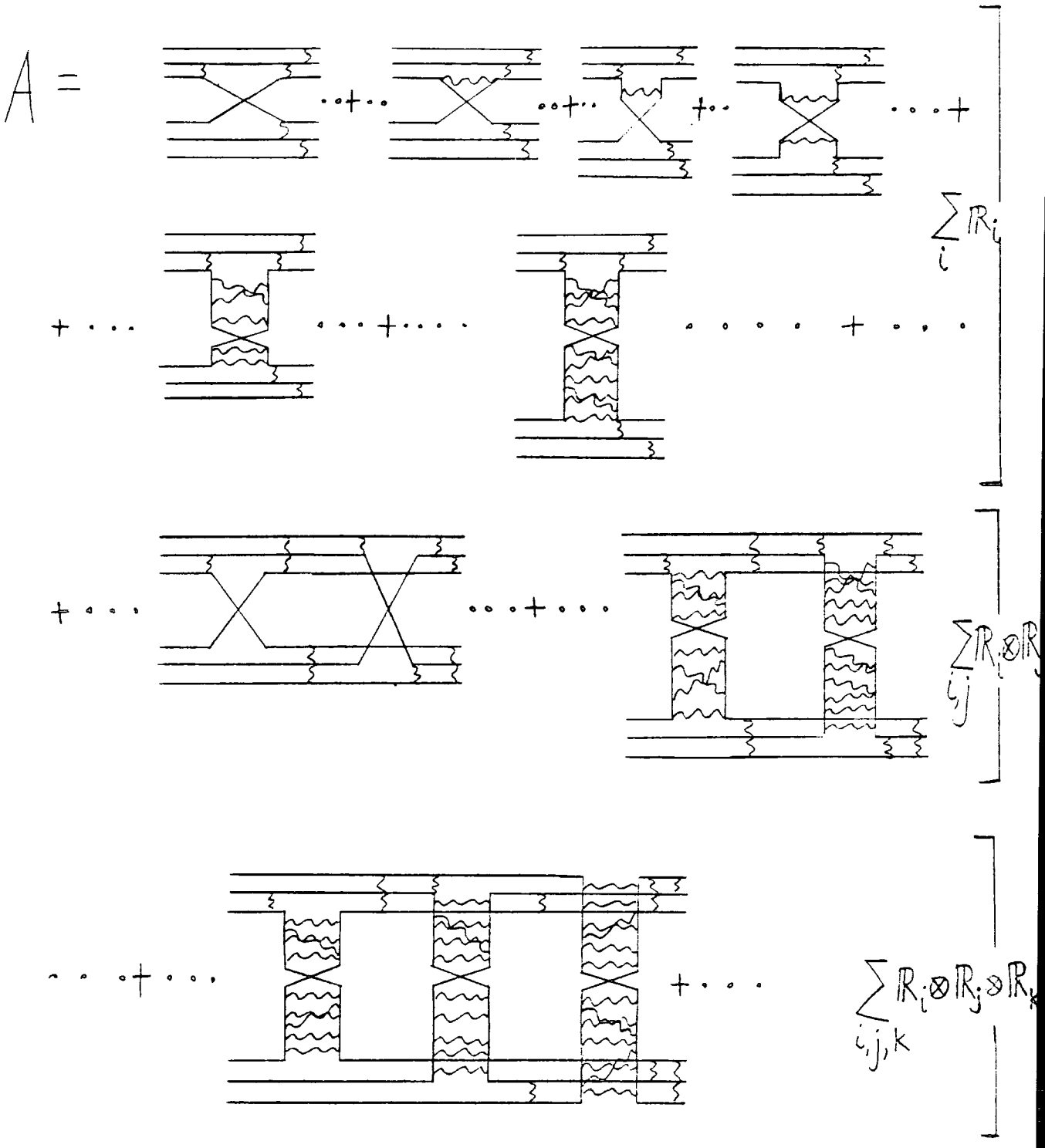

Fig. (2.3.2)

The perturbative series of baryon-baryon quark interchange diagrams

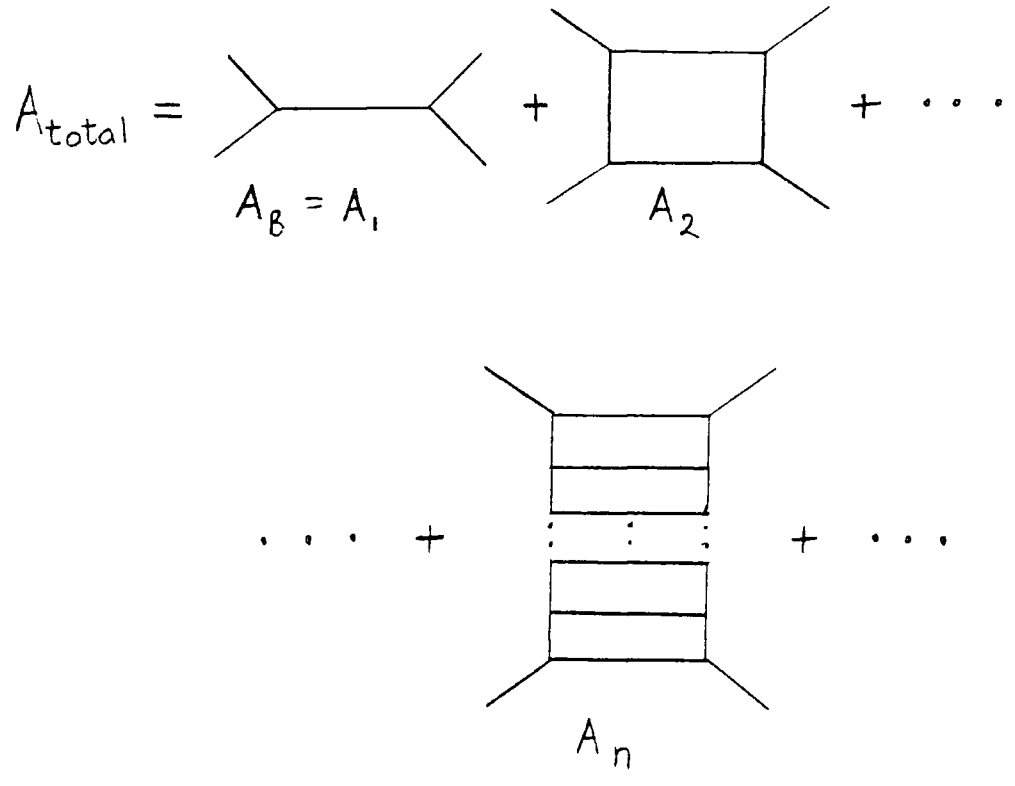

Fig. (2.3.3)

Sum of ladder diagrams in ϕ^3 field theory

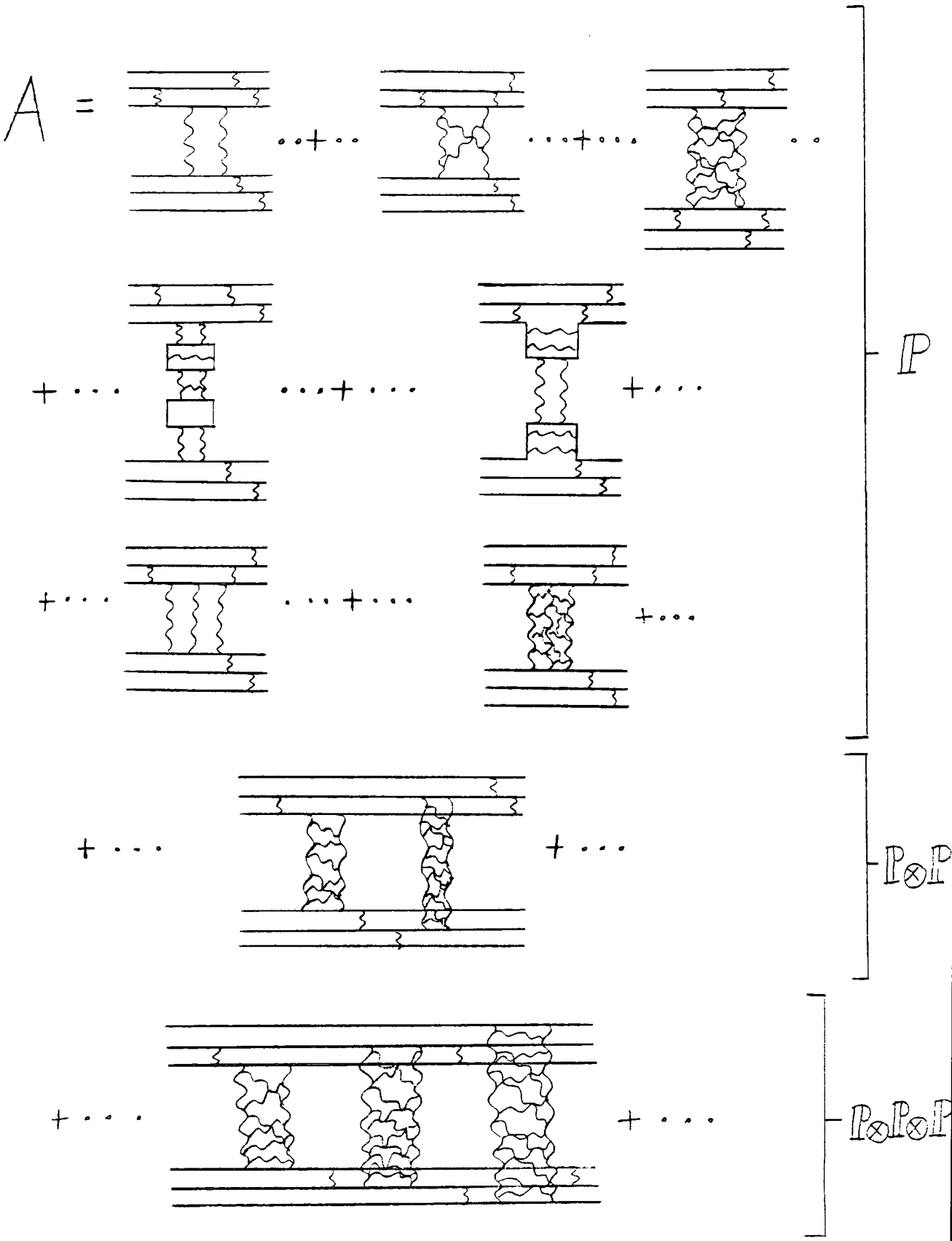

Fig. (2.3.4)

The perturbative series of baryon-baryon gluon exchange diagrams

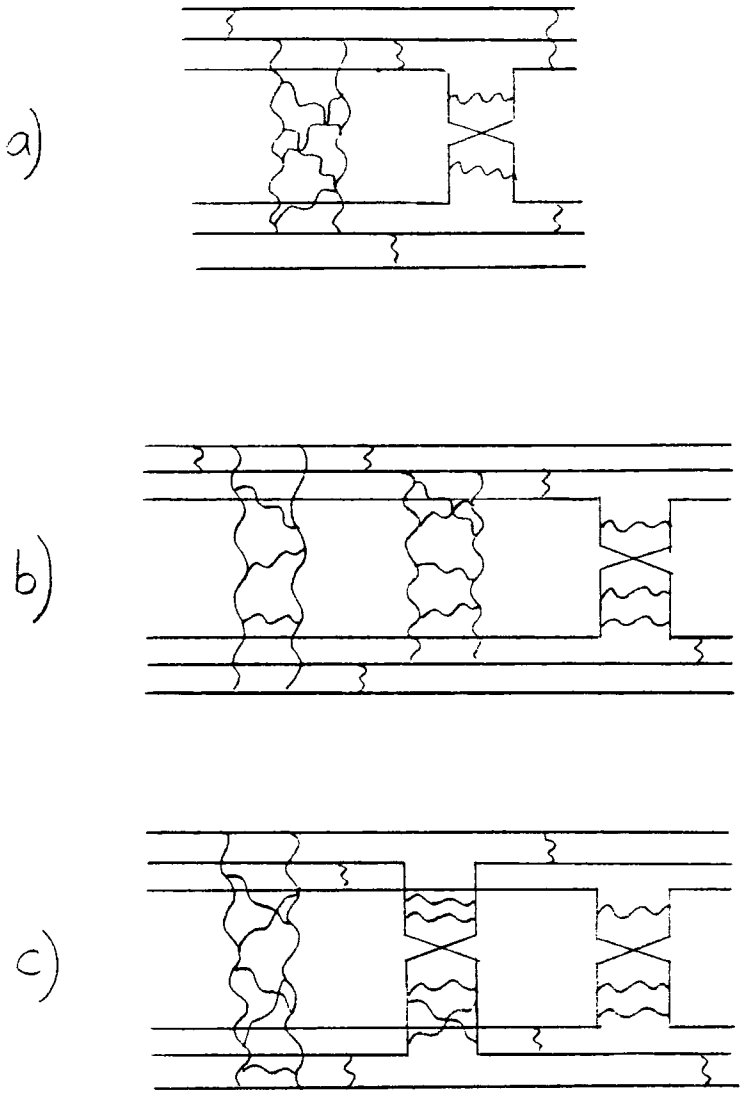

Fig. (2.3.5)

Diagrams contributing to a) an $R \otimes P$ cut, b) an $R \otimes P \otimes P$ cut, c) an $R \otimes R \otimes P$ cut

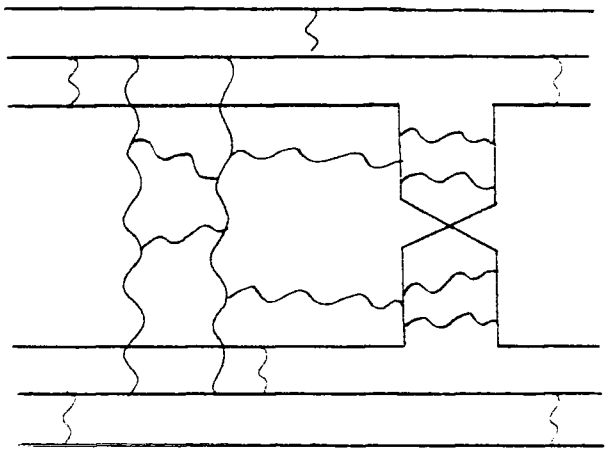

Fig. (2.3.6)

A contribution to a $P \otimes R$ cut with interlinked components

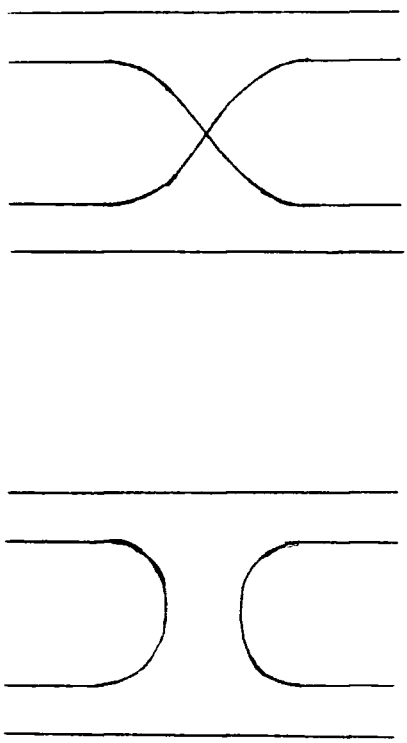

Fig. (2.3.7)

The two QI topologies involved in meson-meson scattering

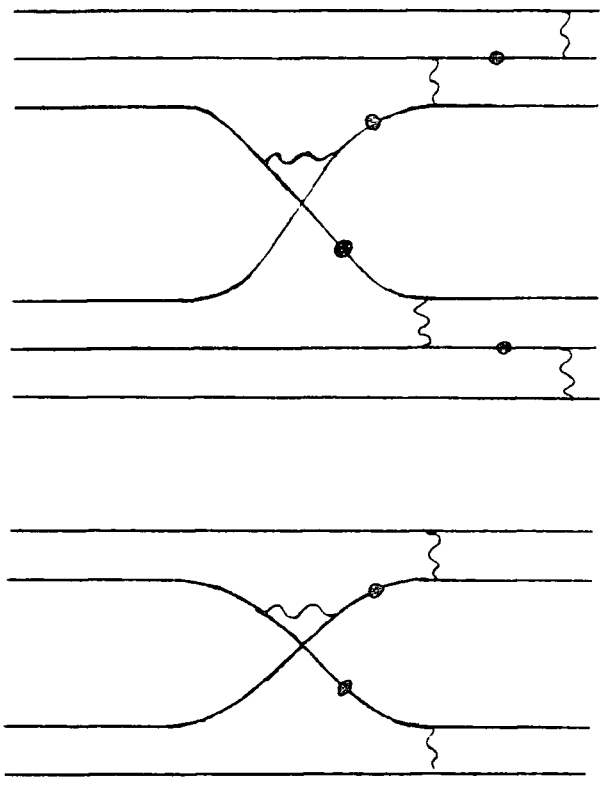

Fig. (2.4.1)

Lowest order baryon-baryon and meson-meson QI diagrams in which momentum is transferred between the interchanged quarks. The dots indicate off mass shell fermion propagators.

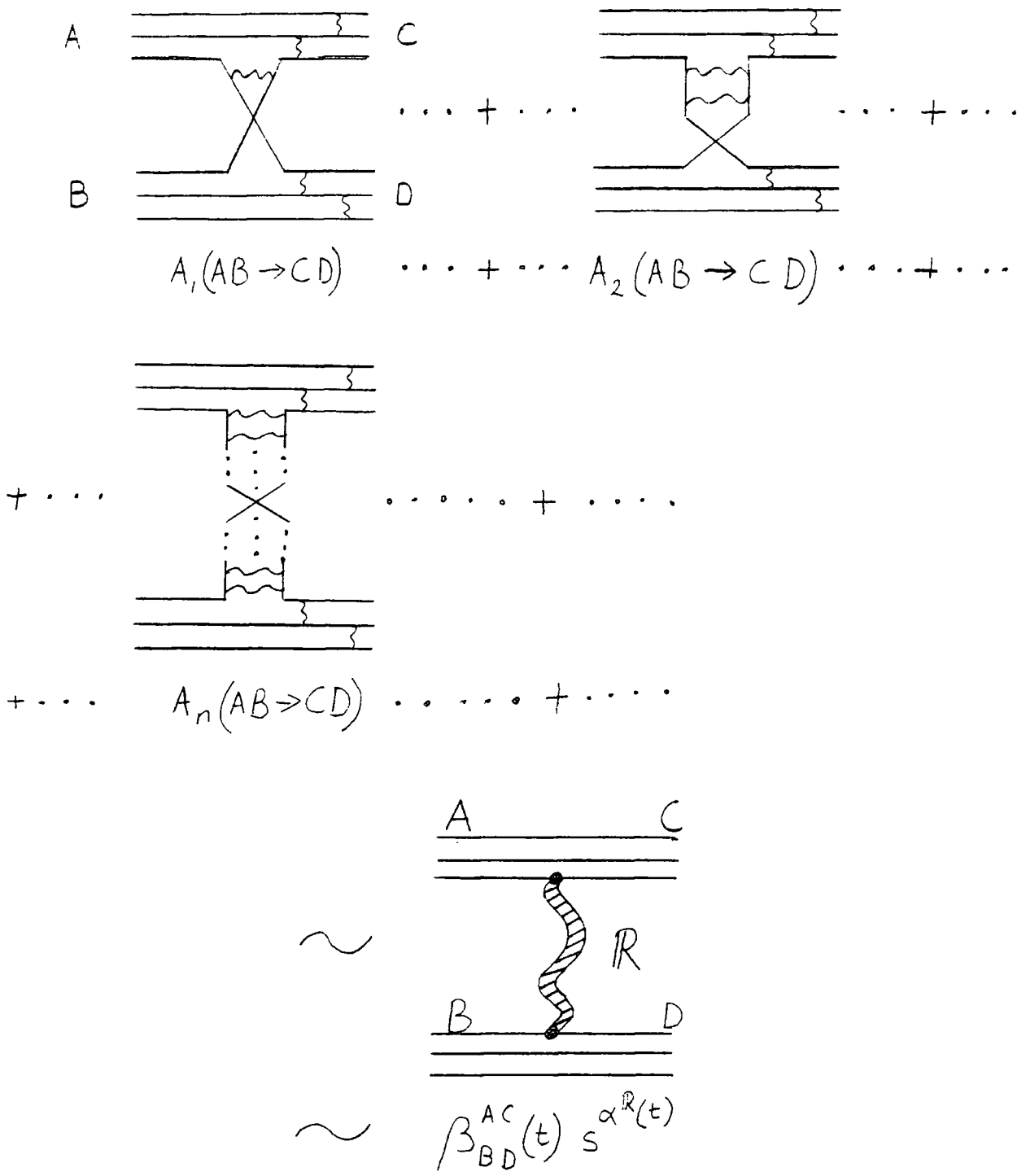

Fig. (2.4.2)

Iteration of gluon exchange between interchanged quarks in Fig. (2.4.1) giving Regge behaviour

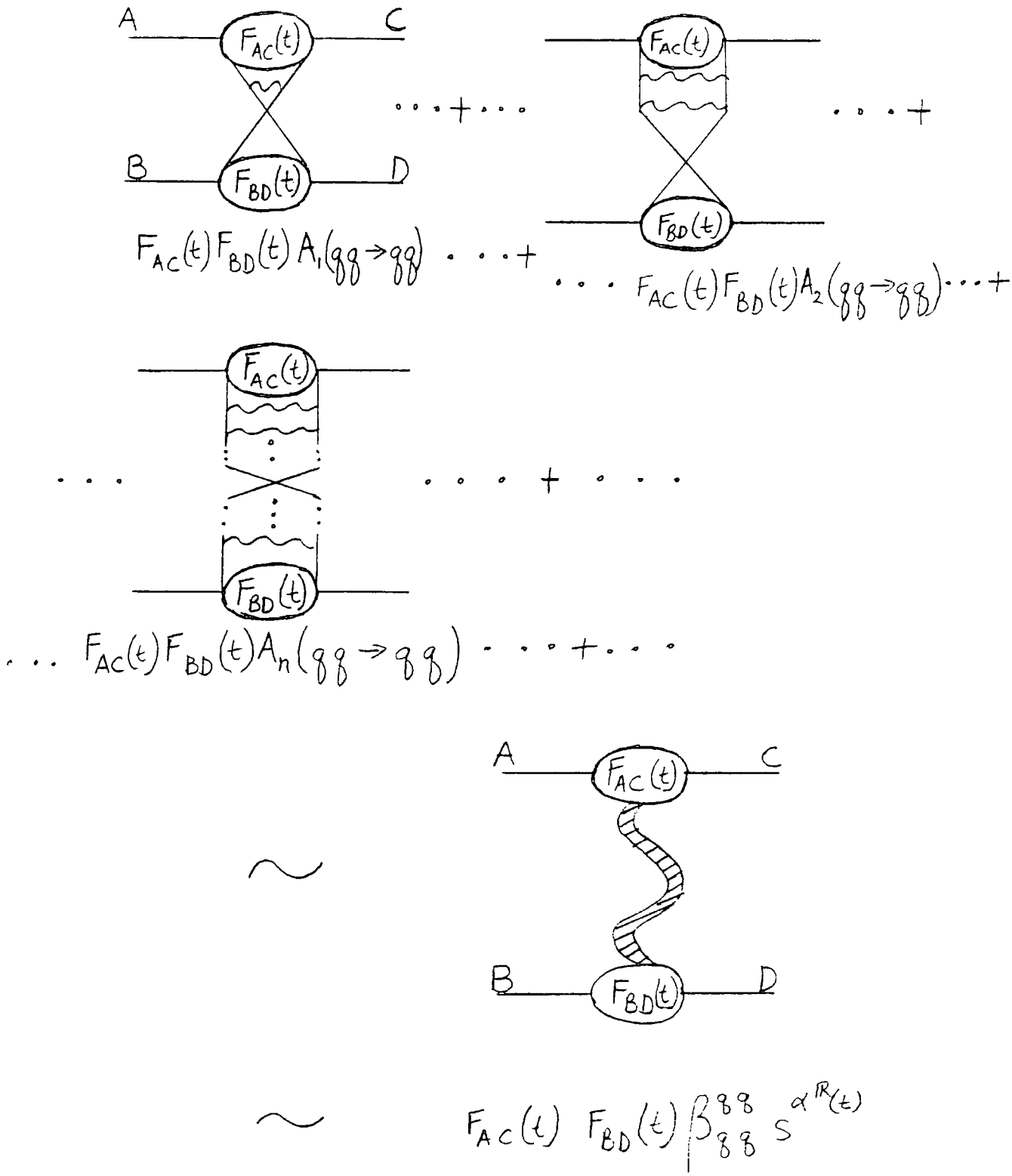

Fig. (2.4.3)

Iteration of gluon exchange between interchanged quarks in factorising kernel diagram giving factorising Regge behaviour

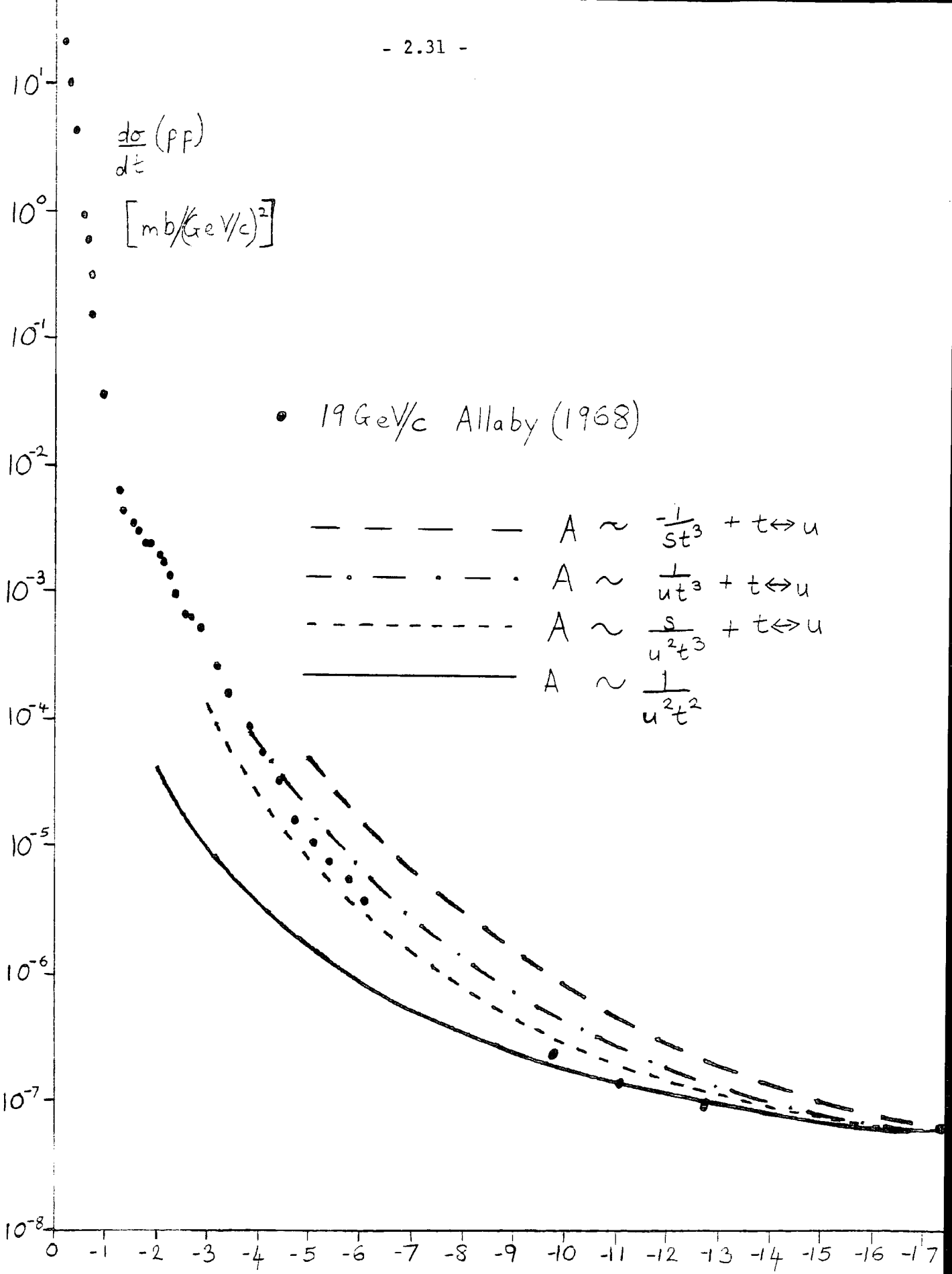

Fig. (2.4.4)

A comparison of curves satisfying the Dimensional Counting Rule with $\frac{d\sigma}{dt}$ (pp) data at p_{lab} = 19 GeV/c

CHAPTER 3

NUCLEON-NUCLEON ELASTIC DIFFERENTIAL CROSS-SECTIONS

3.1 Introduction

The ground has now been prepared and the tools assembled for an attempt at constructing scattering amplitudes which reproduce the measured values of the physical observables in elastic hadronic scattering processes across the complete angular range. A model has been proposed, which combines traditional small angle Regge theory with, at large angles, the Quark Interchange mechanism. This present chapter is concerned with applying this model to the differential cross-sections of N-N scattering processes.

By far the largest amount of elastic scattering data, spanning the greatest range of s and t, is available for the pp→pp process. $\frac{d\sigma}{dt}$ (pp→pp) has been measured out to 90°_{cm} at energies up to $s \simeq 40$ $(GeV/c)^2$. Large -t (but not large θ_{cm}) data is available from the Cern ISR up to $s \simeq 4000$ $(GeV/c)^2$. In contrast to this abundance, the only other NN→NN measurements performed for $t \lesssim -1$ $(GeV/c)^2$ are for $\bar{p}p \rightarrow \bar{p}p$ and pn→pn. The highest energy large $|t|$ pn data is at $s \simeq 25$ $(GeV/c)^2$, while $\bar{p}p$ data is now available at $s \simeq 400$ $(GeV/c)^2$ although the latter does not extend to large angles.

Both Regge theory and the QI approach are valid asymptotically as $s \rightarrow \infty$, so that the proposed combined model should be tested using the highest energy all-angle data available. Data for a range of energies must be used to determine the energy dependence of the scattering amplitudes and to study the evolution of structures in the differential cross-section. If this range extends to too low an energy, however, the risk is run of leaving the region of validity of the theory. Data of $s = 10$ $(GeV/c)^2$ and above will be fitted here, which allows $\frac{d\sigma}{dt}$ for

pp, $\bar{p}p$ and pn to be compared over an s range of about 15 $(GeV/c)^2$, while hopefully remaining in the regions where low energy effects are not too prominent. Due to the greater abundence and wider range of pp data, it will be this process which will determine the energy dependence of the main asymptotic features. $\bar{p}p$ and pn will play a large role in examining the isospin and charge conjugation properties of the contributions to the scattering amplitudes.

The signs of the isospin and charge conjugation eigenstate amplitudes referred to in this and later chapters are defined according to phase conventions such that

$$\left.\begin{aligned} A(pp\to pp) &= (I=0,\ C=+) + (I=0,\ C=-) + (I=1,\ C=+) + (I=1,\ C=-) \\ A(pn\to pn) &= (I=0,\ C=+) + (I=0,\ C=-) - (I=1,\ C=+) - (I=1,\ C=-) \\ A(\bar{p}p\to\bar{p}p) &= (I=0,\ C=+) - (I=0,\ C=-) + (I=1,\ C=+) - (I=1,\ C=-) \end{aligned}\right\} \quad (3.1.1)$$

where (I,C) represents the sum of the contributions with isospin I and charge conjugation C.

The R.P.C.A. model of Collins et al (see Section 1.5) will form the basis of the fit at small angles. This region is examined in Section 3.2. Section 3.3 looks at the intermediate angle region ($t \lesssim -1$ $(GeV/c)^2$, $-t \ll s$ up to $s = 50$ $(GeV/c)^2$ paying particular attention to the role of cuts. The large angle region is considered in Section 3.4. Here the behaviour of the model is determined by the predictions of the QI mechanism. In Section 3.5, the final fits will be presented, covering the whole range of angles and energies and incorporating the lessons learnt in the preceding sections.

3.2 The model at small angles

As mentioned earlier the RPCA model of Collins et al gives a good account of several hadronic scattering processes at small angles. To avoid wasteful repetition of work already performed the RPCA will be adopted as the starting point of the all-angle Regge model. By ensuring that deviations from RPCA become small as $t \to 0$ and as $s \to \infty$ with t fixed a good fit to the data in these kinematical regions should be guaranteed. The RPCA model was described in general terms in Section 1.5. Its application specifically to NN processes will be discussed here. The fits presented in this section are taken from Wright (1978).

The leading trajectories exchanged in NN scattering are P, f, ω, ρ, A_2. All of these possess natural parity, and hence it is expected that at high energies the unnatural parity amplitudes should make only small contributions to $d\sigma/dt$. (See Appendix B for a discussion of the five independent NN amplitudes and for a definition of the notation). In the RPCA, the P, ω, f exchanges, which make the most important contributions at small $|t|$ to the natural parity helicity non-flip amplitude, N_0, have very small couplings to nucleons at helicity-flip vertices. Also, the ρ and A_2, which make the major contributions to flip amplitudes are predicted to have couplings at flip vertices only one third of the f and ω non-flip couplings. A factor of $\sqrt{-t}$, demanded by kinematics at each flip vertex further lessens the ratios of N_1 and N_2 to N_0 at small $|t|$. The dominant contribution to $d\sigma/dt$ is thus expected to come from N_0. This conclusion is supported by the polarization and spin asymmetry (A_{ij}) data, these parameters being small ($\lesssim 0.2$) except at large $|t|$ (see Figs. (1.3.5)-(1.3.9). In this chapter it will be assumed that at

small and intermediate angles, the whole of $d\sigma/dt$ is accounted for by N_0. The consistency of this assumption will later be checked using fits to N_1, N_2, U_0, U_2 obtained in Chapter 4.

The RPCA ρ, A_2, ω, f and P contributions to N_0 (pp-pp) may be obtained by substituting (3.2.1) in (1.5.4) and using the linear trajectories, then making the modifications (1.5.6).

$$\left.\begin{aligned}
\beta_{\frac{1}{2}\frac{1}{2}}\ (pp;\omega) &= f_\omega \sqrt{\frac{\pi\alpha'_\omega}{2}} \\
\beta_{\frac{1}{2}\frac{1}{2}}\ (pp;f) &= f_\omega \sqrt{\frac{\pi\alpha'_\omega}{2}}\ (1+\varepsilon_B) \\
\beta_{\frac{1}{2}\frac{1}{2}}\ (pp;\rho) &= \frac{f_\omega}{3} \sqrt{\frac{\pi\alpha'_\rho}{2}} \\
\beta_{\frac{1}{2}\frac{1}{2}}\ (pp;A_2) &= \frac{f_\omega}{3} \sqrt{\frac{\pi\alpha'_\rho}{2}} \\
\beta_{\frac{1}{2}\frac{1}{2}}\ (pp;P) &= f_\omega \sqrt{\frac{\pi\alpha'_\omega}{2}}\ Ge^{at} \left[1-\frac{t}{\bar{t}}\right]^{-a(1+\varepsilon_B)}
\end{aligned}\right\} \quad (3.2.1)$$

where α'_R is the slope of the appropriate linear trajectory from (1.5.3); $f_\omega = 17.10$, $\varepsilon_B = 0.14$, $a = 0.6$, $\bar{t} = 0.74$, $G = 0.47$ are fitted parameters. Note that for natural parity exchanges

$$\beta_{\frac{1}{2}\frac{1}{2}} = \beta^{\frac{1}{2}\frac{1}{2}} = \beta^{-\frac{1}{2}-\frac{1}{2}} = \beta_{-\frac{1}{2}-\frac{1}{2}}$$

N_0 ($\bar{p}p \to \bar{p}p$) and N_0 ($pn \to pn$) may be obtained by reversing the signs of the appropriate contributions as specified in (3.1.1).

The total cross sections for the three processes can be obtained from the above via the optical theorem.

$$\sigma_T = \frac{.3893}{s} \text{ Im } (A(t=0)) \qquad (3.2.2)$$

Discrepancies between the theoretical and experimental curves at low energies indicate the need for an extra term with isospin 0, charge conjugation + and a low lying trajectory. This is most readily interpreted as a daughter of the f with trajectory

$$\alpha_{f_D} = \alpha_f - 1$$

and its contribution parametrized as for the f except for an extra multiplicative constant, whose value (-8.1) has been determined by fitting to the data. The RPCA curves for the three total cross sections are compared with data in Fig. (3.2.1). Note that the majority of free parameters in the model are determined from fits to σ_T.

At large s, P is almost entirely responsible for the total cross sections, and it is this term, with its trajectory intercept greater than one, which causes the rise in σ_T with increasing s in this region. The flatness of $\sigma_T(pp)$ and $\sigma_T(pn)$ compared to $\sigma_T(\bar{p}p)$ at low energies is explained by the approximate exchange degeneracy of the ρ, A_2 and f,ω pairs - an exchange degenerate pair makes a total contribution to the pp and pn scattering amplitudes which is real, and so has no effect on σ_T in these processes. The small difference between $\sigma_T(pn)$ and $\sigma_T(pp)$ is accounted for by the relatively weak couplings of the I=1 ρ and A_2. The steeper fall of σ_T at very low energies is explained by the presence of the f-daughter term.

Turning now to the differential cross sections, from Fig. (1.4.7) it is seen that $d\sigma/dt$ (pp) is virtually independent of energy for $s \gtrsim 200$ $(GeV/c)^2$. This indicates that the scattering amplitude is almost entirely composed of contributions with trajectories near one. For $|t|<1$, $d\sigma/dt$ in this region can be satisfactorily described by a P alone. At $t \simeq -1.4$ $(GeV/c)^2$, however, a deep interference minimum is observed, and beyond this the variation of $\frac{d\sigma}{dt}$ with t becomes much slower. This large $|t|$ region is interpreted as being due to a $P \otimes P$ cut (see Collins et al (1978b)). The dip at $t = -1.4$ $(GeV/c)^2$ is then caused by interference between the cut and P itself. The depth of the dip depends on the relative phases of P and $P \otimes P$ and hence on the difference between the two trajectories at this point. The cut trajectory is obtained from that of the pole;

$$\alpha_{P \otimes P} = 1 - 2\alpha_P \ (t = 0) + \frac{\alpha'}{2} \qquad (3.2.3)$$

(This assumes that α_{cut} is determined by the position of the branch point).

Since the value of α_P $(t = 0)$ is determined from the σ_T data, α'_P is given by the depth of the dip, $\alpha_P(t)$ and $\alpha_{P \otimes P}(t)$ are thus strongly constrained and little freedom is left for adjustment.

The cut used in the RPCA papers is based on that described in Collins et al (1978b) eqn (8), but with an additional ad hoc term which compensates in the dip region, for changes made to the Pomeron. However it was found that a better overall fit is obtained by reverting to the cut parametrization of Collins et al (1978b). Accordingly the P must also be modified. This was done by replacing the t dependent factors in the Pomeron coupling described in (3.2.1), by

$$e^{\frac{at}{\sqrt{\left[(1 - x) + xe^{bt}\right]}}}$$

and by making the replacement (3.2.4)

$$R(t) \cdot \frac{1}{\Gamma(\alpha(t))} \Longrightarrow R(t = 0) \quad \frac{1}{\Gamma(\alpha(t=0))}$$

in the notation of (1.5.4). This procedure yields the Pomeron t dependence used in Collins et al (1978b) while retaining the RPCA coupling at t = 0. The Pomeron and cut together give an excellent account of the very large s data over a wide range of energies. The RPCA fit is shown in Fig. (1.4.7). All the P and $P \circledcirc P$ parameters are determined in this energy region. The almost complete lack of variation with energy of the data allows no sizable contribution to come from lower lying trajectories at these high energies. Any extra terms required to describe the lower energy data must, therefore, fall off rapidly as s increases, so as to be small in the ISR region.

The natural parity meson-Reggeons ω and f (ρ and A_2 have smaller couplings) make a sizable contribution to $d\sigma/dt$ for $s \lesssim 60$ $(GeV/c)^2$ at $|t| \lesssim 1$ $(GeV/c)^2$. This observation is borne out by a comparison of α^{eff}(expt.) in this region (intermediate between Pomeron and meson-Reggeon trajectories) and the same parameter at very high energies (close to the Pomeron trajectory) - see Fig. (1.4.4.). As can be seen in Fig. (3.2.2), the RPCA fit gives a reasonable account of the pp data for $0 > t > -1$ $(GeV/c)^2$ down to $s \simeq 10$ $(GeV/c)^2$. The model agrees well with the data around $t = -.8$ $(GeV/c)^2$ at $p_{lab} = 24$ (GeV/c), lies below at 5 GeV/c, but in between it is rather too high. This indicates the need for modifications to the detail of the energy dependence in this region.

Fig. (3.2.3) shows the RPCA prediction for $\frac{d\sigma}{dt}$ ($\bar{p}p$). The shape of the dip at $t \simeq -0.5$ $(GeV/c)^2$ in the plab = 5 GeV/c data is reproduced well, although the theoretical magnitude is rather too large. At higher energies, however, the dip persists in the prediction, while it rapidly disappears in the data. Clearly some refinement of the model is required here.

Due to the small values of the ρ and A_2 couplings, the RPCA prediction for $\frac{d\sigma}{dt}$ (pn) is very close to that for $\frac{d\sigma}{dt}$ (pp). As can be seen in Fig. (3.2.4), this is in agreement with the data for $|t| < 1$ $(GeV/c)^2$. The pp and pn differential cross sections separate, however, as $|t|$ grows larger.

The RPCA model thus gives an excellent account of the pp, pn and $\bar{p}p$ total cross section data, using P, ω, f, ρ, A_2 and f-daughter exchange terms. Addition of a $P \otimes P$ cut enables the very high energy pp differential cross-sections to be fitted extremely well. $\frac{d\sigma}{dt}$ for $|t| < 1$ $(GeV/c)^2$ is described reasonably well for all three processes right down to $s = 10$ $(GeV/c)^2$. There are indications (e.g. the evolution of the dip in $\frac{d\sigma}{dt}$ ($\bar{p}p$) at $t \simeq -.5$ $(GeV/c)^2$) that, even at these low $|t|$ values, further terms are becoming significant. These will be discussed in Section 3.3.

3.3 The need for Regge cut terms at medium angles

Looking at the pp differential cross section (Fig.(1.3.1)) a quite abrupt change of behaviour is observed at $t \simeq -1$ to -1.5 $(GeV/c)^2$ for $20 < s < 50$ $(GeV/c)^2$. The steep fall of $\frac{d\sigma}{dt}$ for $|t| < 1$ $(GeV/c)^2$ changes to a much more gradual decline for $|t| \gtrsim 2$ $(GeV/c)^2$, the two regions being linked by a very flat "shoulder". The similarity between this change and the one observed in the ISR data may immediately be seen. In each case a transition occurs from a steeply sloping region to a much flatter one via some form of interference phenomenon.

There can, however, be no simple identification between the $P \otimes P$ cut seen at very high energies and what is observed for $20<s<50$ $(GeV/c)^2$. If the predictions from the small angle RPCA model described in Section 3.2 are plotted against the data in this latter energy range Fig. (2.2.1) results. For $t \lesssim -1$ $(GeV/c)^2$ the theoretical curves are well below the experimental points. The trajectory of the $P \otimes P$ cut is quite firmly determined over a wide range of high energy data. The data does not allow sufficient freedom for both high and low energy regions to be fitted by the cut without major modifications to the parametrisation of its energy dependence.

This problem is illustrated clearly by Fig. (3.3.1), which demonstrates the energy dependence at fixed t in this region. An abrupt change of slope may be seen in the data between p_{lab} = 100 and 200 GeV/c. At energies above this the slope corresponds to $\alpha_{eff} \simeq 1$ while at lower energies α_{eff} $(t = -2.4) \simeq 0.15$. The evidence thus indicates that a Regge term with trajectory lower lying than that of the $P \otimes P$ cut is important for $t \lesssim -1$ $(GeV/c)^2$ and $p_{lab} \lesssim 150$ GeV/c. α_{eff} in this region has a slope of about 0.35, indicating that the trajectory of the extra term is flatter than those of traditional meson-Reggeons, but steeper than that of P or the $P \otimes P$ cut.

More information about this as yet unidentified contribution (henceforward called C, for ease of reference) can be obtained by comparing $\frac{d\sigma}{dt}$ (pp) with $\frac{d\sigma}{dt}$ (pn) and $\frac{d\sigma}{dt}$ ($\bar{p}p$). On first examining the pn data (Fig. (1.3.2)) one is struck by similarity in structure to pp. Clearly, then, the physics of the two reactions must be similar. At medium angles, however, $\frac{d\sigma}{dt}$ (pn) is lower by approximately a factor of 2. If C is the principle contribution in this region, it must, therefore have mixed isospin properties.

Turning to $\frac{d\sigma}{dt}$ ($\bar{p}p$), (Fig. (3.3.2)) at low energies the complicated interference phenomena make conjecture about the nature of individual contributions difficult. The recent measurements at p_{lab} = 50, 100 and 200 GeV/c however, enable interesting comparisons to be made with $\frac{d\sigma}{dt}$ (pp). This data exhibits a sharp dip structure at $t \simeq -1.4$ very reminiscent of that seen in pp at high energies. In pp, however, this dip is not seen until $p_{lab} \simeq 200$ GeV/c. In fact $\frac{d\sigma}{dt}$ ($\bar{p}p$) at 50 GeV/c bears an uncanny resemblance to $\frac{d\sigma}{dt}$ (pp) at 1495 GeV/c and presumably arises from the same origin. Unfortunately, there is no large $|t|$ pp data at 50 GeV/c, but interpolation from Fig. (3.3.2) yields a value for $\frac{d\sigma}{dt}$ (pp) at $t = -2.4$ five times the $\bar{p}p$ value. It appears, then, that whereas the C term adds greatly to the pp differential cross section at this energy, its contribution to $\bar{p}p$ is much smaller, and perhaps of a different phase. C, therefore, seems to possess mixed charge conjugation as well as isospin properties.

This complicated crossing behaviour indicates that C is probably not a single term, but rather a sum of 4 contributions; C(I=1, C=+), C(I=-1, C=+), C(I=1, C=-) and C(I=-1, C=-) each with similar energy dependences. This rules out it being a pre-asymptotic contribution to either P or $P \otimes P$ as both of these are purely I=0, C=+. The next possibility to consider is that C could be a combination of the four leading natural parity mesons, f, ω, ρ and A_2. It has already been suggested that the meson trajectories tend to integer values as -t increases. Could they, then bend in such a way as to account for the energy dependence attributed to C?

The trajectories of ρ and A_2 are well determined for $t \gtrsim -1$ $(GeV/c)^2$ from analysis of $\frac{d\sigma}{dt}(\pi^- p \rightarrow \pi^o n)$ and $\frac{d\sigma}{dt}(\pi^- p \rightarrow \eta^o n)$. (see e.g. Collins (1977) p.189). In this region they are indistinguishable from straight lines with intercepts at about 0.5 and gradients approximately 0.9. (The results of Barnes et al (1978), however indicate possible flattening for $t < -1$ $(GeV/c)^2$). The ω trajectory is less well known, and the f can never be isolated from the Pomeron, but it is reasonable to expect that these will be similar to the ρ and A_2.

Thus, the available evidence indicates that the ρ, A_2, f and ω trajectories have fallen to a value of $\alpha \simeq -0.4$ at $t = -1$ $(GeV/c)^2$. The data indicates that α_c is close to zero at $t \simeq -2$, and subsequently falls with a slope of about .35. If a single trajectory were required to behave like $\alpha_{\rho, A_2, f, \omega}$ for $t > -1$ (GeV/c) and like α_c for $t < -2$ $(GeV/c)^2$ it would have to possess a double kink between these two regions. Since Regge trajectories are required to be Herglotz functions (i.e. all derivatives must be positive; see Collins (1977) p. 81) except when trajectories cross, such behaviour is more or less forbidden. It is thus unlikely that ρ, A_2, f, ω are responsible for the behaviour attributed to C.

As none of the terms used explicitly in the RPCA model is capable of being modified so as to account for the N-N differential cross-sections for $t < -1$ $(GeV/c)^2$ at medium energies, a new contribution (or contributions) must be introduced. This must possess natural parity, a trajectory intermediate between that of the Pomeron and the traditional straight line meson trajectories, and mixed isospin and charge conjugation properties. A promising candidate is a combination of $f \otimes P$, $\omega \otimes P$, $\rho \otimes P$, $A_2 \otimes P$ cuts. The likely properties of such a combination are discussed below.

If the trajectory of a Regge cut is given by the position of the branch point (see eg Collins (1977), Chapter 8), then for a cut composed of two poles with trajectories

$$\alpha_1 = \alpha_1^o + \alpha_1' t \quad \text{and} \quad \alpha_2 = \alpha_2^o t + \alpha_2' t$$

$$\alpha_{cut} = \alpha_1^o + \alpha_2^o - 1 + \frac{\alpha_1' \alpha_2'}{\alpha_1' + \alpha_2'} t \qquad (3.3.1)$$

Thus, denoting f, ω, ρ or A_2 by R, and taking $\alpha_P = 1.07 + 0.1\ t$ and $\alpha_R = 0.5 + 0.9\ t$, the $R \otimes P$ branch point trajectory is expected to be

$$* \qquad \alpha_{R\otimes P} = 0.57 + 0.09\ t \qquad (3.3.2)$$

This gives $\alpha_{R\otimes P}\ (t = -2.5\ (\text{GeV/c})^2) = 0.345$ which is slightly higher than desired for C. Also the slope of (3.3.2) is somewhat low compared with α_{eff}^{expt} in the region under consideration. Nevertheless (3.3.2) is far closer to the C trajectory than anything previously considered. Perhaps the dominant region of the branch cut is not, in fact, the branch point.

---

* Even if α_R becomes flatter at large -t, (3.3.2) remains a good approximation. For example if $\alpha_R = 0.5 + 0.9\ t$ for, say $t > -1$ and then becomes $\alpha_R = 0.1 + 0.5\ t$, $\alpha_{R\otimes P}$ will be given by (3.3.2) for $t > -60$. For $t < -60$ it will be given by $0.1 + \frac{0.05}{0.6}\ t$ (ie. (3.3.1) with $\alpha_1 = \alpha_P$, $\alpha_2 = 0.1 + 0.5t$).

The contribution of an $R \otimes P$ cut to the non-flip scattering amplitude is (again see Collins (1977) Chapter 8)

$$A_{R\otimes P} = \begin{bmatrix} 1 \\ i \end{bmatrix} F(t)\, s^{\alpha_{RxP}(t)}\, e^{-i\pi\alpha_{RxP}(t)/2}\, (\ln s+d)^{-1} \qquad (3.3.3)$$

where F(t) is a real function free of kinematical singularities, d is a constant (in general complex), and the initial factor is 1 if R has signature +1 and i if R has signature -1. The charge conjugation and isospin of the cut are the same as for R. The energy dependence is largely determined by the trajectory except for $d \simeq -\ln s$. The phase of (3.3.3) is

$$-\frac{\pi}{2}\,\alpha_{R\otimes P}(t)\,\begin{bmatrix} +1 \end{bmatrix} + \mathrm{Tan}^{-1}\left[\frac{-\,\mathrm{Im}(d)}{\ln s + \mathrm{Re}(d)}\right] \qquad (3.3.4)$$

For $|d| \gg \ln s$, (3.3.3) thus becomes

$$A_{R\otimes P} \simeq \begin{bmatrix} 1 \\ i \end{bmatrix} F(t)\, s^{\alpha_{R\otimes P}(t)}\, e^{-i\left[\frac{\pi}{2}\alpha_{RxP}(t) - \varphi\right]} \cdot \frac{1}{\sqrt{d^{*}d}} \qquad (3.3.5)$$

where $\varphi = \tan^{-1}\left[\dfrac{-\mathrm{Im}(d)}{\mathrm{Re}(d)}\right]$

If it is assumed that the four $R \otimes P$ cuts have similar trajectories and t dependences but different couplings and complex constants, d, the $R \otimes P$ contribution to the p-p amplitude can be written as

$$\left.\begin{aligned}
A_{R\otimes P}(pp\text{-}pp) &= \left(G_{fp}\, e^{i\varphi_{fP}} + iG_{\omega p}\, e^{i\varphi_{\omega P}} + G_{A_2 p}\, e^{i\varphi_{A_2 P}} + iG_{\rho p}\, e^{i\varphi_{\rho P}}\right) f(t)\, s^{\alpha_{RxP}}\, e^{-i\frac{\pi}{2}\alpha_{R\otimes P}(t)} \\
\text{Similarly} \\
A_{R\otimes P}(pn\text{-}pn) &= \left(G_{fp}\, e^{i\varphi_{fP}} + iG_{\omega p}\, e^{i\varphi_{\omega P}} - G_{A_2 p}\, e^{i\varphi_{A_2 P}} - iG_{\rho p}\, e^{i\varphi_{\rho P}}\right) f(t)\, s^{\alpha_{R\otimes P}}\, e^{-i\frac{\pi}{2}\alpha_{R\otimes P}(t)} \\
\text{and} \\
A_{R\otimes P}(\bar{p}p\text{-}\bar{p}p) &= \left(G_{fp}\, e^{i\varphi_{fP}} - iG_{\omega p}\, e^{i\varphi_{\omega P}} + G_{A_2 p}\, e^{i\varphi_{A_2 P}} - iG_{\rho p}\, e^{i\varphi_{\rho P}}\right) f(t)\, s^{\alpha_{R\otimes P}}\, e^{-i\frac{\pi}{2}\alpha_{R\otimes P}(t)}
\end{aligned}\right) \qquad (3.3.6)$$

Thus, in each of the three reactions, the $R \otimes P$ term can be taken to be multiplied by a different complex constant.

$\frac{d\sigma}{dt}$ (pp-pp) can be fitted out to $t \simeq -4.5$ $(GeV/c)^2$ in the intermediate energy range ($10 \leqslant p_{lab} \leqslant 24$ GeV/c) using the RPCA terms plus an $R \otimes P$ term of the form

$$A_{R\otimes P}\ (pp\text{-}pp) = -G\ f(t)\ e^{-i\left[\frac{\pi}{2}\ \alpha_{RP}(t)-\varphi\right]}\ s^{\alpha_{RP}(t)} \qquad (3.3.7)$$

with $\alpha_{RP}(t) \simeq 0.5 + 0.3\ t$

and $\varphi \simeq \frac{\pi}{2}$.

Interference between the RPCA terms, dominant at small $|t|$ and the $R \otimes P$ term enables a reasonably good account to be obtained of both the shape and energy dependence of the "shoulder". The need to reproduce this shape is a strong constraint on the value of φ.

Now if C were composed of pole contributions (which would not include a factor $(\ln s + d)^{-1}$) of similar trajectories, the value of φ obtained by fitting $\frac{d\sigma}{dt}$ (pp-pp) would enable the charge conjugation properties of C to be deduced directly, since then

$$A_{C\text{-pole}}(pp\text{-}pp) = [G(C=+) + iG(C=-)]f(t)\ s^{\alpha_C(t)}\ e^{-i\frac{\pi}{2}\alpha_C(t)}$$

and

$$A_{C\text{-pole}}(\bar{p}p\text{-}\bar{p}p) = [G(C=+) - iG(C=-)]f(t)\ s^{\alpha_C(t)}\ e^{-i\frac{\pi}{2}\alpha_C(t)} \qquad (3.3.8)$$

with the G's real, i.e.

$$\varphi_{pp} = -\varphi_{\bar{p}p} \qquad (3.3.9)$$

The result $\varphi_{pp} \simeq \frac{\pi}{2}$ would thus indicate that C is approximately odd charge conjugation. Adding to the RPCA prediction for $\bar{p}p$ a term of the form (3.3.7) with parameters obtained from the fit to pp, but with $\varphi \rightarrow -\varphi$, results in a prediction for $\frac{d\sigma}{dt}$ ($\bar{p}p$-$\bar{p}p$) which shows a completely different interference structure to that observed experimentally.

It seems, then, that it is correct to parametrize C as a sum of cut terms rather than of poles. As to whether these are ρ, A_2, f and $\omega \otimes P$, the evidence is not conclusive. They do, however, appear to be the most likely candidates, even though the C-trajectory is then not exactly what would be expected from theory. As a working hypothesis, it will be assumed from now on that $C = f \otimes P \pm \omega \otimes P \pm A_2 \otimes P \pm \rho \otimes P$. This identification is especially attractive in that small $|t|$ and medium angle N_0 amplitudes show an analogous behaviour with energy. At small $|t|$ and high energy, the Pomeron is dominant, while at lower energies the leading meson-Reggeons are also important. For $t \lesssim -2$ $(GeV/c)^2$ the high energy data can be reproduced using only a $P \otimes P$ cut, but at lower energies $R \otimes P$ cuts give the largest contributions to the scattering amplitude. This relation between the dominant contributions in these two angular regions helps explain why the interference features observed at high and medium energies in $\frac{d\sigma}{dt}$ (pp) are so similar both in nature and in position. The detail of the parametrization of the $R \otimes P$ cuts will be discussed in Section 3.4

3.4 Reggeon behaviour at large -t

In Chapter 2 it was proposed that the dominant contribution to $\frac{d\sigma}{dt}$ at large angles, should, in Regge terms, come from meson-Reggeon exchange. At small $|t|$, the behaviour of the leading terms of this type is given by the RPCA model, while many large angle properties may be deduced from QI models. This present section is concerned with developing a parametrization suitable for use throughout the angular range.

For $t \gtrsim -1$ $(GeV/c)^2$ the meson-Reggeon trajectories are known to approximate to straight lines of gradients about 0.9. The leading trajectories of this type (f, ω, A_2, ρ) have intercepts near 0.5. From Chapter 2, we expect that at large -t these leading trajectories will tend to -1 asymptotically. A function is needed, therefore, which is approximately linear for $t \gtrsim -1$ $(GeV/c)^2$ but which bends smoothly to approach an integer value as t becomes more negative. A suitable function is defined by

$$\alpha - \frac{a}{\alpha+I} = lt + b \qquad (3.4.1)$$

where a, b, l and I are constants chosen to give the desired asymptotic properties. Inverting (3.4.1) and choosing the positive square root solution yields

$$\alpha(t) = \frac{(lt + b - I)}{2} + \tfrac{1}{2}\sqrt{\left[(I-lt-b)^2 + 4(a+lIt+Ib)\right]} \qquad (3.4.2)$$

For t large and positive, lt+b is much greater than I and so

$$\alpha(t) \simeq lt + b \qquad (3.4.3)$$

and the traditional linear form is obtained. As $t \to \infty$ (3.4.2) becomes

$$\alpha(t \to -\infty) \simeq - I \qquad (3.4.4)$$

i.e. α is constant as required to match QI predictions. Thus, 1, b and I determine the behaviour of α at either end of the t spectrum. The remaining parameter, a, governs the rate of change from the linear to the constant regions; a small $\Rightarrow$ rapid change, a large $\Rightarrow$ gradu al change.

The arguments presented in Chapter 2 lead to the choice of I = 1 for the leading family of trajectories. $\alpha(0)$ for ρ, A_2, ω and f are precisely known from previous work with the RPCA model. Using the notation

$$\alpha^{RPCA}(t) = \alpha_o + \alpha' t \qquad (3.4.5)$$

we therefore set

$$\alpha(0) = \alpha_o \qquad (3.4.6)$$

Similarly 1 is set equal to α'. All that now remains to be done to fully define $\alpha(t)$ is to choose a value for a (b is then determined by the condition (3.4.6)).

A small value for a is desirable on two counts:

(1) The linear approximation for α used in RPCA is good down to $t \simeq -1$ $(GeV/c)^2$. Here $\alpha^{RPCA} \simeq -0.4$, which is not far off the asymptotic value $\alpha(t \to -\infty) = -1$. The trajectory must therefore bend quite sharply.

(2) Power law scaling fits give a good account of the large angle $\frac{d\sigma}{dt}$ (pp) data down to p_{lab} = 5 GeV/c, at which energy $\theta_{cm} = 90^{o}$ corresponds to $t \simeq -3.5$ $(GeV/c)^2$. Thus $\alpha(t)$ seems already to be very flat by at least, say, $t \simeq -2.5 (GeV/c)^2$.

The transition, therefore, between "traditional Regge" and "consituent" t regions is expected to be quite sharp. It is interesting to note that the meson trajectories extracted by Barnes et al (1978) using triple-Regge theory do in fact exhibit an abrupt flattening at $t \simeq -1$ $(GeV/c)^2$ ($\alpha \simeq -0.2$ to -0.5). On the other hand it would be unrealistic to expect a change of behaviour to occur over a t region much less than the typical hadronic scale of 1 $(GeV/c)^2$. A reasonable compromise is achieved by choosing a = 0.1. A typical leading natural parity meson Reggeon trajectory is shown in Fig. (3.4.1). The parameter values used for this figure are I=1, a=0.1, 1=0.9, b=0.433.

With the trajectory evolved above, the ρ, A_2, ω, f possess, at large -t, the fixed -t energy dependence expected of the leading Regge contribution to the QI mechanism. A suitable t dependence must now also be found so that, at large -t, these terms should exhibit power law scaling behaviour in accordance with the DCR. The successful RPCA parametrization should, however, be retained at small $|t|$. To separate these two requirements the residues will be rewritten in terms of function $B^R(t)$ and $B^Q(t)$ such that

$$B^Q(t) + B^R(t) \equiv \beta(N_A N_C; R)\ \beta(N_B N_D; R) \qquad (3.4.7)$$

(LHS notation is as in (1.5.4), β's are t dependent)

where $B^R(t) \ll B^Q(t)$ for $t \lesssim -2.5$ $(GeV/c)^2$ and $B^Q(t) \ll B^R(t)$ for $t \gtrsim -1$ (GeV/c). It is convenient then to write $B^R(t)$ in the form

$$B^{R}(t) = B^{RPCA}(t) \cdot \bar{s}^{(\alpha_{RPCA}(t) - \alpha(t))} \qquad (3.4.8)$$

so that when $s = \bar{s}$ and $B^{Q}(t) = 0$, the original RPCA term is exactly reproduced. Choosing a suitable $\bar{s}$ should then ensure a satisfactory fit at small $|t|$.

Inserting (3.4.7) in (1.5.4) yields for non-helicity flip at large -t

$$A(N_A N_B \to N_C N_D; R) \simeq \lim_{I \to 1} \frac{-1}{(-I)!} B^{Q}(t) R(-I) \frac{1}{t^2} \frac{1}{s} \qquad (3.4.9)$$

where $R(-I) = \dfrac{1}{\sin\left[\frac{\pi I}{2}\right]}$ for signature +1 (f, A_2)

and $= \dfrac{i}{\cos\left[\frac{\pi I}{2}\right]}$ for signature -1 (ρ, ω)

Thus

$$\left.\begin{aligned} &A(N_A N_B \to N_C N_D; f \text{ or } A_2) \simeq 0 \\ \text{while} \quad &A(N_A N_B \to N_C N_D; \omega \text{ or } \rho) \simeq \frac{2}{\pi} B^{Q}(t) \frac{1}{st^2} \end{aligned}\right\} \qquad (3.4.10)$$

Note that the vanishing of the otherwise imaginary signature + 1 contribution when $\alpha = 1$ is due to the demands of duality. The duality diagram for pp scattering has a crossed line in the t channel exchange, therefore the sum of meson-Reggeon exchanges must be real. Crossing then requires that f and A_2 also vanish in other N-N processes.

The constraint that at large angles the meson-Reggeons should obey the DCR gives

$$B^Q(t)\,\frac{1}{st^2} \sim \frac{1}{s^4}\; f\left[\frac{s}{t}\right]$$

and hence $B^Q(t) \sim \frac{1}{t}$ for $-t$ large (3.4.11)

B^Q must, therefore

1. be small for $t \gtrsim -1$ $(GeV/c)^2$
2. behave like t^{-1} for $-t$ large
3. be free from singularities, since the presence of these would imply poles in the s channel.

The following form was found suitable for the non-flip f, ω, A_2, -exchange terms :

$$B^Q(t) = \left\{ \frac{1}{\left[1 + \left[\frac{B_2}{1+t^2}\right]^2\right]} - \frac{1}{1+B_2^2} \right\} B_1 (-t)^{\alpha(t)} \qquad (3.4.12)$$

B_1 and B_2 may take different values for each exchange degenerate pair of trajectories. No significance should be read into the employment of $\alpha(t)$ except that it gives the expression the desired properties. In general, any number of daughter trajectories may contribute at large angles to the same order in $\frac{1}{s}$ at fixed $\frac{t}{s}$ as do the parent trajectories. These may most easily be included in the model by replacing $B^Q(t)$ in (3.4.7) by $B^Q(t).b\left[\frac{t}{s}\right]$ where

$$b\left[\frac{t}{s}\right] = 1 + b_1 \frac{t}{s} + b_2 \frac{t^2}{s^2} + \ldots . \qquad (3.4.13)$$

In the previous sections of this chapter it has been sufficient to consider the nucleon-nucleon differential cross sections as being due to the helicity non-flip natural parity amplitude N_0. This assumption is not valid at large angles as witnessed by the relatively high values measured for some of the spin asymmetry parameters in this region (See Figs. (1.3.6) and (1.3.7)). In Appendix D the QI model is used to establish relationships among the total meson-Reggeon contributions at large s and $-t$ to the five independent amplitudes (N_0, N_1, N_2, U_0, U_2) of the $pp \to pp$, $np \to np$ and $\bar{p}p \to \bar{p}p$ processes. These relationships are used to define the asymptotic ($s \to \infty$ $\frac{t}{s}$ fixed) ratios of the amplitudes in the parametrization presented here.

Note that although the backward scattering terms in (D.4) and (D.5) etc. are not readily interpretable in terms of forward scattering Reggeon exchanges, account will have to be taken of them in the final parametrization if a reasonable fit to the data is to be obtained. In the case of $pp \to pp$ scattering the symmetry properties required by Fermi-Dirac statistics will have to be built into the complete amplitudes, the final state hadrons being identical Fermions.

To complete this section, there follows a summary of the prescription which will be used to form natural parity non-flip meson-Reggeon amplitudes applicable at all angles.

1. Start with the approximately exchange degenerate pairs of Reggeon amplitudes as given by (1.5.4) together with (1.5.3) and (3.2.1). The couplings (3.2.1) may be factored by exponentials in t.

2. Change the linear trajectories for ones of the form (3.4.2) with I = 1.

3. Replace the product of the couplings by a function of the form given by (3.4.7), with $B^R(t)$ given by (3.4.8) and $B^Q(t)$ given by (3.4.12).

4. Apply to $B^R(t)$ the absorptive corrections detailed in (1.5.6).

5. Multiply $B^Q(t)$ by a function of $\frac{t}{s}$ of the form (3.4.13) to allow for daughter terms becoming important at large angles.

Other refinements applicable to individual exchange terms will be detailed as necessary. A similar procedure will be followed for helicity-flip and unnatural parity contributions. This will be described in Chapter 4.

The parametrization of $\frac{d\sigma}{dt}$ (NN-NN) has now been discussed in the contexts of three main kinematical regions, i.e.

1. $t \gtrsim -1$ $(GeV/c)^2$ where $\frac{d\sigma}{dt}$ is dominated by the Pomeron pole, but where meson-Reggeon pole contributions are also important at lower energies.

2. $t \lesssim -2$ $(GeV/c)^2$, but $-\frac{2t}{s} \ll 1$, where cuts have been found to be important. The $P \otimes P$ cut dominates for plab $\gtrsim$ 200 GeV/c and a combination of $R \otimes P$ cuts does so for plab $\lesssim$ 50 GeV/c.

3. $-\frac{2t}{s}$ of the order of 1, where meson-Reggeons with trajectories tending asymptotically to -ve integers govern the behaviour of $\frac{d\sigma}{dt}$.

In the following section these regions will be linked together and fits to the data over the angular range 0 - 90°_{cm} will be presented.

3.5 Fits to $\frac{d\sigma}{dt}$ (NN-NN) over the angular range $0 < \theta_{cm} < 90^{o}$

The fits to $\frac{d\sigma}{dt}$ ($pp \to pp$), $\frac{d\sigma}{dt}$ ($pn \to pn$) and $\frac{d\sigma}{dt}$ ($\bar{p}p \to \bar{p}p$) shown in Figs. (3.5.1)-(3.5.3) were obtained using the parametrization described below. The values of the parameters are given in Table (3.5.1).

To simplify the problem of ensuring the correct symmetry properties each naturality amplitude will be split into two parts; a "Q" part consisting of those portions of the meson-Reggeons proportional to $B^{Q}(t)$ (or $B^{Q}(u)$) and an "R" part consisting of everything else. The full "R" amplitudes will be obtained from the forward parts as described in Appendix E. Similarly the full "Q" amplitudes will be constructed using (D.1) (subject to certain pre-asymptotic modifications detailed in Chapter 4). The "Q" and "R" contributions will then be summed. An analogous procedure will be applied to the "Q" components of the n-p and $\bar{p}p$ amplitudes via (D.2) and (D.3). The equivalent relations for the "R" parts are not known, however, since these depend on the properties of the pn and $\bar{p}p$ charge exchange amplitudes which are not studied here. The "R" plots of the $\bar{p}p$ and pn amplitudes will thus be approximated by the forward contributions only.

The parametrization of the forward part of N_{0} for the reactions $pp \to pp$, $\bar{p}p \to \bar{p}p$ and $pn \to pn$ will now be detailed. The other naturality amplitudes will be described in Chapter 4, but these are only important as regards $\frac{d\sigma}{dt}$, at large centre of mass scattering angles.

The Pomeron and $P \otimes P$ cut terms used to obtain Figs. (3.5.1)-(3.5.3) are as described in Section 3.2. The f, ω, ρ, A_2 contributions are formed according to the prescription given in Section 3.4 with the following modifications and parametrizational details

a) The f and ω trajectories are based on a linear trajectory slope $\alpha' = 0.85$ rather than the RPCA values of 1 and 0.96. The RPCA values are still used in the couplings, however (see (3.2.1)). This change slightly improves the fit, while making the f, ω, ρ, A_2 trajectory parametrizations identical except for the intercepts.

b) Prior to the absorptive corrections $B^R(t)$ for f and ω is written

$$B^R(t) = e^{rt} \left(\frac{}{s}\right)^{(\alpha_o + 0.85t - \alpha(t))} B^{RPCA}(t) \qquad (3.5.1)$$

while for ρ and A_2

$$B^R(t) = \left(\frac{}{s}\right)^{(\alpha_o + 0.85t - \alpha(t))} \qquad (3.5.2)$$

c) Only the parent and first daughter terms of (3.4.13) are used, i.e. (3.4.13) becomes

$$b\left[\frac{t}{s}\right] = 1 + b_1 \frac{t}{s} \qquad (3.5.3)$$

d) The f-daughter term is the same as the f except that

(1) $\alpha_{fd}(t) = \alpha_f(t) - 1$

(2) the f-daughter coupling differs by a factor of -8.1

(3) $B^Q_{fd}(t) = 0$, since the large -t part of the f-daughter contribution is already included via (3.5.3).

The $R \otimes P$ cut term in pp scattering is as given by (3.3.7), with

$$f(t) = t^2 e^{a_1 t} \frac{\left[1 + X_{RP} e^{a_2 t}\right]}{1 + X_{RP}} \bar{s}_{RP}^{\left[\alpha_{o_{RP}} + \alpha'_{RP} t - \alpha_{RP}(t)\right]} \qquad (3.5.4)$$

The factor of t^2 ensures that the total cross-section and very small -t fits are as for the RPCA. The equivalent contributions in the pn and pp cases differ in the values of G and φ, but use the same f(t). The $f \otimes P$, $\omega \otimes P$, $\rho \otimes P$, $A_2 \otimes P$ components cannot be separated out without information from a similar fit to $\frac{d\sigma}{dt}$ ($\bar{p}n$ $\bar{p}n$), data for which is unavailable.

A further term is needed to account for the behaviour of $\frac{d\sigma}{dt}$ ($\bar{p}p$) for $0.3 \lesssim t \lesssim 1.3$ $(GeV/c)^2$. The sharp dip observed in the data at $t = 0.5$ $(GeV/c)^2$ at $p_{lab} = 5$ GeV/c dies away rapidly as energy increases. The RPCA terms predict the dip at low energy and also give a good account of the data at $p_{lab} = 50$ GeV/c and above for $|t| \lesssim 1$ $(GeV/c)^2$. However, the change with energy of the shape of the $\frac{d\sigma}{dt}$ curve is not well described between these values. The extra term has a phase and energy dependence closely constrained by the evolution of the 0.5 $(GeV/c)^2$ dip structure. It has been parametrized here as a logarithmic correction to the $R \otimes P$ cuts :-

$$A_{R \otimes P}(\bar{p}p) \rightarrow A_{R \otimes P}(\bar{p}p) - \frac{G' t^2}{\ln s} e^{\frac{i\pi\varphi'}{2} - t^2 a'} \qquad (3.5.5)$$

The logarithmically varying term is important only for $-t \lesssim 1.5$ $(GeV/c)^2$. It appears only in the $\bar{p}p \rightarrow \bar{p}p$ scattering case and hence consists of equal even and odd charge conjugation parts.

The $R \otimes P$ trajectory, $\alpha_c(t)$ has been altered from the linear form $\alpha_{RP}^{linear}(t) = \alpha_{o_{RP}} + \alpha'_{RP}\, t$ in the same way that the meson-Reggeon trajectories have been. That $\alpha_{RP}(t)$ should tend to -1 as $t \to -\infty$ can be seen from the following simple argument: From the reasoning of Section 2.3, the $R \otimes P$ contribution at large -t can be regarded as a sum of diagrams of the type shown in Fig. (3.5.4). The trajectory of the gluon exchange component is constant at +1, while that of the quark interchange component is -1. Substituting $\alpha_1 = +1$, $\alpha_2 = -1$ into (3.3.1) yields $\alpha_{cut} = -1$, hence $\alpha_{RP}(t)$ is expected to approach -1 at large -t. The $\alpha_{RP}(t)$ curve used for the final fits is shown in Fig. (3.5.5).

The data confirms that $\alpha_{RP}(t)$ must approach a constant value or at least that it falls slowly at large -t. If the trajectory continued to fall, the phase of the contribution would rotate as -t increased, so that at some value of t, the meson-Reggeon and $R \times P$ terms would be in antiphase. There would be a range of energies where the magnitude of the two contributions would be similar at this value of t and hence an interference minimum would occur in the data. For instance, using the linear trajectory quoted in (3.3.7) and $\varphi = \frac{\pi}{2}$, the $R \otimes P$ phase is real and opposite in sign to the Reggeons when $\alpha_{RP} = -3$ i.e. when $t = -12\ (GeV/c)^2$. Were this the case some structure would be observed in $\frac{d\sigma}{dt}$ (pp) above about $p_{lab} = 18$ GeV/c. No interference dip is seen, however.

Comments

Overall the fits presented in Figs. (3.5.1) - (3.5.3) give a good account of the NN differential cross-section data, over a very large range of energies and angles. Because of the wide range covered,

compromises have inevitably had to be made to obtain the best description of the data as a whole, without unduly complicating the parametrization. As might be expected from an asymptotic model, the standard of agreement with data is least good at the lowest energies covered, where lower order terms become important.

$\frac{d\sigma}{dt}$ (pp) has been the primary source of information as to the structure of the nucleon-nucleon natural parity non-flip amplitude due to the relative abundance of data for this process. The energy dependence of the amplitude for $t \lesssim -1$ $(GeV/c)^2$ has been derived almost entirely from this source, and it was primarily this information which showed the necessity for the term identified as the sum of $R \otimes P$ cuts. The trajectory and phase of this term are heavily constrained by the variation with energy of the shape and magnitude of $\frac{d\sigma}{dt}$ (pp) so that although the interpretation of this contribution is open to argument its properties are well defined.

The shape of the experimental curve for $\frac{d\sigma}{dt}$ (np) is remarkably similar to that obtained for pp indicating that the reaction mechanisms are closely related. This similarity is reflected in the simple way that the theoretical curve for $\frac{d\sigma}{dt}$ (np) is obtained from the parametrization used for pp. At small -t the two fits are essentially the same, the difference being caused by the change in sign of the I=1 ρ and A_2 terms, which have small helicity non-flip couplings as predicted by RPCA. At large angles and large $|t|$ the ratio $\frac{d\sigma}{dt}$(np) / $\frac{d\sigma}{dt}$(pp) is fixed at the value predicted by the QI model. As can be seen from Table (3.5.1), the only parameter that has been freely varied to achieve the np fit has been the real coupling constant of the $R \otimes P$ term. No use has been made of the freedom to alter the $R \otimes P$ phase, and no modifications of the t

dependence were necessary. From Table (3.5.1) the relative strengths of the I=0 and I=1 components of the $R \otimes P$ cut can be determined:

$$\frac{A_{RxP}\ (I=0)}{A_{RxP}\ (I=1)} = \frac{G(pp) + G(pn)}{G(pp) - G(pn)} = \frac{1 + \frac{1}{1.41}}{1 - \frac{1}{1.41}} = \frac{2.41}{0.41} = 5.88 \qquad (3.5.6)$$

The situation in respect of $\bar{p}p$ is rather more complicated. The shape of the $\frac{d\sigma}{dt}$ $(\bar{p}p)$ curve is significantly different from $\frac{d\sigma}{dt}$ (pp). Not only is it rich in interference structures, but the shape also alters rapidly with energy. The recent results at p_{lab} = 50, 100 and 200 GeV/c have helped to clarify the situation as regards the shape of $\frac{d\sigma}{dt}$ at high energy.

Nevertheless the information available for $-t \gtrsim 1$ $(GeV/c)^2$ is sufficient to conclude that both the phase and magnitude of the $R \otimes P$ term are changed from their values in pp :

$$\frac{A_{RxP}(\bar{p}p)}{A_{RxP}(pp)} = \frac{e^{-\frac{i\pi}{2}.0.75}}{2.0} \qquad (3.5.7)$$

$$\frac{A_{RxP}(C=+1)}{A_{RxP}(C=-1)} = \frac{2.0 + e^{-\frac{i\pi}{2}.0.75}}{2.0 - e^{-\frac{i\pi}{2}.0.75}} \simeq 1.4\ e^{-\frac{i\pi}{2}.0.50} \qquad (3.5.8)$$

The $R \otimes P$ parameters in $\bar{p}p$ are only loosely determined, however.

Also, as mentioned previously, the rapid disappearance of the interference minimum at $t = -0.5\ (GeV/c)^2$ requires the presence of an additional term important for $-t \lesssim 1.5\ (GeV/c)^2$ which is apparently not present in np and pp scattering and which has been parametrized as a logarithmic modification to the $R \otimes P$ cut.

Because of the lack of large -t, large angle $\bar{p}p$ data, the behaviour of that part of $\frac{d\sigma}{dt}$ governed by the QI mechanism cannot effectively be studied. The steep drop observed in the $p_{lab} = 5$ GeV/c data for $t \lesssim -3\ (GeV/c)^2$ is probably due to interference between forward and backward scattering components as there is no evidence of such behaviour at these t values at higher energies.

The model has been based on the small angle RPCA model of Collins et al, and extended to account for the behaviour at large angles predicted by quark interchange models. The desirable properties of each of these models have been retained in the appropriate kinematical regions and a smooth transition between the two has been successfully achieved. It has been necessary to introduce extra terms (notably the $R \otimes P$ cut terms), but in each case the additions have been required by the data, and in most instances the properties of these additions are well determined.

3.6 Conclusions

In this chapter the model for elastic hadronic scattering proposed in Chapter One has been prosecuted successfully. The mechanism for reproducing the large angle behaviour of $d\sigma/dt$ using Reggeons whose trajectories approach negative integers has been shown to work very well. The intermediate angle region has been

studied and found to be dominated by Regge cuts for $|t| \gtrsim 1$ (GeV/c)^2, by a $P \otimes P$ cut at high energy and by at least four $R \otimes P$ cuts at lower energies.

The pattern of the non-flip N-N helicity amplitude has been firmly established: Reggeon and Pomeron poles dominant at small, Regge cuts for $|t| \gtrsim 1$ (GeV/c)^2 and the Reggeons re-emerging at large angles. In Chapter 4 other N-N helicity amplitudes will be studied through the Polarization and Correlation Parameter (A_{ij}) data. The focus of attention turns to π-p scattering in Chapter 5 where $d\sigma/dt$ ($\pi^{\pm}p$) will be examined to see if the pattern revealed in N-N scattering is repeated there.

Table (3.5.1)

Parameter values for amplitudes $N_0(NN \to NN)$

Contribution	Parameter	Reference equation:	Applicable to process:	Value
Pomeron and $P \otimes P$ cut	χ	(3.2.4)	all	0.88
meson-Reggeons	r (f,ω)	(3.5.1)	all	0.158
	$\bar{s}$	(3.5.1/2)	all	37.86
	B_1 (f,ω)	(3.4.12)	all	22.95
	B_1 (ρ,A_2)	(3.4.12)	all	$B_1(f,\omega)/9$
	B_2 (f,ω,ρ,A_2)	(3.4.12)	all	30
	b_1	(3.5.3)	all	-4.24
R$\otimes$P cut	G	(3.3.7)	pp	99.7
			$\bar{p}p$	99.7/2
			pn	99.7/1.4
	φ	(3.3.7)	pp,pn	.839
			$\bar{p}p$	.089
	α_{oRP}	(3.5.4)	all	0.30
	α'_{RP}	(3.5.4)	all	0.31
	a_1	(3.5.4)	all	1.12
	a_2	(3.5.4)	all	-1.01
	χ_{RP}	(3.5.4)	all	.0464
	$\bar{s}_{RP}$	(3.5.4)	all	38.6
	G'	(3.5.5)	$\bar{p}p$ only	714
	φ'	(3.5.5)	$\bar{p}p$ only	0.73
	a'	(3.5.5)	$\bar{p}p$ only	1.99

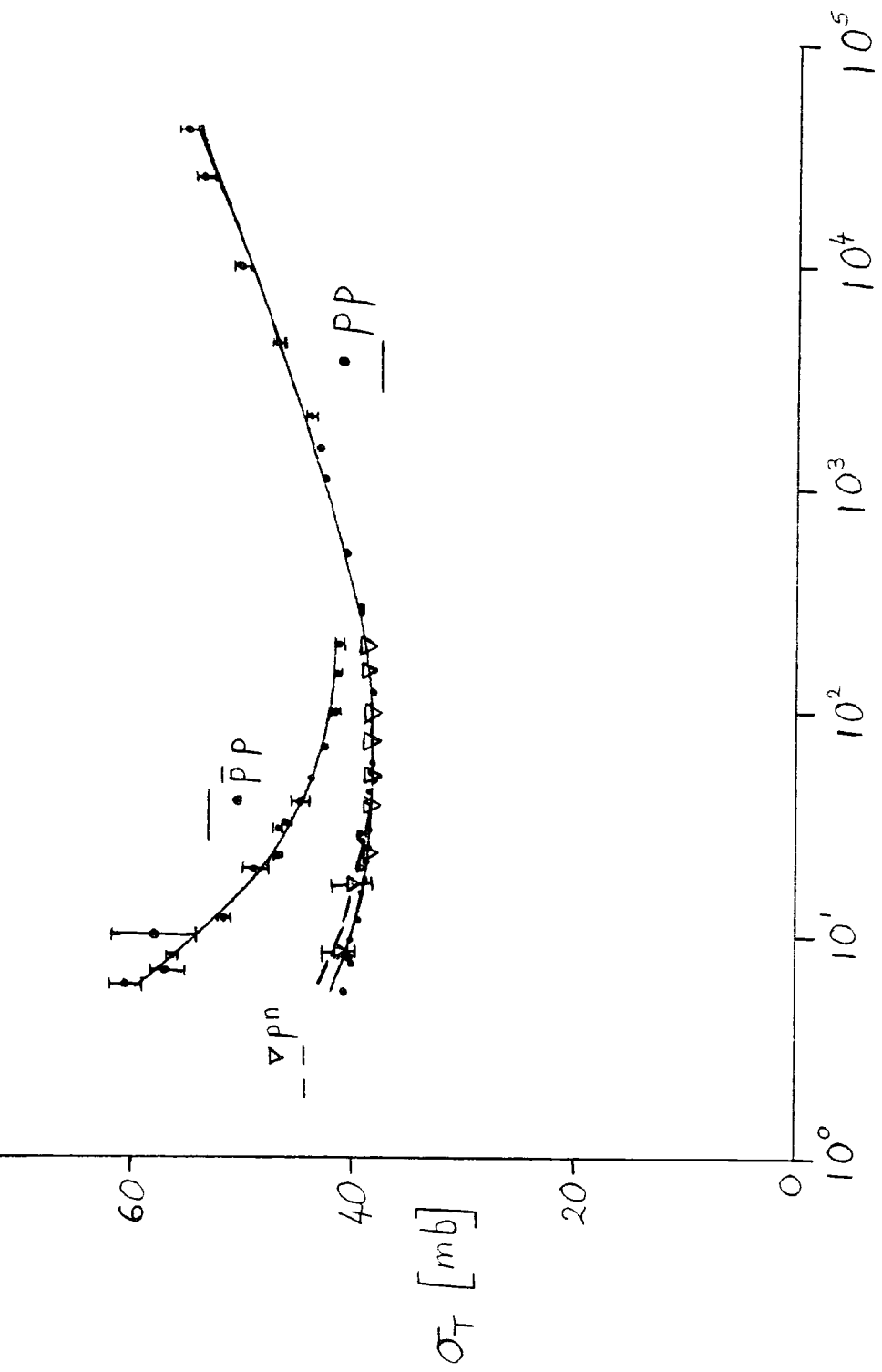

Fig. (3.2.1)

RPCA fits to pp, $\bar{p}p$, pn total cross sections (from Wright (1978))

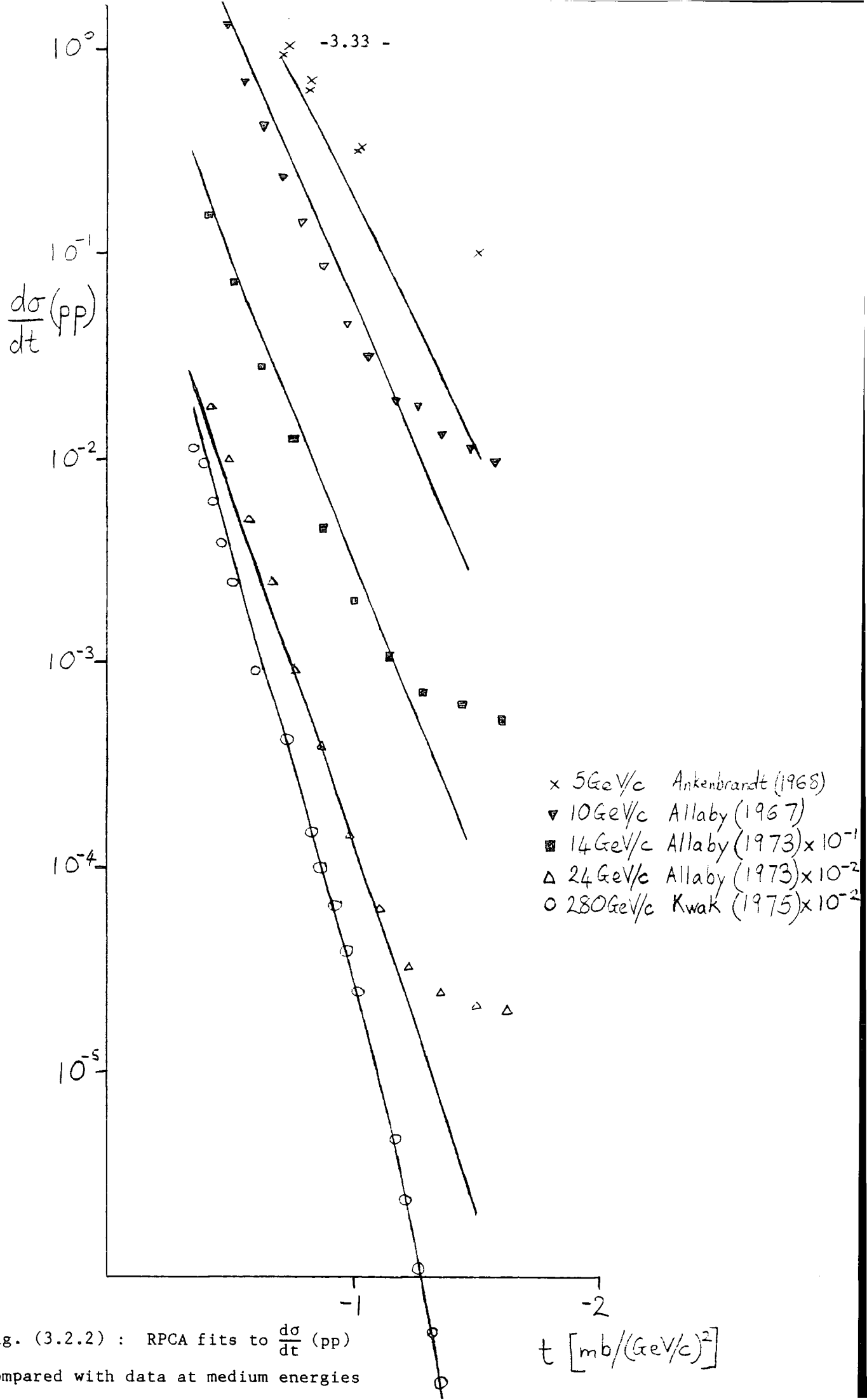

Fig. (3.2.2) : RPCA fits to $\frac{d\sigma}{dt}$ (pp) compared with data at medium energies

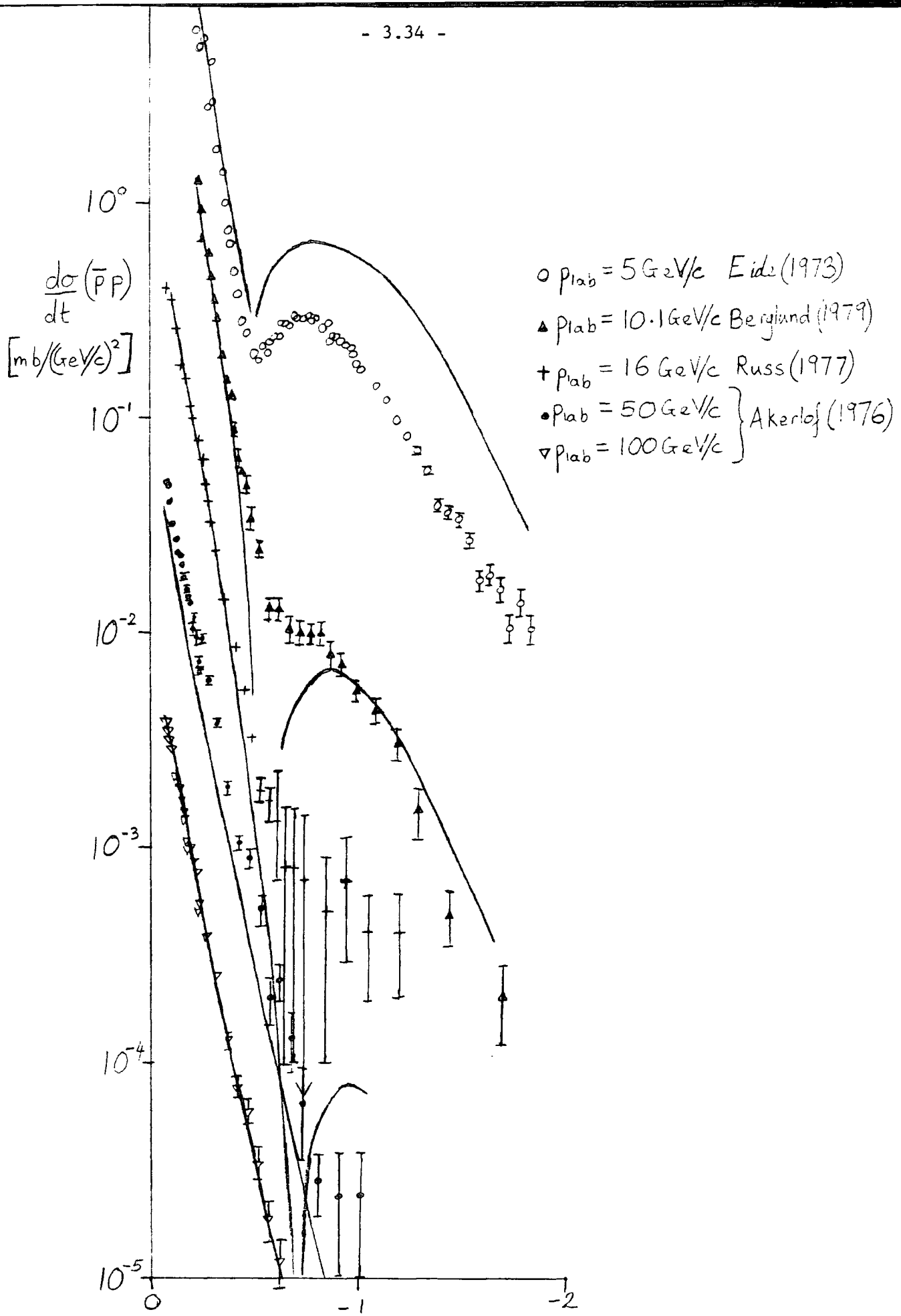

Fig. (3.2.3) : RPCA fit to $\frac{d\sigma}{dt}$ $(\bar{p}p)$

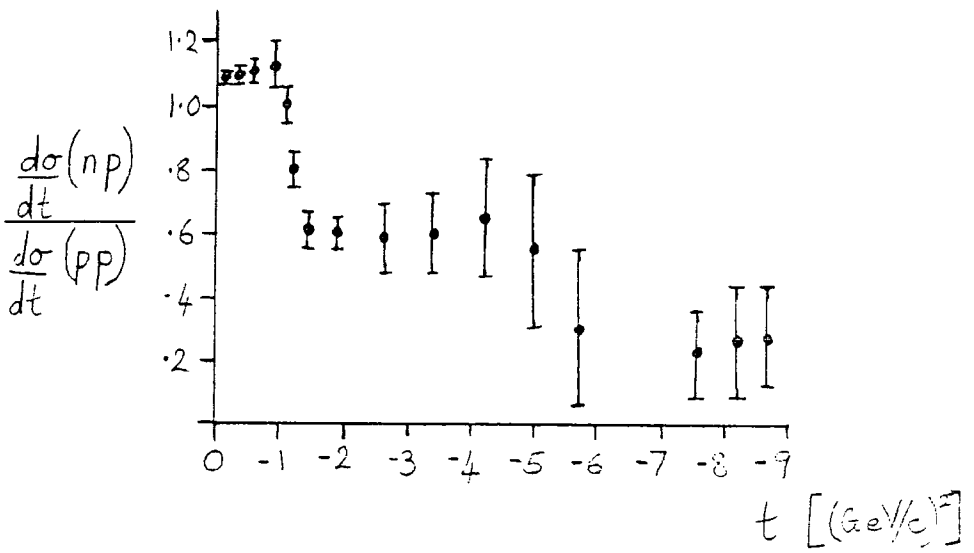

Fig. (3.2.4)

Radio of np to pp differential cross sections at p_{lab} = 10 GeV/c (from Stone (1978))

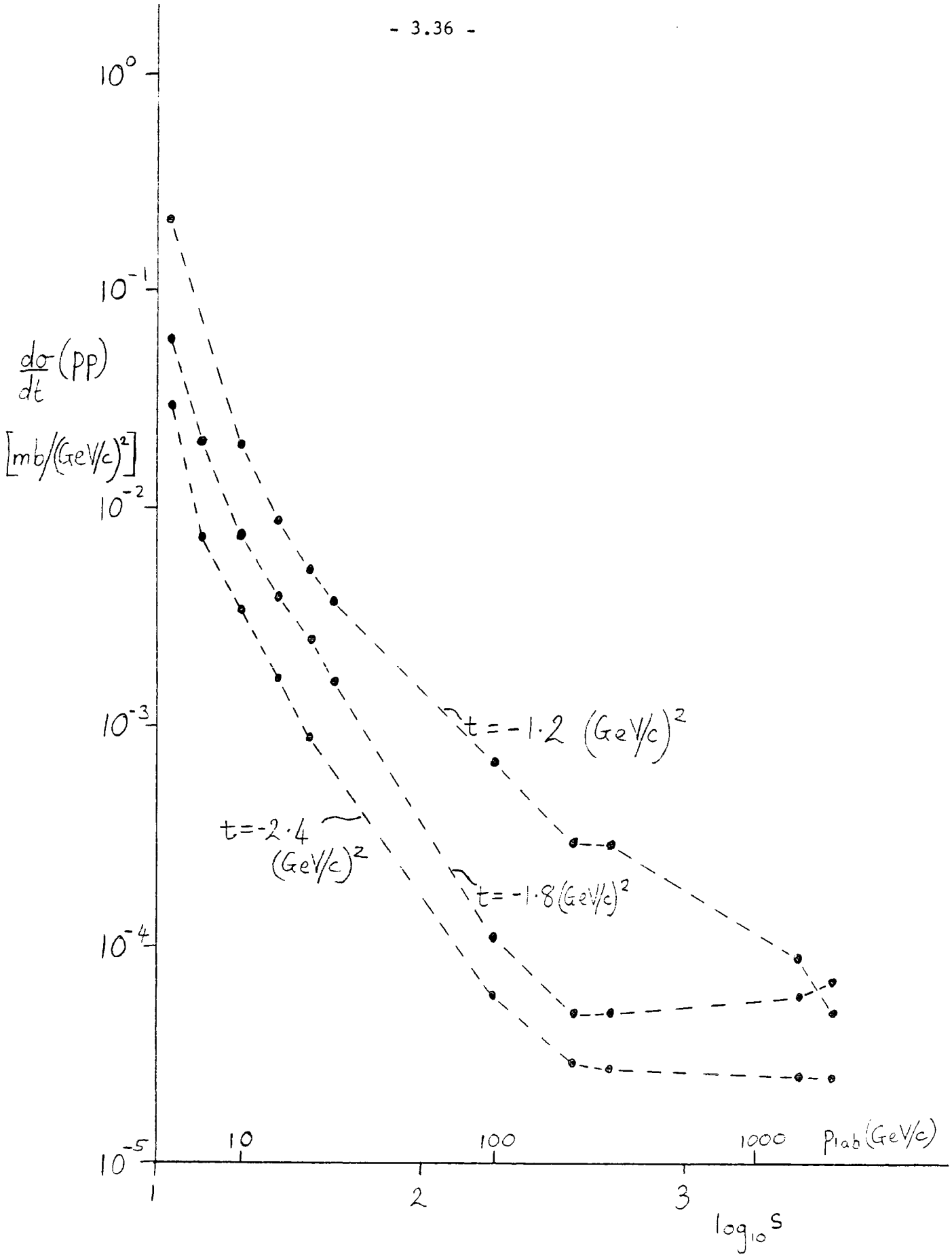

Fig. (3.3.1)

$\frac{d\sigma}{dt}$ (pp) vs. log s for -1 > t > -2.5 $(GeV/c)^2$

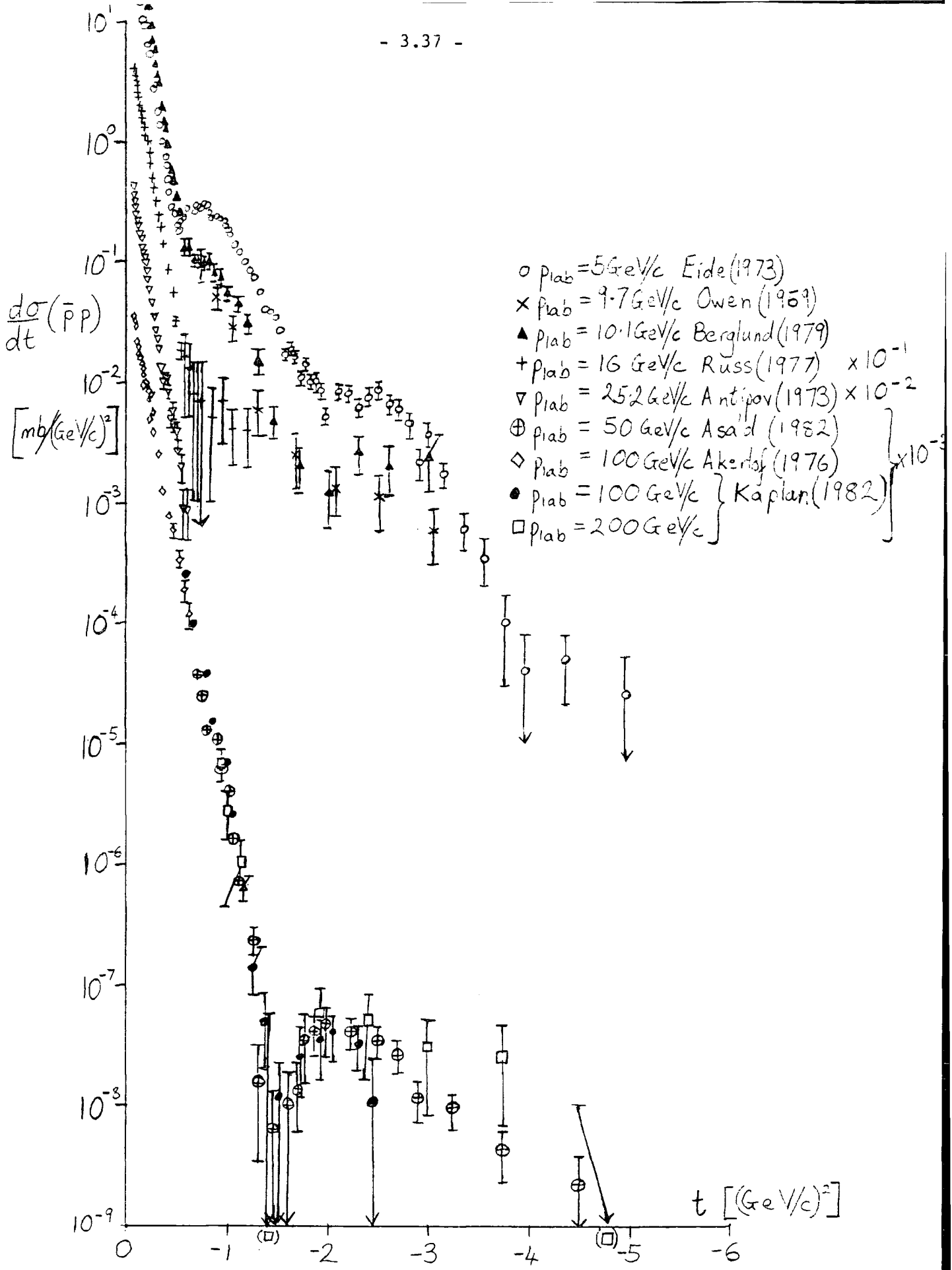

Fig. (3.3.2)

Experimental measurements of $\frac{d\sigma}{dt}$ $(\bar{p}p)$

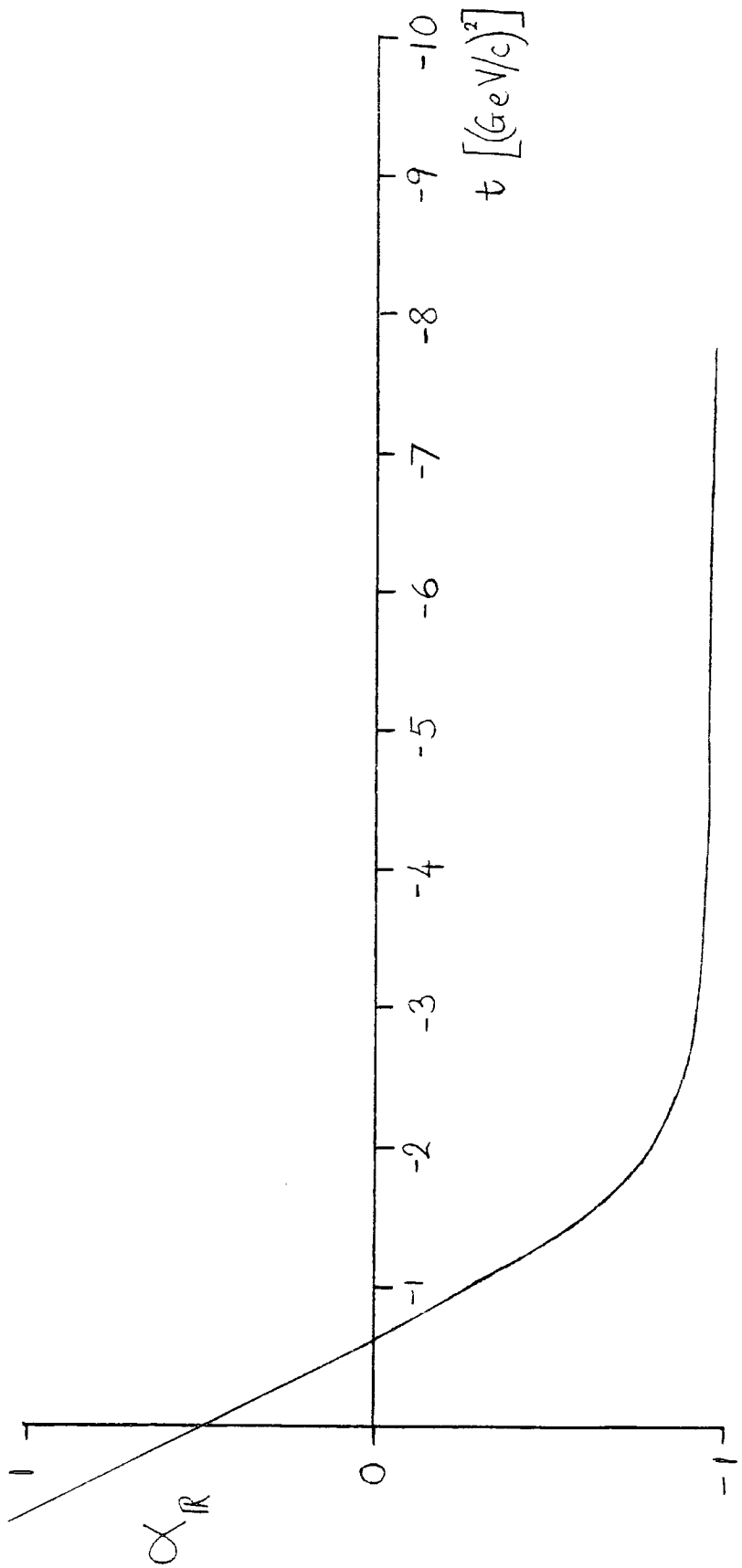

Fig. (3.4.1)

A typical Reggeon trajectory modified to approach -1 as t tends to minus infinity

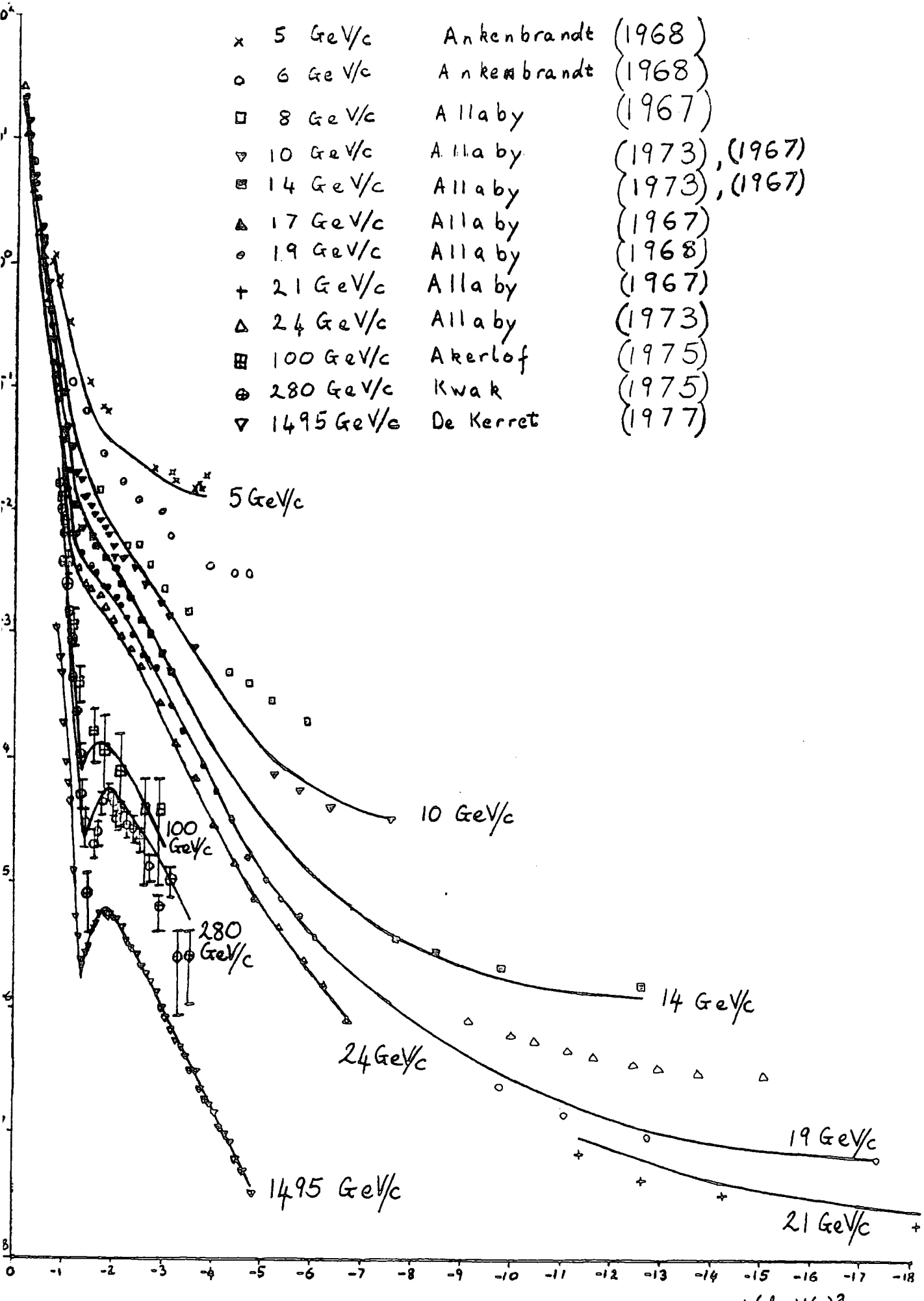

Fig. (3.5.1) : Fit to $\frac{d\sigma}{dt}$ (pp)

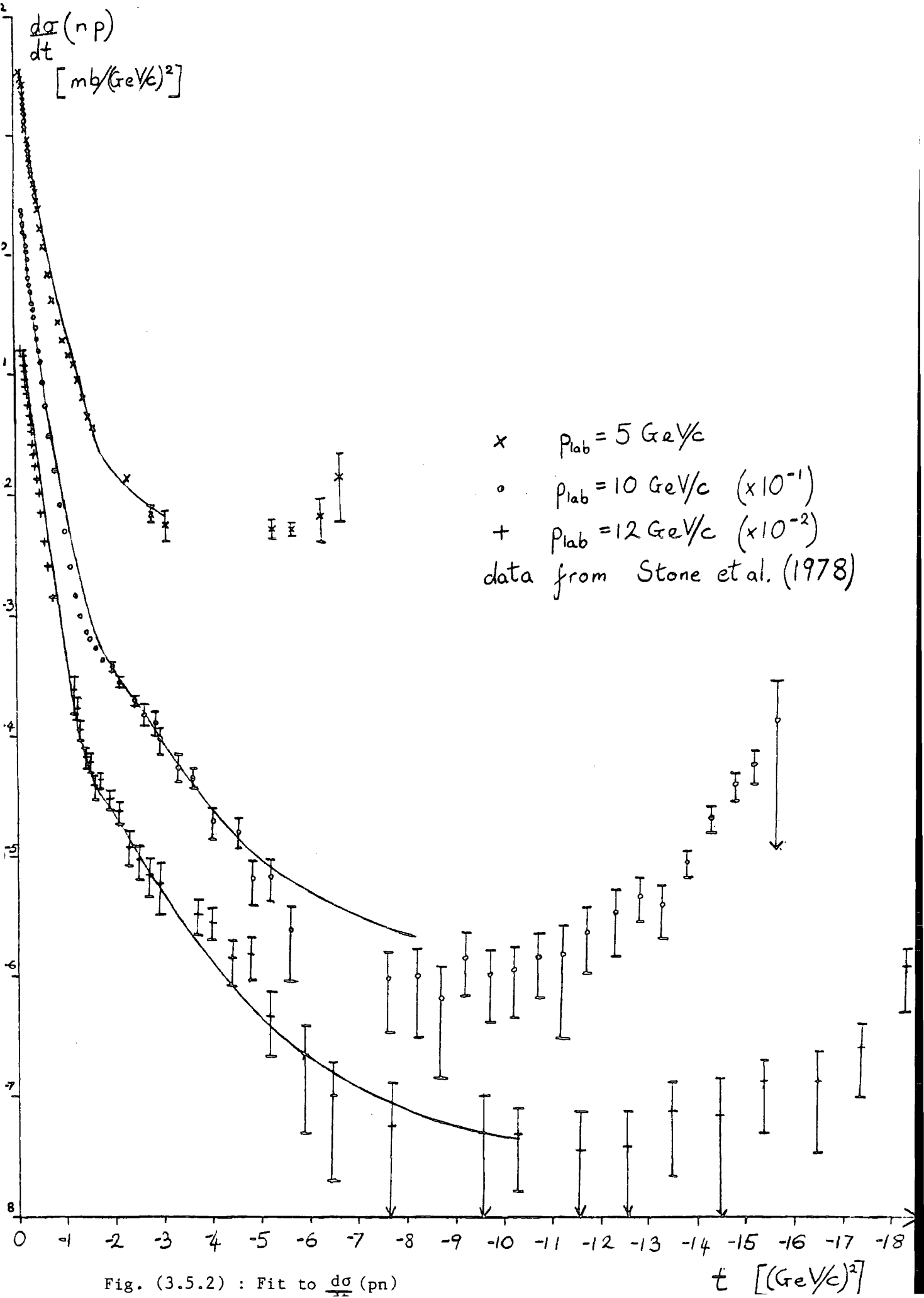

Fig. (3.5.2) : Fit to $\frac{d\sigma}{dt}$(pn)

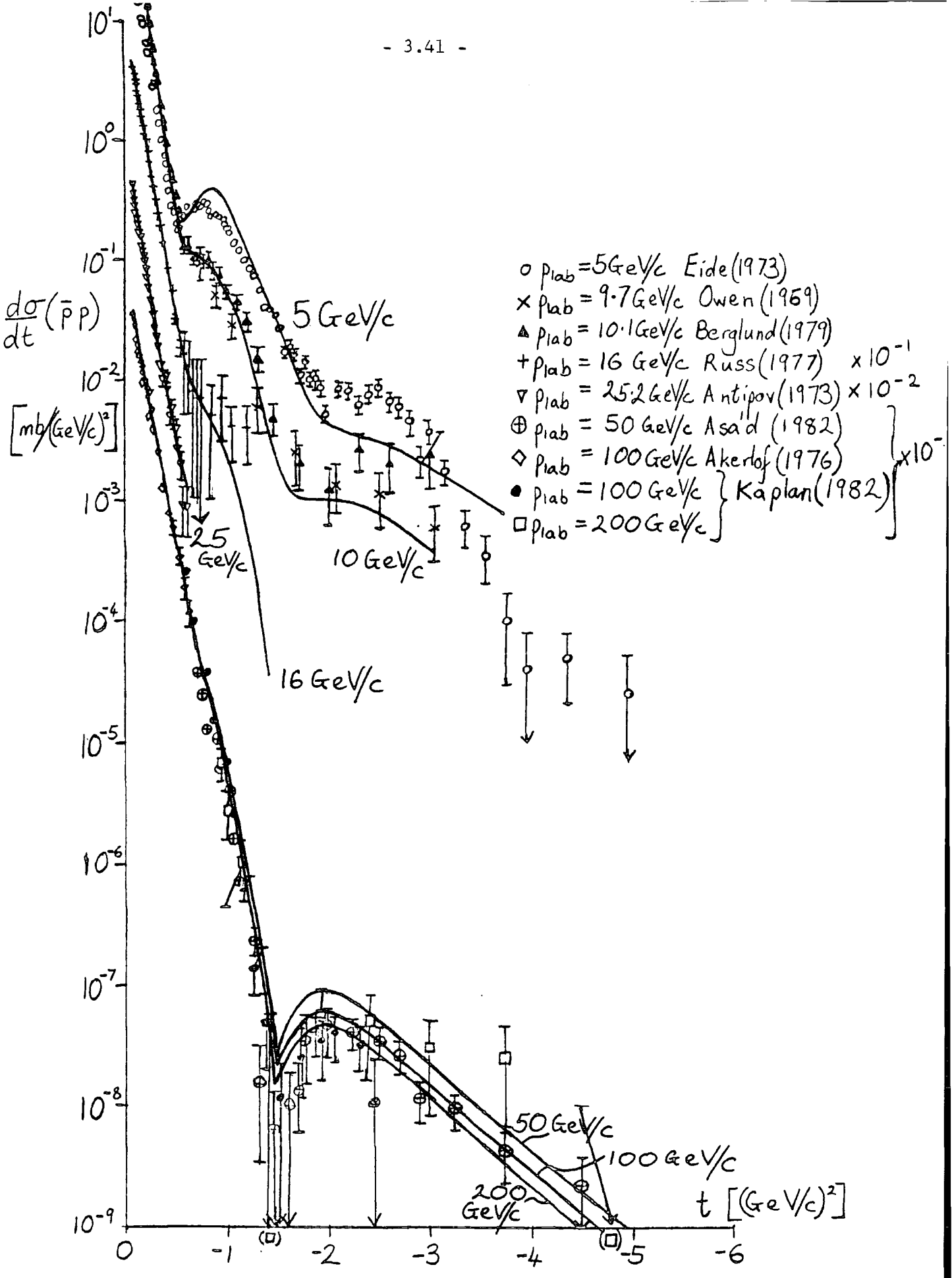

Fig. (3.5.3) : Fit to $\frac{d\sigma}{dt}(\bar{p}p)$

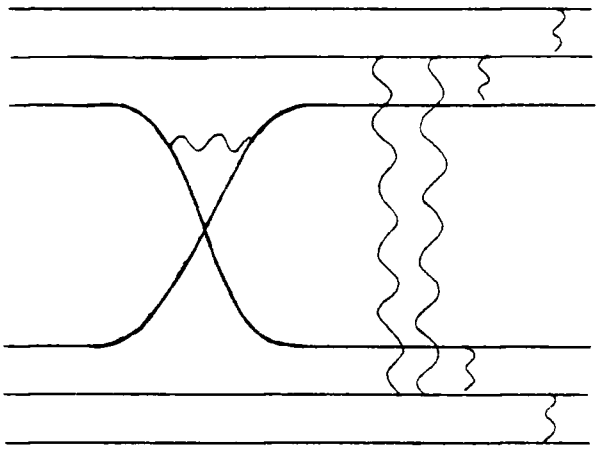

Fig. (3.5.4)

Diagram contributing to an $R \otimes P$ cut

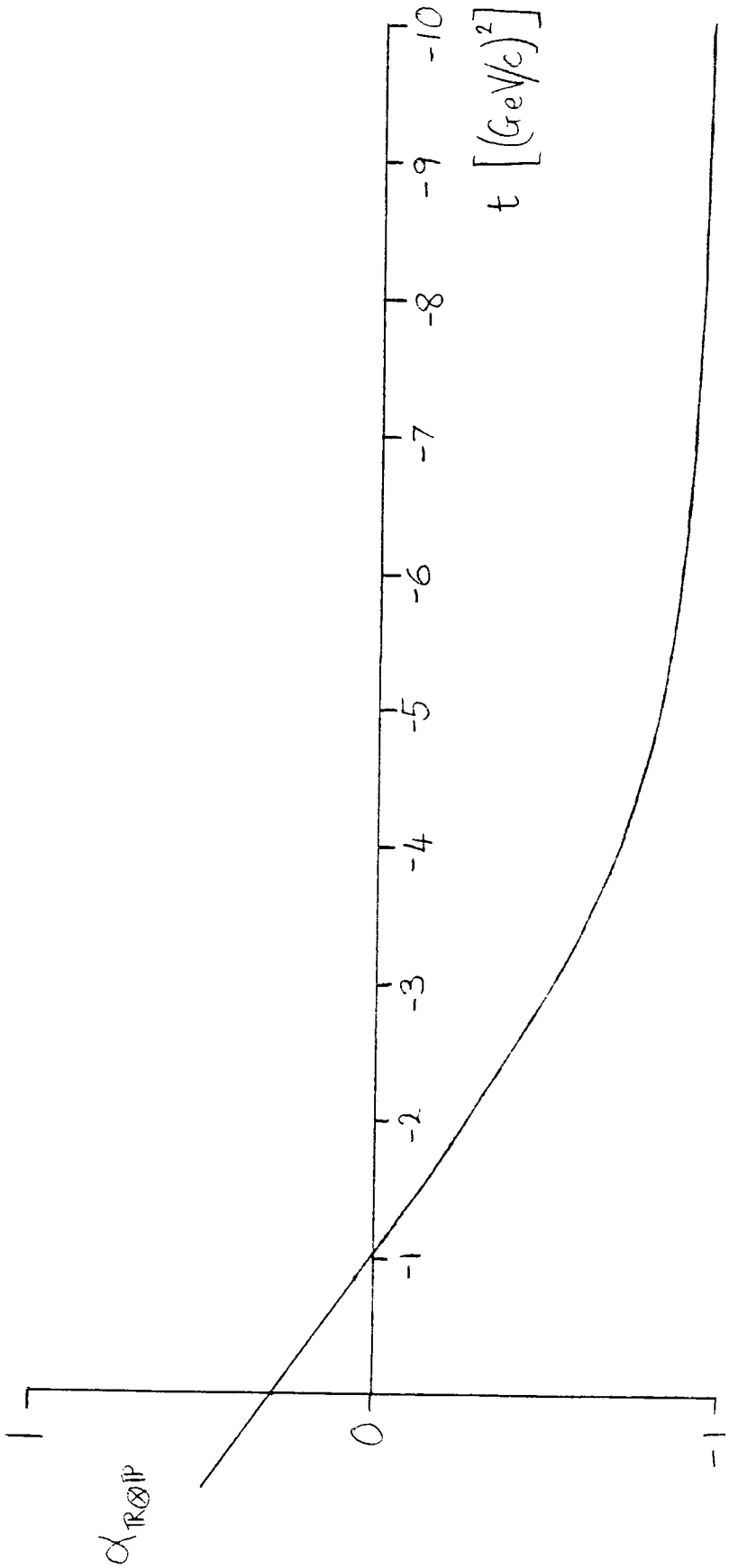

Fig. (3.5.5)

$R\otimes P$ trajectory tending to -1 at large -t

CHAPTER 4

NUCLEON-NUCLEON POLARIZATION AND SPIN CORRELATION PARAMETERS

4.1 Introduction

In this fourth chapter, the Regge-based model for hadronic elastic scattering proposed in Chapter 2, will be applied to the nucleon-nucleon helicity flip amplitudes as revealed in polarization and spin correlation data.

Expressions for the NN natural parity, helicity non-flip amplitudes, N_0 were obtained in Chapter 3 by fitting to the differential cross sections and now these will be used as input to determine N_1, N_2, U_0, U_2. As established in Chapter 3, N_0 is much larger than the other amplitudes except at large angles. Even at 90°_{cm} the QI model predicts that the magnitude of $N_0(pp)$ is three times that of N_2, U_0 and U_2, while $N_1 = 0$.

The expression for the polarization parameter P, is given in equation (B.5). For N_0 much greater than the other amplitudes this simplifies to

$$P\,|N_0|^2 \simeq -\,2\,\mathrm{Im}\left[N_0\,N_1^*\right] \tag{4.1.1}$$

and hence N_1 may be determined from the polarization data. Similarly (B.6), (B.7), (B.8), (B.9) reduce to

$$A_{nn}|N_0|^2 \simeq -\,2\,\mathrm{Re}(N_0 N_2^*) \tag{4.1.2}$$

$$A_{ss}|N_0|^2 \simeq 2\,\mathrm{Re}(N_0 U_2^*) \tag{4.1.3}$$

$$A_{s\ell}|N_0|^2 \simeq 0 \tag{4.1.4}$$

$$A_{\ell\ell}|N_0|^2 \simeq -2\,\mathrm{Re}(N_0 U_0^*) \tag{4.1.5}$$

enabling N_2, U_2 and U_0 to be deduced. The full expressions must, however, be used for the final fits as the approximations may not always be valid, especially at large angles.

The amplitudes will be constructed in an analogous way to N_0. The $t = 0$ couplings of the natural parity contributions will be taken from the RPCA model. The closely related Reggeon-"Weakon" Coupling Analogy model (Collins et al (1978c)) gives predictions for unnatural parity couplings, but detailed studies of scattering processes in terms of this model have not been performed. Instead, the work of Irving, Berger et al (Irving (1975), Berger et al (1978)) will be used as a basis for the structure of the unnatural parity exchange contributions. The trajectories will be based on those of Berger et al, but modified to approach integer values in the same way as the natural parity trajectories. At large angles and large -t the meson-Reggeon contributions will be constrained in accordance to the Q.I. model. It will be assumed that meson-Reggeons appear in approximately exchange degenerate pairs (though the exchange degeneracy may be weakened by absorptive corrections). Contributions other than those from the RPCA and Berger et al models will be introduced if required by the data.

4.2 Polarization

As remarked in Section 1, a study of the polarization parameter data should elucidate the structure of the N_1 amplitude. Polarization, P, is the helicity observable for which the greatest amount of data is available, principally because only the beam or target need be polarized, not both. Nevertheless large $|t|$ data is scarce, and large angles are covered only at low energies.

Good polarization data sets across the complete range 0_{cm}-90^{o}_{cm} are available for pp elastic scattering at or near p_{lab} = 6 GeV/c and 12 GeV/c. At the same energies pn data exists, though only at 6 GeV/c does it extend to large angles. Thus a limited isospin decomposition may be made at these energies. The quality of the $\bar{p}p$ data is poor, so the charge conjugation breakdown is less well determined. In addition, pp data for $t \gtrsim -2$ $(GeV/c)^2$ is available at energies up to p_{lab} = 300 GeV/c. Summaries of the data are shown in Figs. (4.2.1)-(4.2.3).

At the lower end of the energy scale, the pp polarization is everywhere positive and exhibits two clear peaks. The first is at $t \simeq -0.3$ $(GeV/c)^2$, and the second, higher than the first, is at $t \simeq -1.5$ to -2.0 $(GeV/c)^2$. The small magnitude of the data reflects the correctness of the assumption that $N_0 >> N_1$.

The first peak is present throughout the energy range, and its height decreases with increasing energy indicating that N_1 falls off more rapidly with energy than does N_0. In this small t region it is to be expected that the most important contributions come from pole trajectories, and indeed the energy dependence of P(pp) is consistent with N_1 ($t>-1$ $(GeV/c)^2$) being the sum of a leading natural parity meson-Reggeon (f, ω, A_2, ρ) trajectory exchange and exchange of a daughter trajectory ($\alpha_{Daughter} = \alpha_{Parent} - 1$). (See e.g. Kroll et al (1979) and Berger et al (1978)). This is illustrated by Fig. (4.2.4) which compares the energy dependence of the small -t P(pp) data with that naively expected if N_1 were dominated by a parent $\left(\frac{N_1}{N_0} \sim s^{-.5} \rightarrow s^{-.8}\right)$ or a daughter $\left(\frac{N_1}{N_0} \sim s^{-1.5} \rightarrow s^{-1.8}\right)$ pole.

The secondary peak also decreases in height between p_{lab} = 6 GeV/c and 12 GeV/c so that in this region also, N_1 appears to have a lower effective trajectory than N_0. At very high energies this secondary peak structure is lost, however, and the dominant feature for $t < -1$ $(GeV/c)^2$ becomes a sharp dip at $t \simeq -1.2$ $(GeV/c)^2$ (See in particular the p_{lab} = 150 GeV/c data).

P(pn) at p_{lab} = 6 GeV/c exhibits a very similar structure to that seen in P(pp) at this energy, but shifted downwards on the scale. Thus the shape of the polarization curve is determined by the I = 0 part of the N_1 amplitude. The I = 1 part, in contrast, seems to be structureless, at least for $-t \lesssim 1.5$ $(GeV/c)^2$. Little can be deduced about the shape of P(np) from the data at 11.8 GeV/c. An isospin decomposition of P(NN) at p_{lab} = 6 GeV/c for $t > -1.4$ $(GeV/c)^2$ can be found in Kroll et al (1979).

A good fit to P(pp) and P(pn) for $t \gtrsim -1$ $(GeV/c)^2$ can be obtained using the following meson-Reggeon contributions to N_1: exchange degenerate f, ω and A_2, ρ pairs together with a lower lying I = 0 trajectory (referred to here as f-daughter) see e.g. Berger et al (1978). The behaviour of the contribution to P of such an exchange degenerate term in N_1 (in this case the A_2, ρ term) is illustrated in Fig. (4.2.5). The term is as given by (1.5.4) with

$$\beta^{+-}(pp\to pp;\ A_2,\ \rho)\ \beta_{++}(pp\to pp;\ A_2,\ \rho) = \frac{2}{9}\ e^{r_1 t}\ s^{-(\alpha_{0_\rho}+\alpha'_\rho t-\alpha_\rho(t))} \qquad (4.2.1)$$

The t = 0 couplings of the A_2, ρ are those given by the RPCA model. The RPCA predicts a zero coupling of the f and ω at a helicity-flip vertex whereas the data requires a substantial I = 0 term. Thus, either (1) the RPCA is wrong or applies strictly only at very small $|t|$, or (2) the leading I = 0 term is not in fact f + ω.

A resolution to this problem is proposed below. Since the QI model predicts $N_1 = 0$ at large angles, no term corresponding to $B_Q(t)$ in (3.4.7) has been introduced in (4.2.2).

A parameterization based on exchange degenerate pairs of contributions cannot, however, be used to fit the data at larger -t (see e.g. Kroll et al (1978) and (1979)). In the pp and pn reactions such a parameterization of N_1 would be entirely real. Thus, from (4.1.1)

$$P \propto \mathrm{Im}(N_0)N_1 \qquad (4.2.2)$$

Now in the p_{lab} range 6-12 GeV/c $\mathrm{Im}(N_0)$ changes sign around $t = -1$ $(\mathrm{GeV/c})^2$ (see Fig. (4.2.6)) where cuts replace the P pole as the dominant contribution. If N_1 were real, the polarization would be zero at this point (See e.g. Fig. (4.2.5)). The highly structured portion of P due to the I = 0 part of N_1 does seem to possess a zero in this region, and hence $N_1(I=0)$ could be approximately real. The I=1 part clearly does not, however - the 6 GeV/c pp and pn data do not cross or even approach each other - so N_1 (I=1) must have a significant imaginary part.

Thus, there is a term, important for $-t \gtrsim 1(\mathrm{GeV/c})^2$ (i.e. the region of the second peak in P(pp)), which is not governed by exchange degeneracy. This is just the region in which N_0 is dominated by the $R \otimes P$ cut. It seems likely, then, that a similar phenomenon is contributing to the single flip amplitude. The alternative explanation would be to propose large scale strong-exchange-degeneracy breaking between meson-Reggeon pairs in N_1. (As noted earlier, N_1 is varying faster with energy than N_0, so that a term with a high lying trajectory, such as a flip-Pomeron can be immediately excluded).

The general form expected of a cut is given by (3.3.3). The $R \otimes P$ trajectory has been determined in Chapter 3 during consideration of $\frac{d\sigma}{dt}$, but some freedom remains through choice of the parameter, d. An energy dependence consistent with the observed behaviour of the polarization is obtained with $|d| = \frac{\pi}{2}$. The data is insufficient to allow discrimination between this power/logarithm energy dependence and the pure s^{α} dependence of a Regge pole. Since the concept of exchange degeneracy has been found to work well in a variety of situations, and because of the similarities in the structure of the N_0 and N_1 amplitudes, the exchange degeneracy breaking term will be parametrized here as a combination of single-helicity-flip $R \otimes P$ cuts rather than an extra meson-Reggeon exchange term.

There are four leading $R \otimes P$ cuts which may be contributing to $N_1(NN)$; $f \otimes P$, $\omega \otimes P$, $A_2 \otimes P$, $\rho \otimes P$, each having a different combination of isospin and charge conjugation properties. If, for simplicity, it is assumed that the trajectory and d parameter are the same for all four terms, the total $R \otimes P$ contribution may be written, from (3.3.3)

$$A_{R \otimes P}(pp) = \left[F_{0+}(t) + iF_{0-}(t) + F_{1+}(t) + iF_{1-}(t)\right] \frac{s^{\alpha_{RxP}(t)} e^{-i\frac{\pi}{2}\alpha_{RxP}(t)}}{(\ln s + d)} \quad (4.2.3)$$

where the F's are real and the subscripts indicate isospin and charge conjugation. Figs. (4.2.7) and (4.2.8) show the contribution to P of such terms. Fig. (4.2.7) represents a C = + contribution with

$$F_+(t) \equiv F_{0+}(t) + F_{0-}(t) = Gf(t) \times \frac{2\sqrt{-t}}{m_p} \times (-2.11) \times e^{1.9t} \quad (4.2.4)$$

where f(t) is the t-dependence function of the $R \otimes P$ component of N_0, defined by (3.5.10) and G is the corresponding coupling factor. Fig. (4.2.8) represents a C = - contribution with

$$F_-(t) = G\, f(t) \times \frac{2\sqrt{-t}}{m_p} \times (-0.352) \times e^{1.9t} \quad (4.2.5)$$

The parameter d is chosen to be $+\frac{i\pi}{2}$.

The C = + contribution (Fig. (4.2.7)) possesses features seen in the P(pp) data. It has a minimum at t = -0.7 $(GeV/c)^2$ at P_{lab} = 6 GeV/c, which becomes deeper and moves to larger -t values as the energy increases (t = -1.2 $(GeV/c)^2$ at p_{lab} = 150 GeV/c). At t ≃ -1.5 $(GeV/c)^2$ a large peak occurs after which the contribution rapidly tends to zero as -t increases. Thus much of the structure in the data is consistent with being due to a C = + $R \otimes P$ cut. As noted earlier P(pp) and P(np) data have similar shapes (atleast at p_{lab} = 6GeV/c) and hence the structure can be associated with I = 0 exchanges. Thus it is reasonable to assume that this C = + cut has I = 0 and hence is $f \otimes P$ (though some admixture of $A_2 \otimes P$ cannot be excluded).

The principle feature present in the data, but missing from the $f \otimes P$ cut contribution is the peak at small -t. The change in height of the I = 0 component of this peak indicates the presence at small -t of a low lying trajectory exchange contribution in N_1 (I = 0). It is thus proposed that the I = 0 component of the N_1 amplitude is composed principally of f-daughter exchange (important for small -t) and $f \otimes P$ cut exchange. This is consistent with the RPCA model prediction of a zero $fN\bar{N}$ helicity flip coupling.

Turning now to the I = 1 component of the polarization, it may readily be seen, that a combination of $\rho + A_2$ and C = - $R \otimes P$ cut terms can give a contribution which is roughly constant between t = -0.1 $(GeV/c)^2$ and t = -1.5 $(GeV/c)^2$ as required by the 6 GeV/c P(pp) and P(pn) data.

Thus, most features of the polarization data can be reproduced using an N_1 amplitude composed of two I = 0 contributions ($f \otimes P$ cut and f-daughter) and three I = 1 contributions ($\rho \otimes P$ cut and exchange degenerate ρ and A_2 poles).

There is one notable region, however, where this is not the case – $p_{lab} \simeq 6$ GeV/c, $t \lesssim -2$ $(GeV/c)^2$, particularly in pn scattering. Here, the Minnesota pn data rapidly decreases from zero at $t \simeq -2$ $(GeV/c)^2$ through ~ -.3 at $t = -5$ $(GeV/c)^2$ (90°_{cm}) to ~ -.45 at $t \simeq -8$ $(GeV/c)^2$.+ Unfortunately, higher energy large -t pn data is not available to establish the energy dependence of this feature. Nor is its isospin behaviour clear, as $N_1(pp)$ (and hence P(pp)) is constrained by Fermi statistics to be zero at 90°_{cm}, so that all contributions must cancel at this point. If a term similar to that giving the large negative contribution to P(pn) were present in $N_1(pp)$, its effects near 90°_{cm} would be disguised by the cancelling contributions. Direct comparison of P(np) and P(pp), thus yields little information.

Large -t data for pp is, of course available at higher energies. If the large t term is a) present in pp scattering and b) has a relatively slow s dependence at fixed t (i.e. is a "forward" scattering term), then it should make its presence felt in P(pp) at 12 GeV/c. The data at this energy, however, remains close to zero ($\lesssim .08$) for $t \lesssim -2.5$ $(GeV/c)^2$. Neverthless, there does appear to be a change in curvature of the -t side of the secondary peak between 6 GeV/c and 12 GeV/c, which is not explained by the $f \otimes P$ cut in N_1. This could be an indication that the term producing the large negative values

+ This is particularly interesting in that the QIM predicts that the polarization, in both pp and pn scattering, should be zero to leading order at large -t and large angles.

a) is present also in $N_1(pp)$ (but cancelled at large angles by terms with more rapidly varying fixed t energy dependence - "backward" terms)

b) has a relatively low lying trajectory, so that its importance decreases rapidly with increasing energy.

One of the premises upon which the model is based is that the asymptotic behaviour of the scattering amplitudes at large angle is as given by the Quark Interchange model. In nucleon-nucleon scattering, the leading QIM contributions to the amplitudes behave like $\frac{1}{s^4}$ at fixed large angle. Now the QIM predicts that $N_1 = 0$ to this order. Thus to maintain consistency with QIM any large angle terms in N_1 must have a fixed angle variation with energy which is faster than $1/s^4$.

To model the large angle pn behaviour an extra, low-lying, term has been introduced into the parametrization. For convenience its structure has been based on that of the $R \otimes P$ cut. To obtain the necessary antisymmetry of $N_1(pp)$ about 90°_{cm}, the term is again divided into "forward" and "backward" parts (as in (3.5.6)). To account for the large difference between P(pp) and P(np) at large -t, $p_{lab} = 6$ GeV/c, it is assumed that the "forward" part is I = 1, while the "backward" part is written as I = 0. The "forward" parametrization is obtained from (4.2.3) by replacing the total F(t) by

$$\frac{1}{s^2} F_X(t) = \frac{-G_x}{s^2} X(t) \cdot 2\sqrt{-t}/m_p \cdot G_x f(t) \qquad (4.2.6)$$

where $X(t) = \left(1 - e^{\alpha_x t}\right)^4$

The factor X(t) has been introduced so as to give the required rise in magnitude of P(pn) at large angles and low energy, while retaining a positive total (ie. forward plus backward) X contribution to P(pp) for $\theta_{cm} < 90^{o}$. The S^{-2} factor gives the necessary low lying trajectory ($\alpha_x(t) \to -3$ at $t \to \infty$) while the exponential t-dependence of f(t) ensures that the fixed angle energy dependence is more rapid than the QI power law form.

The curves shown in Fig. (4.2.9) - (4.2.11) are obtained using ρ, A_2, f-daughter, $f \otimes P$ and $\rho \otimes P$ terms together with the X term just described. As may be seen, a good account of the data is obtained over the whole range of energies and angles considered.

The ρ and A_2 terms used are as given by (4.2.1) and (1.5.4). The $f \otimes P$ and $\rho \otimes P$ are as given by (4.2.3), with

$$F_{f\otimes P}(t) = Gf(t) \times 2\frac{\sqrt{-t}}{M_p}\left[K_1 \frac{e^{a_3 t}}{(-t)} + \alpha_t(t)K_3\right] - F_x(t)/24^2 \qquad (4.2.7)$$

$$F_{\rho\otimes P}(t) = Gf(t) \times 2\frac{\sqrt{-t}}{M_p} \cdot K_2 . e^{a_3 t} . (1 + 2t) \qquad (4.2.8)$$

Note that (4.2.7) is not in fact singular at t = 0 since $f(t) \propto t^2$. The changes from (4.2.4) and (4.2.5) have been introduced to give better agreement with the data in the region $t \lesssim -1.5$ $(GeV/c)^2$ ie. the large $|t|$ side of the second peak. The function $\alpha_t(t)$ is obtained by following the trajectory bending procedure from Chapter 3 starting with a linear form defined by $\alpha_t^0 = 1$, $\alpha_t' = 1$. Thus $\alpha_t(0) = 1$ and $\alpha_t(-\infty) = -1$. The structures of (4.2.7) and (4.2.8) are a product of the history of the parametrization - it is the shapes of $F_{f\otimes P}(t)$ and $F_{\rho\otimes P}(t)$ that are important not the way they are written down. The simpler forms were used earlier so as to make clear, in particular,

that the dip-peak structure seen in Fig. (4.2.7) arises naturally, and is not the result of an artificially imposed t-dependence.

The f-daughter term takes the form

$$A_{++}^{+-}\,(pp\text{-}pp;f\text{-daughter}) = \frac{1}{S}\,D\,e^{r_2 t} \times \frac{A_{++}^{+-}(pp;f)}{\beta^{+-}(pp\text{-}pp;f)\beta_{++}(pp\text{-}pp;f)} \qquad (4.2.9)$$

where $A_{++}^{+-}\,(pp\text{-}pp;f)$ is as given by (1.5.4). The fitted parameters are listed in Table (4.2.1).

Note that $N_1(pp)$ must be antisymmetric about $\theta_{cm} = 90^{\circ}$. This has been ensured by adding a "backward" part of $N_1(pp)$ to the "forward" part described above, as prescribed by equation (3.5.6). The curves presented in Fig. (4.2.9) are obtained using the full expression for the polarization parameter, P, (see B.5) rather than the approximate form, (4.1.1). The parametrization of N_2 used, is that obtained (along with U_0 and U_2) in Section 4.3, which now follows. In practice, neglecting N_2 is found not to affect greatly the polarization parameter results.

4.3 Spin-Spin Correlation Parameters

In section 4.2, polarization data was used, in conjunction with a previously formulated expression for N_0, to obtain information about the single helicity flip amplitude, N_1. In a similar way the correlation parameters, A_{nn}, A_{ss} and A_{ll} can be used to shed light on the structure of the N_2, U_2 and U_0 amplitudes respectively (see equations (4.1.2) to (4.1.5)). Unfortunately, data for these parameters at moderate and large -t are far from abundant, being limited, principally, to pp scattering at or below $p_{lab} = 12$ GeV/c.

A_{nn}(pp) data at 6 and 12 GeV/c are shown in Fig. (1.3.6), together with two points representing recent measurements of A_{nn}(pn) at 6 GeV/c. The most prominent feature is the rapid rise which occurs for $-t>4$ $(GeV/c)^2$, leading to peak values of around 0.6 (p_{lab} = 11.75 GeV/c, $7 \lesssim -t \lesssim 10.2$ $(GeV/c)^2$. NB 90°_{cm} corresponds at this energy to $t = -10.19$ $(GeV/c)^2$). For $-t < 4$ $(GeV/c)^2$, A_{nn} is small which is consistent with the assumption that $N_2 << N_0$ except at large -t. This apparent split into two t-regions fits in well with the philosophy (outlined in Section 3.5) of parametrizing the scattering amplitudes in "Q" and "R" parts, with

$$N_0^R >> N_1^R, \quad N_2^R, \quad U_0^R, \quad U_2^R$$

and $\dfrac{N_0^Q}{N_2^Q}$ $(t \to -\infty)$ etc. given by the Q.I. model.

With such a parametrization one would expect A_{nn} to be small in the low -t region ("R" parts of the amplitudes dominant), but approach the QI-predicted value of $\frac{1}{3}$ as $\theta_{cm} \to 90^\circ$, s large. It is interesting to note that the data, in fact, exceeds $\frac{1}{3}$ at 90°_{cm}, plab = 11.75 GeV/c. Clarification of whether this indicates that the QI model needs modifying, or merely that "large" energies have yet to be reached, will have to await future experiments at higher energies.

At small to medium -t, A_{nn} exhibits a double peak structure reminiscent of that seen in the polarization parameter. The first peak occurs about $t = -0.7$ $(GeV/c)^2$, and is seen clearly both at 6 GeV/c and 11.75 GeV/c. At 11.75 GeV/c this is followed by a sharp dip ($t = -0.9$ $(GeV/c)^2$), then the second peak at around $t = -1.8$ $(GeV/c)^2$. This dip-second peak structure is much less obvious at 6 GeV/c.

For t between -1 and -3 $(GeV/c)^2$ A_{nn} appears to be slowly increasing with increasing energy. This indicates either that a) $|N_2|/|N_1|$ is increasing with energy, or b) The relative phase of N_2 and N_1 is changing. These possibilities will be discussed in more detail later.

Fig.(1.3.7) shows data for A_{11}, A_{s1} and A_{ss} at 6 GeV/c. There is no medium to large -t data available for these observables at higher energies and all have low values at small -t as expected. At larger angles the data is reasonably consistent with an approach toward the values predicted by the QI model at 90°_{cm} (For more detailed comment refer back to Table (1.4.2)).

As was the case for the N_0 and N_1 amplitudes, in this model the behaviour at small -t of the Regge pole terms contributing to N_2, U_0 and U_2, will be based on traditional Regge models. All meson-Reggeon contributions will be constrained to give the behaviour predicted by the Quark Interchange model at large s and -t.

As noted above, the double polarization observable for which most data is available is A_{nn}, and it is to this parameter that attention is first turned. From equation (4.1.2) it may be seen that $A_{nn}.D$ (Appendix B) is approximately proportional to the product of those parts of N_0 and N_2 which are in phase. The RPCA model predicts that the dominant Regge-pole contribution to N_2 at small -t should come from the (approximately) exchange degenerate ρ and A_2 trajectories. (The helicity flip couplings of the P, f, ω to $N\bar{N}$ are predicted to be zero). Fig. (4.3.1) shows the contribution to $A_{nn}(pp)$ made by a $\rho+A_2$ term in $N_2(pp)$ whose "R" part (see Section 3.5) is given by (1.5.4.) with

$$\left[\beta^{+-}(pp;\rho,A_2)\beta_{+-}(pp;\rho,A_2)\right]^R = \frac{1}{9}\ \bar{s}^{[0.51+0.85t-\alpha_\rho(t)]} \qquad (4.3.1)$$

At t = 0, this reduces to the RPCA coupling.

Comparing this picture with Fig.(1.3.6) it is readily seen that although the magnitude of the $\rho+A_2$ contribution for $-t\lesssim 1$ $(GeV/c)^2$ is comparable with that of the data, it has the wrong sign.

Clearly, either the RPCA prediction of the Reggeon helicity flip coupling strengths is grossly wrong, or else another term (or terms) is present which gives a positive contribution to $A_{nn}(pp)$ at small -t, of roughly twice the magnitude of that of $\rho+A_2$. The model of Berger et al (1978) does, in fact include such a positive contribution. This arises from the introduction of absorption corrections to the π and β exchange amplitudes (These are found necessary to explain the forward spike in np pn scattering). The corrections are applied using the Williams prescription (Williams (1970)) as follows: The basic Reggeon exchange amplitude in the Berger et al model is given by

$$A_{\lambda_A\lambda_B}^{\lambda_A\lambda_C}(AB\to CD;R) = \mp\left(\frac{\sqrt{-t}}{2m_N}\right)^{|\lambda_C-\lambda_A|}\left(\frac{\sqrt{-t}}{2m_N}\right)^{|\lambda_D-\lambda_B|}\beta^{\lambda_A\lambda_C}(AC;R)\beta_{\lambda_B\lambda_D}(BD;R)$$

$$\frac{1}{2}\left[1+(-1)^{S_R}e^{-i\pi\alpha_R}\right]\Gamma(\ell_R-\alpha_R)(\alpha')^{1-\ell_R}(\alpha' S)^{\alpha_R} \qquad (4.3.2)$$

where S_R and ℓ_R are respectively the spins of exchange R and of the lowest occurrence on the exchange degenerate trajectory $\alpha_R(t)$. See Table (4.3.1) for parameter values. For an exchange degenerate pair the amplitudes sum to give (4.3.2) with the signature phase factor

(square bracket) replaced by 2. To obtain the absorbed π+B amplitude the further replacement

$$\left[\frac{-t}{4m_N^2}\right]^{(n+x)/2} \rightarrow \left[\frac{-t}{4m_N^2}\right]^{n/2}\left[\frac{-m_\pi^2}{4m_N^2}\right]^{x/2} \qquad (4.3.3)$$

is made, where $n = |\lambda_C-\lambda_A-\lambda_D+\lambda_B|$ and $n+x = |\lambda_C-\lambda_A|+|\lambda_D-\lambda_B|$

Now, for φ_2 ($\equiv A^{+-}_{+-}$), $n = 0$ and $n+x = 2$, while for φ_4 ($\equiv A^{+-}_{-+}$) $n = 2$ and $n+x = 2$. Because $\left|\varphi_2^{\pi,B}/\varphi_4^{\pi,B}\right| \neq 1$, the absorbed π and B exchanges do not have definite naturality, and hence contribute both to N_2 and to U_2 (see table B.3). In the case of N_2 the π+B term contains the factor (corresponding to (4.3.3))

$$\frac{1}{2}\left[\frac{-t}{4m_N^2}+\frac{m_\pi^2}{4m_N^2}\right] \qquad (4.3.4)$$

while in U_2 this becomes

$$\frac{1}{2}\left[\frac{-t}{4m_N^2}-\frac{m_\pi^2}{4m_N^2}\right] \qquad (4.3.5)$$

The above prescription gives only a rough and ready approximation to the true absorptive effects, but it should provide a reasonable guide, at least small $|t|$. Fig. (4.3.2) shows the contribution to A_{nn} of an absorbed π+B term in N_2. This term is as described above, except in that

a) the linear trajectory used by Berger et al (see Table (4.3.1)) has been modified so as to tend to -1 at $t\rightarrow-\infty$. The same prescription has been used as for f, ω, ρ, A_2 (see Section (3.4)).

b) An extra factor of

$$E\ e^{r_3\left[\alpha_{o_\pi} - \alpha'_\pi - \alpha_\pi(t)\right]} \qquad (4.3.6)$$

with $E = 1.4$ and $r_3 = 2.0$

has been used to modify the Berger et al coupling product, $\beta^{+-}\beta_{+-}$ in order to improve agreement with the data.

The effects of this modification are felt mainly at large -t, where the accuracy of the Williams prescription is uncertain anyway. A comparison between Figs. (4.3.1) and (4.3.2) shows that the $\rho+A_2$ and $\pi+B$ terms are capable of producing a "hump" for $-t \lesssim 1$ $(GeV/c)^2$ such as is seen in the data. The positive contribution of the $\pi+B$ dominates at very small -t, but the negative $\rho+A_2$ gains in importance with increasing -t. The sum of the terms is zero at $t = -1.3$ $(GeV/c)^2$ for $p_{lab} = 6$ GeV/c.

It seems, then that the behaviour of A_{nn} for $-t \lesssim 1$ $(GeV/c)^2$ can be explained reasonably well in terms of a $\pi+B$ term with absorbtive corrections plus a $\rho+A_2$ term (perhaps even by a $\pi+B$ term alone). It is unlikely, however, that this combination can successfully account for A_{nn} in the region $1 \lesssim -t \lesssim 3$ $(GeV/c)^2$. As was mentioned earlier, the available data in this region indicates that A_{nn} is growing with increasing s, implying, at least superficially, that the effective trajectory of the N_2 amplitude is higher lying than that of N_0. Note, however, that this conclusion applies only if the relative phases of N_2 and N_0 at a given t value vary little over the energy range under consideration.

Now in this intermediate t region, the most important contribution to N_0 is from the $R \otimes P$ cut terms. The growth with energy of A_{nn} could thus be explained if N_2 were dominated by a contribution with a much higher lying trajectory. The only pole term which fulfils this requirement is the Pomeron, P. If it is assumed that $N_0 >> N_1$, N_2, U_0, U_2, then

$$A_{nn} \propto \mathrm{Re}(N_0 N_2) / |N_0|^2 \qquad (4.3.7)$$

Further assuming that N_0 and N_2 are each dominated by a single Regge pole, then at fixed t

$$A_{nn} \propto \frac{s^{\alpha_{N_0}} s^{\alpha_{N_2}}}{s^{2\alpha_{N_0}}} = s^{\alpha_{N_2} - \alpha_{N_0}} \qquad (4.3.8)$$

Replacing α_{N_2} by α_P and α_{N_0} by $\alpha_{R \otimes P}$, then in the t-region under consideration A_{nn} is expected to vary roughly as s^{+1}. Thus, between p_{lab} = 6 GeV/c (s = 13.2 $(\mathrm{GeV/c})^2$) and p_{lab} = 12 GeV/c (s = 24.4 $(\mathrm{GeV/c})^2$), A_{nn} would increase by a factor of 2, which for $1 \lesssim -t \lesssim 3$ $(\mathrm{GeV/c})^2$ is reasonably consistent with the data.

Pomeron exchange, having even charge conjugation and a trajectory near +1 is mainly imaginary. Since A_{nn} is approximately proportional to $\mathrm{Re}(N_0 N_2)$, the P contribution to A_{nn} depends on the product $\mathrm{Im}(N_0)\, N_2^P$. As may be seen from Fig. (4.2.6) Im (N_0) has a zero at about $t = -1.2$ $(\mathrm{GeV/c})^2$ in the energy range being considered. A P contribution to A_{nn} would thus be expected to change sign near this value of t. Notice that the p_{lab} = 11.75 (GeV/c) data has a minimum at $t \simeq -0.9$ $(\mathrm{GeV/c})^2$. This could well originate from a near cancellation between the π+B (absorbed) and ρ+A_2 contributions, together with a small negative value from $\mathrm{Re}(N_0 N_2^P)$. The combined meson-Reggeons would give the required positive A_{nn} for $-t < .9 (\mathrm{GeV/c})^2$ and N_2^P would be responsible for the maximum seen at

$t \simeq -1.8$ $(GeV/c)^2$. The negative Pomeron contribution at small-t would have to be small so that an unreasonably large π+B term is not needed to reproduce the positive experimental results.

The above arguments make a plausible case for the existence of a double helicity flip P contribution. There are, however, several reasons why this interpretation of the data is unattractive :

(1) Comparison of the two available A_{nn}(pn) data points (at plab = 6 GeV/c) with the pp results indicates the presence of a large isospin 1 component which is positive in pp. The ρ+A_2 and π+B contributions are both I = 1, but have opposite signs, producing a small net effect compared with the observed pn values. The Pomeron is I = 0, hence whether or not P is present, a further I = 1 contribution would still be needed.

(2) In the RPCA model, the helicity flip coupling of the Pomeron is zero. This prediction is borne out by the lack of evidence for a Pomeron term in N_1. If factorization holds for P its contribution to N_2 should be even smaller than to N_1.

(3) Although a cancellation between the ρ+A_2 and π+B terms in N_2 together with the sign change in $Re(N_0)$ and the imaginary nature of P can explain the minimum at $t \simeq -.9$ $(GeV/c)^2$ in A_{nn} at p_{lab} = 12 GeV/c, this mechanism will also produce a similar minimum at p_{lab} = 6 GeV/c. There is some evidence for a dip at p_{lab} = 6 GeV/c, but it is much shallower and does not occur until $t \simeq -1.3$ $(GeV/c)^2$. This shift is too large to be caused by a change with energy of the relative magnitudes of π+B and ρ+A_2, since the two trajectories are close together in this t region.

(4) Throughout this work it has been observed that Regge pole contributions are large at small $|t|$, becoming relatively small for $-3 \gtrsim t \gtrsim -1$ $(GeV/c)^2$. (The meson-Reggeons do re-emerge at large angles, however). It thus seems strange that a Pomeron pole contribution to N_2 should grow significant in just that region where in N_0 it becomes very small. The N_2 contribution could of course be re-interpreted as a $P \otimes P$ cut term.

(5) A Pomeron term in N_2 of appropriate strength to account for the A_{nn}(pp) data would have a noticeable effect on the pp differential cross section at very high energy. Because the Pomeron trajectory is near +1 its contribution to $d\sigma/dt$ falls very slowly with increasing energy, and $|N_2^P|^2$ is found to be sufficiently large partly to fill in the interference minimum which occurs in the $|N_0|^2$ term at $t = -1.4$ $(GeV/c)^2$. It may be possible to compensate for this by an adjustment of the N_0 fit parameters, but it seems unwise to draw conclusions about this very high energy region from such a small amount of low energy data.

There is an alternative interpretation of the A_{nn} data which circumvents most of the difficulties encountered with the Pomeron. When considering both N_0 and N_1, the most satisfactory explanation of the behaviour of the data in the intermediate t region was in terms of $R \otimes P$ cuts. Since, in the same region, N_2 also exhibits properties which are difficult to understand in terms of Regge pole terms, it is sensible at least to consider the possibility that this helicity amplitude also contains an important $R \otimes P$ contribution. An immediate problem with this hypothesis is that $\alpha_{R \times P}$ as determined from studies of $d\sigma/dt$ is similar to $\alpha^{eff}(N_0)$ for $-t > 1.5$ $(GeV/c)^2$, and thus from trajectory considerations the $R \otimes P$ contribution to A_{nn} is expected to be roughly constant.

Notice from (3.3.3), however, that the energy dependence of the $R \otimes P$ term depends not only on its trajectory, but also on the factor $(\ln s + d)^{-1}$. It was found necessary previously to choose a different value of the complex constant d_1 for N_0 and N_1. Some freedom in the energy dependence still exists, therefore, through the choice of d appropriate to N_2. If d is chosen to be a complex number with a negative real part, then for $\ln s < -\mathrm{Re}(d)$, the effective trajectory of the term is raised relative to the actual trajectory. The asymptotic properties are of course unchanged.

Fig. (4.3.3) shows the contribution to A_{nn} from an $R \otimes P$ term in N_2 of the form (4.2.3) with

$$F_+(t) + F_-(t) = G_+^f(t) \times \left(\frac{2\sqrt{-t}}{M_p} \right)^2 \times K_3 \, e^{a_4 t} \, e^{i\sigma} \qquad (4.3.9)$$

$$\sigma = -0.161 \; ; \quad d = -3.18 + \frac{i}{2} \; ; \quad K_3 = .0176 \; ; \quad a_4 = 1.0$$

As before $G_+^f(t)$ refers to the t-dependence function of the non-flip $R \otimes P$ term described in Section 3.5. As may be seen, the phase of this term at $p_{lab} = 12$ is such as to produce a minimum close to where one is observed in the data. Furthermore, as well as raising the effective trajectory, the logarithmic factor introduces an energy dependence to the phase. At $p_{lab} = 6$ (GeV/c) the phase is such that no minimum appears in the $R \otimes P$ contribution to A_{nn}. Note that the shape of the contribution is similar to that of the data for $1 \lesssim -t \lesssim 3$ $(\mathrm{GeV/c})^2$ and that this is achieved using a simple modification to the t-dependence found necessary to reproduce the $d\sigma/dt$ data.

An estimate of the ratio of the strengths of the I=1 to I=0 $R \otimes P$ terms can be obtained by comparing $A_{nn}(pp)$ and the available two $A_{nn}(pn)$ points at $p_{lab} = 6$ GeV/c. It appears that the $R \otimes P$ contributions to the $N_2(pp)$ and $N_2(pn)$ are in the proportions 1 : 4, hence

$$\frac{N_2\ (R\otimes P;I=1)}{N_2\ (R\otimes P;I=0)} = -\frac{3}{5} \qquad (4.3.10)$$

Turning now to the large -t region, it is expected from previous arguments that this will be dominated by meson-Reggeon contributions, the asymptotic ($s\to\infty$, $\frac{t}{s}$ fixed) behaviour of which are predicted by the Quark Interchange Model. A first attempt at reproducing the large -t A_{nn} data is shown in Fig. (4.3.4). This picture was obtained by taking the "Q" parts of the "forward" and "backward" contributions to N_0, and scaling them by factors predicted by QIM to produce the "Q" parts of the other helicity amplitudes (see Appendix D). The full expression for A_{nn} is used, as N_2 U_2 and U_0 cannot be said to be $<< N_0$. All terms in N_0 are included.

There are two obvious deficiencies in this first attempt. Firstly, the QIM predicts a value for A_{nn} of $\frac{1}{3}$ at $\theta_{cm} = 90^\circ$ and high energy. The curve in Fig. (4.3.4) is always close to this value for $-t \gtrsim 6$ $(GeV/c)^2$, whereas the data rises to about 0.6 - the experimental values also grow more rapidly. This difficulty may be resolved if some t dependence is introduced into the ratio of the forward "Q" type parts of N_0 and N_2. Secondly, the "backward" component of N_2 (which ensures the behaviour required by Fermi statistics) is having a large effect on the theoretical curve at $p_{lab} = 6$ GeV/c for $-t \gtrsim 2$ GeV. [Note that this backward component comprises not only the crossed "Q"-type parts of various helicity amplitudes, but also upon the "R"-type part of N_0 (see Appendix E)]. If the "forward" component alone were present, then the shape and position (in t) of the rise in the theoretical curve would be similar at the two energies, but this is not the case in Fig. (4.3.4).

The situation is clarified by referring to equation (D.1) which shows that QIM predicts the "forward" and "backward" parts of N_2 to be of the same order at 90°_{cm}. Since the forward part of N_2 is still rising at t = -5 (GeV/c), (as indicated by both the prediction and the data for A_{nn} at p_{lab} = 11.75 GeV/c), the implication of (D.1) is that at p_{lab} = 6 GeV/c with θ_{cm} large, but $<90^\circ$ the "backward" part of N_2 is, in fact, larger than the "forward" part.

It is clear, then, that modifications need to be applied both to the "forward" and "backward" parts of N_2. Equation (E.2) gives the structure of N_2 in terms of the "unsymmetrised" helicity amplitudes, $\tilde{\phi}_i$, in accordance with the requirements of Fermi-Dirac statistics. From this equation it can be seen that the most economical way to effect such improvements while retaining asymptotic agreement with QIM, is to introduce a suitable non-zero ϕ_2 (ϕ_2 = 0 to leading order by QIM), which falls off more quickly than ϕ_1, ϕ_3, ϕ_4 as $s\to\infty$, $\frac{t}{s}$ fixed. Since ϕ_2 is symmetric under interchange of t and u (see (E.1)) this results in the same increment being applied to both forward and backward parts of N_2 at a given t. If ϕ_2^Q is written as follows, using the same notation as in (D.1)

$$\phi_2^Q = \frac{17}{18}\left[Y(t,u)-1\right]\left[f(s,t,u) + f(s,u,t)\right]$$

with Y(t,u) = Y(u,t), then the modified QIM prediction for the pp naturality amplitudes are given by Table (4.3.2).

A form for Y(t,u) which solves both problems outlined above is

$$Y(t,u) = \frac{(2.72 + t)^2}{\left[5 + (3.9+t)^2\right]} \cdot \frac{(2.72 + u)^2}{\left[5 + (3.9+u)^2\right]} \qquad (4.3.11)$$

As t and u tend to $-\infty$

$$Y \sim \frac{t^2}{t^2}\,\frac{u^2}{u^2} = 1$$

thus agreement with DCR and asymptotic QIM predictions is retained. Similarly in the Regge limit ($s\to\infty$, t fixed) $Y(t,u) \to Y(t)$ and hence the leading Regge trajectory is unaltered. Since $Y(t,u)$ can be expanded in the form

$$Y(t,u) \cong \bar{Y}(t)\left\{1 + a\,\frac{t}{s} + b\,\frac{t^2}{s^2} + \ldots.\right\} \quad s\to\infty,\ t \text{ fixed} \qquad (4.3.12)$$

all that has been done is to introduce extra Regge-daughter terms.

Fig. (4.3.5) is obtained using an N_2 composed of $\rho+A_2$ ("R" + "Q") , $f + \omega$ ("Q" only), and $R \otimes P$ terms as discussed above. The "backward R" part of N_2 is defined via (E.5). Note that N_1, U_0, U_2 also contribute to Fig. (4.3.5). N_1 is as given by Section 4.2, the parameterizations of U_0 and U_2 are discussed below and are summarized together with that of N_2 at the end of this section. The theoretical curves give a good account of all the features and trends of the data. It will be interesting to see whether future experiments at higher energies confirm the deductions made in the above account .

The parametrization of the unnatural parity amplitudes U_0 and U_2, used here is based at small -t on the work of Berger et al and at large -t on the predictions of the Quark Interchange model. Berger et al consider U_0 to comprise three components as follows :

a) An exchange degenerate A_1 + Z term of the form

$$U_0(pp\to pp;\ A_1+Z) = -\,(4.4)^2\,\Gamma(1 - \alpha^{\circ}_{A_1Z} - \alpha'_{A_1Z}t)\,(0.9s)^{(\alpha^{\circ}_{A_1Z}+\alpha'_{A_1Z}t)} \qquad (4.3.13)$$

with linear trajectory defined by

$$\alpha^{\circ}_{A_1Z} + \alpha'_{A_1Z}\,t = -0.19 + 0.9\,t$$

In the spirit of the modifications applied previously to other Reggeon terms, this is transformed into the "R" part of the A_1+Z term used here by (1) replacing the straight line trajectory by $\alpha_{A_1Z}(t) \to -1$ as $t \to -\infty$, obtained using the prescription of Section (3.4), and

(2) multiplying by $\bar{s}^{\alpha^o_{A_1Z}+\alpha'_{A_1Z}t-\alpha_{A_1Z}(t)}$ with $\bar{s} = 30$ (4.3.14) $(GeV/c)^2$ to ensure that the "R" part is small at large -t.

b) An imaginary EXD-breaking term important at small -t and parametrized as

$$-i26\, e^{4t}\, (\alpha'_{A_1}\, s)^{\alpha_{A_1}} \tag{4.3.15}$$

c) A non-asymptotic (but non-negligible) "contamination" of U_0 by N_0 (U_0 has definite naturality only to leading order in $\frac{1}{s}$). This takes the form

$$U_0\ (\text{"contamination"}) = \frac{-t}{2s}\ N_0^R \tag{4.3.16}$$

Only the "R" component of N_0 is used in (4.3.16) as the derivation is strictly valid only for small -t.

The t-dependence of the forward Q-type part of the U_0 amplitude is obtained by factoring the "Q" part of N_0 by the QI prediction for the ratio of these amplitudes, as specified in Table (4.3.2). The backward R and Q parts of U_0 are defined by equations (E.5) and Table (4.3.2) respectively. Since all the leading meson-Reggeon trajectories (natural and unnatural parity) tend to -1 at large -t, U_0/N_0 approaches the value predicted by QI as $s\to\infty, \frac{-t}{s}$ fixed.

Berger et al hold that the dominant contribution to U_2 at small -t originates from the same absorbed π+B term that appears in the parametrization of N_2 (see equations (4.3.2) and (4.3.5)). This term is used here to approximate the forward "R" part of U_2. The forward Q-type part is obtained by analogy to N_0, with an extra factor of

$$\frac{17}{45} \left[2 - Y(t,u)\right] \qquad (4.3.17)$$

(see Table (4.3.2)). The backward R and Q parts of U_2 are also defined by equations (E.5) and Table (4.3.2) respectively.

The resulting curves for A_{11}, A_{s1} and A_{ss} (pp) are compared with the available data in Fig. (4.3.6). The overall standard of agreement is good, especially considering that no adjustment of the model was made to improve its account of these parameters.

Summary of N_2, U_0 and U_2 parametrization

N_2 (forward): The parametrization of N_2 may be divided into three t regions with dominant contributions as follows :

a) $-t \lesssim 1$ $(GeV/c)^2$:-

(1) "R"-type part of absorbed π+B term defined by (4.3.2) modified by (4.3.4) and (4.3.6) and with $\alpha_\pi(t) \to -1$ as $t \to -\infty$. (2) "R"-type part of ρ+A_2 term defined by (1.5.4) and (4.3.1).

b) $1 \lesssim -t \lesssim 3$ $(GeV/c)^2$:-

An $R \otimes P$ cut term defined by (4.2.3) and (4.3.9). The I = 1 and I = 0 component of this term are roughly in the ratio -3 : 5.

c) $-t \gtrsim 3.5\ (\mathrm{GeV/c})^2$:

A "Q"-type Reggeon term obtained by factoring the "Q" contribution to N_0 by the amount predicted by QIM, and then multiplying by Y(t,u) (see (4.3.11) and Table (4.3.2)).

U_0 (forward): This amplitude is written as three terms

a) An A_1 + Z term with real part defined by (4.3.13) and (4.3.14) with the linear trajectory replaced by $\alpha_{A_1Z}(t) \to -1$ as $t \to -\infty$; and imaginary part, important at small -t, defined by (4.3.15).

b) A non-asymptotic "contamination" of U_0 by N_0 written as (4.3.16).

c) "Q"-type Reggeon term obtained by analogy to the "Q"-type part of N_0 factored by the amount predicted by QIM.

U_2 (forward): This is written in two parts

a) An "R"-type π+B (absorbed) contribution : see equations (4.3.2) and (4.3.5).

b) A "Q" type Reggeon term obtained by analogy to the "Q" part of N_0 factored by (4.3.17).

The requirements of Fermi statistics are satisfied by adding "backward" Q and R parts to the amplitudes. These are obtained via Table (4.3.2) and equation (E.5) respectively.

4.4 Conclusions

Examination of polarization and spin correlation parameter (A_{ij}) data has yielded information on the structures of the naturality amplitudes N_1, N_2, U_0, U_2. Regge exchange models have been constructed for each of these scattering amplitudes, which when used together with the model for N_0 described in Chapter 3 reproduce the data well. The models are based on the philosophy which was evolved in Chapters 1 and 2 and applied to $d\sigma/dt$ (NN) in Chapter 3.

The structures of N_1, N_2, U_0, U_2 seem to follow closely the pattern established for N_0: Conventional Regge pole terms are important at small -t. The meson-Reggeon trajectories bend for $t \lesssim -1$ $(GeV/c)^2$ to approach -1 as $t \to -\infty$. At large angles these meson-Reggeons again dominate the amplitudes (except for N_1) and exhibit the behaviour predicted by Dimensional Counting as $s \to \infty$, t/s fixed. As in N_0 an extra term is found necessary at intermediate angles in N_1 and N_2. In each case the most likely source is a sum of $R \otimes P$ cuts.

The study of 0°-90°_{cm} elastic scattering will next be extended to the πp system.

Table (4.2.1)

Contribution	Parameter	Ref. equation	Value
ρ, A_2	r_1	(4.2.1)	0.79
f-daughter	D	(4.2.9)	23.6
	r_2		1.37
$f \otimes P$	K_1	(4.2.7)	-1.61
	a_3		1.738
	K_3		0.029
$\rho \otimes P$	K_2	(4.2.8)	-0.351
X	G_x	(4.2.6)	21
	a_x		0.7

Table (4.3.1)

Parameters from Berger et al (1978) for use in eqn. (4.3.2)

$$\alpha_\pi = \alpha_B = 0.9\ (t - m_\pi^2)$$

$$\alpha_{A_1} = \alpha_Z = -0.19 + 0.9\ t$$

$$\beta^{+-}(pp;\pi) = \beta^{+-}(pp;B) = 25.2$$

$$\beta^{++}(pp;A_1) = \beta^{++}(pp;Z) = 4.4$$

Table (4.3.2)

Naturality amplitudes for pp scattering as predicted by QIM modified by including a non-zero φ_2:-

$$\varphi_2 = \frac{17}{18} [Y(t,u)-1] [f(s,t,u) + f(s,u,t)]$$

with $Y(t,u) = Y(u,t) \to 1$ as $s \to \infty$, $\frac{t}{s}$ fixed and negative i.e. $t,u \to -\infty$.

$$N_0^Q = \frac{1}{18} \left[45\ f(s,t,u) + 48\ f(s,u,t) \right]$$

$$N_1^Q = 0$$

$$N_2^Q = \frac{-1}{18} \left[17\ f(s,t,u)\ Y(t,u) + f(s,u,t)\ \{ 17Y(t,u)-3 \} \right]$$

$$U_0^Q = \frac{1}{18} \left[17\ f(s,t,u) + 14\ f(s,u,t) \right]$$

$$U_2^Q = \frac{-1}{18} \left[17\ f(s,t,u)\ \{ 2 - Y(t,u) \} + f(s,u,t)\{ -17\ Y(t,u) + 31 \} \right]$$

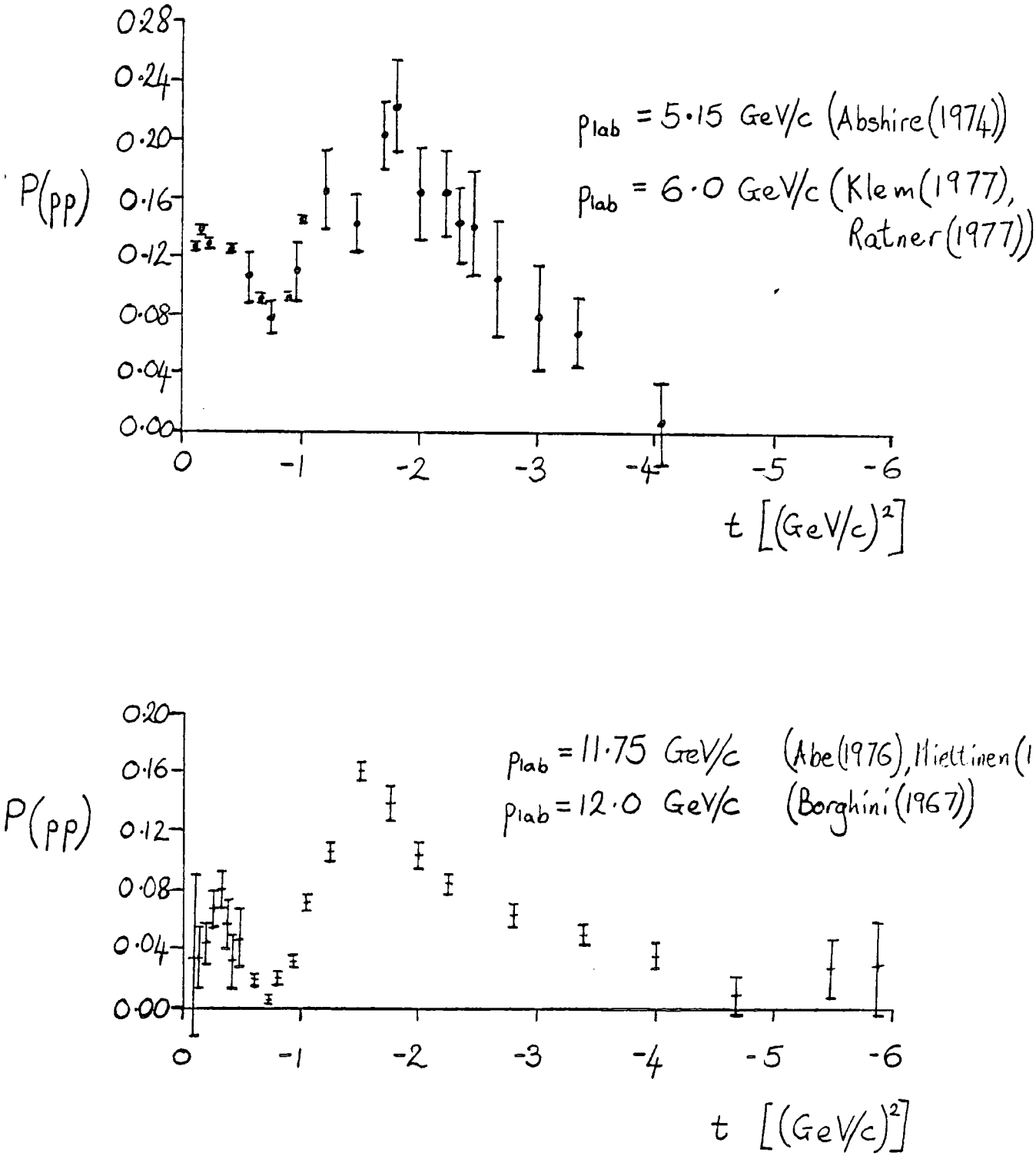

Fig. (4.2.1)

Experimental measurements of P(pp)

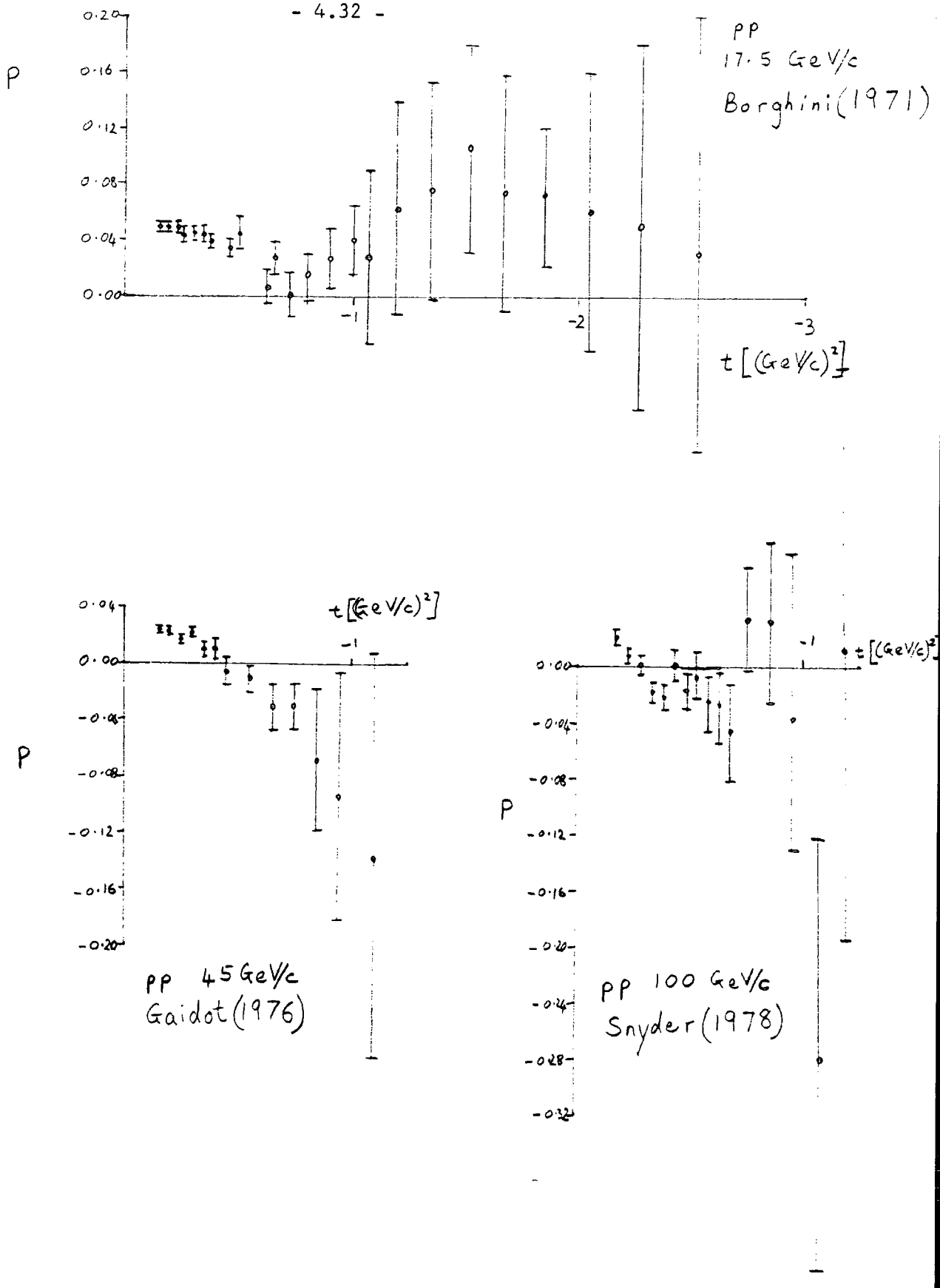

Fig. (4.2.1) continued

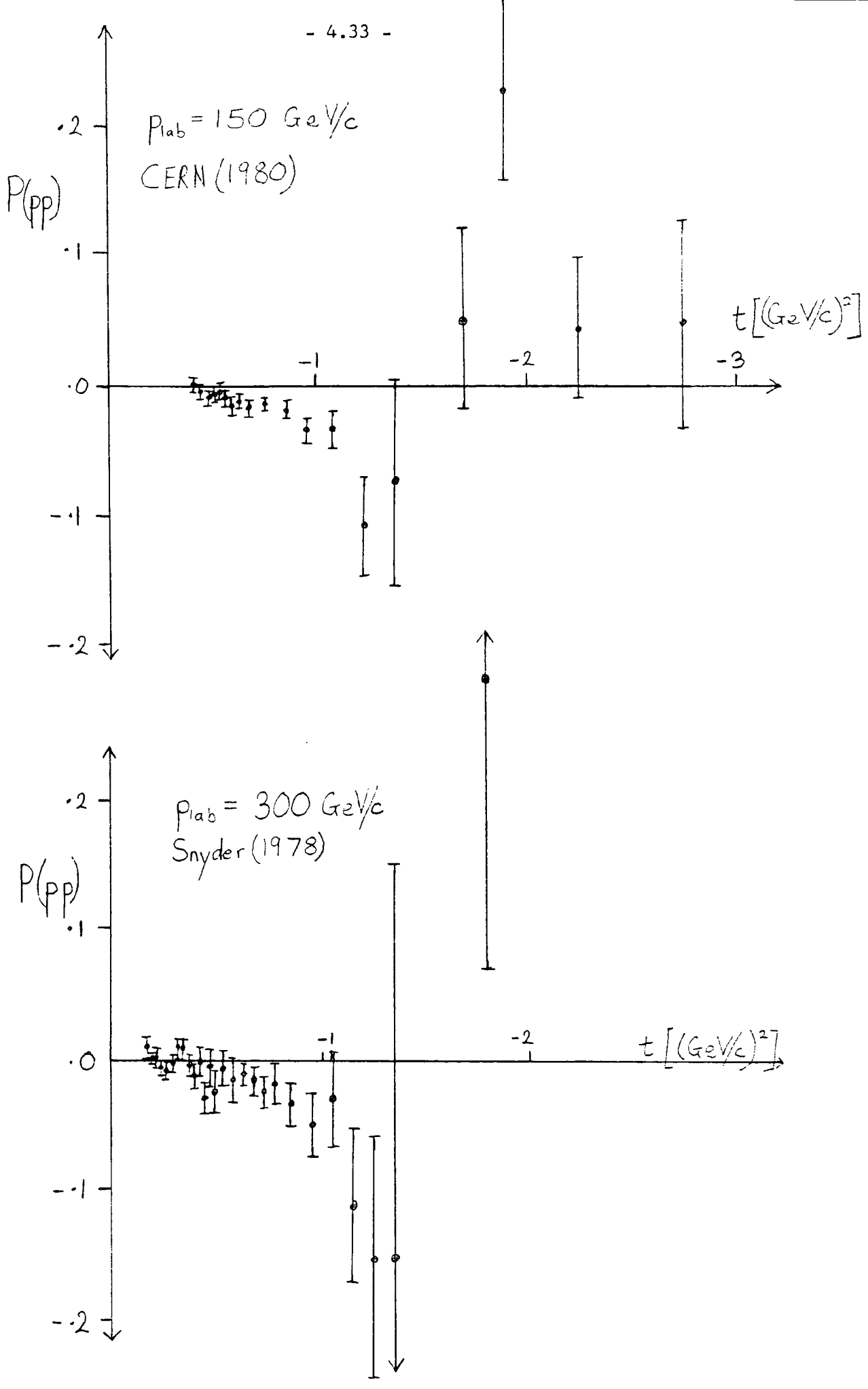

Fig. (4.2.1) continued

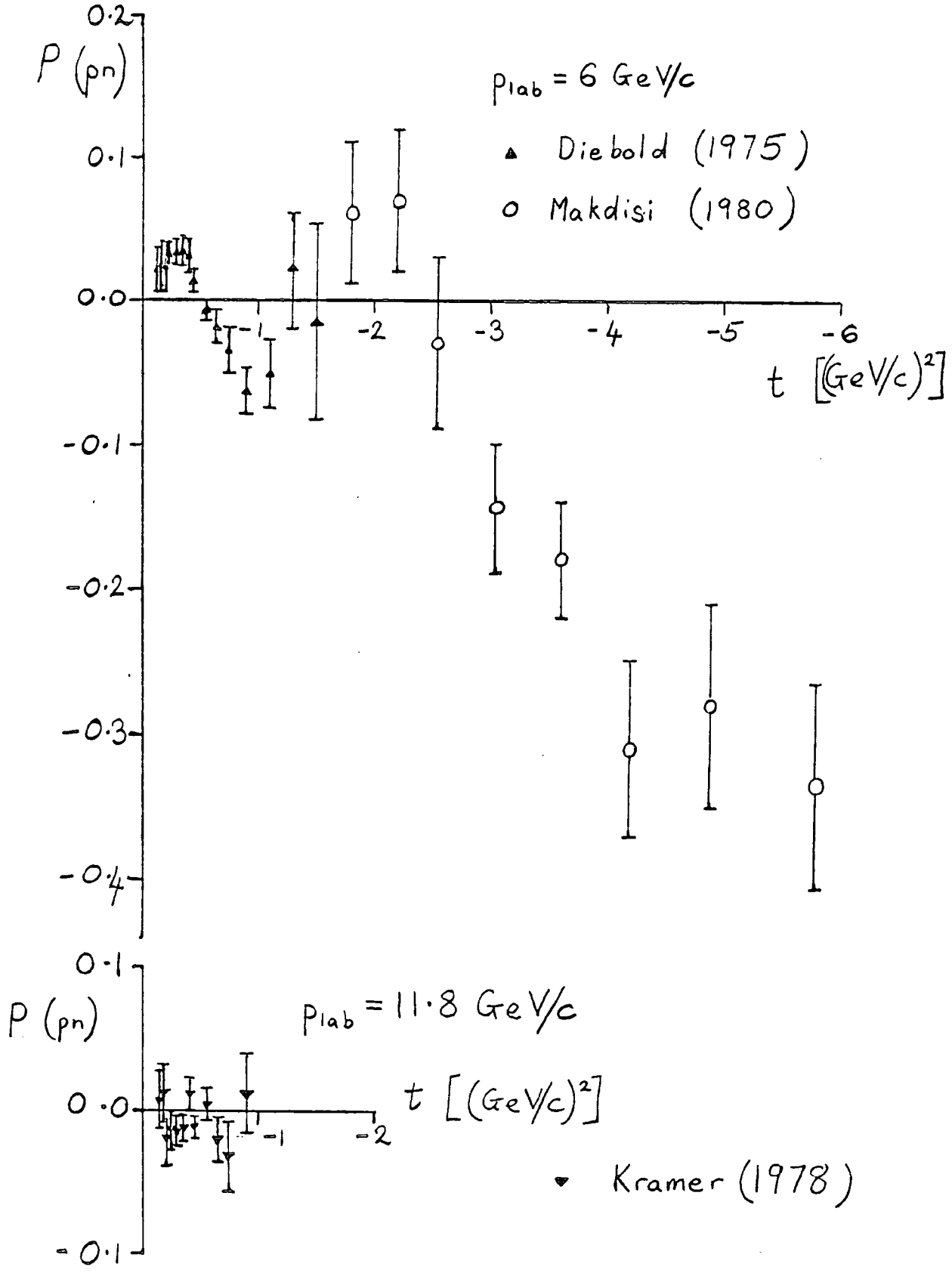

Fig. (4.2.2)

Experimental measurements of P(pn)

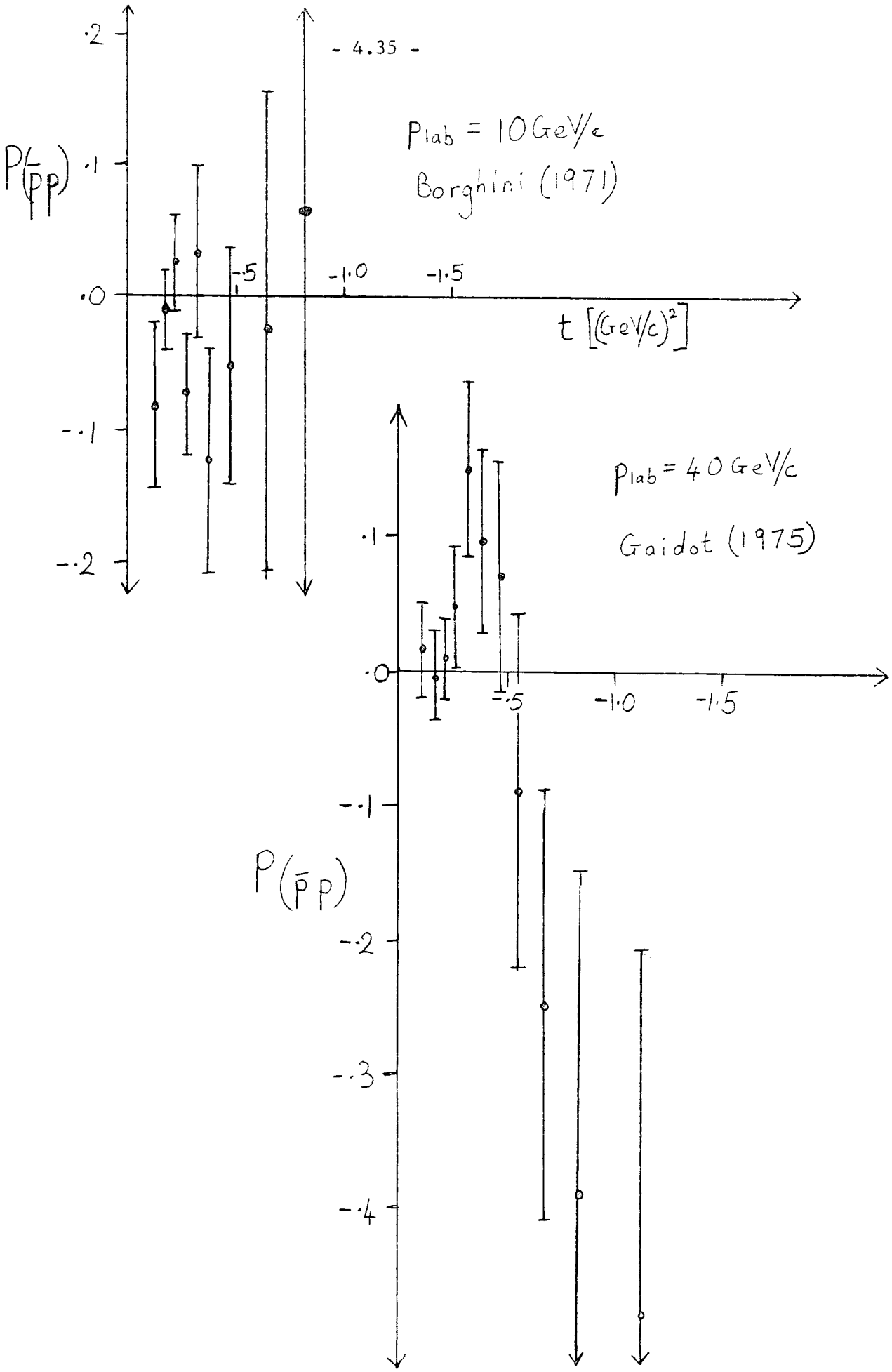

Fig. (4.2.3)

Experimental measurements of $P(\bar{p}p)$

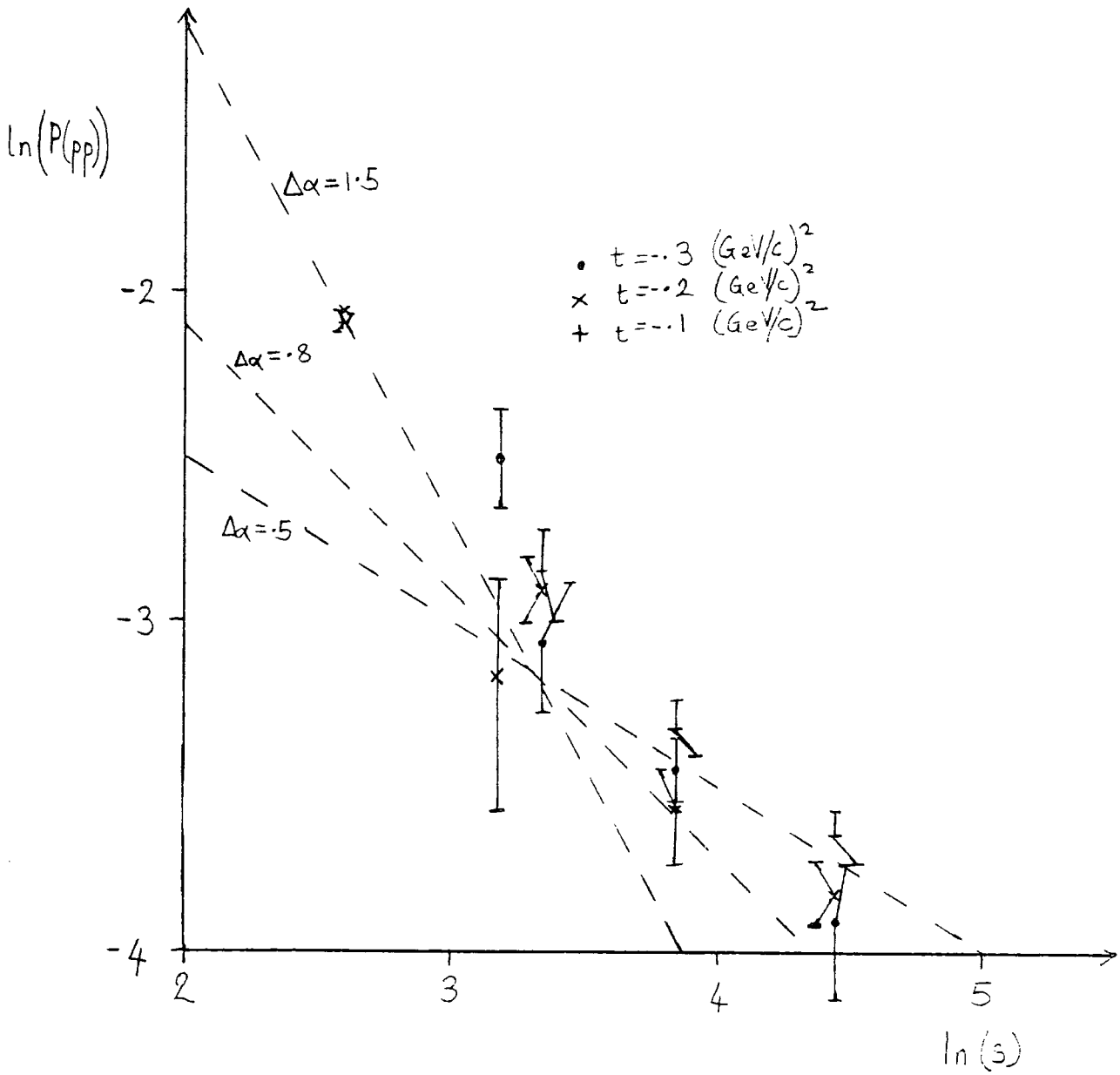

Fig. (4.2.4)

The energy dependence of P(pp) at small -t

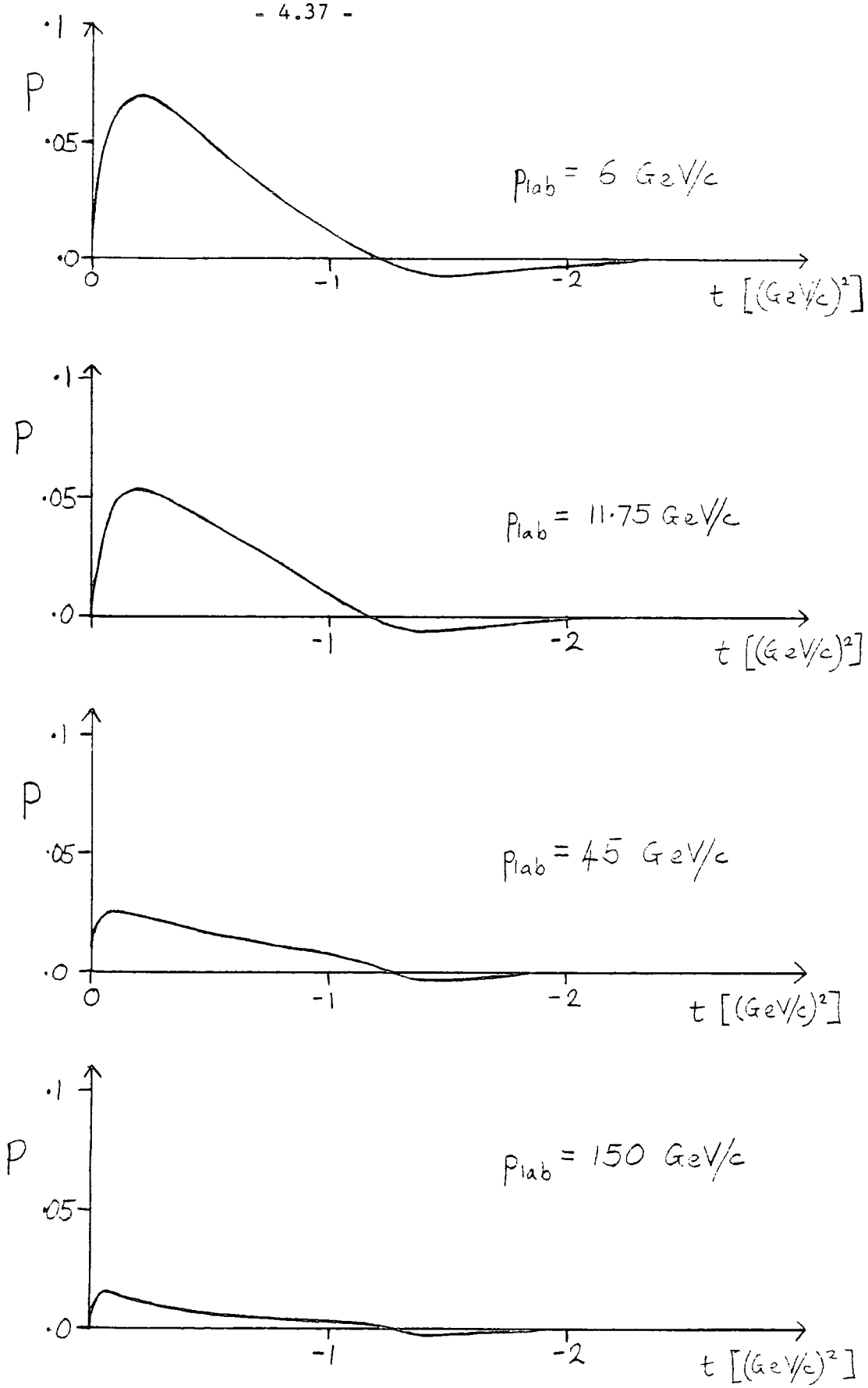

Fig. (4.2.5)

The contribution of the $\rho+A_2$ pair to P(pp)

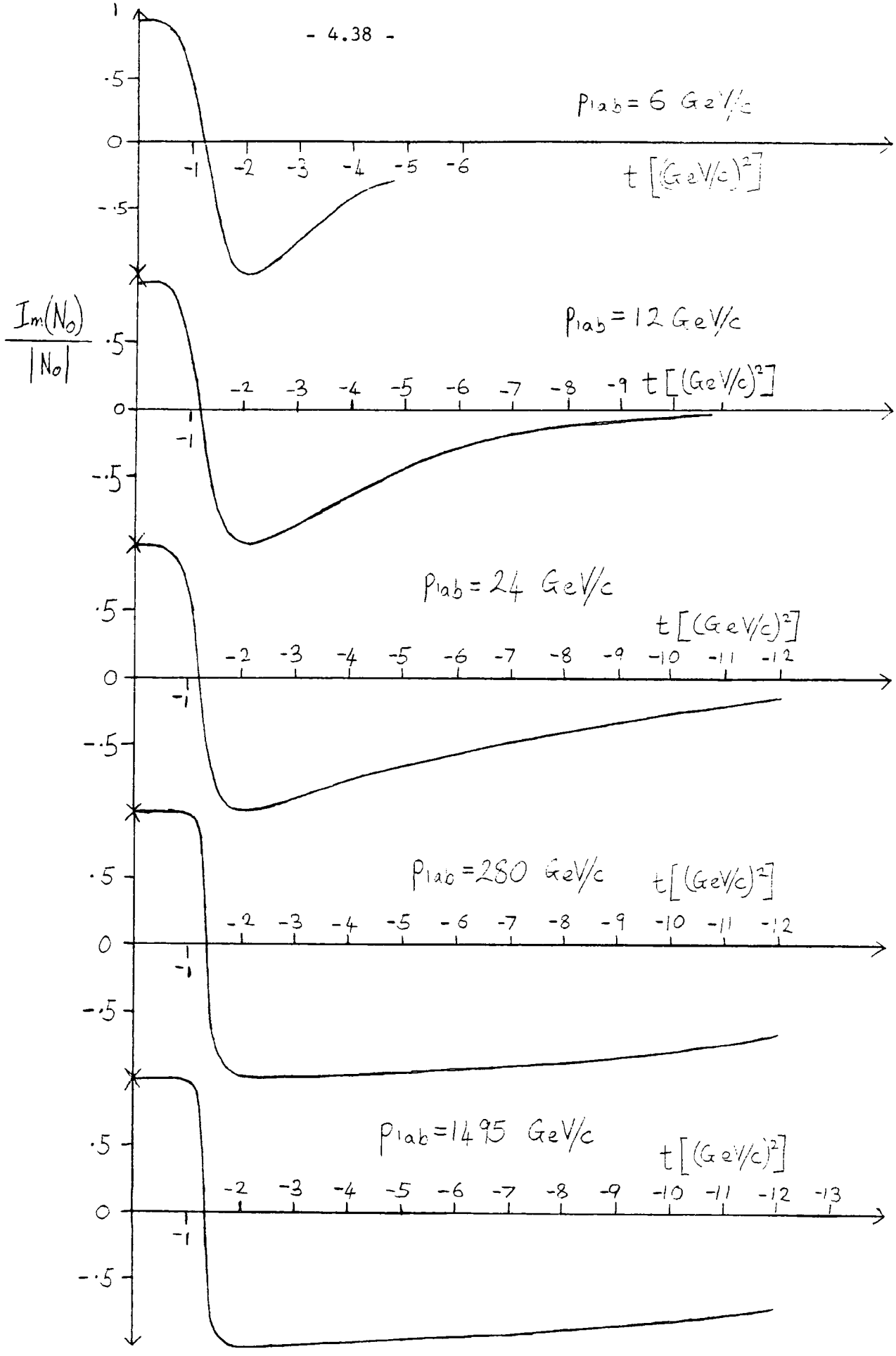

Fig. (4.2.6)a

The ratio of Im (N_0) to $|N_0|$

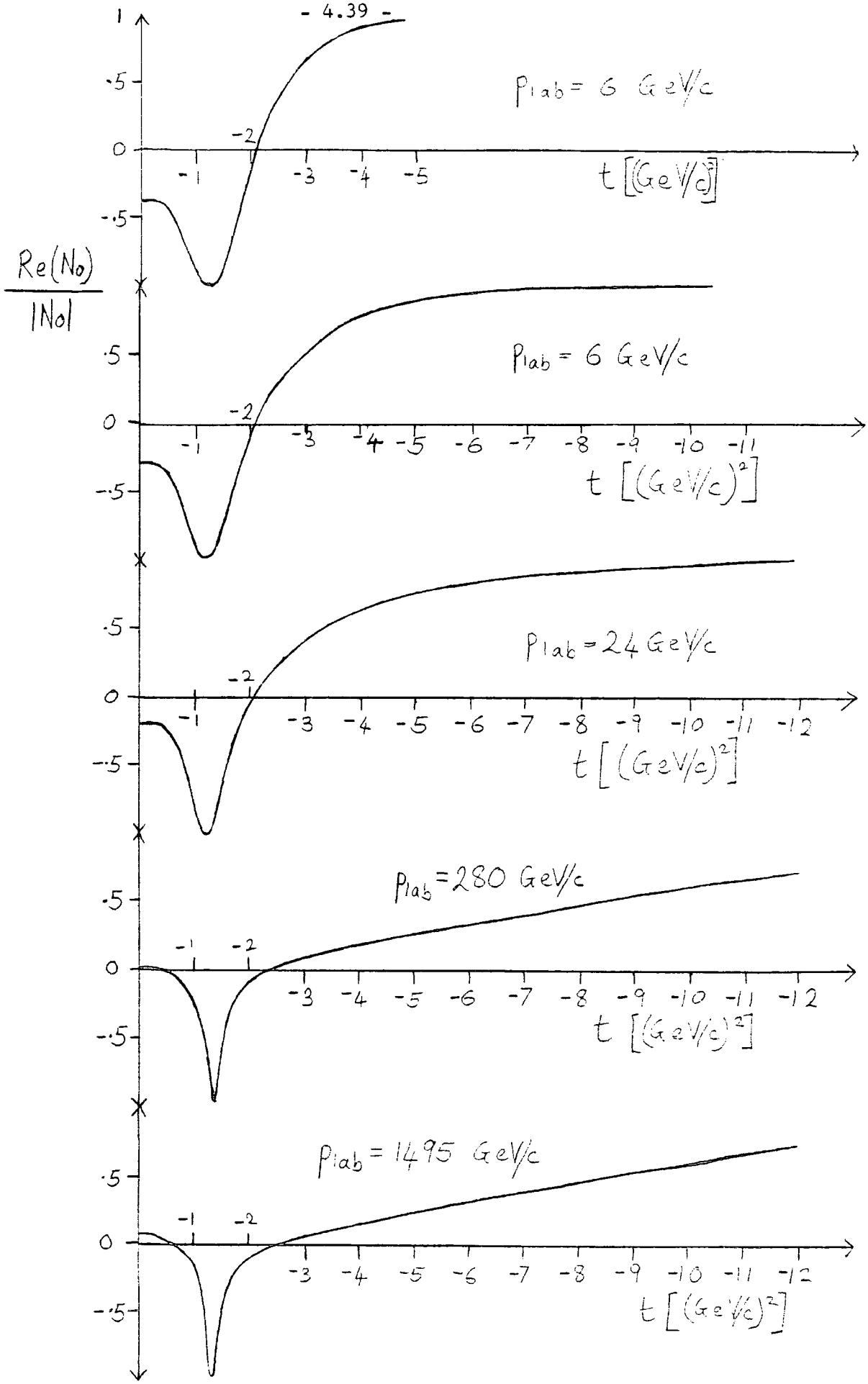

Fig. (4.2.6)b

The ratio of Re (N_0) to $|N_0|$

Fig. (4.2.7)

The contribution of a C = + $R \otimes P$ cut to P(pp)

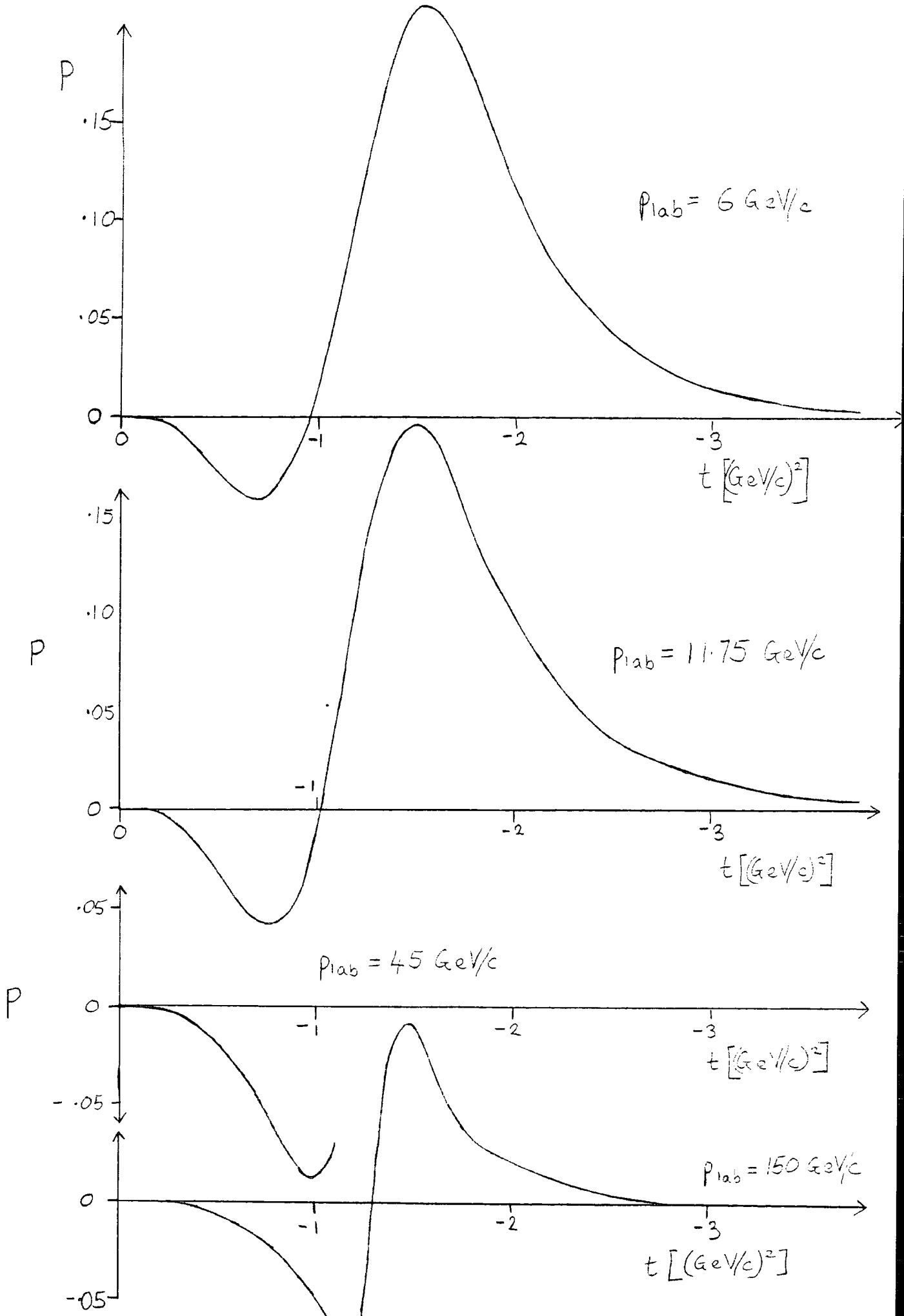

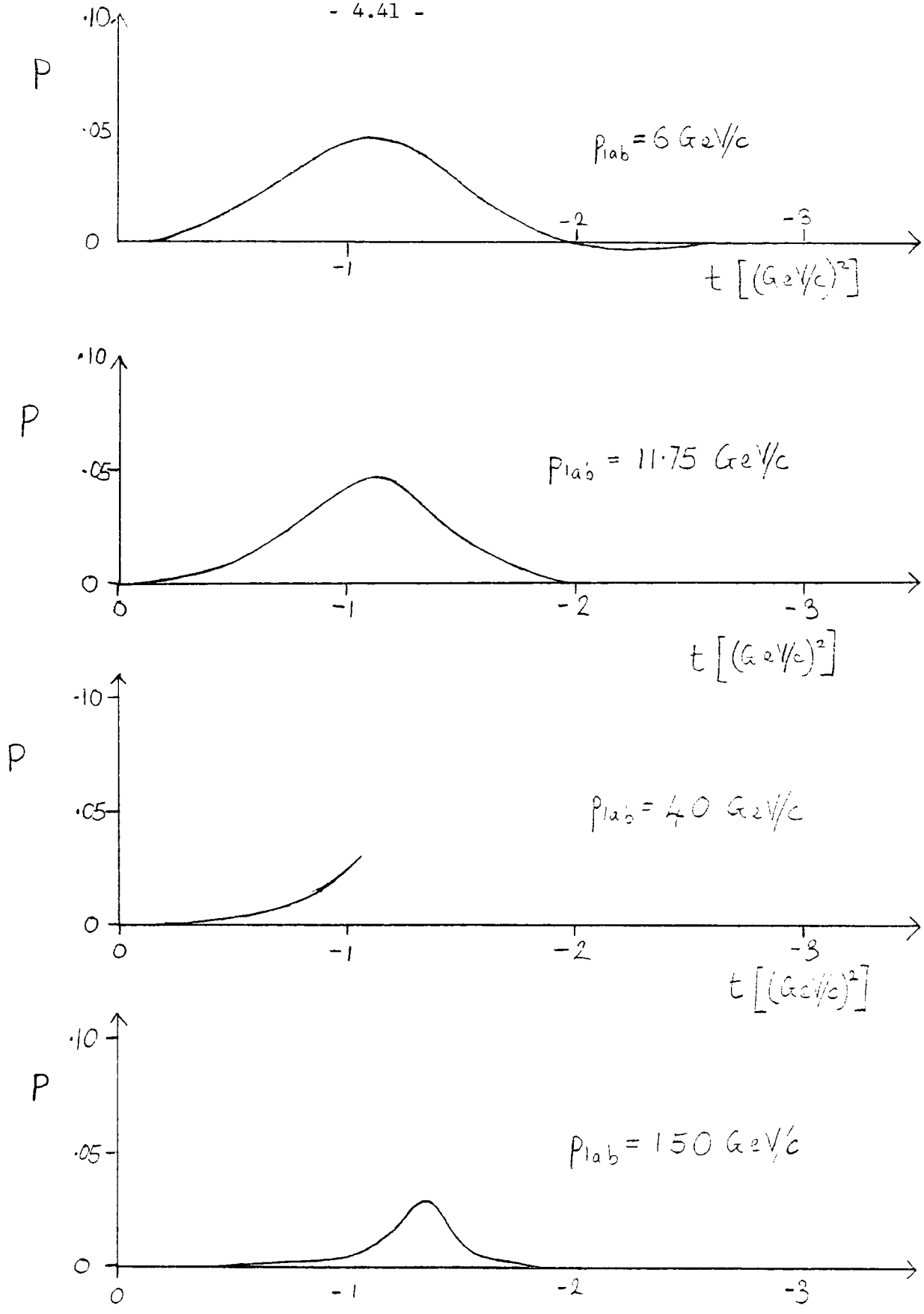

Fig. (4.2.8)

The contribution of a C = - $R \otimes P$ cut to P(pp)

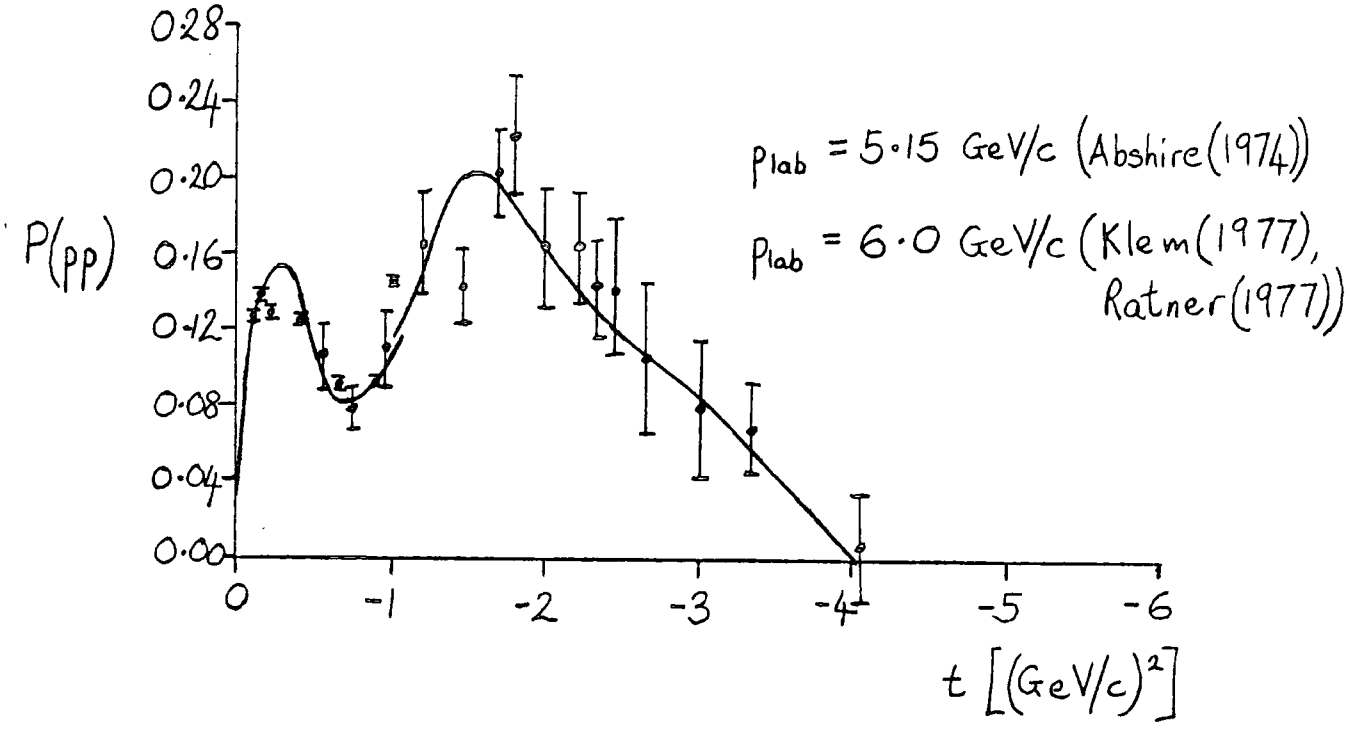

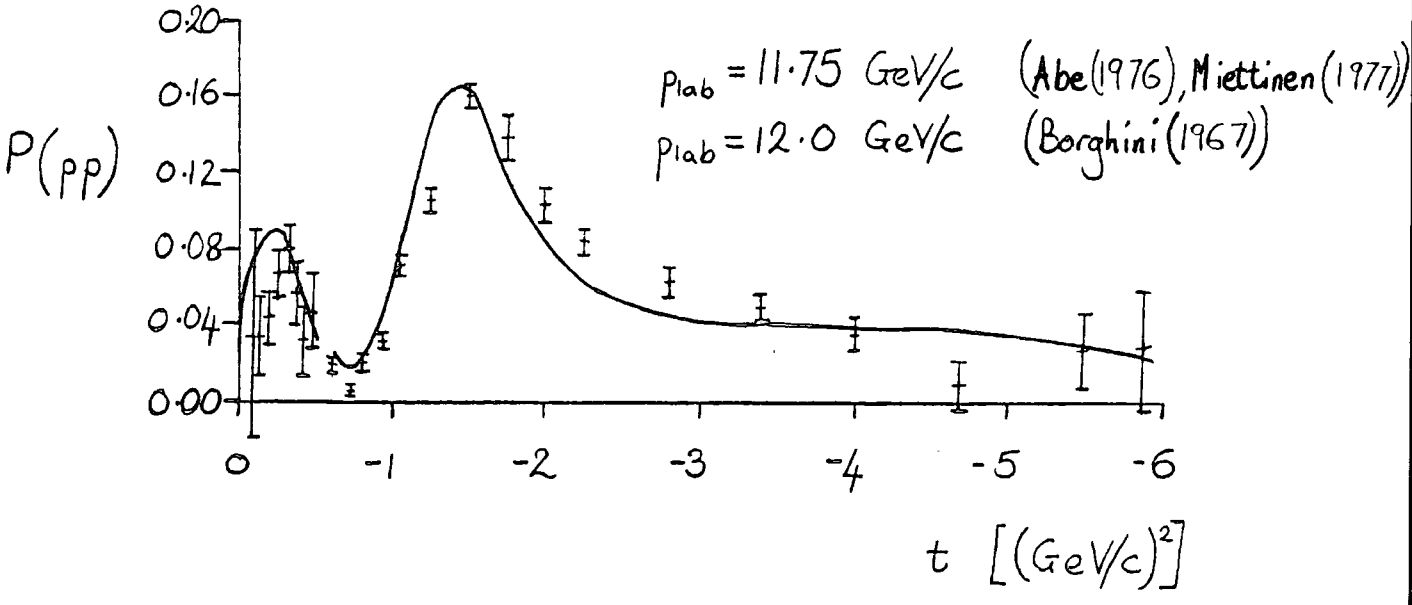

Fig. (4.2.9)

The fit to P(pp)

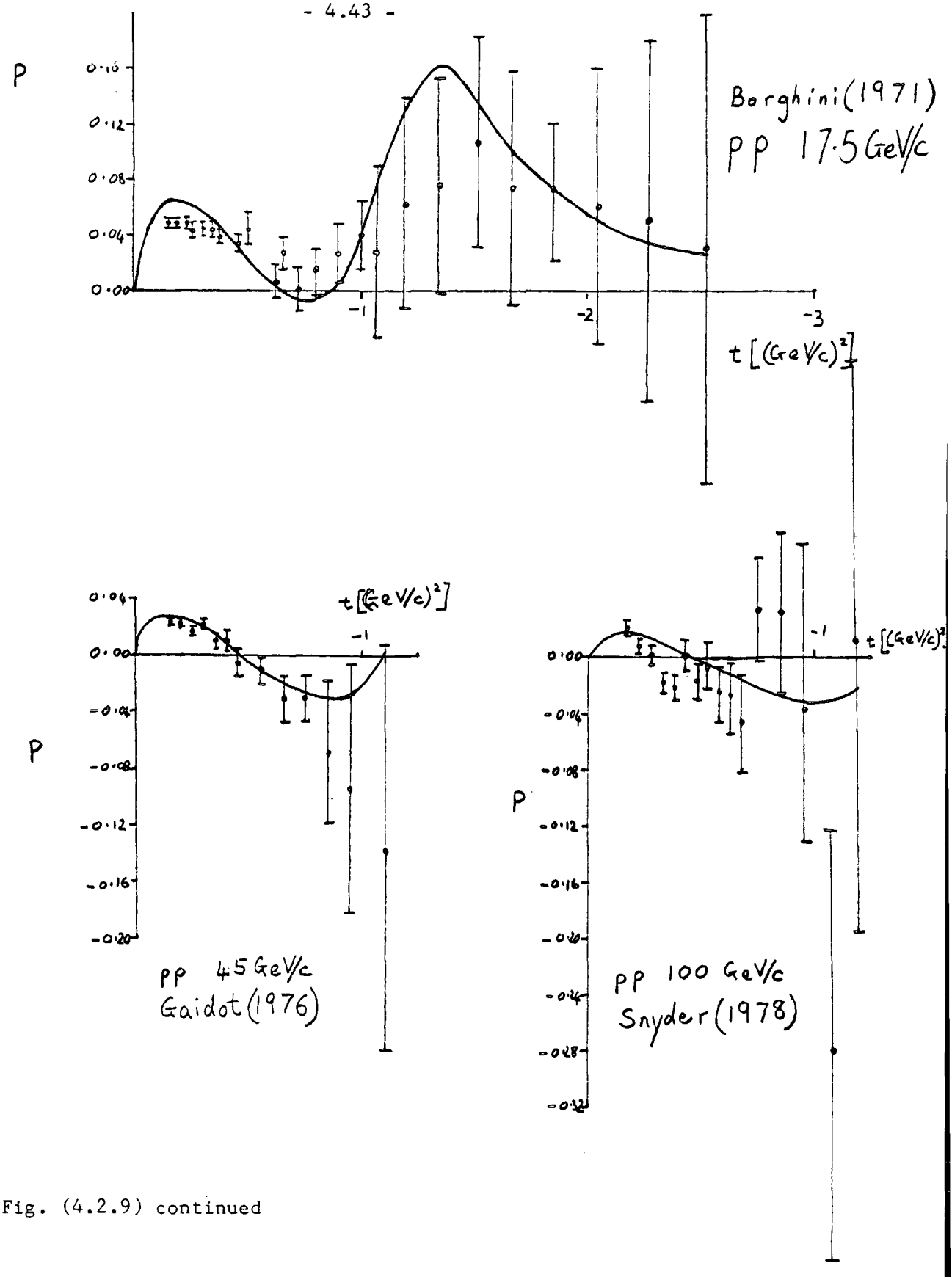

Fig. (4.2.9) continued

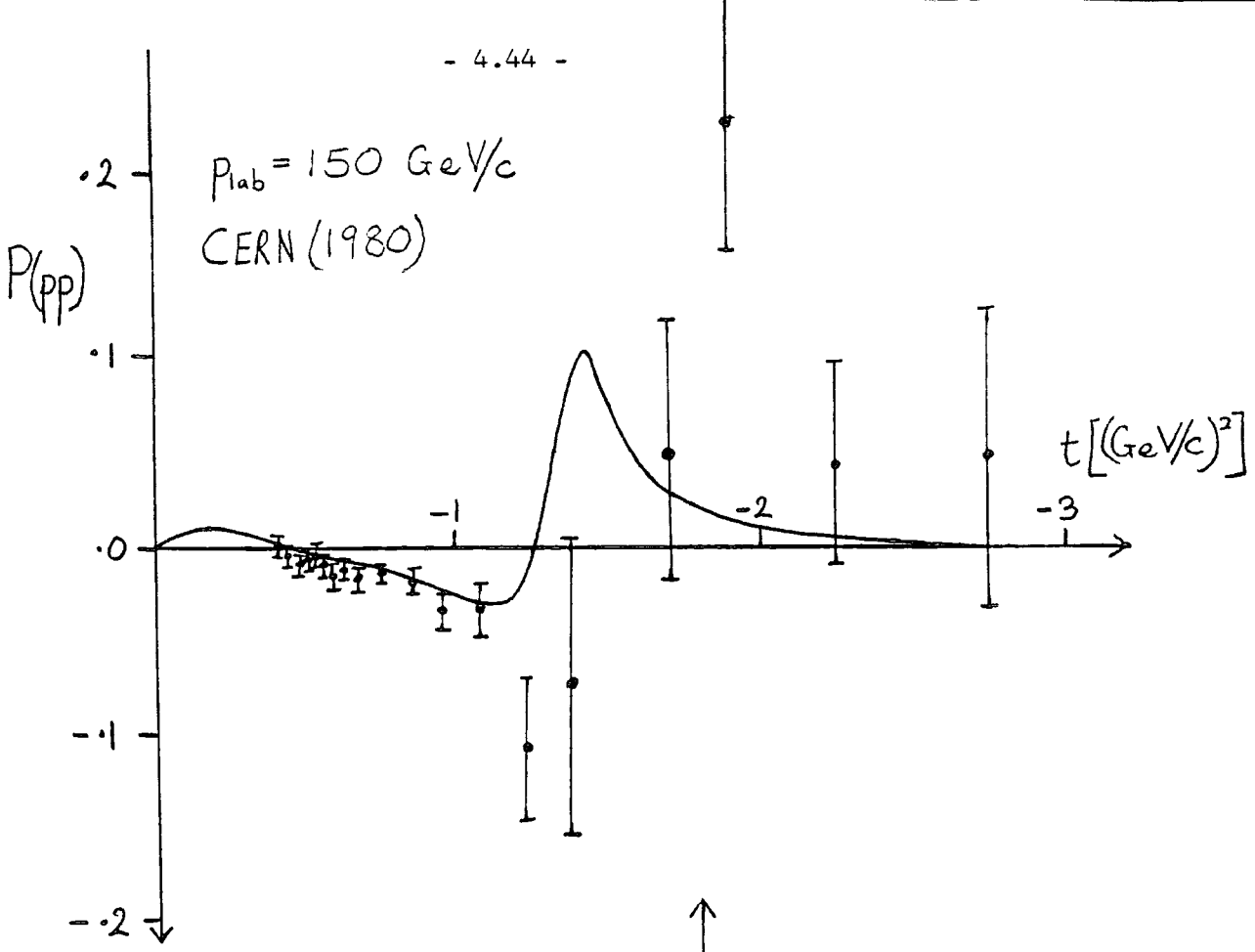

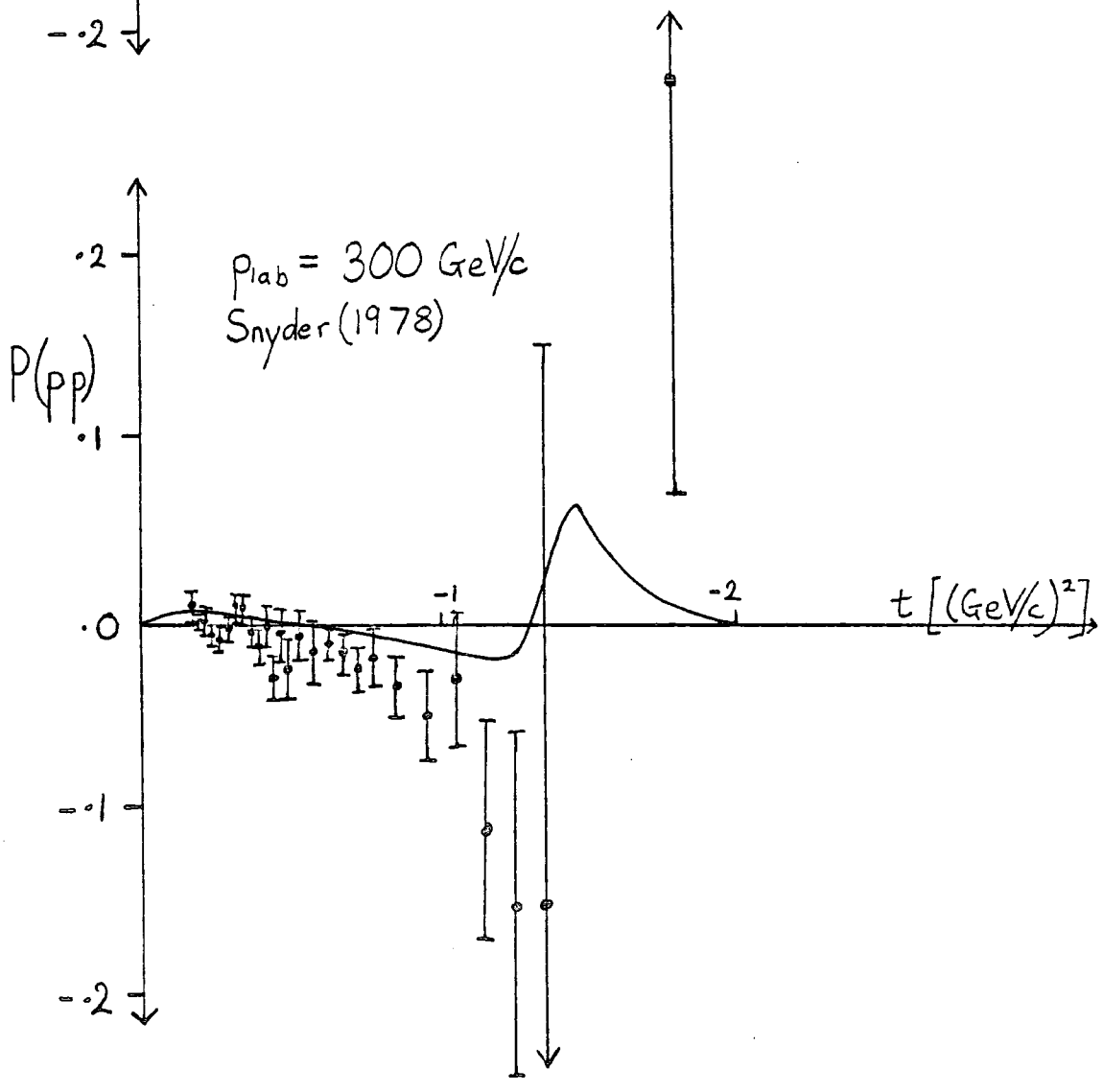

Fig. (4.2.9) continued

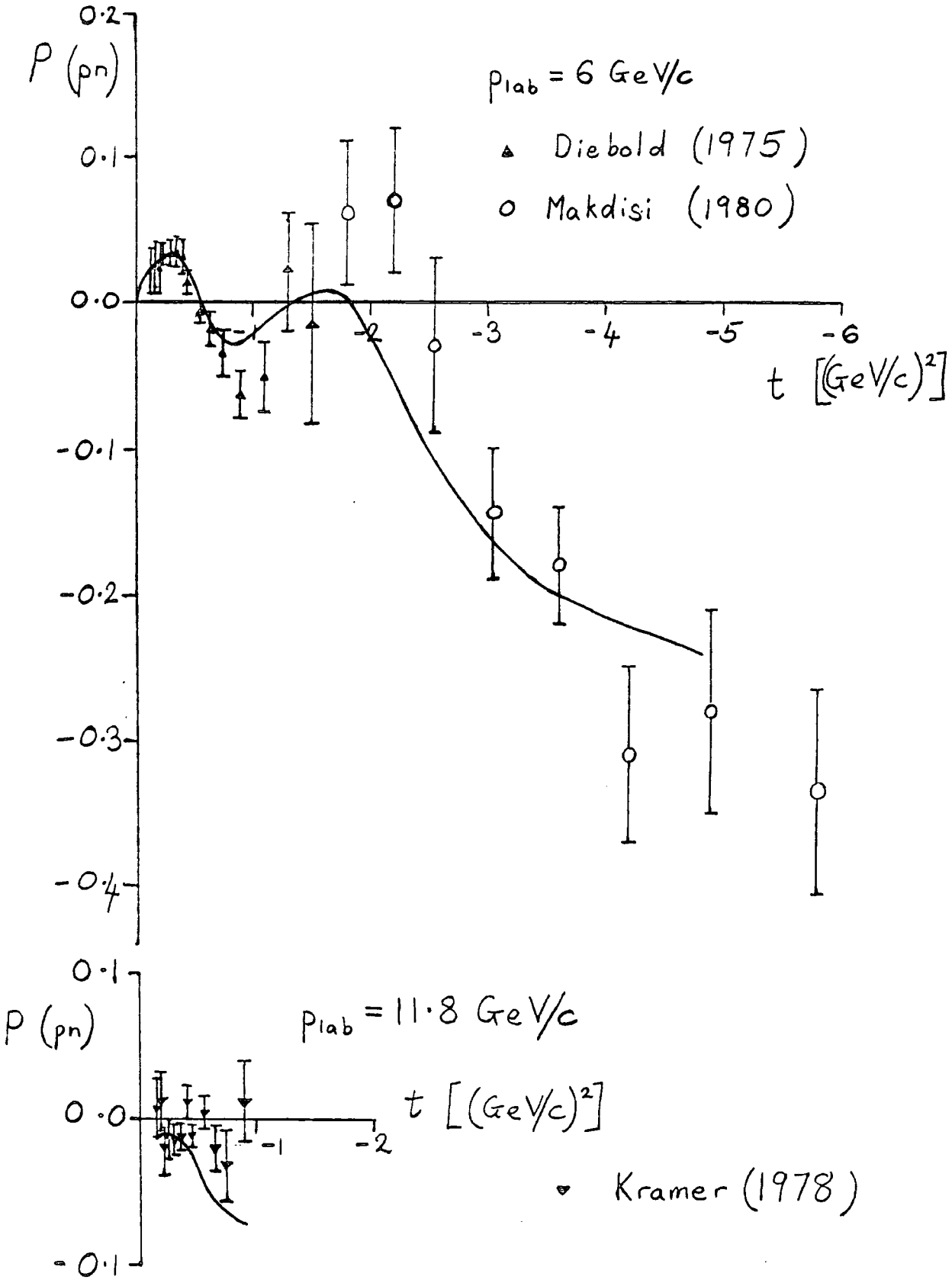

Fig. (4.2.10)

The fit to P(pn)

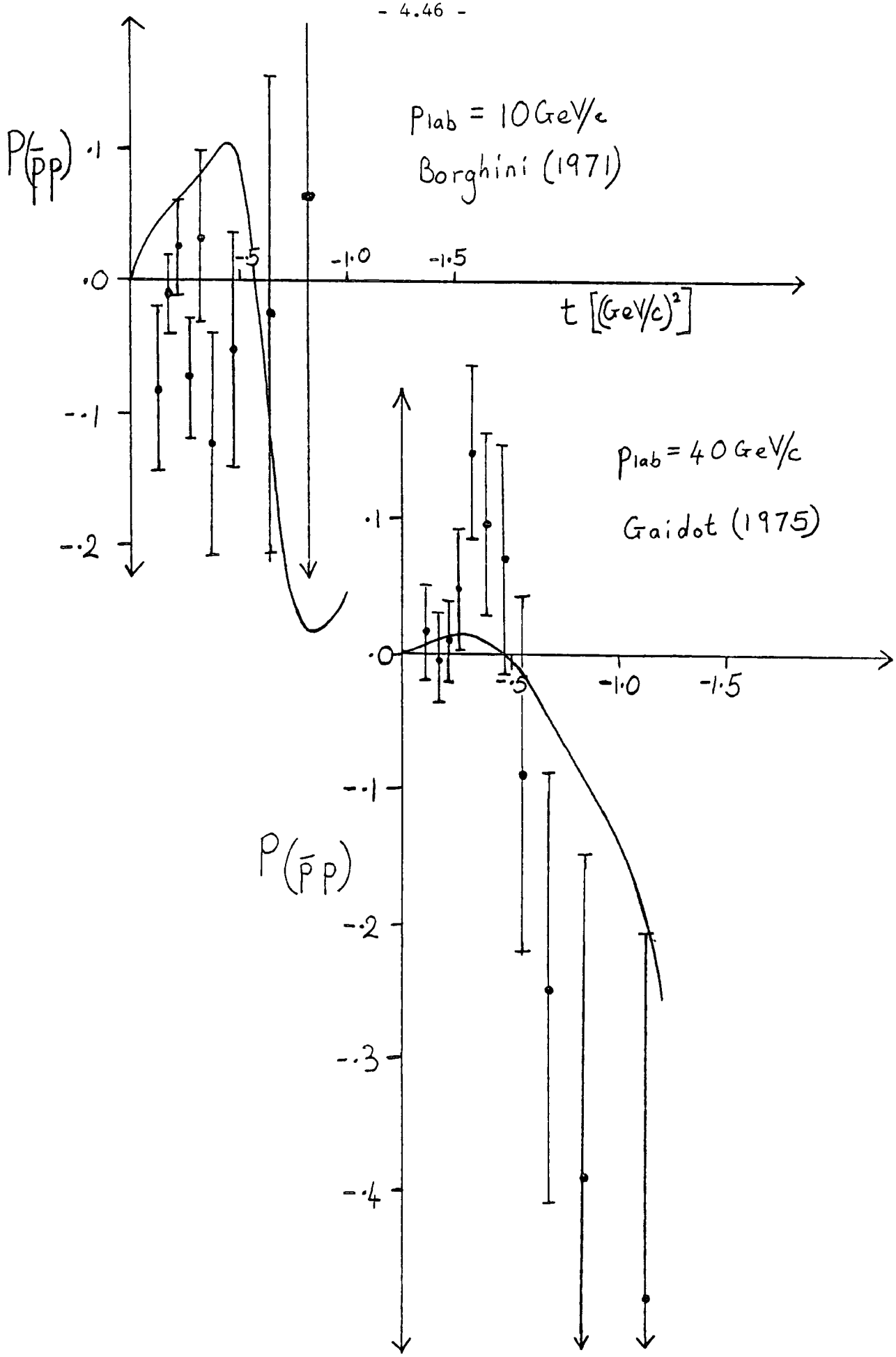

Fig. (4.2.11)

The fit to P($\bar{p}p$)

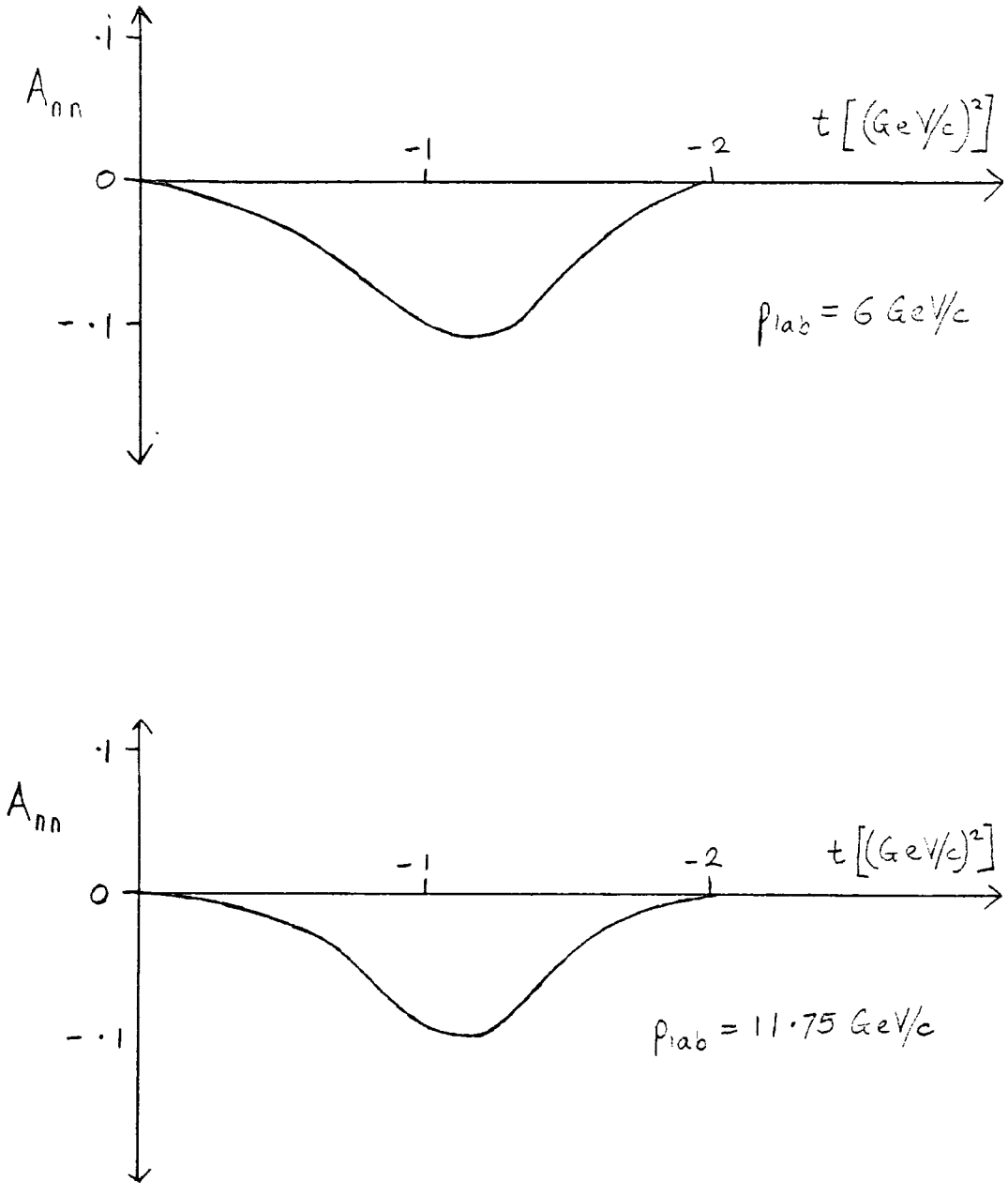

Fig. (4.3.1)

The contribution to $A_{nn}(pp)$ of the "R"-type part of the $\rho+A_2$ term in N_2

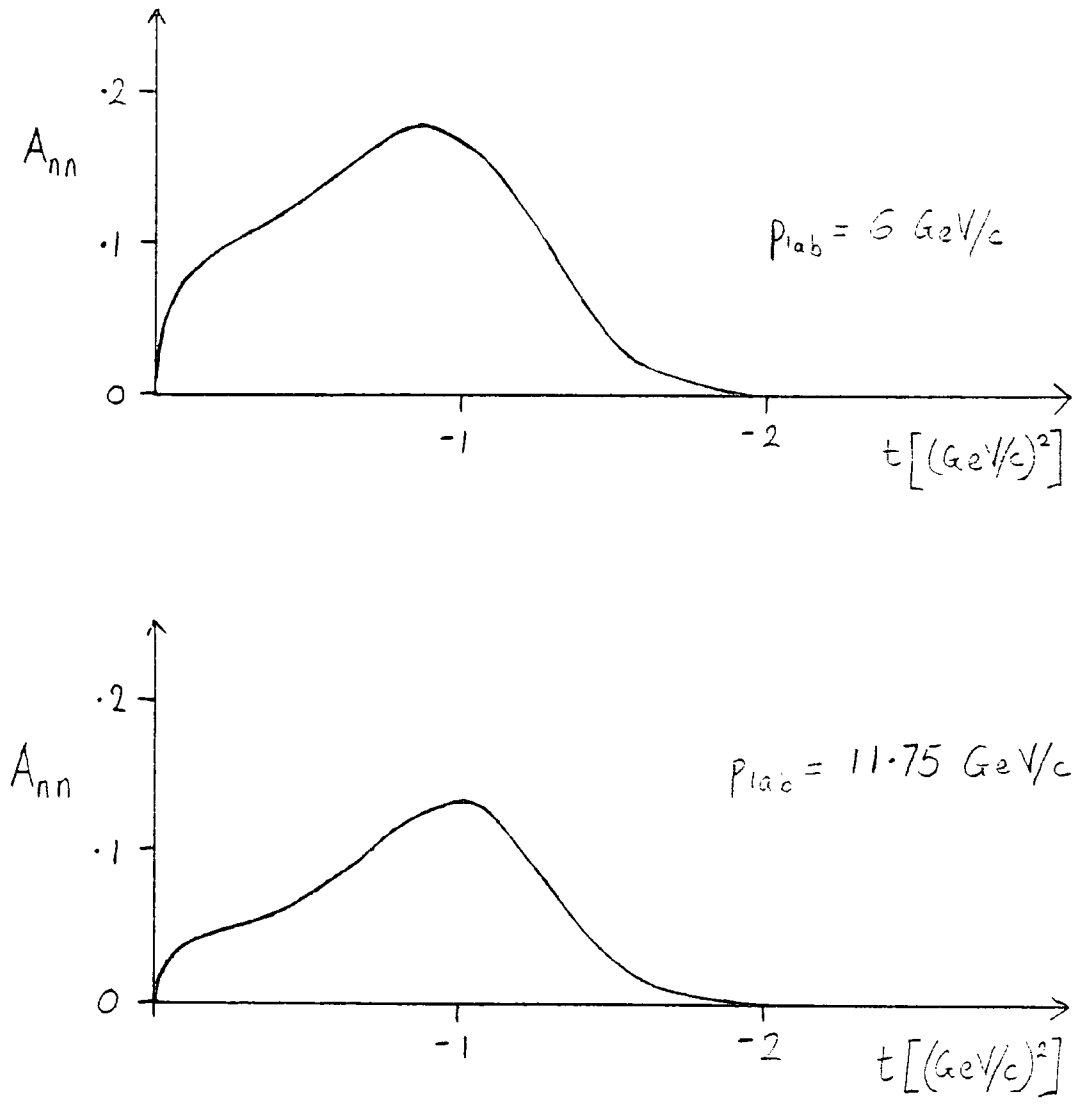

Fig. (4.3.2)

The contribution of A_{nn}(pp) of the absorbed π+B term in N_2

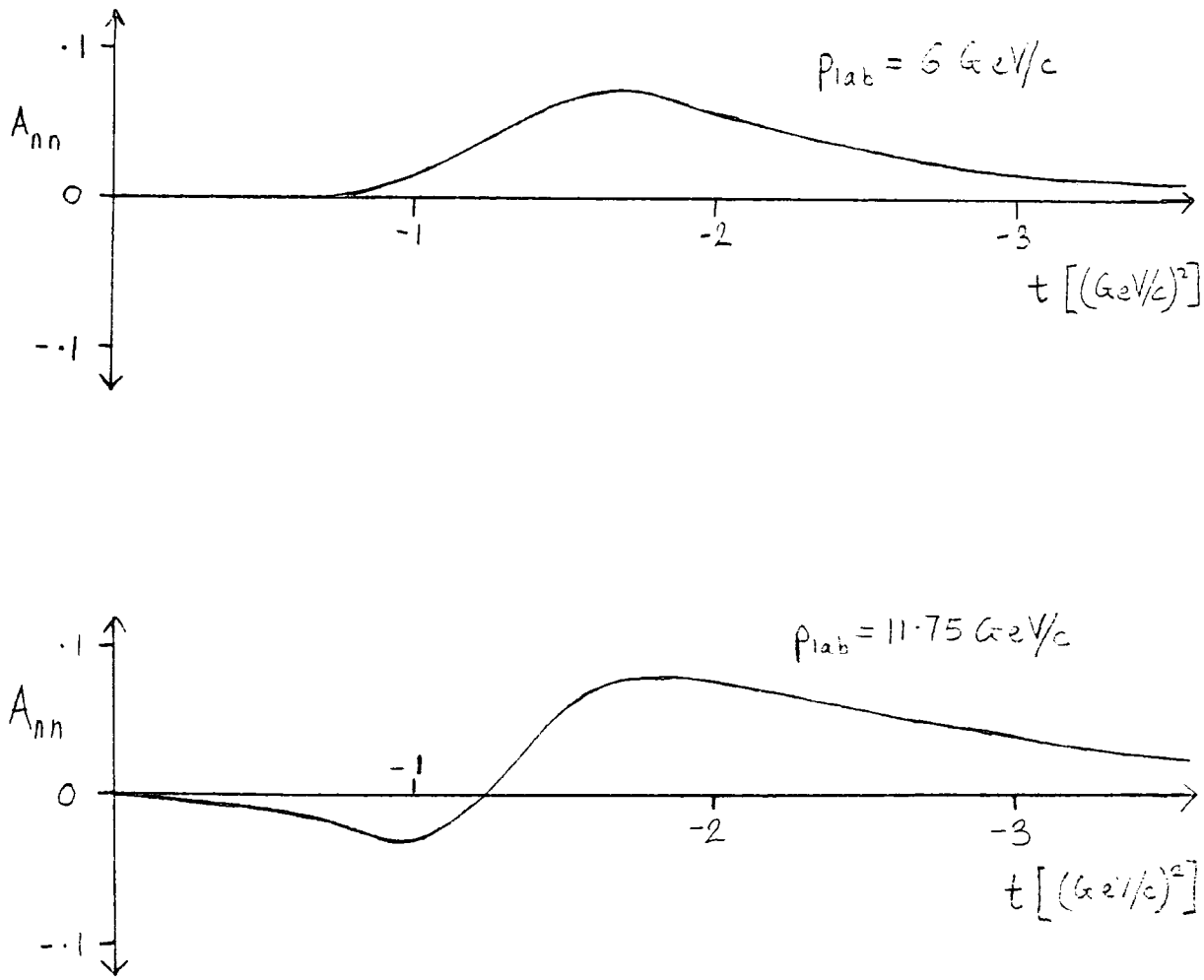

Fig. (4.3.3)

The contribution to $A_{nn}(pp)$ of the $R \otimes P$ cut term in N_2

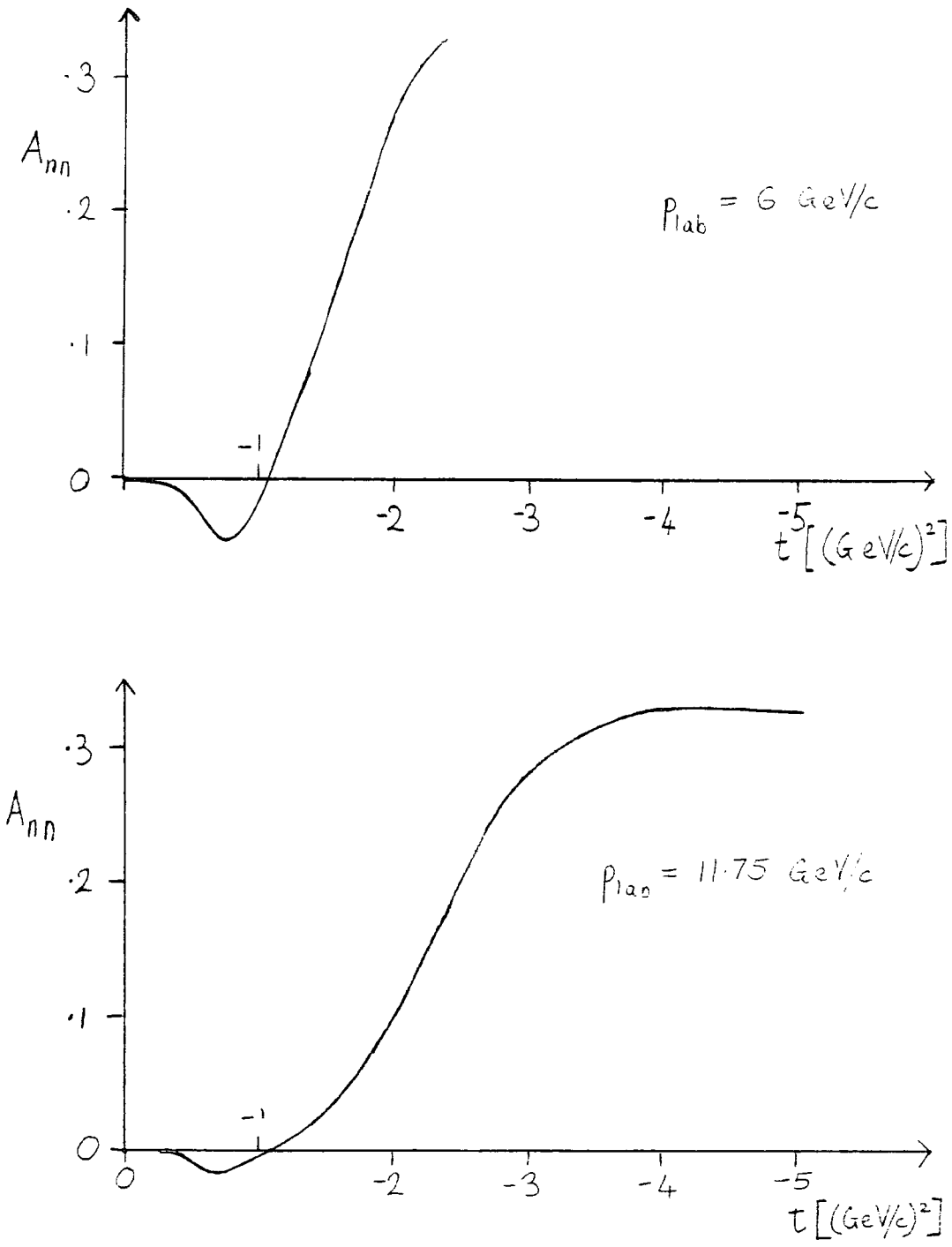

Fig. (4.3.4)

The contribution to $A_{nn}(pp)$ of the "Q"-type Reggeon terms scaled from N_0

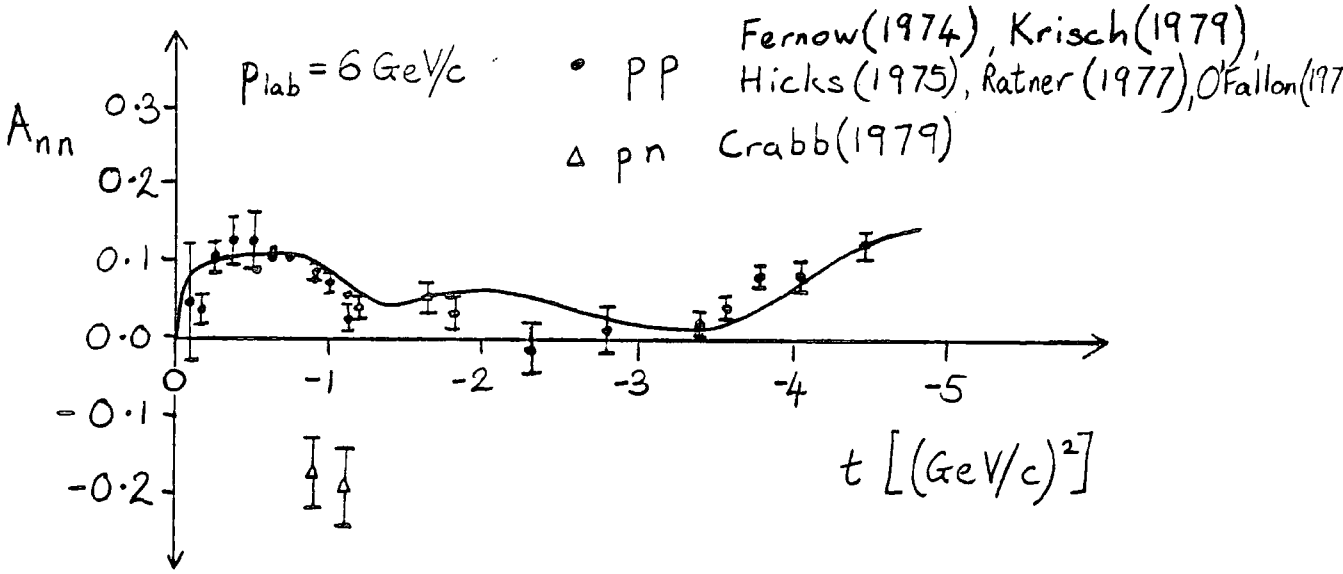

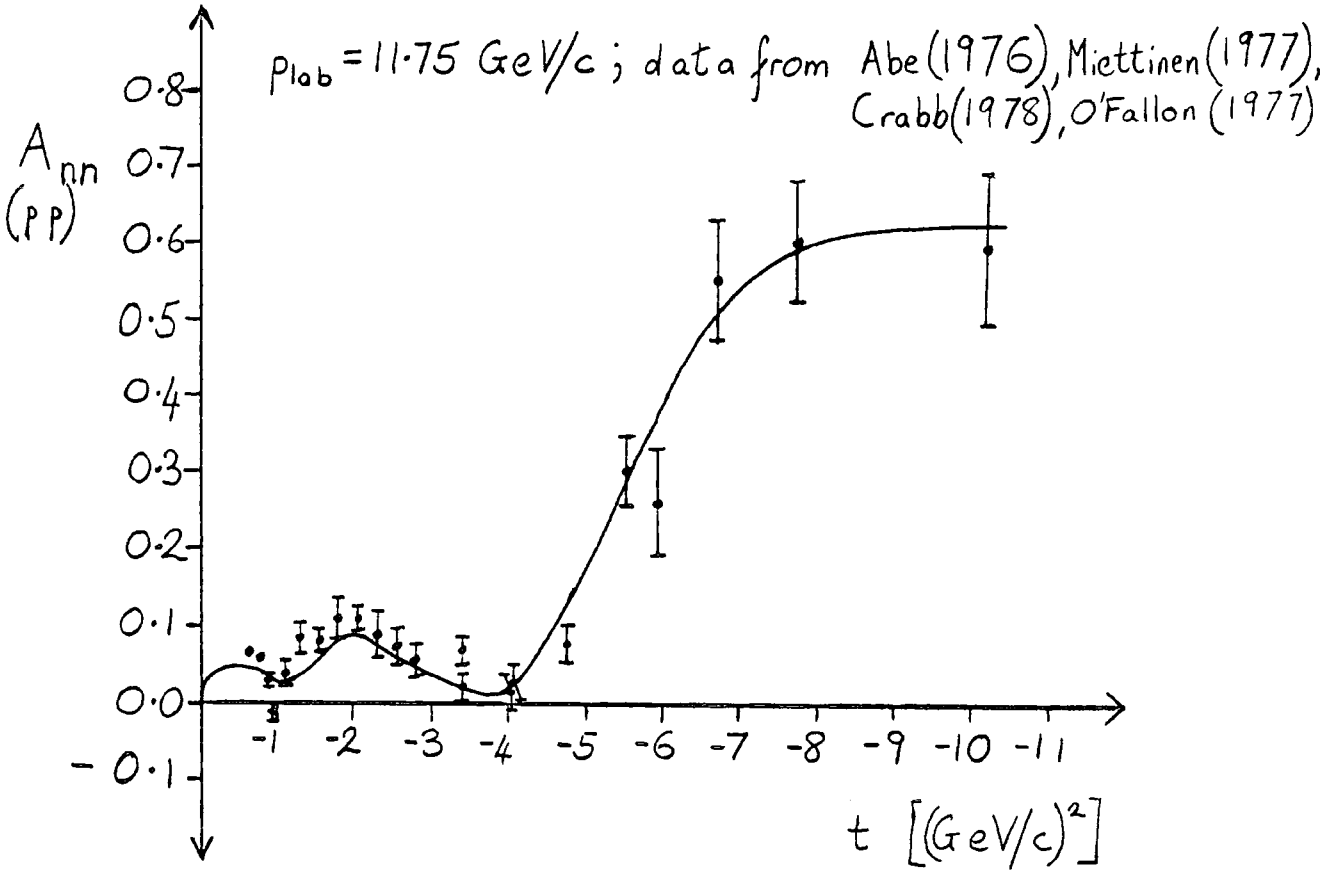

Fig. (4.3.5)

The fit to A_{nn}

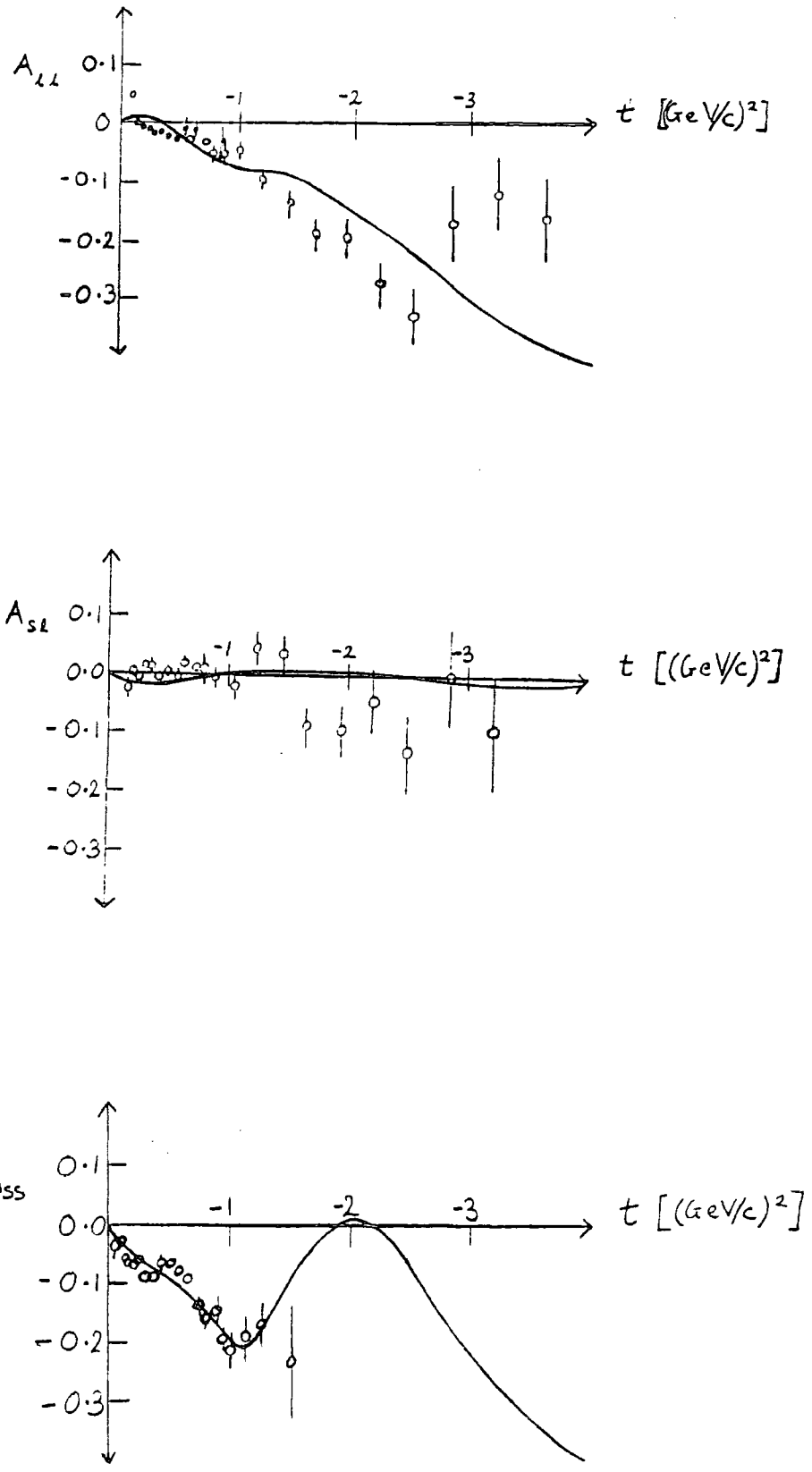

Fig. (4.3.6)

The fits to A_{11}, A_{s1} and A_{ss}

CHAPTER 5

PION-PROTON ELASTIC DIFFERENTIAL CROSS-SECTIONS

5.1 Introduction

In Chapters 3 and 4 a Regge model has been developed that describes all available N-N elastic scattering data for $s \gtrsim 10$ $(GeV/c)^2$. The philosophy behind this model will now be applied to a study of πp scattering to test the conclusions of the previous chapters and in the hope of throwing further light on the underlying reaction mechanisms.

The πp elastic scattering system is potentially simpler to study than the NN system. Quantum number conservation restrictions limit the types of Regge exchange which may occur - e.g. of the leading natural parity meson-Reggeon trajectories f, ω, A_2 and ρ only the f and ρ may be exchanged. A further simplification is that there are only two independent helicity amplitudes (helicity flip and non-flip, both natural parity) compared with the five in NN scattering. It will be assumed here that the total, I = 1 plus I = 0, helicity flip amplitude, $A^{O}_{\frac{1}{2}\ -\frac{1}{2}}$ is everywhere small compared to the total non-flip amplitude, $A^{OO}_{\frac{1}{2}\frac{1}{2}}$. Justification for this may be found in the small magnitude of the polarization data and the QIM prediction of no helicity flip scattering at large angles (see (1.4.34) and (1.4.35). The differential cross-section data will, therefore, be interpreted in terms of a single amplitude - helicity non-flip.

Section 5.2 will describe the available $\frac{d\sigma}{dt}(\pi^{\pm}p)$ data for $p_{lab} \gtrsim 10$ GeV/c and compare these with the unaltered RPCA model and C.I.M. Improved fits to the data for $0 < \theta_{cm} < 90^{O}$ will be developed and presented in Section 5.3. Every attempt will be made to maintain consistency with

a) RPCA at small -t

b) the Quark Interchange model at large angle.

c) the parametrization developed in preceeding chapters to describe N-N scattering.

5.2 An Examination of the Data

A representative selection of $\pi^{\pm}p$ differential cross section data over a wide angular range is shown in Figs. (1.3.3) and (1.3.4). For -t between 0 and 1 $(GeV/c)^2$, $d\sigma/dt$ falls rapidly in a similar way to that for pp and pn in the same t range. This kinematic region is accounted for reasonably well by the basic RPCA model (see Fig. (1.5.1)), but for $-t \gtrsim 1$ $(GeV/c)^2$ a large discrepancy develops. There is a change in slope of the $d\sigma/dt$ at $t \simeq -0.9$ $(GeV/c)^2$. This new slope prevails until $t \simeq -3$ $(GeV/c)^2$, and in this region there is no discernible difference between $d\sigma/dt$ (π^+p) and $d\sigma/dt$ (π^-p).

Fig. (5.2.1) shows the variation with s of the data at -2.0 $(GeV/c)^2$. It is clear from the non-linear nature of this log-log plot that at least two Regge-trajectories are being exchanged. The small variation with energy of $d\sigma/dt$ for p_{lab} between 50 GeV/c and 200 GeV/c shows that one of the trajectories must be the Pomeron. Identification of the other contributing term or terms is less easy. The likely candidates are

a: ρ-pole

b: f-pole

c: $R \otimes P$ cut.

Of these, a and b are already known to be exchanged at small -t, while c was discovered to be important in N-N scattering for $-t > 1$ $(GeV/c)^2$ below about $p_{lab} = 100$ GeV/c. (ie. in just the kinematic region where an extra term is now needed in πp scattering).

In order to narrow down the range of possibilities, the following investigation was performed: The scattering amplitude was assumed to be composed of two pole contributions, one of them being due to Pomeron exchange. Thus dσ/dt could be written (for a given value of t) as

$$\frac{d\sigma}{dt} = \frac{f}{s^2} \left| s^{\alpha_p} + g\, i^{(1-C_x)/2}\, e^{-i\frac{\pi}{2}(\alpha_x-\alpha_p)}\, s^{\alpha_x} \right|^2 \qquad (5.2.1)$$

where C_x is the charge conjugation of exchange X, and f and g are real constants. Curves were then obtained for the three options, $\alpha_x = \alpha_\rho$, α_f, α_{RxP} at $t = -2.0$ $(GeV/c)^2$, with f and g chosen independently each time so as to agree with the data at $p_{lab} = 200$ GeV/c and 10 GeV/c*. Note that there are two possible solutions for f and g which satisfy these conditions ($g > 0$ and $g < 0$), thus 6 sets of calculations were carried out. The results are shown in Fig. (5.2.1).

Clearly, the ρ (I = 1) can be immediately eliminated since its phase relative to the Pomeron is such that it would produce a substantial difference between $d\sigma/dt$ (π^+p) and $d\sigma/dt$ (π^-p) in the energy range where both contributions were of comparable magnitude.

* $C_{RxP} = +$ was assumed because of the similarity of the $\pi^\pm p$ data.

It is more difficult to discriminate between the other two candidates, however. The phases of the f and $R \otimes P$ contributions are such that, although their energy dependences are different, in combination with the Pomeron they produce similar results for $d\sigma/dt$. This last statement does not apply, of course, to the case where the f and Pomeron interfere desctructively. The best agreement with the data in the middle energy range is achieved by the curve produced by $R \otimes P$ and the Pomeron with slight destructive interference.

Although the above evidence is inconclusive and the precise shape of curves such as shown in Fig. (5.2.3) depends strongly on the relative phases of the contributions, there are two reasons why the $R \otimes P$ option is preferred to the f:

1. The sign of its couplings at small -t means that unless the residue of the f exchange contains a zero for $0 < -t < 1$ $(GeV/c)^2$, the f and P contributions actually interfere destructively in the t region being considered. No evidence for such a zero was seen in the preceding study of N-N interactions.

2. The ideas of duality require that the total Reggeon-exchange contributions to the scattering amplitudes of processes such as pp→pp with exotic s channels must be real. In the belief that this concept is, to a good approximation, valid, the Reggeon terms in the model have been constructed in exchange degenerate pairs (modulo absorptive corrections and small differences in trajectory). The f and ω exchanges form such a pair. Now the f term is purely imaginary and the ω term purely real when their common trajectory passes through an odd integer. Thus for the combination to be real in pp, the f residue must contain a zero at these points. While there is no such constraint applying to πp scattering factorization requires that

$$A(pp\to pp;f) = \frac{A(\pi p\to\pi p;f)\ A(\pi p\to\pi p;f)}{A(\pi\pi\to\pi\pi;f)} \qquad (5.2.2)$$

and hence the zeroes are present in $A(\pi p\to\pi p;f)$ and $A(\pi\pi\to\pi\pi;f)$ unless a pole occurs in $A(\pi\pi\to\pi\pi;f)$. Now for $-t \gtrsim -2(\text{GeV/c})^2$ α_f is close to -1 [see Fig. (3.4.1)] and thus close to a zero in the residue. It thus seems unlikely that the f contribution can be large in this region unless either the parametrization of $\alpha_f(t)$ is inaccurate, or the assumption of exchange degeneracy or factorization of the Reggeons is invalid.

A further change in the behaviour of the data is observed at $-t = 3\text{-}4\ (\text{GeV/c})^2$. At larger -t values than this the slope of $d\sigma/dt$ is smaller. At low energies ($p_{lab} = 10$ GeV/c and below) the transition is marked by a sharp dip. A similar structure is also visible in the recent 200 GeV/c measurements, though at $t = -4\ (\text{GeV/c})^2$.

In the light of what has been said in the previous chapters it is logical to attempt to interpret the large angle region in terms of quark interchange scattering, or in Regge language exchange of meson-Reggeon trajectories which approach negative integers as $t\to-\infty$. The leading trajectories of this type which contribute to π-p scattering are the ρ and the f, which tend to -1. Now since the f has even charge conjugation, and hence its contribution is imaginary when $\alpha = -1$, by argument 2 above it must have a zero in its residue at this value of the trajectory. Thus at large -t and large angle, the most important contribution is expected to be from exchange of the $I = 1$ ρ.

Now the Dimensional Counting Rule (1.2.7) predicts that the large angle meson-baryon differential cross-section behaves like

$$\frac{d\sigma}{dt}(MB) \sim \frac{1}{s^8} F^2\left(\frac{t}{s}\right) \qquad (5.2.3)$$

and hence the corresponding scattering amplitude,

$$A(MB) \sim \frac{1}{s^3} F\left(\frac{t}{s}\right) \qquad (5.2.4)$$

To agree with this prediction, the ρ residue must vary as $(-t)^{-2}$ as $t \to \infty$, so that

$$A(MB;\rho) \sim \frac{1}{st^2} \quad \text{as } t \to -\infty \qquad (5.2.5)$$

Fig. (5.2.2) shows this behaviour to be in reasonable agreement with the data.

A further term is needed, however, to explain the behaviour of the data in the region of the interference at $-t = 3\text{-}4\ (GeV/c)^2$. This term must:

(a) possess a similar phase, but opposite sign to the $R \otimes P$ term which dominates $-t \lesssim 3\ (GeV/c)^2$ in order to produce the interference observed in the data.

(b) have $I = 0$, since there is no consistent difference between the measurement of $\frac{d\sigma}{dt}(\pi^{\pm} p)$.

(c) have a similar energy dependence to the amplitude at lower $-t$ as the position of the interference changes little with energy.

(d) fall off more quickly with energy at constant $\frac{t}{s}$ than does the large angle ρ term, to preserve the agreement with the D.C.R.

Points (a) and (b) rule out the possibility of a modification to the ρ being the extra term. Both the f pole and I = 0 $R \otimes P$ (ie. $f \otimes P$) cut satisfy the first three requirements (the fourth merely restricts their t dependence properties) . Furthermore, the f and also the $f \otimes P$ (provided that the phase of this contribution is close to that given by its trajectory) are out of phase with the ρ at large -t, when all three trajectories are close to -1. This means that despite the I = 1 nature of the ρ no difference between $\frac{d\sigma}{dt}$ $(\pi^{\pm}p)$ would be expected where the contributions of the ρ and the extra term are of comparable magnitude (see point (b) above).

The lack of precision of the data and the proximity of the f and $R \otimes P$ trajectories at large -t mean that the two candidates cannot be discriminated on grounds of energy dependence. However, since by argument 2. from the preceding discussion, the f term is expected to be small when $\alpha_\rho(t) \simeq -1$, (and also to ease the parametrization) the extra term will be written as part of the $f \otimes P$ cut.

The recent p_{lab} = 200 GeV/c $\pi^- p$ data indicates that a term with a higher lying trajectory becomes important at high energy for $-t \gtrsim 4$ $(GeV/c)^2$. Such a term is needed to explain the similarity in magnitude of the large -t measurements at 50 and 200 GeV/c. It is very likely that this term is a $P \otimes P$ cut. This conclusion is consistent with argument (c) above since at high energies the Pomeron, (whose energy dependence is similar to that of the $P \otimes P$ cut) dominates the scattering amplitudes at smaller $|t|$ values. It is interesting to notice the similarities between this interference minimum at $t \simeq -4$ $(GeV/c)^2$ in $\frac{d\sigma}{dt}$ $(\pi^- p)$ and those at $t \simeq -1.4$ $(GeV/c)^2$ and high energies in $\frac{d\sigma}{dt}$ (pp) and $\frac{d\sigma}{dt}$ $(\bar{p}p)$ which are also believed to be due to interference between the Pomeron and the $P \otimes P$ cut.

5.3 The Fit to the Differential Cross-Section

The examination of the available $\frac{d\sigma}{dt}(\pi^{\pm}p)$ data in the preceding section identified three regions of behaviour. These are

(1) $0 \lesssim -t \lesssim 1$ $(GeV/c)^2$ where the experimental results can be explained in terms of conventional (linear trajectory) P, f and ρ exchanges.

(2) $1 \lesssim -t \lesssim 3.5$ $(GeV/c)^2$ where an extra term, tentatively identified as an $f \otimes P$ cut, is required.

and (3) $-t \gtrsim 3.5$ $(GeV/c)^2$ where the Dimensional Counting Rule is obeyed (modulo some pre-asymptotic modifications). A $P \otimes P$ cut is probably also present, becoming important for large s and -t, but with $\theta_{cm} << 90^{\circ}$.

It is convenient to divide up the description of the parametrization in a similar way.

(1) Regge pole contributions at small -t

The three leading Regge pole trajectories exchanged in πp scattering are the P, f and ρ. As was the case in the analysis of N-N scattering it is convenient to write each meson-Reggeon residue in terms of two functions, $B_R(t)$ and $B_Q(t)$ such that

$$\beta(\pi^{\pm}\pi^{\pm};R)\ \beta(pp;R) \equiv \left[B^R(t) + B^Q(t)\right] \qquad (5.3.1)$$

with notation as for (1.5.4) and (3.4.7); such that

$B^R(t) << B^Q(t)$ for $-t \gtrsim 3$ $(GeV/c)^2$ and

$B^Q(t) << B^R(t)$ for $-t \lesssim 2$ $(GeV/c)^2$. Note that the B's are in general different for each exchange and need not be the same for πp as for N-N scattering. The RPCA model may then be used to deduce properties of $B^R(t)$ and the QIM to determine properties of $B^Q(t)$. The parametrization of the Pomeron and R-type parts of the ρ and f will now be specified.

The RPCA model predicts the ratio of the Pomeron contributions to πp and pp helicity non-flip amplitudes to be (see (1.5.4) and the following description)

$$\left[\frac{A(\pi p\to\pi p;P)}{A(pp\to pp;P)}\right]_{\text{RPCA, non-flip}} = \frac{\beta(\pi\pi;P)}{\beta_{\frac{1}{2}\frac{1}{2}}(pp;P)}\left(1-\frac{t}{0.9}\right) = \frac{2}{3}\times\frac{1}{1.14}\left(1-\frac{t}{0.9}\right) \qquad (5.3.2)$$

where $\left(1-\frac{t}{0.9}\right)$ is an approximation to the ratio of electromagnetic form factors, and the 1.14 is the f/ω EXP-breaking factor which is applied only at baryon vertices. It was found, however, that better agreement with the higher energy $\frac{d\sigma}{dt}$ (πp) data could be achieved by multiplying the pp Pomeron (defined by (1.5.4), (3.2.1) and (3.2.4)) by the modified factor :

$$\frac{A(\pi p\to\pi p;P)}{A(pp\to pp;P)} = \frac{2}{3}\cdot\frac{1}{1.14}\left[\left(1-\frac{t}{0.9}\right)+2.09\,t^2\,e^{1.7t}\right] \qquad (5.3.3)$$

which reduces to (5.3.2) at $t = 0$ and as $t\to-\infty$.

Similarly, the "R" type parts of the ρ and f contributions by multiplying the parametrization used for $N_0(pp)$ by the ratio of the $\pi\pi R$ to pp RPCA vertex couplings and by the ratio of the e-m form factors, $\left(1-\frac{t}{0.9}\right)$. The pp$R$ vertex couplings are given by (3.2.1). The $\pi\pi R$ couplings are

$$\beta^{\text{RPCA}}(\pi\pi;f) = \frac{2}{3}\,f_\omega\sqrt{\frac{\pi\alpha'_\omega}{2}}$$

$$\beta^{\text{RPCA}}(\pi\pi;\rho) = \frac{2}{3}\,f_\omega\sqrt{\frac{\pi\alpha'_\omega}{2}}\cdot\begin{cases}+1 \text{ for } \pi^+p \text{ scattering}\\ -1 \text{ for } \pi^-p \text{ scattering}\end{cases} \qquad (5.3.4)$$

(notation as in (3.2.1)). It was also found necessary to modify the absorptive correction to the ρ (see 1.5.6) by multiplying the real part by $(1-53.6t)e^{8t}$. This is to prevent substantial differences arising between $\frac{d\sigma}{dt}$ ($\pi^\pm p$) in the range $-1>t>-3$ $(GeV/c)^2$. This modification makes only a slight difference to the NN fits presented in Chapter 3.

(2) $\underline{1 \lesssim -t \lesssim 3.5\ (\mathrm{GeV/c})^2}$

As discussed in Section 5.2 an extra I = 0 term is needed for $-1 \lesssim t \lesssim -3.5\ (\mathrm{GeV/c})^2$ in addition to the P, f and ρ of the RPCA model. This is likely to be an $f \otimes P$ cut, the general form for which is given by (3.3.3). The same $R \otimes P$ trajectory is used here as in N-N scattering. Making the assumption that d>>lns in the fitted energy range, a suitable t dependence is achieved with

$$\frac{F(t)}{d} = -105.1\ e^{1.3t} \cdot \bar{s}_{RP}^{(\alpha^{o}_{RP} + \alpha'_{RP}t - \alpha_{RP}(t))} \qquad (5.3.5)$$

(notation as for (3.5.10)).

(3) $\underline{t \lesssim -3.5\ (\mathrm{GeV/c})^2}$

It was argued in Section 5.4, that an I = 0 term with properties consistent with an $f \otimes P$ cut is necessary to explain the behaviour of the measured differential cross section on the large -t side of the interference phenomenon at $t \simeq -3.5\ (\mathrm{GeV/c})^2$. This is included in the parametrization by adding an extra term to the t dependence of the $f \otimes P$ cut, thus

$$(5.3.5) \rightarrow (5.3.5) - \left[\frac{1}{1+\left(\frac{15}{1+t^2}\right)^2} - \frac{1}{1+15^2}\right] \times 82.4 \times e^{1.06t} \left[1+0.047\ e^{-0.5t}\right] \qquad (5.3.6)$$

The exponential factor ensures that the $f \otimes P$ cut, which does not contribute to the Quark Interchange kernel diagrams (see Chapter 2) falls off faster as $s \to \infty$, $\frac{t}{s}$ fixed than the s^{-3} Dimensional Counting Rule behaviour. This means that the ρ (to be described next and which obeys the DCR) is the leading term in this limit.

A good account of the large angle $\pi^{\pm}p$ data is obtained with the following parametrization of the "Q" part of the ρ. A suitable t dependence, consistent with the requirements of the D.C.R. (see (5.2.5)), is achieved by multiplying the t dependence of the Q type part of the ρ contribution to $N_0(pp)$ by a constant times the ratio of the electromagnetic form factors of the pion and proton ie. by substituting

$$B_Q^{\pi p}(t) = B_Q^{pp}(t) \times 0.90, \begin{matrix}(+1 \text{ for } {}^{+}_{-}p \\ (-1 \text{ for } {}^{+}_{-}p\end{matrix} \qquad (5.3.7)$$

into (1.5.4) via (5.3.1) with N = 1 for $\pi p \to \pi p$. The value of the constant has been defined by fitting to the data.

As noted in Section 2.3 any number of daughters may contribute to leading order in $\frac{1}{s}$ as $s \to \infty$ with $\frac{t}{s}$ fixed, becoming important at large scattering angles. The effect of such daughter terms is to multiply the parent contribution by a polynomial in $\frac{t}{s}$ (see (2.3.5)). That such daughters must be present can be seen by noting that π^+p and π^-p scattering are related by crossing $s \leftrightarrow u$, and that the ρ exchange has C = -1 and so contributes with opposite sign to π^+p and π^-p scattering. The ρ contribution must therefore be antisymmetric under interchange of s and u. This condition cannot be satisfied if only the parent contribution occurs.

The parametrization of the ρ contribution is completed by replacing

$$B_Q^{\pi p}(t) \to B_Q^{\pi p}(t) \times b\left(\frac{t}{s}\right) \qquad (5.3.8)$$

where

$$b\left(\frac{t}{s}\right) = \frac{1}{2}\left[1 + \frac{1}{1 + \frac{t}{s}}\right] = \frac{1}{2}\left[2 - \frac{t}{s} + \left(\frac{t}{s}\right)^2 - \ldots\right]$$

In the region where s, -t, -u are all large, the ρ amplitude then behaves like

$$A(\pi p;\rho) \sim \frac{1}{st^2}\left[1 + \frac{1}{1+\frac{t}{s}}\right] \sim \frac{1}{t^2}\left[\frac{1}{s} - \frac{1}{u}\right] \qquad (5.3.9)$$

since $u \simeq -(s+t)$. The ρ contribution is therefore approximately antisymmetric under $s \leftrightarrow u$ at large angles and high energy. This particular antisymmetric form was chosen as it gives a slightly improved fit to the large angle data.

Using this parametrization a good description is achieved of all the data except for the recent $\pi^- p$ at $p_{lab} = 200$ GeV/c. The theoretical curve does not posses the minimum observed at $t \simeq -4$ $(GeV/c)^2$ or the subsequent maximum, but continues to fall rapidly with increasing -t.

This shortcoming can readily be rectified if a $P \otimes P$ term is added to the parametrization , together with a modification to the Pomeron t dependence at large -t. These contributions can be successfully written as

$$-1.59\ s^{\alpha_P}\ e^{-i\frac{\pi}{2}\alpha_P + 0.8t} + \frac{1.40}{\left(\ln s - i\frac{\pi}{2}\right)}\ S^{\alpha_{P\otimes P}}\ e^{-i\frac{\pi}{2}\alpha_{P\otimes P}+0.05t} \qquad (5.3.10)$$

where $\alpha_P = 1.067 + 0.1t$ and $\alpha_{P\otimes P} = 1.134 + .05t$ (see equation (3.3.1)). The first term is an addition to the previously described Pomeron which is important only for $-t \gtrsim 3$ $(GeV/c)^2$ and the second term is the $P \otimes P$ cut. These interfere destructively to produce the required minimum.

The final fits to $\frac{d\sigma}{dt}(\pi^{\pm}p)$ are shown in Figs. (5.3.1) and (5.3.2) and give a good overall account of the data.

5.4 Conclusion

In this chapter the philosophy of hadronic elastic scattering developed in Chapters 1 and 2 has been applied to the study of the $\pi^{\pm}p$ differential cross-seciton data. A good fit to $\frac{d\sigma}{dt}(\pi^{\pm}p)$ has been obtained with a parametrization based on those evolved in Chapters 3 and 4 to account for the experimental measurements of the various N-N elastic scattering observables. Indeed the structure of the helicity non-flip $\pi^{\pm}p$ scattering amplitudes is found to be remarkably similar to that deduced earlier for the N-N helicity amplitudes.

i.e. 1. for $-t \lesssim 1$ $(GeV/c)^2$ the principal contributions come from Regge pole terms - the Pomeron which dominates at high energy, supplemented by meson-Reggeons which gain in relative importance as energy falls.

2. for $-t \gtrsim 1$ $(GeV/c)^2$, but with θ_{cm} still not large Regge cuts are important, although the evidence for these is less clear cut in the πp system.

3. at large centre of mass scattering angles meson-Regge pole terms are again important. At these large -t values their trajectories are approaching integers — the leading ones, -1 — and their residues are such that the fixed angle energy dependence is in accordance with the Dimensional Counting Rule.

Fig. (5.2.1)

Energy dependence of $\frac{d\sigma}{dt}$ $(\pi^- p)$ at $t = -2$ $(GeV/c)^2$

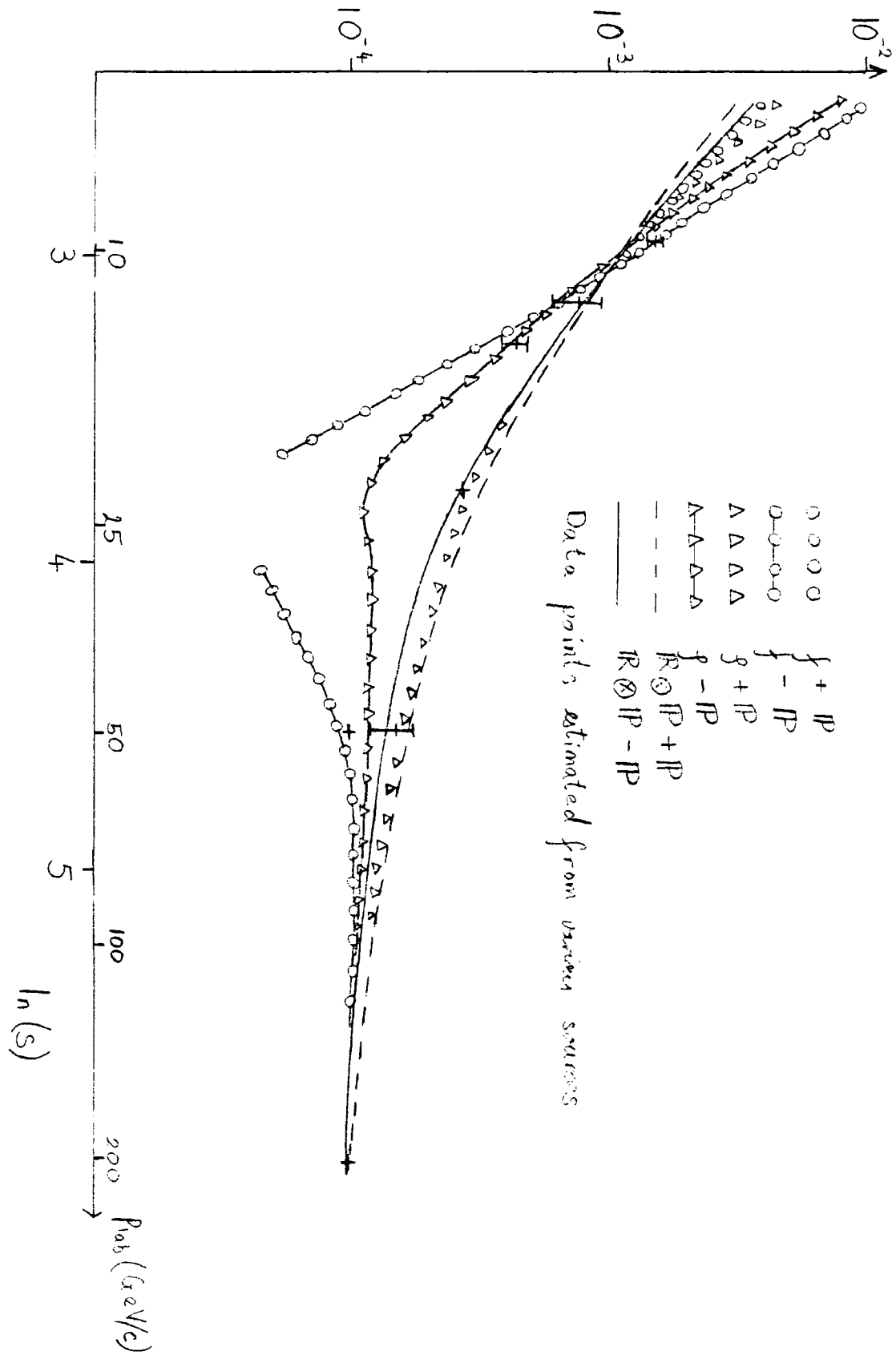

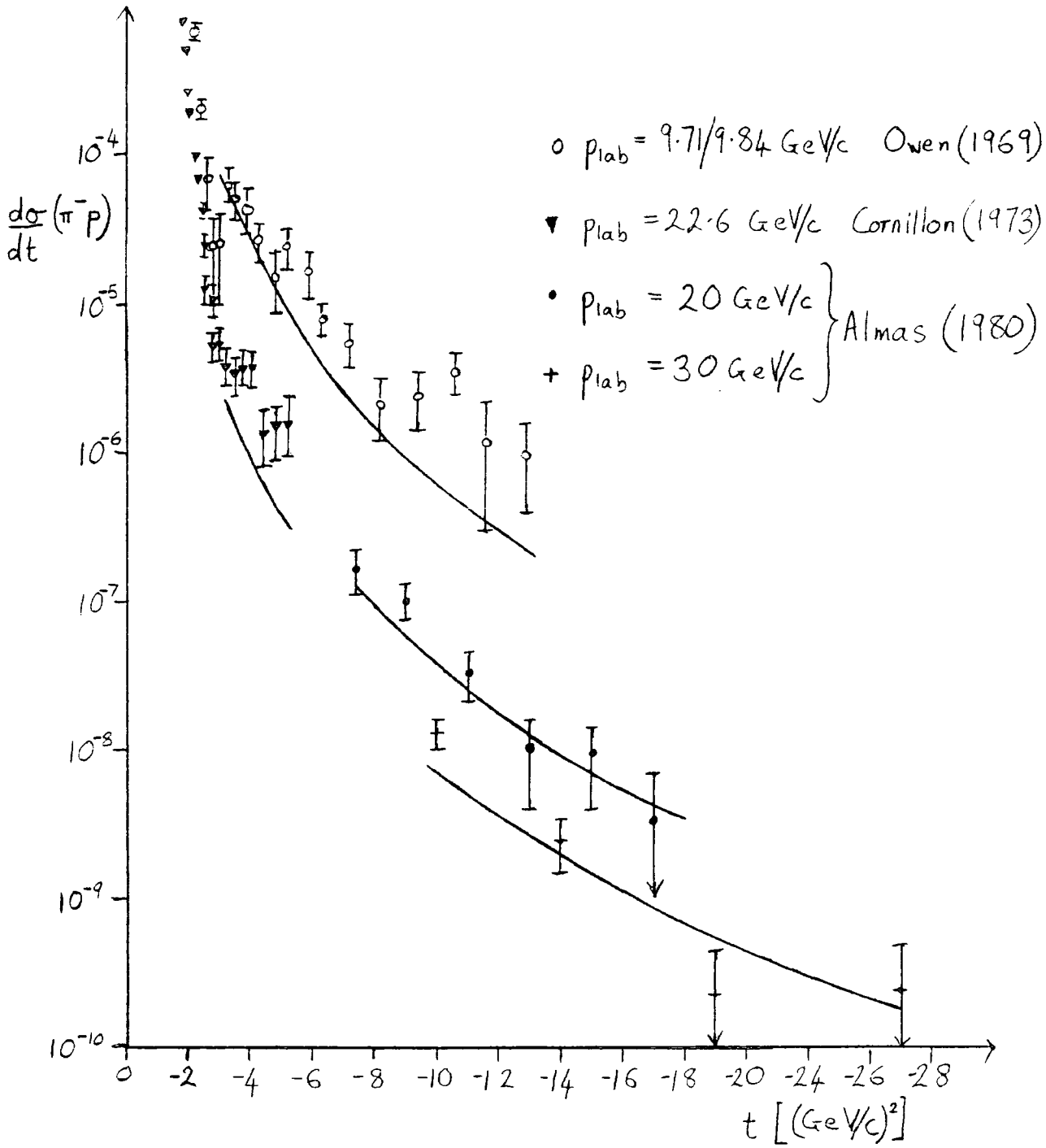

Fig. (5.2.2)

Curves corresponding to A ~ $\frac{1}{st^2}$ compared with $\frac{d\sigma}{dt}$ (π^-p) data at large angles

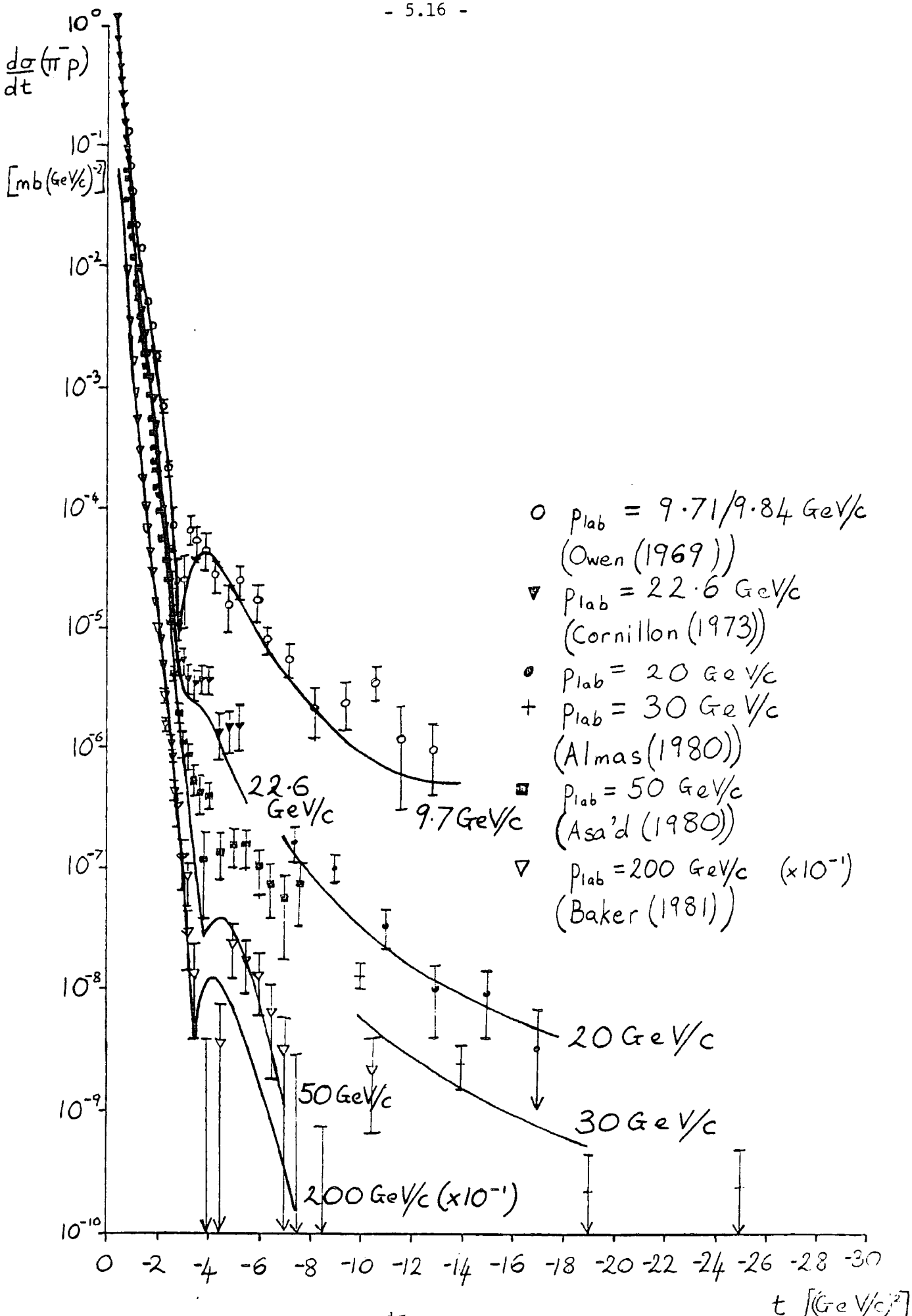

Fig. (5.3.1) : The fit to $\frac{d\sigma}{dt}$ ($\pi^- p$)

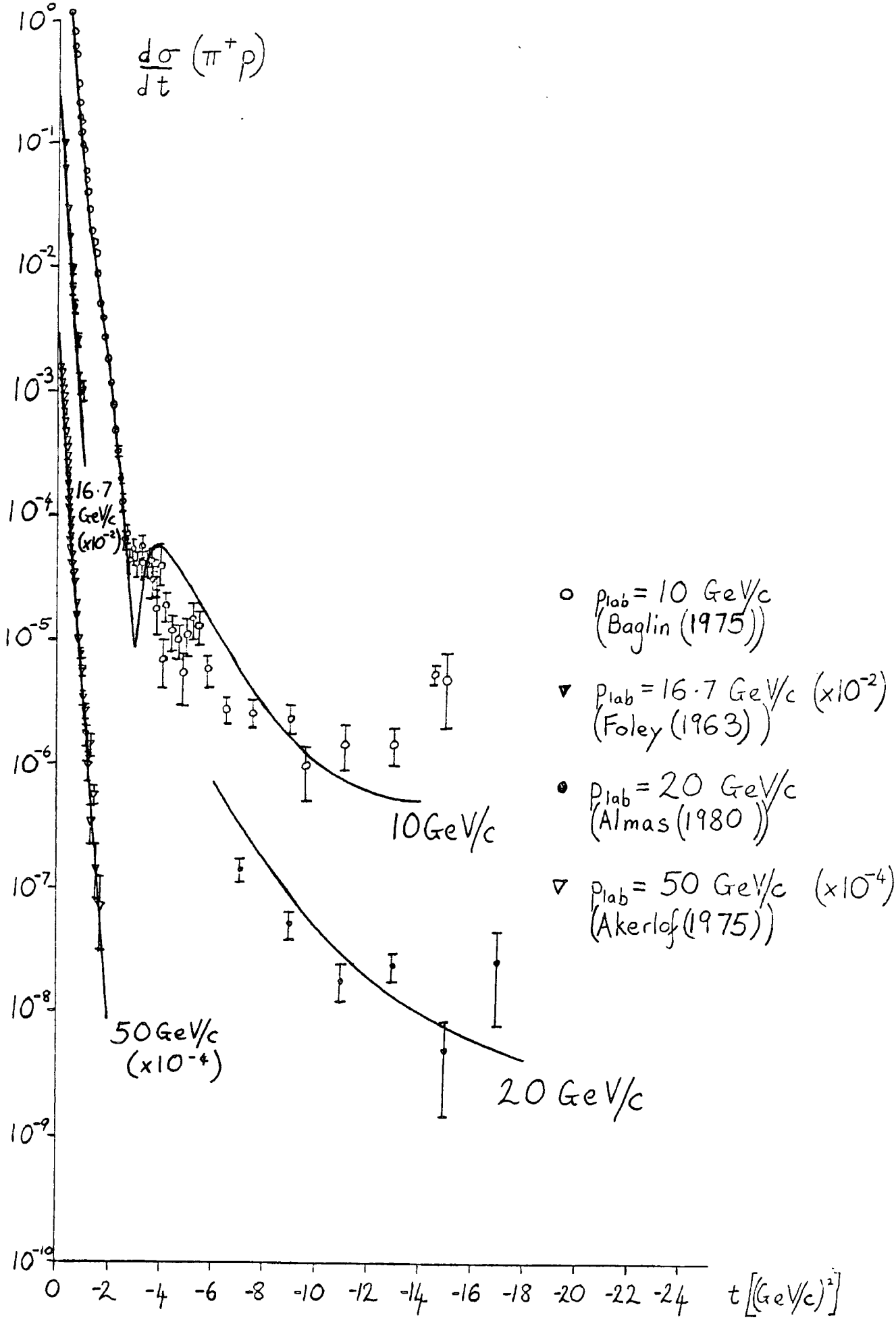

Fig. (5.3.2) : The fit to $\frac{d\sigma}{dt}(\pi^+ p)$

Conclusions

A Regge model for the elastic scattering of hadrons at all angles has been developed, which combines the best features of a conventional Regge model and a constituent exchange model. The Regge pole model for small angles is based on the Reggeon-Photon Coupling Analogy (RPCA) of Collins et al. The Quark Interchange mechanism of Brodsky et al has been selected as best able to describe large angle elastic scattering. (This results in power law scaling behaviour given by the Dimensional Counting Rule). It is argued that the Quark Interchange kernel diagrams provide the large -t limit of meson-Reggeon exchange, and that the highest lying of these trajectories approach -1 as $t \to -\infty$. The RPCA trajectories have been modified accordingly. Similarly the Reggeon residues are constrained to result in Dimensional Counting Rule behaviour in the limit $s \to \infty$ $\frac{-t}{s}$ fixed. The ratios of helicity amplitudes in this limit are as predicted by the Quark Interchange model.

This structure has been applied to the study of nucleon-nucleon differential cross sections, polarizations and spin correlation parameters, and the πp differential cross sections. A consistent pattern has emerged which is at its clearest in $d\sigma/dt$ (pp). For $-t \lesssim 1$ $(GeV/c)^2$ conventional Regge pole terms dominate. In this region their trajectories approximate to straight lines.

For $-t \gtrsim 1$ $(GeV/c)^2$, but with $\frac{-t}{s}$ still small, cut terms become important. Clear evidence now exists for the presence of a $\mathbb{P} \otimes \mathbb{P}$ cut in the natural parity helicity non-flip amplitudes of the pp, $\bar{p}p$ and $\pi^- p$ processes. Minima caused by Pomeron - $\mathbb{P} \otimes \mathbb{P}$ interference are observed at

$t \simeq -1.4$ $(GeV/c)^2$, p_{lab} = 200 GeV/c and above in $d\sigma/dt$ (pp); at $t \simeq -1.4$ $(GeV/c)^2$, p_{lab} = 50 GeV/c and above in $d\sigma/dt$ ($\bar{p}p$); and at $t \simeq -4$ $(GeV/c)^2$, p_{lab} = 200 GeV/c in $d\sigma/dt$ ($\pi^- p$).

In this intermediate t region at lower energies all observables for which there are significant amounts of data have shown the need for an extra term or terms with properties inconsistent with those of the meson-Reggeons, Pomeron or $\mathbb{P}\otimes\mathbb{P}$ cut. This contribution has been successfully parametrized as a combination of $\mathbb{R}\otimes\mathbb{P}$cuts (a single $f\otimes\mathbb{P}$ cut in the case of πp scattering) with a common trajectory intermediate between the Reggeons and the Pomeron, but with different factors of the form $(d + \ln s)^{-1}$, where d is a complex number.

At large angles, the meson-Reggeons re-emerge to become the dominant contribution resulting in power law scaling behaviour. Fits have been presented which give a good overall account of the experimental data at all angles for pp, pn, $\bar{p}p$ differential cross-sections, polarization and spin correlation parameters (where available) and $\pi^- p$ and $\pi^+ p$ differential cross-sections.

To conclude, it has been demonstrated that all the available data on elastic scattering of hadrons can be explained in terms of the exchange of Regge poles and cuts, provided that the trajectories and residues of the meson-Reggeons are constrained to give Dimensional Counting Rule behaviour at large -t.

References

Abe et al (1976) Physics Letters 63B p.239

Abshire et al (1974) Physcial Review Letters 32 p.1261

Akerlof et al (1975) Physics Letters 59B p.197 and
Physical Review Letters 35 p.1406

Akerlof et al (1976) Physical Review D14 p.2864

Allaby et al (1967) Physics Letters 25B p.156

Allaby et al (1968) Physics Letters 28B p.68

Allaby et al (1973) Nuclear Physics B52 p.316

Almas et al (1980) Physics Letters 93B p.199

Ankenbrandt et al (1968) Physcial Review 170 p.1223

Antipov et al (1973) Nuclear Physics B57 p.333

Asa'd et al (1980) Paper presented at Madison Conference July 1980

Asa'd et al (1982) Physics Letters 108B p.51

Auer et al (1977) Physics Letters 70B p.475

Baglin et al (1975) Nuclear Physics B98 p.365

Baker et al (1981) Physics Review Letters 47 p.1683

Barnes et al (1978) Physical Review Letters 41 p.1260

de Bellefon et al (1978) Cern preprint, 1978

Berger et al (1978) Physical Review D17 p.2971

Berglund et al (1979) Nuclear Physics B137 p.276

Borghini et al (1967) Physics Letters 24B p.77

Borghini et al (1971) Physics Letters 36B p.501

Brodsky et al (1973a) Physical Review D8 p.287

Brodsky et al (1973b) Physical Review D8 p.4117

Brodsky et al (1973c) From "High Energy Collisions", Ed. Quigg, Pub. A.I.P.

Brodsky et al (1975a) Physical Review D11 p.1309

Brodsky et al (1977) SLAC Preprint SLAC-PUB-2057 (Dec. 1977)

Brodsky et al (1979a) Physical Review D20 p.2278

Brodsky et al (1979b) SLAC Preprint SLAC-PUB-2294 (March 1979)

Brodsky et al (1979c) Brodsky, Lepage, Frishman, Sachrajda - private communication

CERN (1980) Preprint EP 80/29

Chabaud et al (1972) Physics Letters 38B p.449

Collins et al (1976a) Nuclear Physics B113 p.34

Collins et al (1977) "An Introduction to Regge Theory and High Energy Physics", P.D.P. Collins, ~~Oxford~~ Cambridge University Press.

Collins et al (1978b) Physics Letters 73B p.330

Collins et al (1978c) Durham University preprint Sept. 1978

Collins et al (1978d) Journal of Physics G4 p.L201

Collins et al (1981) Durham University Preprint Sept. 1981

Coon et al (1978) Physical Review D18 p.1451

Crabb et al (1978) Physical Review Letters 41 p.19 and Physical Review Letters 41 p.1257

Crabb et al (1979) Physcial Review Letters 43 p.983

Diebold et al (1975) Physical Review Letters 35 p.632

Drell and Yan (1970) Physical Review Letters 24 p.181

Eide et al (1973) Nuclear Physics B60 p.173

Faisler et al (1981) Physical Review D23 p.33

Farrar and Wu (1975) Nuclear Physics B85 p.50

Fernow et al (1974) Physics Letters 52B p.243

Foley et al (1963) Physical Review Letters 11 p.425

Gaidot et al (1975) Physics Letters 57B p.389

Gaidot et al (1976) Physics Letters 61B p.103

Hicks et al (1975) Physical Review D12 p.2594

Irving (1975) Nuclear Physics B101 p.263

Jacob and Wick (1959) Annals of Physics (N.Y.) 7 p.404

Kaplan et al (1982) Fermilab preprint 82/40 - Exp.

de Kerret et al (1977) Physics Letters 68B p.374

Klem et al (1977) Physical Review D15 p.602

Kramer et al (1978) Physical Review D17 p.1709

Krisch et al (1979) Brookhaven National Laboratory Report No. BNL 50947, p. 346

Kroll et al (1978) Journal of Physics G 4 p.1003

Kroll et al (1979) Journal of Physics G5 p.1179

Kwak et al (1975) Physics Letters 58B p.223

Landshoff and Polkinghorne (1973) Physics Letters 44B p.293

Landshoff (1974a) Physical Review D10 p.1024

Landshoff and Pritchard (1980) Cambridge University DAMTP Preprint 80/4

Makdisi et al (1980) Physical Review Letters 45 p.1529

Miettinen et al (1977) Physical Review D16 p.549

Nagy et al (1979) Nuclear Physics B150 p.221

Nussinov (1976a) Physical Review D14 p.246

O'Fallon et al (1974) Physical Review Letters 32 p.77

O'Fallon et al (1977) Physical Review Letters 39 p.733

Owen et al (1969) Physical Review 181 p.1794

Politzer (1974) Physics Reports 14C p.130

Ratner et al (1977) Physical Review D15 p.604

Russ et al (1977) Physical Review D15 p.3139

Sivers et al (1976) Physics Reports 23C p.1

Shijong Ryang (1978) Osaka University preprint OU-HET, 22nd June, 1978

Snyder et al (1978) Physical Review Letters 41 p.781

Stone et al (1977) Physical Review Letters 38 p.1315

Stone et al (1978) Nuclear Physics B143 p.20

West (1970) Physics Review Letters 24 p.1206

Williams (1970) Physical Review D1 p.1312

Wright (1978) Ph.D.Thesis, Univ. of Durham

Appendix A : Definitions and Notation

Fig. (A.1) demonstrates some of the notation for 2→2 scattering processes used throughout this work. p_i and λ_i (i = A, B, C,D) are respectively the 4-momentum and the helicity of particle i. As only particles of spin $\frac{1}{2}$ and spin zero are dealt with, λ_i takes one of three values, + (for $+\frac{1}{2}$), 0, or - (for $-\frac{1}{2}$). $\beta^{\lambda_A\lambda_C}(AC;\mathbb{R})$ illustrates the notation for the coupling of a Regge exchange, $\mathbb{R}$, to the vertex AC.

An helicity amplitude for such a diagram would be written

$$A^{\lambda_A\lambda_B}_{\lambda_C\lambda_D}(AB\rightarrow CD;\mathbb{R})$$

Frequent use is made of the Mandelstam variables; s,t,u; which are now defined :

$$\begin{aligned} s &= (p_A + p_B)^2 \\ t &= (p_A - p_C)^2 \\ u &= (p_A - p_D)^2 \end{aligned} \qquad (A.1)$$

The incident momentum in the laboratory frame, p_{lab}, is often used to label a data set.

Natural units are used throughout this work, with energies given in GeV and cross sections in millibarns.

A differential cross section in this sytem of units is obtained thus for large s

$$\frac{d\sigma}{dt}\ (mb/(GeV/c)^2) = \frac{0.3893}{16\ \pi s^2}|A(s,t)|^2 \qquad (A.2)$$

and a total cross section thus

$$\sigma_T \text{ (mb)} = \frac{0.3893}{s} \text{ Im } [A(s,t=0)] \qquad \text{(A.3)}$$

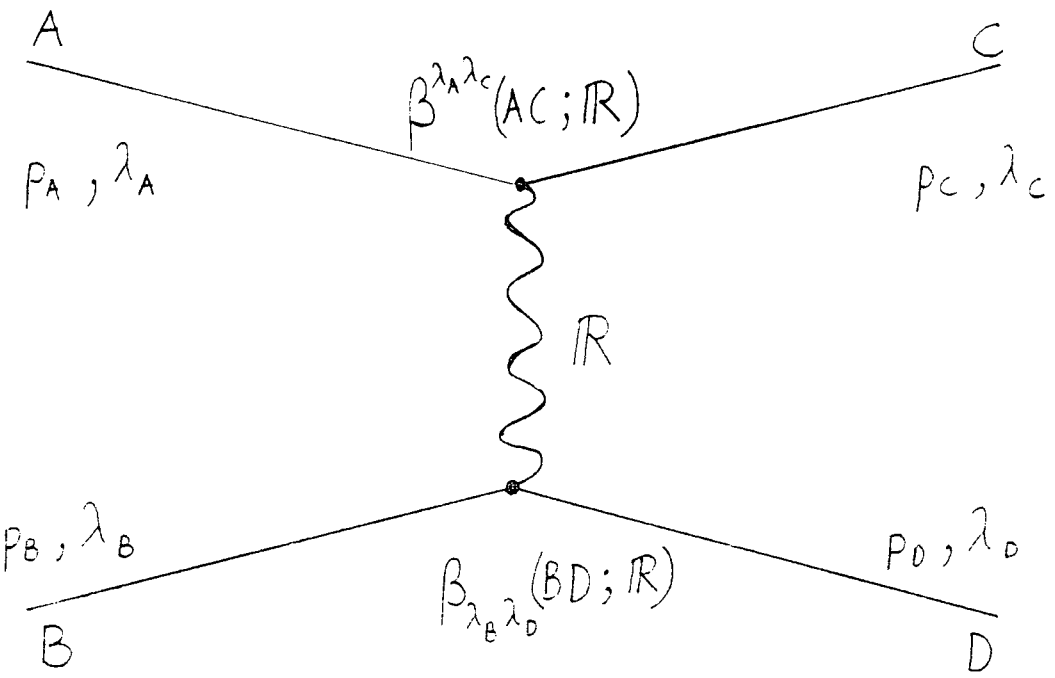
A
C
$\beta^{\lambda_A\lambda_C}(AC;\mathbb{R})$
p_A, λ_A
p_C, λ_C
$\mathbb{R}$
p_B, λ_B
p_D, λ_D
$\beta_{\lambda_B\lambda_D}(BD;\mathbb{R})$
B
D

FIG. A.1

Appendix B : Helicity amplitudes and spin observables for nucleon-nucleon scattering

Jacob-Wick helicity conventions (Jacob and Wick (1959)) are used throughout.

Before imposing symmetry laws upon the system there are sixteen independent N-N helicity amplitudes $A^{\lambda_A\lambda_C}_{\lambda_B\lambda_D}$. Parity invariance relates certain of these, reducing the number of independent amplitudes to eight:

$$A^{\lambda_A\lambda_C}_{\lambda_B\lambda_D} = A^{-\lambda_A-\lambda_C}_{-\lambda_B-\lambda_D} \tag{B.1}$$

These are further reduced to six by applying time reversal invariance:

$$A^{\lambda_A\lambda_C}_{\lambda_B\lambda_D} = A^{\lambda_C\lambda_A}_{\lambda_D\lambda_B} \tag{B.2}$$

Additionally, for identical particle scattering

$$A^{\lambda\ +}_{\lambda\ -} = A^{\lambda\ -}_{\lambda\ +} \tag{B.3}$$

(nucleons are identical for this purpose). The above relations are summarized in Table (B.1). The five independent N-N amplitudes are conventionally named ϕ_i (i = 1,2,3,4,5). These are defined in Table (B.2).

It is frequently convenient to use helicity amplitudes which are purely natural or unnatural parity. The natural parity amplitudes N_0, N_1, N_2 and unnatural parity amplitudes U_0 and U_2 are given in terms of the ϕ's in Table (B.3). The subscripts of the N's and U's refer to the number of flip vertices in a diagram contributing to the amplitude. Note that there is no single flip unnatural parity amplitude.

In terms of helicity amplitudes, the differential cross section (spin averaged) is given by

$$\frac{d\sigma}{dt} = \tfrac{1}{2}K(s)\left[|\phi_1|^2 + |\phi_2|^2 + |\phi_3|^2 + |\phi_4|^2 + 4|\phi_5|^2\right] \qquad (B.4)$$

$$= K(s)\left[|N_0|^2 + 2|N_1|^2 + |N_2|^2 + |U_0|^2 + |U_2|^2\right]$$

$$\equiv K(s)\, D$$

where $K(s)\left[= \dfrac{0.3893}{16\,\pi\, s^2} \text{ in the units used here}\right]$ is a kinematical factor. The spin dependent observables used in this work are now given:

Polarization (or analysing power), P, by

$$P\,D = -\,\mathrm{Im}\left[\left(\phi_1 + \phi_2 + \phi_3 - \phi_4\right)\phi_5^*\right] \qquad (B.5)$$

$$= -\,2\,\mathrm{Im}\left[\left(N_0 - N_2\right)N_1^*\right]$$

Correlation parameters A_{ij}, by

$$A_{nn}\,D = \mathrm{Re}\left[\phi_1\,\phi_2^* - \phi_3\,\phi_4^*\right] + 2|\phi_5|^2 \qquad (B.6)$$

$$= -\,2\,\mathrm{Re}\left[N_0\,N_2^* - U_0\,U_2^*\right] + 2|N_1|^2$$

$$A_{ss}\,D = \mathrm{Re}\left[\phi_1\,\phi_2^* + \phi_3\,\phi_4^*\right] \qquad (B.7)$$

$$= 2\,\mathrm{Re}\left[N_0\,U_2^* - U_0\,N_2^*\right]$$

$$A_{s1}\,D = \mathrm{Re}\left[\left(\phi_1 + \phi_2 - \phi_3 + \phi_4\right)\phi_5^*\right] \qquad (B.8)$$

$$= 2\,\mathrm{Re}\left[\left(U_0 + U_2\right)N_1^*\right]$$

$$A_{11}\,D = \tfrac{1}{2}\left[-|\phi_1|^2 - |\phi_2|^2 + |\phi_3|^2 + |\phi_4|^2\right] \qquad (B.9)$$

$$= 2\,\mathrm{Re}\left[U_2\,N_2^* - N_0\,U_0^*\right]$$

The definition of the A_{ij} in terms of experimentally measured quantities may be found in Section 1.3.

Table (B.1)

The independent N-N helicity amplitudes

$$A^{++}_{++} = A^{--}_{--}$$

$$A^{+-}_{+-} = A^{-+}_{-+}$$

$$A^{+-}_{-+} = A^{-+}_{+-}$$

$$A^{++}_{--} = A^{--}_{++}$$

$$\left.\begin{aligned} A^{++}_{+-} = A^{++}_{-+} = A^{--}_{+-} = A^{--}_{-+} \\ A^{+-}_{++} = A^{-+}_{++} = A^{+-}_{--} = A^{-+}_{--} \end{aligned}\right\}$$ all equal for C and D identical particles

Table (B.2)

Definition of ϕ_i's for N-N scattering

$$\phi_1 \equiv A^{++}_{++}$$

$$\phi_2 \equiv A^{+-}_{+-}$$

$$\phi_3 \equiv A^{++}_{--}$$

$$\phi_4 \equiv A^{+-}_{-+}$$

$$\phi_5 \equiv A^{++}_{+-}$$

Table (B.3)

The Natural and Unnatural Parity Helicity Amplitudes

$$N_0 = (\phi_1 + \phi_3)/2$$

$$N_1 = \phi_5$$

$$N_2 = (\phi_4 - \phi_2)/2$$

$$U_0 = (\phi_1 - \phi_3)/2$$

$$U_2 = (\phi_4 + \phi_2)/2$$

Appendix C : Implications of Fermi-Dirac statistics for nucleon-nucleon helicity amplitudes

Since all the external particles in proton proton elastic scattering are identical fermions the pp helicity amplitudes (see Appendix B) must obey the following relations :

$$\begin{aligned} \phi_1^{PP}(\theta) &= \phi_1^{PP}(\pi-\theta) \\ \phi_2^{PP}(\theta) &= \phi_2^{PP}(\pi-\theta) \\ \phi_3^{PP}(\theta) &= -\phi_4^{PP}(\pi-\theta) \\ \phi_5^{PP}(\theta) &= -\phi_5^{PP}(\pi-\theta) \end{aligned} \qquad (C.1)$$

(θ is the centre of mass scattering angle)

Considering protons and nutrons to be identical except for the value of the I_3 quantum number, similar relationships apply to combinations of np→np and np→pn scattering amplitudes. Defining

$$\phi_i^{+} = \phi_i^{np\to np} + \phi_i^{np\to pn} \qquad (C.2)$$

and $$\phi_i^{-} = \phi_i^{np\to np} - \phi_i^{np\to pn}$$

these are

$$\begin{aligned} \phi_1^{+}(\theta) &= \phi_1^{+}(\pi-\theta) \\ \phi_2^{+}(\theta) &= \phi_2^{+}(\pi-\theta) \\ \phi_3^{+}(\theta) &= -\phi_4^{+}(\pi-\theta) \\ \phi_5^{+}(\theta) &= -\phi_5^{+}(\pi-\theta) \end{aligned} \qquad (C.3)$$

and

$$\begin{aligned}
\bar{\phi}_1(\theta) &= -\bar{\phi}_1(\pi-\theta) \\
\bar{\phi}_2(\theta) &= -\bar{\phi}_2(\pi-\theta) \\
\bar{\phi}_3(\theta) &= \bar{\phi}_4(\pi-\theta) \\
\bar{\phi}_5(\theta) &= \bar{\phi}_5(\pi-\theta)
\end{aligned} \tag{C.4}$$

Appendix D : Relationships between contributions to the NN helicity amplitudes in the Quark interchange model

The natural and unnatural parity amplitudes are given in terms of the ϕ's in Appendix B, Table B.3. Inserting the pp QI helicity amplitudes (1.4.27) into these relations yields

$$\left.\begin{aligned} N_0 &= \frac{1}{18}\left[45\, f(s,t,u) + 48\, f(s,u,t)\right] \\ N_1 &= 0 \\ N_2 &= U_2 = -U_0 = \frac{-1}{18}\left[17f(s,t,u) + 14f(s,u,t)\right] \end{aligned}\right\} \quad (D.1)$$

Similarly for $np \to np$

$$\left.\begin{aligned} N_0 &= \frac{1}{18}\left[36\, f(s,t,u) + 42f(s,u,t)\right] \\ N_1 &= 0 \\ N_2 &= U_2 = -U_0 = \frac{1}{18}\left[8f(s,t,u) + 8f(s,u,t)\right] \end{aligned}\right\} \quad (D.2)$$

and for $\bar{p}p \to \bar{p}p$

$$\left.\begin{aligned} N_0 &= \frac{1}{18}\left[48f(u,t,s) + 48f(u,s,t)\right] \\ N_1 &= 0 \\ N_2 &= U_2 = -U_0 = \frac{-1}{18}\left[14\, f(u,t,s) + 17f(u,s,t)\right] \end{aligned}\right\} \quad (D.3)$$

(D.1) and (D.2) can be combined to produce I = 0 and I = 1 amplitudes :

$$\left.\begin{aligned} N_0\ (I=0) &= \tfrac{1}{2}\left[N_0(pp) + N_0(pn)\right] = \frac{1}{36}\left[81f(s,t,u) + 90f(s,u,t)\right] \\ N_1\ (I=0) &= \tfrac{1}{2}\left[N_1(pp) + N_1(pn)\right] = 0 \\ N_2\ (I=0) &= U_2(I=0) = -U_0(I=0) = \tfrac{1}{2}\left[N_2(pp)+N_2(pn)\right] = \frac{-1}{36}\left[9f(s,t,u)+6f(s,u,t)\right] \end{aligned}\right\} \quad (D.4)$$

$$\left.\begin{aligned} N_0(I=1) &= \tfrac{1}{2}\left[N_0(pp)-N_0(pn)\right] = \frac{1}{36}\left[9f(s,t,u) + 6f(s,u,t)\right] \\ N_1(I=1) &= \tfrac{1}{2}\left[N_1(pp)-N_1(pn)\right] = 0 \\ N_2(I=1) &= U_2(I=1) = -U_0(I=1) = \tfrac{1}{2}\left[N_2(pp)-N_2(pn)\right] = \frac{-1}{36}\left[25f(s,t,u)+22f(s,u,t)\right] \end{aligned}\right\} \quad (D.5)$$

Now, at large s and -t the forward scattering parts of these isospin amplitudes can be identified with meson-Reggeon exchange contributions as follows

Natural parity, I=0, forward $\leftrightarrow$ f + ω + daughters

Unnatural parity, I=0, forward $\leftrightarrow$ ~~A_1~~ + Z + daughters

Natural parity, I=1, forward $\leftrightarrow$ A_2 + ρ + daughters

Unnatural parity, I=1, forward $\leftrightarrow$ π + B + daughters

Thus, from (D.4) and (D.5) the forward Reggeon components are related by

$$\left.\begin{aligned} &A_0(f+\omega) = -9A_2(f+\omega) = -9A_2(A_1+Z) = 9A_0(A_1+Z) \\ &= 9A_0(\rho+A_2) = -\frac{81}{25}A_2(\rho+A_2) = -\frac{81}{25}A_2(\pi+B) = +\frac{81}{25}A_0(\pi+B) \end{aligned}\right\} \quad (D.6)$$

A similar recombination of pp and $\bar{p}p$ amplitudes to separate components of different charge conjugation is much less useful since the relation between f(s,t,u) and f(u,t,s) depends on the detailed structure of the parametrization chosen.

Appendix E : Symmetry properties of the pp helicity amplitudes assuming N_0 to be dominant

The pp helicity amplitudes must have certain symmetry properties determined by Fermi-Dirac statistics (see Appendix C). In consequence the amplitudes can always be written in the form

$$\begin{aligned}
\phi_1 &\equiv \tilde{\phi}_1(s,t,u) + \tilde{\phi}_1(s,u,t) \\
\phi_2 &\equiv \tilde{\phi}_2(s,t,u) + \tilde{\phi}_2(s,u,t) \\
\phi_3 &\equiv \tilde{\phi}_3(s,t,u) - \tilde{\phi}_4(s,u,t) \\
\phi_4 &\equiv \tilde{\phi}_4(s,t,u) - \tilde{\phi}_3(s,u,t) \\
\phi_5 &\equiv \tilde{\phi}_5(s,t,u) - \tilde{\phi}_5(s,u,t)
\end{aligned} \tag{E.1}$$

Combining these to form natural and unnatural parity amplitudes

$$\begin{aligned}
N_0 &= \tfrac{1}{2}\left[\tilde{\phi}_1(s,t,u) + \tilde{\phi}_3(s,t,u)\right] + \tfrac{1}{2}\left[\tilde{\phi}_1(s,u,t) - \tilde{\phi}_4(s,u,t)\right] \\
N_{\not 0} &= \tilde{\phi}_5(s,t,u) - \tilde{\phi}_5(s,u,t) \\
N_2 &= \tfrac{1}{2}\left[\tilde{\phi}_4(s,t,u) - \tilde{\phi}_2(s,t,u)\right] - \tfrac{1}{2}\left[\tilde{\phi}_3(s,u,t) + \tilde{\phi}_2(s,u,t)\right] \\
U_0 &= \tfrac{1}{2}\left[\tilde{\phi}_1(s,t,u) - \tilde{\phi}_3(s,t,u)\right] + \tfrac{1}{2}\left[\tilde{\phi}_1(s,u,t) + \tilde{\phi}_4(s,u,t)\right] \\
U_2 &= \tfrac{1}{2}\left[\tilde{\phi}_4(s,t,u) + \tilde{\phi}_2(s,t,u)\right] - \tfrac{1}{2}\left[\tilde{\phi}_3(s,u,t) - \tilde{\phi}_2(s,u,t)\right]
\end{aligned} \tag{E.2}$$

Since the proposed model is a Regge one, it is convenient to choose

$$\tilde{\phi}_i(s,t,u) \gg \phi_i(s,u,t) \quad \text{as} \quad s \to \infty, \ t \text{ fixed} \tag{E.3}$$

Thus, for instance, the P, ρ, A_2, ω, f poles, the $P \otimes P$ and $R \otimes P$ cuts discussed in Chapter 3 all contribute to $\frac{1}{2}[\phi_1(s,t,u)+\phi_3(s,t,u)]$, which, for convenience will be referred to as the forward part of N_0.

Now, except at large angles N_0 is much larger than other naturality amplitudes. Hence, away from this region, the following approximations can be made

$$\begin{aligned} &N_0 >> U_0 \Rightarrow \quad \tilde{\phi}_1(s,t,u) \simeq \tilde{\phi}_3(s,t,u) \\ &N_0 >> N_2,\ U_2 \Rightarrow \tilde{\phi}_2(s,t,u),\ \tilde{\phi}_4(s,t,u) << \tilde{\phi}_1(s,t,u) \\ &N_0 >> N_1 \Rightarrow \tilde{\phi}_5(s,t,u) << \tilde{\phi}_1(s,t,u) \end{aligned} \qquad (E.4)$$

Substituting back into (E.2) gives

$$\begin{aligned} N_\phi &\simeq \tilde{\phi}_1(s,t,u) + \tfrac{1}{2}\tilde{\phi}_1(s,u,t) \\ N_2 &\simeq -\tfrac{1}{2}\tilde{\phi}_1(s,u,t) \\ N_1 &\simeq 0 \\ U_0 &\simeq +\tfrac{1}{2}\tilde{\phi}_1(s,u,t) \\ U_2 &\simeq -\tfrac{1}{2}\tilde{\phi}_1(s,u,t) \end{aligned} \qquad (E.5)$$

Thus, for N_0 much greater than the other maplitudes the requirements of Fermi-Dirac statistics can be satisfied to a good approximation, by adding to the forward parts of the helicity amplitudes crossed terms as follows

$$\begin{aligned} &\text{forward} && \text{backward} \\ N_0 &= \tilde{N}_0(s,t,u) + \tfrac{1}{2}\tilde{N}_0(s,u,t) \\ N_1 &= \tilde{N}_1(s,t,u) - \tilde{N}_1(s,u,t) \\ N_2 &= \tilde{N}_2(s,t,u) - \tfrac{1}{2}\tilde{N}_0(s,u,t) \\ U_0 &= \tilde{U}_0(s,t,u) + \tfrac{1}{2}\tilde{N}_0(s,u,t) \\ U_2 &= \tilde{U}_2(s,t,u) - \tfrac{1}{2}\tilde{N}_0(s,u,t) \end{aligned} \qquad (E.6)$$

This procedure is used to define the total "R"-type contributions to the helicity amplitudes from their forward parts.